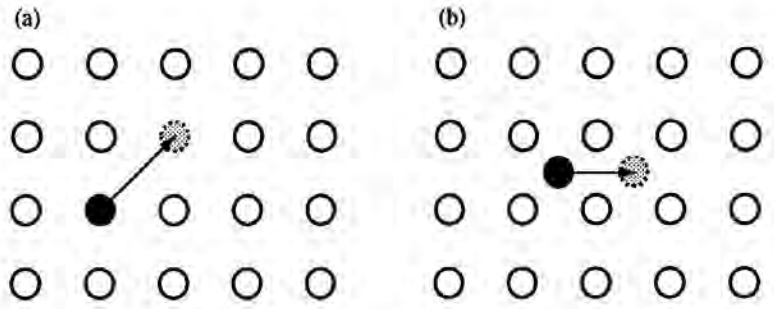


Fig. 8.6. Schematic illustration of (a) substitutional diffusion proceeding through vacancies and (b) interstitial diffusion proceeding through interstitial sites of the lattice.

examples illustrate that completely different dependences are expected for different types of diffusion processes. In the following sections, the characteristics of several diffusion processes are analyzed.

8.3.1 Substitutional diffusion

The diffusion process via vacant substitutional lattice sites is called substitutional impurity diffusion. It is assumed that impurities occupy only substitutional sites of the lattice and that an impurity hop occurs to a vacant, *adjacent* lattice site as illustrated in Fig. 8.6(a). Since *one* vacancy is required for *one* diffusion hop, the substitutional diffusion coefficient is proportional to the vacancy concentration, i.e.

$$D \propto [\mathrm{V}] \,. \tag{8.20a}$$

where the concentration of vacancies, [V], is either the group-III or the group-V vacancy concentration depending on the site which the impurity preferentially occupies. The vacancy concentration depends on a number of parameters such as growth conditions, annealing conditions, stoichiometry of the semiconductor, Fermi level, etc. Consequently, the magnitude of the diffusion coefficient can vary for different diffusion conditions.

Next we consider an impurity with *all* adjacent lattice sites being occupied. Then the impurity cannot diffuse at all. However, not only the impurity, but also a lattice vacancy can diffuse. The probability that the vacancy diffuses to a site adjacent to the impurity is proportional to the vacancy diffusion constant D_V. Thus, the diffusion constant of the impurity is proportional to the product of the vacancy concentration and the vacancy diffusion constant, i.e.

INNOSCIENCE EXHIBIT 1032
INNOSCIENCE v. EPC
IPR2023-01381

https://doi.org/10.1017/CBO9780511599828.011 Published online by Cambridge University Press

$$D \propto [\mathrm{V}] D_{\mathrm{V}} \,. \tag{8.20b}$$

Finally the diffusion constant for substitutional diffusion can be written as

$$D = f[\mathrm{V}] D_{\mathrm{V}} \tag{8.20c}$$

where f is a constant which depends on the crystal structure of the semiconductor (see, for example, Manning, 1968).

Phillips (1973) concluded that the probability of substitutional diffusion does not depend on the atomic size of the diffusing impurity. The author pointed out that different impurities of the same group have similar activation energies in Si and Ge. It was concluded that the similarity in diffusion activation energy indicates that the atomic radii do not play an important role in the activation process. Even though this conclusion seems plausible, the irrelevance of the atomic radius has not been demonstrated in III–V semiconductors. Phillips (1973) further suggested that the long-range Coulomb interaction between charged impurities and charged vacancies influences the probability of substitutional diffusion of impurities. The author suggested that impurities and vacancies with opposite charge tend to associate (electrostatic attraction) resulting in a higher diffusion coefficient. In contrast, the long-range coulombic interaction between impurities and vacancies with the same charge tends to increase the diffusion activation energy, i.e. decrease the probability of diffusion. The role of the charge state of vacancies and other native defects will be further discussed in the following section.

8.3.2 Impurity-defect complex diffusion

Frequently impurities diffuse as impurity-defect complexes rather than as isolated impurity atoms. Two examples of defects which can participate in the diffusion of a complex are shown in Fig. 8.7. The ***Schottky defect*** (Fig. 8.7a) is a vacancy formed by the transfer of a lattice atom to the crystal surface. Schottky defects are more likely to occur in the vicinity of semiconductor surfaces. The ***Frenkel defect*** (Fig. 8.7b) is a vacancy–interstitial pair which is formed by moving a lattice atom to an interstitial site.

The diffusion of impurity-defect complexes has very different characteristics as compared to the diffusion of isolated atoms. Defects can assume different charge states. Shockley and Last (1957) showed that any flaw (defect) can be represented by a series of energy levels which can be occupied or empty depending on the position of the Fermi level. The defect can assume the charge states ..., 2+, 1+, 0, 1−, 2−, ... Depending on the charge state, the interaction of the impurity with the defect will be different. The diffusion of a complex formed by the impurity and the defect of charge state ..., 2+, 1+, 0, 1−, 2−, ... will be

https://doi.org/10.1017/CBO9780511599828.011 Published online by Cambridge University Press

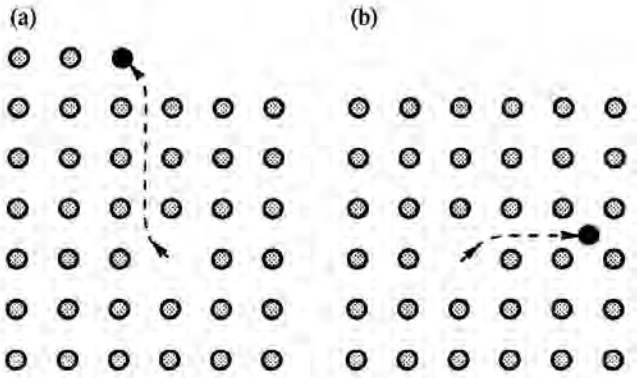


Fig. 8.7. Schematic illustration of point defects: (a) Schottky defect and (b) Frenkel defect.

different for each charge state of the impurity. Assuming that the diffusion coefficient of each complex is independent of other complexes, the effective diffusion coefficient is the linear combination of the diffusion coefficient of each complex (Shaw, 1975). As an example, we assume that the defect is a vacancy with charge states ..., V^{2+}, V^{+}, V^{0}, V^{-}, V^{2-}, ... For an *intrinsic* semiconductor, the effective diffusion is then given by

$$D_i = D_i^0 + D_i^+ + D_i^- + D_i^{2+} + D_i^{2-} + \cdots \tag{8.21}$$

where D_i^s is the diffusion coefficient of the complex formed by a vacancy of charge state s and the impurity under intrinsic conditions*. Under extrinsic conditions, the concentration of vacancies changes. If the concentration of vacancies is much smaller than the total concentration of impurities, then the diffusion coefficient for each complex is proportional to the concentration of the particular vacancy. The *effective* diffusion coefficient in then given by

$$D = D_i^0 \frac{[V^0]}{[V^0]_i} + D_i^+ \frac{[V^+]}{[V^+]_i} + D_i^- \frac{[V^-]}{[V^-]_i} + D_i^{2+} \frac{[V^{2+}]}{[V^{2+}]_i} + D_i^{2-} \frac{[V^{2-}]}{[V^{2-}]_i} + \cdots \tag{8.22}$$

where $[V^s]_i$ and $[V^s]$ are the concentrations of vacancies with charge state s under intrinsic and extrinsic conditions, respectively.

* The provision that a semiconductor be intrinsic *and* contain impurities seems to contradict. However, intrinsic conditions can be achieved in a doped semiconductor with $N_D = N_A$ and $n = p = n_i$, i.e. in a fully compensated semiconductor.

https://doi.org/10.1017/CBO9780511599828.011 Published online by Cambridge University Press

The relative concentrations of vacancies with charge state s depends on the position of the Fermi level. Fermi–Dirac statistics applies to the energy levels of defects. As the Fermi level rises in n-type semiconductors, more vacancy states become populated, i.e. the concentration of negatively charged vacancies increases with the Fermi level. Consider a neutral and a negatively charged vacancy. The ionization of the vacancy is given by

$$e + V^0 \leftrightarrow V^- \,. \tag{8.23}$$

The relative concentrations of V^0 and V^- are obtained from the law of mass action

$$\frac{[V^-]}{n[V^0]} = K(T) = ce^{-\Delta E/kT} \tag{8.24}$$

where $K(T)$ is the temperature-dependent equilibrium constant. Under intrinsic conditions one obtains

$$\frac{[V^-]_i}{n_i[V^0]_i} = K(T) \,. \tag{8.25}$$

Assuming that most of the vacancies are in the neutral state, i.e. $[V^0] \gg [V^-]$, then $[V^0]_i \cong [V^0]$; the combination of Eqs. (8.24) and (8.25) then yields

$$\frac{[V^-]}{[V^-]_i} = \frac{n}{n_i} \,. \tag{8.26}$$

Thus, the concentration of negatively charged vacancies increases with the free electron concentration. As an example, consider an impurity–vacancy complex that readily diffuses if the vacancy is negatively charged. The formation of the complex is then more likely in n-type semiconductors. As a result the diffusion characteristic depends on the free electron concentration, i.e. on the position of the Fermi level. In order to quantify the above result, Eq. (8.26) can be generalized for different charge states s of the vacancy.

$$\frac{[V^s]}{[V^s]_i} = \left(\frac{n}{n_i}\right)^s \,. \tag{8.27}$$

Insertion of the result into Eq. (8.22) yields the *extrinsic* diffusion coefficient

$$D = D_i^0 + D_i^+\left(\frac{p}{n_i}\right) + D_i^-\left(\frac{n}{n_i}\right) + D_i^{2+}\left(\frac{p}{n_i}\right)^2 + D_i^{2-}\left(\frac{n}{n_i}\right)^2 + \cdots \,. \tag{8.28}$$

For n-type (p-type) semiconductors the terms containing the hole (electron)

https://doi.org/10.1017/CBO9780511599828.011 Published online by Cambridge University Press

337-TA-1366 RX-0255

concentration can be neglected.

The energy levels of various defects in GaAs have been calculated (Baraff and Schlüter, 1985). The authors also estimated the concentration of defects for a given position of the Fermi level and predicted abundant native defects in either highly doped p-type or highly doped n-type material. Not only the defect states, but also the diffusion behaviour of the impurity-defect complex should be known in order to quantitatively estimate the relevance of impurity-defect complexes with respect to their diffusion characteristics. Unfortunately, the precise diffusion characteristics of impurity-defect complexes are unknown for III–V semiconductors. Nevertheless, the quantitative analysis given above allows one to appreciate and understand the complexity of the diffusion of impurity-defect complexes and their dependence on doping.

8.3.3 Interstitial diffusion

In the pure interstitial diffusion process, impurities hop from one interstitial site to another, and and never occupy substitutional lattice sites. Therefore, the interstitial diffusion process is of limited practical relevance for common group-IIa, -IIb, -IV, -VI impurities in III–V semiconductors, as the major fraction of these impurities occupies substitutional sites in the III-V zincblende lattice.

Interstitial sites in a zincblende lattice are of tetrahedral symmetry; either four anions or four cations are closest to the center of the interstitial void. Impurities with a small atomic radius are more easily accommodated in interstitial sites. A small atomic radius is also advantageous for diffusion hops from one interstitial site to another. In III–V semiconductors, hydrogen (H) occupies interstitial sites and diffuses interstitially (Pankove and Johnson, 1991). The interstitial diffusion mechanism and the small size allows H to diffuse rapidly in semiconductors, even at relatively low temperatures. For a further discussion of H in III–V semiconductors see Chap. 9. Lithium (Li) is a well-known interstitial diffuser in Si. Of atomic number 3, Li is a rather small atom.

8.3.4 Substitutional–interstitial diffusion

The substitutional–interstitial diffusion mechanism is one of the most important impurity diffusion mechanisms in semiconductors. It was proposed and analyzed by Frank and Turnbull (1956). It is assumed in the substitutional–interstitial model that the majority of impurities occupy substitutional sites. However, these substitutional impurities have a very small probability of diffusing substitutionally. It is further assumed that a minor fraction of impurities occupies interstitial sites. These interstitial impurities have a much higher diffusion constant since they are less strongly bound to the lattice. The diffusion process is

https://doi.org/10.1017/CBO9780511599828.011 Published online by Cambridge University Press

Innoscience1366-00139017

RX-0255.344

337-TA-1366 RX-0255

then dominated by the highly mobile interstitials.

Any substitutional impurity atom can hop into an interstitial site according to

$$S \leftrightarrow I + V \tag{8.29a}$$

where S, I, and V represent the substitutional impurity, interstitial impurity and a vacancy, respectively. It is further assumed that the three species, S, I, and V, are neutral. The concentrations of S, I, and V can be inferred from the law of mass action provided the formation energy of the reaction is known. Usually $[I] \ll [S]$, i.e. the concentration of interstitials is much smaller than the concentration of substitutional impurities.

The validity of Eq. (8.29a) is restricted to the case where S, I, and V are neutral. However, it is the very nature of substitutional impurities to be charged. As an example, we assume that the substitutional impurity is singly negatively charged (acceptor) and that the interstitial is positively charged. Then Eq. (8.29a) needs to be modified according to

$$S^- + 2h \leftrightarrow I^+ + V \tag{8.29b}$$

where h represents a positively charged hole. Under equilibrium conditions, the concentrations are given by the law of mass action

$$\frac{p^2[S]}{[I][V]} = K_1 = ce^{-\Delta E/kT} \tag{8.30}$$

where p is the hole concentration. With $[I] \ll [S]$ and $p \cong [S]$ the equation simplifies to

$$K_1[S]^3 = [I][V] \,. \tag{8.31}$$

If the impurities diffuse through the crystal then [S] and [I] are a function of the spatial coordinate, z, and the time t. On the other hand the vacancy concentration [V] can be assumed to be constant for all spatial positions. Then there is no vacancy gradient and consequently no net diffusion of vacancies. It follows from Eq. (8.31) that the concentration of interstitials, [I], increases strongly with the impurity concentration. Recalling that interstitials diffuse much faster than substitutionals, it is evident that the effective diffusion coefficient increases with impurity concentration.

In order to quantify the increase of the diffusion coefficient, we apply Fick's second law to the substitutional–interstitial model. Note that the total impurity concentration is given by $N = [S] + [I]$. The diffusion equation then reads

https://doi.org/10.1017/CBO9780511599828.011 Published online by Cambridge University Press

Innoscience1366-00139018

RX-0255.345

$$\frac{\partial[\mathrm{I}]}{\partial t} + \frac{\partial[\mathrm{S}]}{\partial t} = D_\mathrm{I} \frac{\partial^2[\mathrm{I}]}{\partial z^2} + D_\mathrm{S} \frac{\partial^2[\mathrm{S}]}{\partial z^2} \tag{8.32a}$$

where D_I and D_S are the diffusion coefficients for interstitial and substitutional diffusion, respectively. Since $D_\mathrm{I} >> D_\mathrm{S}$, the equation reduces to

$$\frac{\partial[\mathrm{I}]}{\partial t} + \frac{\partial[\mathrm{S}]}{\partial t} = D_\mathrm{I} \frac{\partial^2[\mathrm{I}]}{\partial z^2} \,. \tag{8.32b}$$

The concentration of interstitials, [I], can be replaced by [S] by using Eq. (8.31), which gives

$$\left(\frac{3K_1[\mathrm{S}]^2}{[\mathrm{V}]} + 1 \right) \frac{\partial[\mathrm{S}]}{\partial t} = D_\mathrm{I} \frac{\partial}{\partial z} \left(\frac{3K_1[\mathrm{S}]^2}{[\mathrm{V}]} \frac{\partial[\mathrm{S}]}{\partial z} \right) . \tag{8.33}$$

If K_1 on the left-hand side of the equation is substituted with Eq. (8.31), the first term in the bracket becomes $3[\mathrm{I}]\,[\mathrm{S}]/p^2$ which is much smaller than one since $[\mathrm{I}] << p$ and $p \equiv [\mathrm{S}]$. Equation (8.33) then simplifies to

$$\frac{\partial[\mathrm{S}]}{\partial t} = \frac{\partial}{\partial z} \left(\frac{3K_1 D_\mathrm{I}}{[\mathrm{V}]} [\mathrm{S}]^2 \frac{\partial[\mathrm{S}]}{\partial z} \right) . \tag{8.34}$$

Comparison of the coefficients of the equation with Fick's law (Eq. (8.10a)) yields the *effective* diffusion coefficient

$$D = \frac{3K_1 D_\mathrm{I}}{[\mathrm{V}]} [\mathrm{S}]^2 \,. \tag{8.35}$$

Note that the diffusion coefficient is proportional to the *square of the substitutional impurity concentration*. Since $N \equiv [\mathrm{S}]$, that is nearly all impurities are on substitutional sites, the diffusion coefficient is proportional to the square of the overall impurity concentration. As a result, diffusion occurs more rapidly at high concentrations as compared to lower doping concentration.

Inspection of Eq. (8.35) reveals that the 'power of two' ($D \propto N^2$) is a result of the difference of two in the charge states between the substitutional S^- and the interstitial I^+. If, for example, the substitutional were S^- and the interstitial were I^{2+}, then the diffusion coefficient were proportional to the *third* power of the doping concentration, i.e. $D \propto N^3$.

Note that the interstitial–substitutional model results in non-linear Fickian diffusion. The individual atomic jumps are correlated since the probability of a diffusion jump depends on the concentration of the impurities. By adopting the concentration-dependent diffusion constant of Eq. (8.35), the Fickian diffusion equation (Eq. (8.10a)) can be used.

https://doi.org/10.1017/CBO9780511599828.011 Published online by Cambridge University Press

Interstitial impurities can reoccupy a substitutional lattice site by (i) occupying a previously vacant lattice site or (ii) via the '***kick-out***' mechanism. In the 'kick-out' mechanism, an initially interstitial impurity displaces a substitutional lattice atom which is forced into an interstitial lattice site. The final configuration of the 'kick-out' reaction is a substitutional impurity atom and a interstitial host atom. Analogously, an interstitial host lattice atom can 'kick-out' an impurity atom and force it into an interstitial site. The formation energy of the 'kick-out' reaction is smaller than the formation energy of a Frenkel defect. Accordingly, the 'kick-out' reaction is a fairly common reaction in semiconductors.

8.3.5 Interchange diffusion

Interchange diffusion effects involve the interchange of positions of one impurity atom and one or several atoms of the host semiconductor. Two examples of interchange diffusion effects are illustrated in Fig. 8.8 which shows (a) a ***direct interchange*** diffusion hop and (b) a ***cooperative interchange*** diffusion hop. The direct interchange diffusion involves two neighboring atoms. Three or more atoms take part in cooperative interchange diffusion processes.

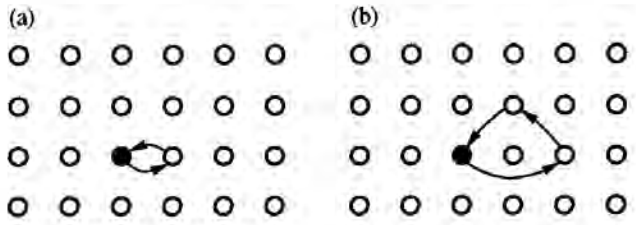


Fig. 8.8. Schematic illustration of (a) the direct interchange diffusion mechanism and (b) the cooperative interchange diffusion mechanism.

Interchange diffusion effects do not require vacant lattice sites or interstitials. Certainly, the diffusion of impurities via vacancies or interstitials is more effective as compared to the diffusion via interchange effects. However, when diffusion via interstitials or vacancies is unlikely, interchange diffusion may be the dominant diffusion mechanism. The probability of interchange diffusion hops is relatively low. The probability further decreases if the interchange process involves more than two atoms.

https://doi.org/10.1017/CBO9780511599828.011 Published online by Cambridge University Press

8.3.6 Combination of diffusion mechanisms

Each of the previous sections focused on a single, pure diffusion mechanism. Under realistic conditions a combination of several mechanism occurs. For example, pure substitutional and the substitutional–interstitial mechanism may occur simultaneously. It is reasonable to consider the different diffusion mechanisms as independent. A diffusion hop is a relatively seldom event, i.e. impurities predominantly occupy substitutional lattice sites. As a result, the different diffusion processes can be considered as *independent*. The overall diffusion process is then the *sum* of all individual diffusion processes. In this context it is useful to recall that the diffusion constants of different diffusion processes can differ by many orders of magnitude. It is likely that a single specific diffusion mechanism dominates the entire diffusion process. It is therefore frequently sufficient to consider only the dominant diffusion process despite the simultaneous occurrence of several diffusion processes.

8.3.7 Enhanced diffusion along imperfections

Spatially extended imperfections in semiconductors are preferred diffusion channels for impurities. The structural stability of the semiconductor is lower in the vicinity of imperfections. Such imperfections are, for example, grain-boundaries, interfaces between mismatched semiconductors, misfit dislocations, surfaces, or spatially extended clusters of defects. Due to the low structural perfection of extended defects, it is quite evident that the formation energy of point defects such as vacancies, interstitials, etc., is lower in the vicinity of the imperfection. As a result of the lower formation energy, the defects have a higher concentration at or in the vicinity of the structural imperfection. Diffusion processes including impurity diffusion processes are therefore more likely to occur in the vicinity of the imperfections, since the diffusion processes depend on the concentration of point defects as mentioned in the preceding sections.

A well-known example of enhanced diffusion along imperfections is ***pipe diffusion***, which occurs along dislocation lines in semiconductors. The diffusion probability along the one-dimensional dislocation line is enhanced leading to a pipe-like distribution of impurities and to a preferential movement of impurities along the dislocation line.

8.4 Some specific impurities

The diffusion mechanisms of impurities in compound semiconductors are clearly more complicated and involved than those in the elemental semiconductors Si and Ge. The number of types of native defects is much larger in compound

https://doi.org/10.1017/CBO9780511599828.011 Published online by Cambridge University Press

semiconductors as compared to elemental semiconductors. The native defects include group-III and group-V vacancies, group-III and group-V interstitials, and antisite defects which cannot occur in elemental semiconductors. In addition, compound semiconductors may suffer from non-stoichiometry. The occurrence of anion-rich or cation-rich semiconductors also depends on the epitaxial growth technique. While gas-phase epitaxial techniques work under anion-rich conditions, liquid-phase epitaxy grows under cation-rich conditions. Furthermore, if the impurity diffusion process occurs in the vicinity of the surface, out-diffusion of group-V elements may occur, which further complicates the nature of the impurity diffusion process. Due to the complexity of diffusion processes in III–V semiconductors, a detailed analysis of diffusion processes for specific impurities is presently not available. Therefore, this section primarily emphasizes the experimental findings for different impurities.

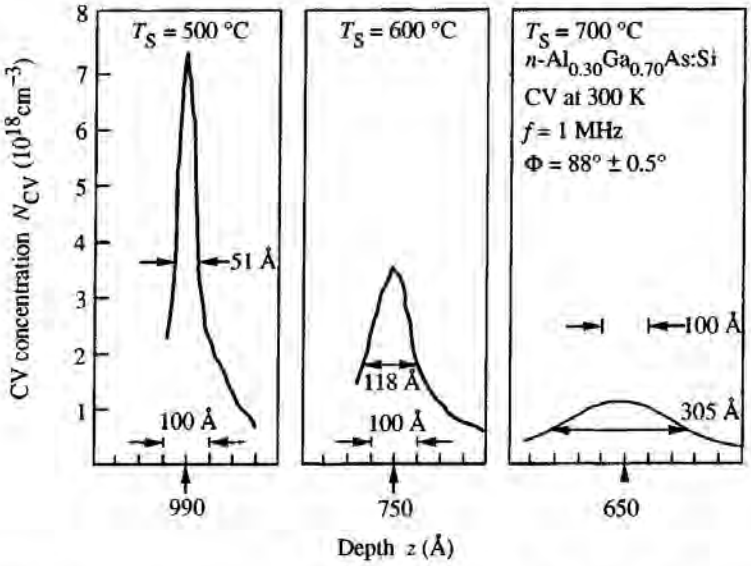


Fig. 8.9. Capacitance–voltage profiles of Si δ–doped $Al_{0.30}Ga_{0.70}As$ grown at 500, 600 and 700 °C by molecular-beam epitaxy.

Diffusion of impurities in semiconductors can occur during crystal growth or during post-growth annealing. The importance of diffusion during epitaxial growth is illustrated in Fig. 8.9 (Schubert et al., 1989). Figure 8.9 shows the capacitance–voltage profiles of Si δ-doped $Al_{0.30}Ga_{0.70}As$ grown by molecular-beam epitaxy at the three temperatures of 500 °C, 600 °C, and 700 °C. The

https://doi.org/10.1017/CBO9780511599828.011 Published online by Cambridge University Press

broadening of the profiles from 51 Å to 305 Å illustrates that different growth temperatures can have a drastic effect on the impurity distribution by means of diffusion effects.

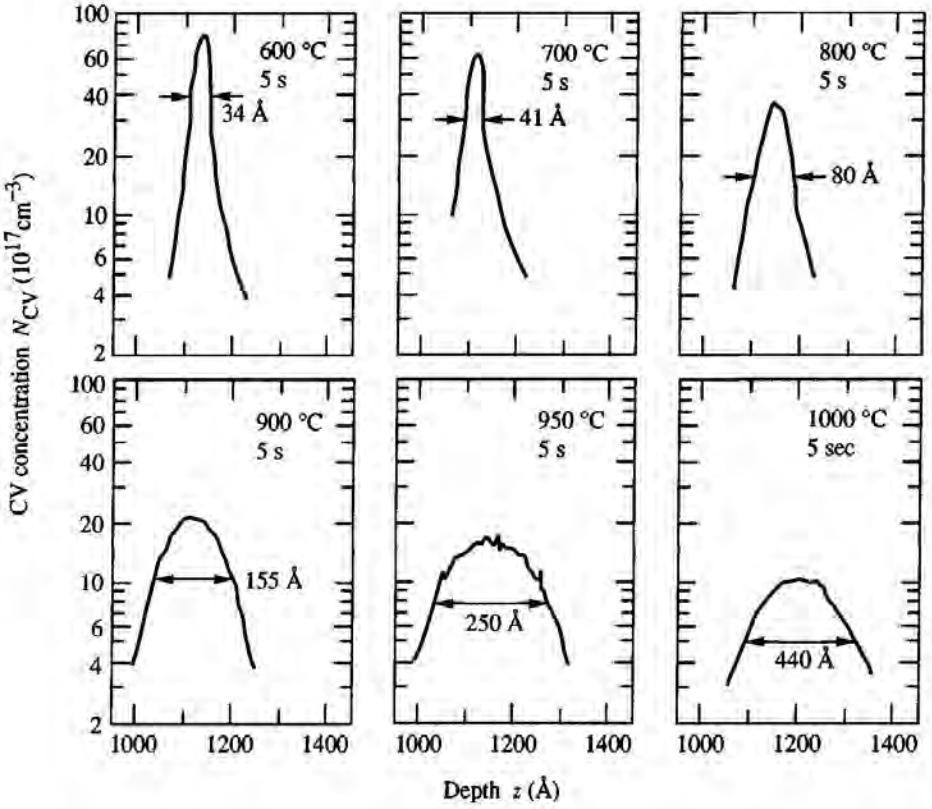


Fig. 8.10. Capacitance–voltage profiles of different pieces of an MBE-grown Be δ-doped GaAs sample annealed at temperatures of 600 to 1000 °C for 5 s.

Many diffusion experiments are performed with semiconductors coated with a film of impurities. Upon annealing, impurities diffuse into the semiconductor. However, this method is obviously very sensitive to the surface condition, i.e. surface contamination, out-diffusion of group-V elements, and other surface effects. A method less sensitive to surface effects employs δ-doped semiconductors (Schubert et al., 1988). In the case of δ-doped semiconductors the impurity reservoir is buried ≥ 1000 Å below the surface. Surface effects are therefore drastically reduced. Epitaxial growth under appropriate conditions (low temperatures) insures that the diffusion occurring during epitaxial growth is

https://doi.org/10.1017/CBO9780511599828.011 Published online by Cambridge University Press

insignificant. Post-growth annealing of the δ-doped samples allows one to choose well-defined temperature profiles during different annealing cycles. The diffusion length and the diffusion coefficient can be inferred from the broadening of the doping profile. An example of impurity distribution measurements on GaAs:Be annealed at temperatures between 600 °C and 1000 °C is shown in Fig. 8.10. The impurity profile broadening ranges from 34 Å at an annealing temperature of 600 °C to 440 Å at an annealing temperature of 1000 °C. The annealing time is kept constant at 5 s.

The diffusion shown in Fig. 8.10 is next modeled in terms of linear fickian diffusion. Assuming that the profiling measurement technique has a gaussian resolution function and that the impurity distribution is gaussian as well, the *measured* impurity distribution of an initially δ-function-like doping distribution is given by

$$N(z) = \frac{N^{2D}}{\sqrt{2\pi}\,\sigma} e^{-(z - z_0)^2/(2\sigma^2)} \tag{8.36}$$

The broadening (standard deviation) of this gaussian function, σ, is composed of the ***resolution broadening***, σ_r, and the ***diffusion broadening***, σ_{diff}, according to

$$\sigma^2 = \sigma_r^2 + \sigma_{diff}^2 . \tag{8.37}$$

The diffusion constant can be extracted from the experimental results (see Fig. 8.10) using

$$\sigma_{diff} = \sqrt{2}\, L_D = \sqrt{2Dt} \tag{8.38}$$

where L_D is the diffusion length.

The experimental procedure described above (see also Fig. 8.10) avoids surface effects since the doped layer can be buried in the bulk. Note however, that the analysis using Eqs. (8.36) to (8.38) is valid for a concentration-independent diffusion constant. If the diffusion constant is concentration dependent, other methods, such as the Boltzmann–Matano technique, must be used. The following sections summarize the diffusion characteristics of technologically important impurities in III–V semiconductors.

8.4.1 Beryllium (Be)

Beryllium is one of the major doping impurities in III–V semiconductors. The first report on Be diffusion in GaP dates back to 1972 (Ilegems and O'Mara, 1972). The authors studied Be diffusion with concentrations $> 10^{20}$ cm^{-3}. At such high concentrations the diffusion coefficient strongly increases over its low-

https://doi.org/10.1017/CBO9780511599828.011 Published online by Cambridge University Press

concentration value. A Boltzmann–Matano analysis of the 1000 °C anneal temperature indicated a coefficient of $\cong 10^{-7}$ cm^2/s for concentrations $N_{Be} > 10^{20}$ cm^{-3}. Subsequently Ilegems (1977) and McLevige et al. (1978) studied Be diffusion in GaAs grown by molecular-beam epitaxy. The epitaxial layers were annealed at 900 °C after growth. Diffusion constants at this temperature were $10^{-13} - 10^{-14}$ cm^2/s for concentrations of approximately 10^{19} cm^{-3}.

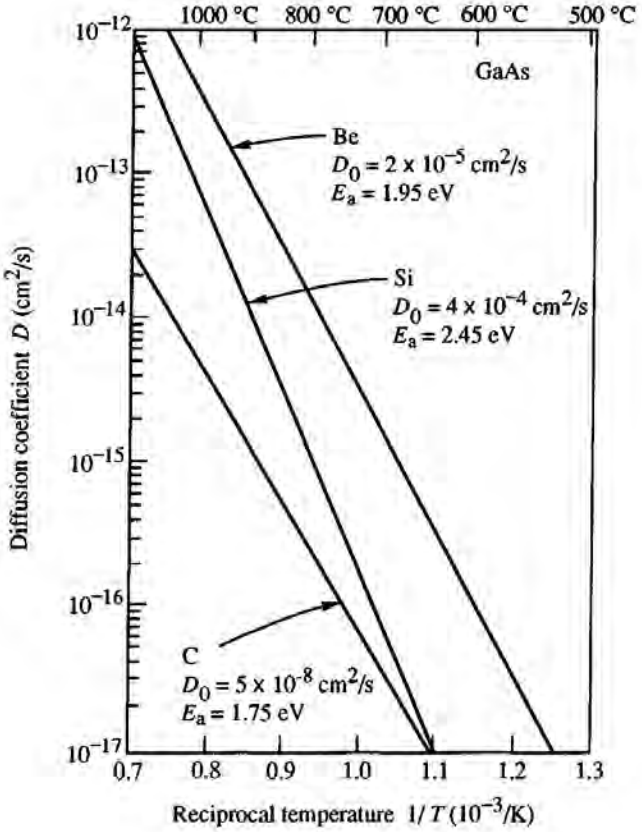


Fig. 8.11. Diffusion coefficients of C, Si, and Be in GaAs versus reciprocal temperature.

The diffusion constant of Be in GaAs was determined as a function of temperature in the range 600 °C ≤ T ≤ 1000 °C (Schubert et al., 1990b). The concentration of Be was in the 10^{18} cm^{-3} range. The temperature-dependence of the diffusion constant is shown in Fig. 8.11 and can be described by an activation energy of $E_a = 1.95$ eV and $D_0 = 2 \times 10^{-5}$ cm^2/s using the equation $D = D_0 \exp(-E_a/kT)$. The values shown for Be in Fig. 8.11 agree with the data published by Ilegems (1977) and McLevige et al. (1978).

https://doi.org/10.1017/CBO9780511599828.011 Published online by Cambridge University Press

Beryllium redistributes strongly in GaAs at doping concentrations exceeding 10^{19} cm^{-3} (Schubert et al., 1990b). The redistribution was found to be directed towards the substrate as well as towards the surface of the epitaxial layers. Doping concentrations exceeding 10^{20} cm^{-3} could not be achieved at typical growth temperatures due to the strong Be redistribution (see also Sect. 5.3.1 and 7.5.2). Similar results were obtained for Be in InP and $Ga_{0.47}In_{0.53}As$ (Panish et al. 1991).

8.4.2 Magnesium (Mg)

Experimental results on Mg diffusion in GaAs have been reported by Small et al. (1982). The authors point out that Mg diffuses slowly when buried in the semiconductor but diffuses rapidly from the free surface. The diffusion profiles had a rapidly decreasing concentration at the diffusion front and a roughly constant concentration near the surface. Such profiles indicate that the diffusion coefficient is either strongly concentration-dependent or that a different redistribution mechanism occurs at high Mg concentrations.

8.4.3 Zinc (Zn)

The diffusion of Zn in III–V semiconductors was studied by a large number of groups; this is due to the versatility of Zn which is used for many purposes including pn-junction formation, ohmic contacts, and for doping during epitaxy. The diffusion behavior of Zn is also one of the best understood.

Diffusion of Zn in GaP has been studied by Chang and Pearson (1964a and 1964b), Luther and Wolfstirn (1973) and Tuck and Jay (1977a and 1977b). Zn diffusion was investigated at temperatures ranging from 850 °C to 1100 °C. The diffusion coefficient of Zn in GaP as a function of Zn concentration is shown in Fig. 8.12. The diffusion temperature is 1000 °C. The diffusion constant increases with Zn concentration approximately as $D \propto N_{Zn}^2$. The increase of D with the square of the Zn concentration is consistent with the substitutional–interstitial diffusion model discussed previously. Note that the Zn concentrations are very high; it is not likely that the square-dependence of D also applies to the low-concentration regime.

Zn diffusion in GaAs has been reported by Cunnell and Gooch (1960) and by Goldstein (1961). These early studies already indicated that Zn diffusion does not follow simple Fickian diffusion with a constant diffusion coefficient. Subsequent work by Kadhim and Tuck (1972) showed that the diffusion constant of Zn in GaAs increases quadratically with Zn concentration. The experimental results are shown in Fig. 8.12 for an anneal temperature of 1000 °C. The diffusion experiments were carried out under excess arsenic pressure in order to avoid the

https://doi.org/10.1017/CBO9780511599828.011 Published online by Cambridge University Press

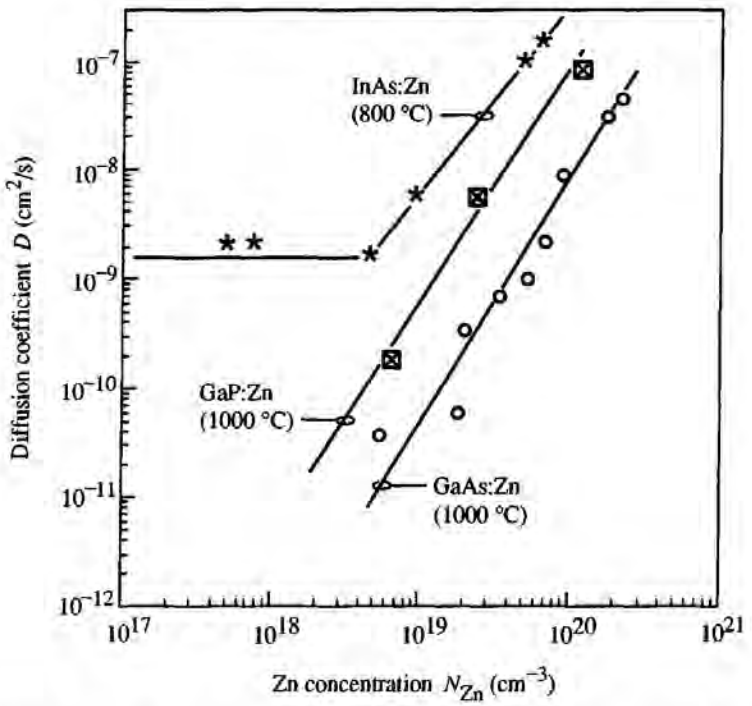


Fig. 8.12. Diffusion coefficient of Zn in GaP at 1000 °C (Chang and Pearson, 1964a and 1964b), Zn in GaAs at 1000 °C (Kadhim and Tuck, 1972), and Zn in InAs at 800 °C (Boltaks et al., 1969) as a function of Zn concentration.

out-diffusion of As from the specimen. Note again that the concentration range studied is very high ($10^{19} - 10^{20}$ cm^{-3}). The squared dependence of D on N_{Zn} has not been demonstrated at lower concentrations.

Zinc diffusion into InP was first reported by Chang and Casey (1964) at temperatures of 600 – 900 °C. The authors analyzed the diffusion profiles using the Boltzmann–Matano method and concluded that the Zn diffusion coefficient is not constant but increases with Zn concentration. Subsequent work by Kundukhov et al. (1967) indicated that only a small fraction of the Zn atoms diffused into InP are electrically active; that is the major fraction (e.g. 90%) of the Zn occupies sites other than the substitutional In site. The low electrical activity of Zn in InP was confirmed by independent measurements (Tuck and Zahari, 1977a and 1977b) who found only 1% of the Zn atoms to be electrically active as acceptors. The physical origin of the low electrical Zn activity has been proposed to be due to Zn–V_P complexes, where V_P represents one or more phosphorus vacancies (Tuck and Hooper, 1975; Young and Pearson, 1970; Yamada et al.,

https://doi.org/10.1017/CBO9780511599828.011 Published online by Cambridge University Press

1983). The P vacancies were assumed to be generated during the annealing cycle. Despite the problematic electrical behaviour of Zn in InP, Tuck and Zahari (1977a and 1977b) determined the Zn diffusion constant in InP. A value of 2×10^{-8} cm^2/s was obtained at 800 °C. The diffusion constant was weakly dependent on the Zn concentration.

The diffusion of Zn in InAs was studied by Boltaks et al. (1969). Their experimental results for 800 °C are shown in Fig. 8.12. The Zn diffusion coefficient is a constant for 'low' concentrations ($< 5 \times 10^{18}$ cm^{-3}) and increases quadratically at higher concentrations; the quadratic increase is consistent with the substitutional–interstitial diffusion model.

Zn diffusion in AlSb was reported by Showan and Shaw (1969). The authors found values of D of $10^{-9} - 10^{-8}$ cm^2/s for Zn concentrations in the 10^{19} cm^{-3} range.

8.4.4 Carbon (C)

Carbon is an impurity with an exceptionally low diffusion constant in III–V semiconductors. This property makes C an attractive doping impurity in devices with stringent requirements of the doping distribution. The low diffusion constant of C provides long-term stability of the operating characteristics of such devices. The diffusion coefficient of C in GaAs is shown in Fig. 8.11 versus reciprocal temperature. The epitaxial samples used for the diffusion experiments have C concentrations in the 10^{18} cm^{-3} range. Comparison of the C diffusion constant with the Be diffusion constant reveals that the C coefficient is about 2 orders of magnitude lower in the temperature range of interest.

C diffusion in GaAs has been studied at 800 °C for epitaxial samples grown by flow-rate modulation epitaxy (Kobayashi, 1987). The concentration of C was in the mid 10^{17} cm^{-3} to the low 10^{18} cm^{-3} range. The authors inferred a diffusion constant of 2×10^{-16} cm^2/s in agreement with the data shown in Fig. 8.11.

8.4.5 Silicon (Si)

Silicon has a rather low diffusion constant in many III–V semiconductors. The diffusion coefficient of Si in epitaxial GaAs is shown in Fig. 8.11 for Si concentrations in the 10^{18} cm^{-3} range (Schubert et al., 1988). The Si diffusion constant is higher than the constant of C but lower than that of Be. The diffusion constant of Si in GaAs was also measured by Beall et al. (1989) at a temperature of 600 °C. The authors found $D \cong 5 \times 10^{-18}$ cm^2/s for Si doping in the 10^{18} cm^{-3} range. The authors noted that either substitutional Si diffusion or substitutional–interstitial diffusion could prevail. They further note that Si-pair

https://doi.org/10.1017/CBO9780511599828.011 Published online by Cambridge University Press

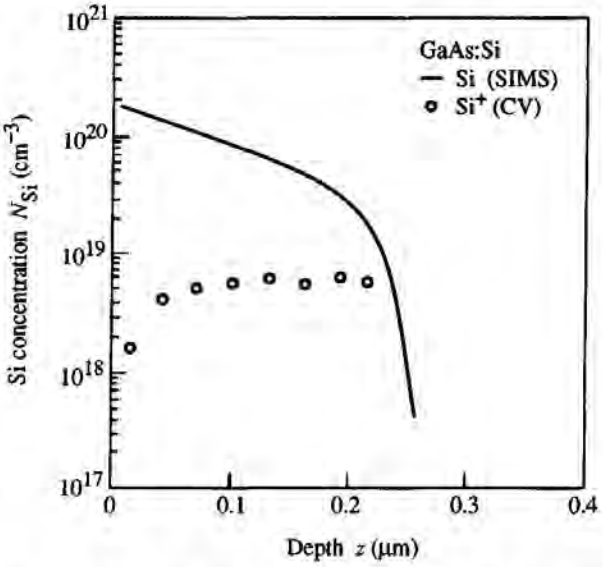


Fig. 8.13. Depth profile of total Si concentration (solid line) and electrically active Si concentration (circles) in GaAs. Silicon was diffused from a Si film on the surface into GaAs at 1050 °C for 3 s (Greiner and Gibbons, 1984).

diffusion is unlikely at sufficiently low concentrations.

Silicon diffusion experiments at very high Si concentrations were performed by Greiner and Gibbons (1984). The authors diffused impurities from a Si film into a GaAs layer. The samples were thermally annealed at 1050 °C for 3 s. The resulting Si profile measured by secondary ion mass spectrometry (SIMS) and electrochemical capacitance–voltage (CV) profiling are shown in Fig. 8.13. While SIMS measures the total Si atom concentration, CV-measurements yield the electrically active net electron concentration. Figure 8.13 reveals that 90 – 99% of the total Si-atom concentration is electrically inactive or compensated. The authors concluded that the Si impurities diffuse predominantly as $Si_{Ga} - Si_{As}$ compensating pairs. These pairs are assumed to have a much larger diffusion coefficient than isolated Si impurities. The diffusion constant determined by the authors for Si-pair diffusion is indeed approximately two orders of magnitude higher than the Si diffusion data shown in Fig. 8.11.

8.4.6 Germanium (Ge)

Since Ge is strongly amphoteric in III–V semiconductors, Ge is not of high technological significance. There is only one report on Ge diffusion in III–V semiconductors. Schneider and Nebauer (1975) studied the diffusion of Ge in

https://doi.org/10.1017/CBO9780511599828.011 Published online by Cambridge University Press

GaP at temperatures of 900 – 1000 °C. The authors found that the Ge diffusion constant is inversely proportional to the square of the phosphorus ambient pressure. It was concluded that the Ge diffusion occurs predominantly via P vacancies. Unfortunately, the authors do not report electrical measurements. Therefore, the conductivity type of GaP:Ge is unknown.

8.4.7 Tin (Sn)

There are a number of reports on Sn diffusion in III–V semiconductors (Goldstein and Keller, 1961; Fane and Goss, 1963; Gibbon and Ketchow, 1971; Yamazaki et al., 1975; Tuck and Badawi, 1978; Arnold et al., 1984). Sn can be diffused into III–V semiconductors from Sn films, from Sn-doped glass films, or from a gas-phase precursor.

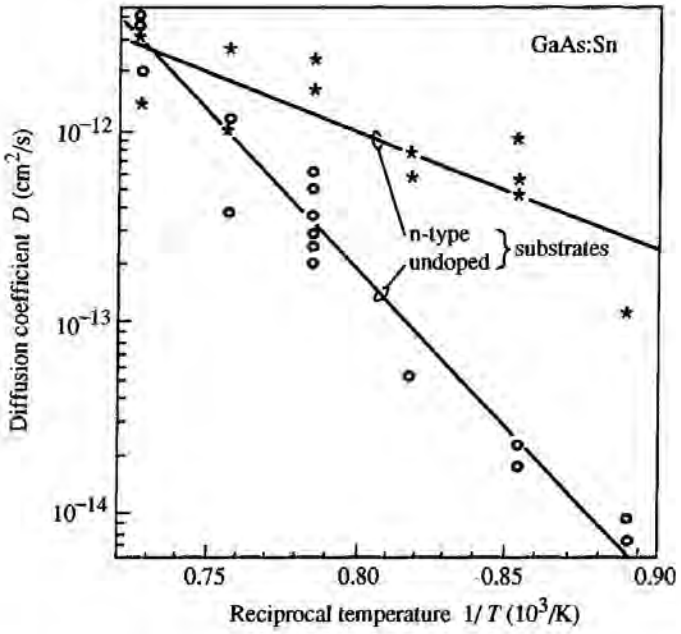


Fig. 8.14. Diffusion coefficient of Sn in GaAs as a function of reciprocal temperature using undoped and n-type GaAs substrates as starting materials (Tuck and Badawi, 1978).

The diffusion constant of Sn in GaAs is shown in Fig. 8.14 (Tuck and Badawi, 1978). Tin was diffused into GaAs from the gas phase. Two types of substrates were used, namely undoped and n-type substrates. The diffusion experiments were carried out under excess As pressure in order to avoid loss of As from the

https://doi.org/10.1017/CBO9780511599828.011 Published online by Cambridge University Press

GaAs substrates. The diffusion coefficients shown in Fig. 8.14 illustrate that the diffusion depends sensitively on the properties of the host. However, at high temperatures (≅1100 °C) there is no appreciable difference between the two substrates. The authors attribute the similarity of the diffusion constant at high temperatures to the similarity in electron concentration: At such high temperatures both types of semiconductor substrates are intrinsic, i.e. the free electron concentration is the same. It was concluded that most of the Sn occupies Ga sites and that Sn diffuses via Ga vacancies.

Tin diffusion was also studied in GaSb (Uskov, 1974) and in InSb (Sze and Wei, 1961). In InSb, the diffusion constant was determined in the temperature range 385–512 °C and was described by $D_0 = 5.5 \times 10^{-8}$ cm^2/s and an activation energy of $E_a = 0.75$ eV.

8.4.8 Sulfur (S)

Sulfur diffusion studies have been reported for several III–V semiconductors including GaAs (Vieland, 1961; Frieser, 1965; Kendall, 1968; Young and Pearson, 1970; Matino, 1974; Prince et al., 1986), GaP (Young and Pearson, 1970), InP (Dutt et al., 1984; Chin et al., 1983a, 1983b), and InAs (Schillmann, 1962). The diffusion of S in GaAs has been characterized by D_0 and an activation energy, E_a. The parameters are shown in Table 8.1. The diffusion constants for S in GaAs at 900 °C inferred from Table 8.1 are in the $10^{-12} - 10^{-13}$ cm^2/s range, i.e. 1–2 orders of magnitude larger than the diffusion constant for Si in GaAs.

Table 8.1. *Diffusion parameters for S in GaAs*

D_0 (cm^2/s)	E_a (eV)	Reference
1.2×10^{-4}	1.80	Vieland (1961)
2.6×10^{-5}	1.86	Frieser (1965)
1.6×10^{-5}	1.63	Kendall (1968)
1.85×10^{-2}	2.6	Young & Pearson (1970)
10.9	2.95	Matino (1974)
0.27	3.0	Prince et al. (1986)

8.4.9 Selenium (Se)

Diffusion of Se in GaAs has been studied by Khludkov and Lavrishchev (1976). Selenium was used to form a pn-junction in a p-type GaAs substrate. It was diffused from the semiconductor surface. The authors assumed that the Se surface concentration is approximately 10^{20} cm^{-3}. An erfc function was used to

https://doi.org/10.1017/CBO9780511599828.011 Published online by Cambridge University Press

fit the impurity distribution in order to get an effective diffusion coefficient. It is questionable if fickian diffusion theory can be applied at such high concentrations, since correlation effects become increasingly important at high impurity concentrations.

Diffusion of Se in InSb has been reported by Rekalova et al. (1969 and 1971). Selenium was diffused from a surface film containing 1% Se and 99% In. Diffusion temperatures ranged from 350 °C to 500 °C in a reducing hydrogen atmosphere. The technique was used to form pn-junctions in p-type InSb. Diffusion of Se has also been studied in InAs (Schillmann, 1962) and in InP (Dutt et al., 1984).

8.4.10 Tellurium (Te)

Diffusion of Te in GaAs was studied by Karelina et al. (1974) in order to form a pn-junction in a p-type substrate. Annealing temperatures were 1000–1150 °C while simultaneously maintaining an ambient arsenic pressure. The authors concluded that Te diffuses mainly via As vacancies and divacancies.

The diffusion of Te in InSb was also reported by Rekalova et al. (1969 and 1971). The Te was diffused from a surface film containing 0.5% Te and 99.5% In. Diffusion temperatures ranged from 350 °C to 500 °C in a reducing hydrogen atmosphere. The technique was used to form pn-junctions in p-type InSb . Diffusion of Te has also been studied in InAs (Schillmann, 1962).

8.4.11 Chromium (Cr)

Chromium is a deep acceptor in GaAs and has an energy level close to the center of the gap. It is used for co-doping residual n-type GaAs in order to render the semiconductor semi-insulating. Chromium is an impurity of significant technological importance. There is an abundance of technical papers on the diffusion of Cr in GaAs; many of these publications report similar results.

Diffusion experiments in GaAs using an external gas-phase chromium source were carried out at 800 – 1100 °C by Tuck and Adegboyega (1979). The authors found that the Cr profiles after diffusion did not resemble erfc-function-like profiles as expected from linear fickian diffusion. It was found that the Cr diffuses deeply into the GaAs substrates, with diffusion lengths of several tens of microns for diffusion times of one hour. Diffusion lengths >>100 μm were achieved for diffusion times of several hours. (Note that the term 'diffusion length' is not defined for non-fickian diffusion).

Out-diffusion of Cr from Cr-doped GaAs substrates into epitaxial layers grown on top of the substrate has proven to be a significant problem. Linh et al. (1980) grew epitaxial layers by molecular-beam epitaxy on Cr-doped GaAs

https://doi.org/10.1017/CBO9780511599828.011 Published online by Cambridge University Press

substrates and demonstrated a significant pile-up of Cr ($N_{Cr} \cong 10^{18}$ cm^{-3}) at the substrate–epilayer interface. Similar results were obtained with epilayers grown by organometallic vapor-phase epitaxy (Huber et al., 1982). Further out-diffusion experiments were reported by Deal and Stevenson (1986), Tuck and Adegboyega (1979), Vasudev et al. (1980), Watanabe et al. (1982), and Wilson (1982).

8.4.12 Iron (Fe)

Iron is a deep acceptor in InP and has an energy level close to the center of the gap. It is used for co-doping n-type InP in order to render the semiconductor semi-insulating. Iron has significant technological importance in InP.

The diffusion of Fe in InP has been studied by Shishiyanu et al. (1977) at temperatures of 720–940 °C and by Brozel et al. (1981, 1982) at a temperature of 900 °C. The experimental results revealed that Fe diffuses deeply into InP. Shishiyanu et al. (1977) fitted erfc functions to the experimental Fe profiles in order to obtain the diffusion coefficient. The authors estimated the diffusion constant $D \cong 10^{-9} - 10^{-10}$ cm^2/s at temperatures of 720–940 °C.

The out-diffusion of Fe from Fe-doped substrates into epitaxial InP layers was studied by Holmes et al. (1981), Oberstar et al. (1981) and Chevrier et al. (1980). The former group grew epitaxial InP on Fe-doped InP substrates using liquid-phase epitaxy. The Fe profiles were measured by secondary ion mass spectrometry (SIMS). The profiles were fitted with a erfc distribution in order to obtain the Fe diffusion constant in the temperature range 600 °C to 710 °C. The temperature dependence of the diffusion coefficient was expressed in terms of $D = D_0 \exp(-E_a/kT)$ with $D_0 = 6.8 \times 10^5$ cm^2/s and $E_a = 3.4$ eV. It should be noted that the activation energy of 3.4 eV is surprisingly high. Chevrier et al. (1980) also used SIMS to analyze Fe out-diffusion from InP into undoped epitaxial layers grown by vapor-phase epitaxy. The authors found that the Fe concentration in the epitaxial layer was almost as high as the Fe doping level in the substrate. In addition, a peak of the Fe concentration occurred at the epilayer–substrate interface. Such Fe peaks are not expected from an erfc distribution.

8.5 Surface segregation and surface migration

Many impurities have the tendency to redistribute preferentially towards the surface of the semiconductor. The redistribution is *anisotropic* which is in contrast to the isotropic redistribution occurring during diffusion. The preferential redistribution towards the surface can occur during bulk or epitaxial crystal growth. Surface segregation and surface migration are two mechanisms

https://doi.org/10.1017/CBO9780511599828.011 Published online by Cambridge University Press

which both describe the redistribution of impurities towards the surface. ***Segregation*** describes the effect that impurities accumulate on the surface and are *segregated* from the crystal bulk. Segregating impurities mainly remain on the surface during epitaxial growth and only a minor fraction incorporates into the crystal. The term ***migration*** is used if impurities are incorporated in the crystal but redistribute within the crystal preferentially towards the crystal surface. In the following, three surface segregation/migration mechanisms will be discussed which are (i) zero-order surface segregation, (ii) first-order surface segregation, and (iii) Fermi-level-pinning induced surface migration.

8.5.1 Zero-order surface segregation

The incorporation of impurities into a growing semiconductor crystal can be described by a rate equation which takes into account the (i) arrival rate, (ii) desorption rate, (iii) incorporation rate of impurities, and (iv) the density of impurities on the growing semiconductor surface. The rate equation can be expressed as

$$\frac{dN_s}{dt} = J - k_d N_s - k_i^{(m)} N_s^m \tag{8.39}$$

where dN_s/dt denotes the change in impurity surface density, J is the incident impurity flux (per cm^2 and per s), $K_d N_s$ is the desorption flux, and $k_i^{(m)} N_s^m$ is the density of incorporated impurities per unit time, i.e. the incorporation rate of order m. For $m = 0$ the incorporation rate is $k_i^{(0)} N_s^0 = k_i^{(0)}$ which is a constant. Eq. (8.39) then simplifies to

$$\frac{dN_s}{dt} = J - k_d N_s - k_i^{(0)} \tag{8.40}$$

which is the rate equation describing ***zero-order segregation***. The implications of the rate equation are as follows. First, since the incorporation rate is constant, the impurity concentration in the bulk (per cm^3) is constant as long as $N_s > 0$ and the growth rate remains constant. The impurity concentration in the bulk is then given by $N = k_i^{(0)}/v_g$ where v_g is the growth rate. The concentration in the bulk remains constant until $N_s = 0$, i.e. the surface impurity reservoir is depleted.

Zero-order surface segregation is schematically illustrated in Fig. 8.15. An impurity flux impinges on the surface during the time interval $t_1 \le t \le t_2$. The incorporation rate of impurities is lower than the incident flux and results in a bulk impurity concentration N. Impurities also accumulate on the surface in the time interval $t_1 \le t \le t_2$. (Desorption of impurities is neglected). After termination of the incident impurity flux, impurity incorporation continues from

https://doi.org/10.1017/CBO9780511599828.011 Published online by Cambridge University Press

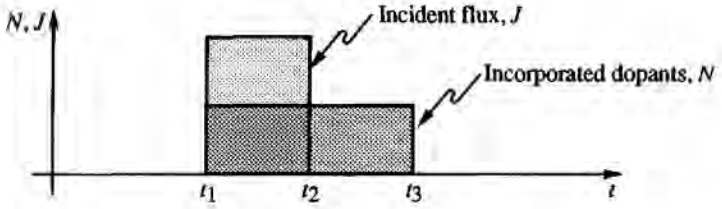


Fig. 8.15. Schematic illustration of incident dopant flux and concentration of incorporated dopants versus time for zero-order segregation. The time axis can be transformed into distance along the growth direction, z, by using $z = v_g t$, where v_g is the growth rate.

the surface reservoir until the surface reservoir is depleted ($N_s = 0$). The resulting impurity distribution is a top-hat distribution with a constant impurity concentration in the interval $t_1 \leq t \leq t_3$.

We now consider the case where $(J - k_d N_s) < k_t^{(0)}$. Then $dN_s/dt < 0$, i.e. the surface impurity reservoir is depleting. At some time the surface concentration becomes $N_s = 0$. Then Eq. (8.40) is no longer valid since N_s cannot become a negative quantity. Instead, the incorporation rate equals the arriving impurity flux diminished by the desorption rate.

Various physical mechanisms can be envisaged to account for the constant incorporation rate. For example, the constant incorporation rate can be given by the maximum achievable impurity concentration in the bulk as discussed in Chap. 7. Examples for zero-order segregation are found in the very high doping regime where the resulting impurity profiles are top-hat shaped (Schubert et al., 1990b; Hamm et al., 1989; Panish et al., 1990).

8.5.2 First-order surface segregation

First-order segregation of impurities on a semiconductor occurs if the rate of impurity incorporation is proportional to the surface density of impurity atoms. The appropriate rate equation (Eq. (8.39)) is obtained by selecting $m = 1$, i.e.

$$\frac{dN_s}{dt} = J - k_d N_s - k_t^{(1)} N_s \,. \tag{8.41}$$

We will now show that the impurity concentration *decreases exponentially* towards the surface after the incident impurity flux is terminated ($J = 0$). As a further simplification, assume that impurities do not desorb from the crystal, i.e. $k_d = 0$. Eq. (8.41) then reduces to

https://doi.org/10.1017/CBO9780511599828.011 Published online by Cambridge University Press

$$\frac{dN_s}{dt} = -k_t^{(1)} N_s \,. \tag{8.42}$$

The solution of the differential equation is given by

$$N_s(t) = N_s^0 \, e^{-k_t^{(1)} t} \tag{8.43}$$

where it is assumed that the surface concentration at $t = 0$ equals $N_s^0 = N_s(t = 0)$. The impurity concentration incorporated in the bulk (per unit time) is given by $N = -dN_s(v_g\,dt)^{-1}$. The impurity concentration in the bulk can hence be obtained by differentiation of Eq. (8.43)

$$N(t) = (k_t^{(1)} N_s^0 / v_g) \, e^{-k_t^{(1)} t} \,. \tag{8.44a}$$

The important result of Eq. (8.44) is that impurity concentrations decrease exponentially towards the surface. Note that the time-dependence of the equation can be easily transformed in a spatial dependence by the growth rate $v_g = z/t$. Using $k_t^{(1)} t = k_z z$, Eq. (8.44a) can be written as

$$N(z) = k_z N_s^0 \, e^{-k_z z} \,. \tag{8.44b}$$

The physical driving force for first-order surface segregation can be a lower surface energy. Hofman and Erlewein (1978) and Harris et al. (1984) modeled first-order surface segregation in terms of a lower surface energy. A schematic diagram of the total free energy of the impurity in the bulk and the surface is shown in Fig. 8.16 (Harris et al., 1984). The authors considered Sn in [001] GaAs; therefore the energy minima correspond to Ga planes in a GaAs lattice. The separation of the energy minima, a, is half a lattice constant, i.e. $a = \frac{1}{2}a_0$. It was assumed in the model that the activation energy E_2 (see Fig. 8.16) is so large that no hopping of impurity atoms to the adjacent minimum occurs. The activation energy E_1 was assumed to be sufficiently small such that an equilibrium distribution between the surface layer (s) and the layer (s − 1) was achieved. If the transition probability from the sub-surface layer to the surface is p_1 and the transition probability of the reverse process is p_2 than the relative impurity densities per layer are

$$\frac{N_{s-1}}{N_s} = \frac{p_2}{p_1} = A \, e^{-\Delta G/kT} \tag{8.45}$$

where ΔG is the free energy difference between the surface and the sub-surface layer and the constant A contains other factors such as the attempt frequency (vibrational frequency).

https://doi.org/10.1017/CBO9780511599828.011 Published online by Cambridge University Press

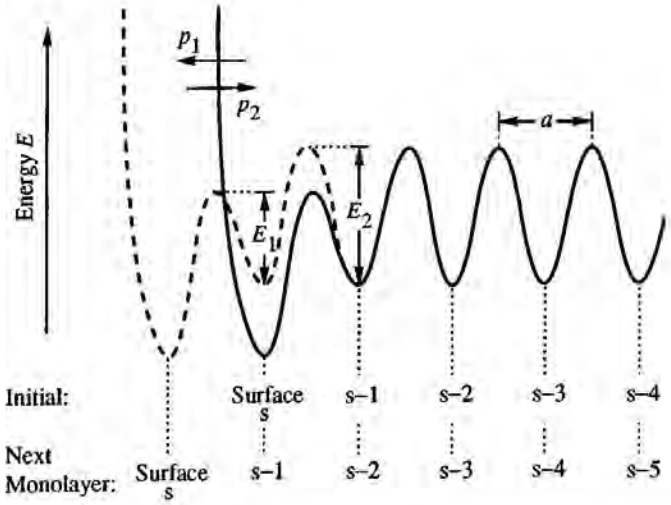


Fig. 8.16. Schematic representation of the energy of a Sn atom in GaAs as a function of depth in the vicinity of the GaAs surface. The energy minima represent Ga sublattice planes spaced by $a = a_0/2$ in the [001]-direction. The solid line is the initial potential energy whereas the dashed line is the potential energy after the growth of an additional GaAs monolayer (after Harris et al., 1984).

Harris et al. (1984) considered two cases for the segregation, i.e. (i) the equilibrium case and (ii) the kinetically limited case. If equilibrium is reached, Eq. (8.45) applies and gives the appropriate ratio of the impurity density in the surface and sub-surface layer. The constant $k_i^{(1)}$ is then obtained as

$$ak_i^{(1)} v_g = ak_z \cong \mathrm{A}\ \mathrm{e}^{-\Delta G/kT} \tag{8.46}$$

where $k_z v_g = k_i^{(1)}$ describes the spatial decrease of the doping profile (see Eqs. (8.44a) and (8.44b)). In this case the segregation is given only by the difference in free energy of the surface layer and the sub-surface layer. The equilibrium case applies to low growth rates and high temperature growth.

In the second case, impurities do not reach equilibrium. Impurities are buried under the top semiconductor layer and do not have sufficient time to equilibrate with the surface. The non-equilibrium case applies to fast growth rates or low growth temperatures. Assuming that the transfer of impurities between layers is kinetically limited, the probability for an impurity to hop to the surface is given by (Harris et al., 1984)

https://doi.org/10.1017/CBO9780511599828.011 Published online by Cambridge University Press

$$p_1 = p_0 \, e^{-E_1/kT} \tag{8.47}$$

where E_1 is the energy barrier shown in Fig. 8.16, and p_0 is a constant. The decay constant is then given by

$$\ln(ak_z) = p_0(a/v_g) \, e^{-E_1/kT} \tag{8.48}$$

which can be quite different from the equilibrium value. Note that the models of equilibrium and kinetically limited surface segregation predict that segregation is minimized for fast growth as well as for growth at low temperatures. On the other hand, small growth rates and high-temperature growth result in enhanced segregation of impurities.

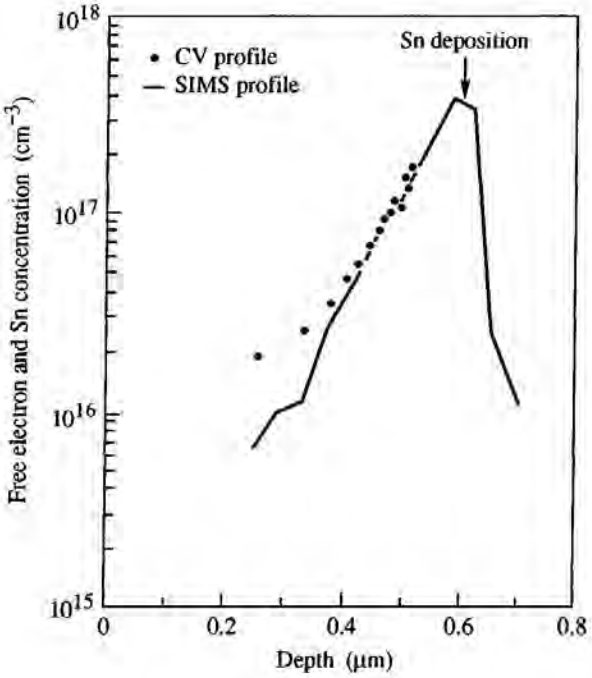


Fig. 8.17. Secondary ion mass spectrometry (SIMS) and capacitance–voltage (CV) profiles of GaAs δ-doped with Sn at a level of 3×10^{12}cm^{-2} during growth interruption (after Harris et al., 1984).

The model of kinetically limited segregation of impurities was used to explain the redistribution of Sn impurities in GaAs during growth by molecular-beam epitaxy (Harris et al., 1982 and 1984). The doping profile of epitaxially grown GaAs:Sn is shown in Fig. 8.17. Tin was deposited on a GaAs surface. Subsequently, a 0.6 μm thick GaAs top layer was deposited. The C-V and SIMS profiling techniques show a pronounced tail towards the surface. The decrease of the Sn concentration follows an exponential dependence which is in agreement

https://doi.org/10.1017/CBO9780511599828.011 Published online by Cambridge University Press

with the model.

An alternative model for impurity surface segregation was proposed by Wood and Joyce (1978). They assumed that the *incorporation* of impurities from the surface is limited and that most of the impurities remain on the surface. In order to incorporate impurities from the surface, a large surface density must build up before a significant concentration of impurities is incorporated into the semiconductor. If indeed a surface reaction limits the incorporation of impurities, the incorporation rate is expected to strongly depend on the surface stoichiometry. Wood and Joyce (1978) investigated the system GaAs:Sn and proposed that the Sn incorporation rate depends on the Ga vacancy concentration which in turn is related to the V/III flux ratio. The authors found that the Sn incorporation increases with the group-V flux, which supports their assumption that the Sn incorporation depends on the Ga vacancy concentration. However, Harris et al. (1984) did not observe a clear dependence of the incorporated Sn concentration on the As_4 or As_2 flux. Therefore, they concluded that the model of surface rate-limitation to incorporation proposed by Wood and Joyce (1978) is incorrect.

8.5.3 Fermi-level-pinning induced surface drift

Surface effects can have a strong influence on the redistribution of impurities during epitaxial growth. In this section we consider the influence of Fermi-level pinning on the distribution of impurities near the semiconductor surface. The pinning of the Fermi level at a semiconductor surface results in the trapping of free carriers at the surface and the formation of a dipole field near the surface. The electric dipole field exerts a force on charged impurities which tend to drift to the surface, i.e. they redistribute towards the surface.

Fermi-level pinning at an interface of a semiconductor and a second medium, such as a metal, insulator, or vacuum, is a classic phenomenon in semiconductor physics. The Fermi level at the interface is frequently pinned at a specific energy $e\phi_B$ below the bottom of the conduction band. Bardeen (1947) attributed Fermi-level pinning to interface states which are of donor and acceptor type. Energetically, such Bardeen states can be in the conduction or valence band (e.g., for InAs); more frequently, the states are located close to the middle of the fundamental gap (e.g., GaAs). In an earlier model, Schottky (1938, 1940) and Mott (1938) proposed that the energy $e\phi_B$ of a metal–semiconductor contact equals the difference of the work function of the metal and the electron affinity of the semiconductor. The physical origin of Bardeen's interface or surface states was ascribed to metal-induced gap states (Heine, 1965) or to localized states at the semiconductor surface or interface. Such localized states could be due to

https://doi.org/10.1017/CBO9780511599828.011 Published online by Cambridge University Press

atomic steps of the surface (Huijser et al., 1977) defects, (Spicer et al., 1975, 1980) or surface reconstruction (Ihm et al., 1983, Chiang et al., 1983). Different pinning energies were found for different crystal orientations, e.g., the ⟨100⟩ and ⟨110⟩ GaAs orientations (Kahng, 1964). Using angle-resolved photoemission of GaAs (100) surfaces, Chiang et al. showed that the Fermi level is pinned at 0.55 ± 0.1 eV above the valence-band maximum for all reconstructed surfaces studied by the group. They proposed that defect states associated with slight non-stoichiometry pin the Fermi level. Fermi-level pinning was found to be insensitive to temperature in the entire temperature range $20\ °C \leq T \leq 500\ °C$ (Nanichi and Pearson, 1969), consistent with the fact that the thermal energy kT is much smaller than other relevant energies.

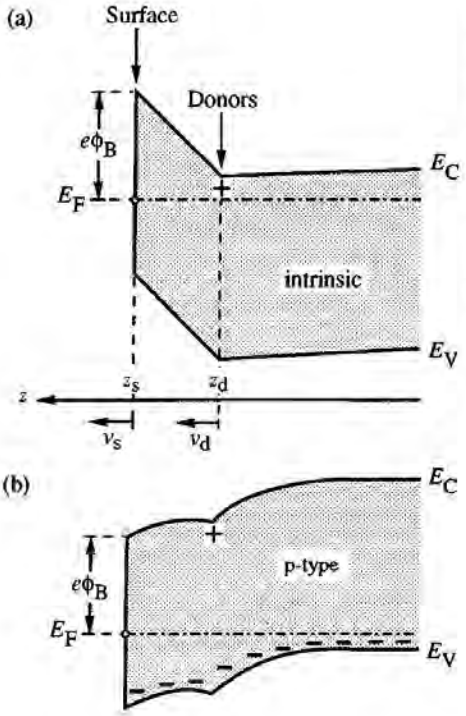


Fig. 8.18. (a) Band diagram of a semiconductor subject to Fermi-level pinning which contains a δ-function-like donor spike. (b) Band diagram of a semiconductor subject to Fermi-level pinning which contains p-type background doping and a δ-function-like donor spike. The coulombic dipole interaction between the surface and the donor layer can be reduced by p-type background doping.

The band diagram of a semiconductor with a Fermi level pinned at the surface is shown in Fig. 8.18(a). A sheet of impurities is located at $z = z_d$. Since the semiconductor is assumed to grow epitaxially, the surface moves with the velocity v_s (i.e. growth rate). Impurities in the sheet are subject to the electric field and drift along the growth direction with a velocity v_d. For a two-dimensional doping density of N_D^{2D}, the electric field of the dipole is given by

https://doi.org/10.1017/CBO9780511599828.011 Published online by Cambridge University Press

$$\mathcal{E} = eN_D^{2D}/\varepsilon\,, \tag{8.49a}$$

$$\mathcal{E} = \phi_B/(z_s - z_d) \tag{8.49b}$$

where e is the elementary charge, ε is the permittivity, and $z_s = v_s t$ and z_d are the position of the surface and the doped layer, respectively. Equation (8.49a) is valid if the doped layer is depleted of all free carriers, i.e., $z_s - z_d \leq \phi_B \varepsilon/eN_D^{2D}$, while Eq. (8.49b) is valid if the doped layer is partly depleted of free carriers, i.e., $z_s - z_d \geq \phi_B \varepsilon/eN_D^{2D}$. The drift velocity of dopants is given by

$$v_d = \frac{dz_d}{dt} = \mu\mathcal{E} \tag{8.50}$$

where μ is the ion mobility, which is obtained from the Einstein relation $\mu = De/kT$. Note that Eq. (8.50) and the Einstein relation apply to any diffusion mechanism, for example, the substitutional mechanism or the substitutional–interstitial mechanism, provided that the initial and final sites of the atomic-diffusion jump are substitutional sites on which the impurity is ionized.

For small distances between the doped layer and the surface, the dipole field is given by Eq. (8.49a) and the drift velocity of the dopants is given by

$$v_d = \frac{De}{kT}\,\frac{eN_D^{2D}}{\varepsilon}\,. \tag{8.51}$$

As an example, we consider the drift of Si impurities in $Al_xGa_{1-x}As$ (Schubert et al., 1988, 1989). At a low growth temperature of 500 °C, the diffusion coefficient of Si in $Al_{0.30}Ga_{0.70}As$ is $D = 2.5 \times 10^{-16}$ cm^2/s and Eq. (8.51) yields $v_d = 0.1$ Å/s for the drift velocity, which is relatively small. However, at $T = 660$ °C, $D = 6 \times 10^{-15}$ cm^2/s, and the drift velocity is 2 Å/s, which is comparable in magnitude to the growth velocity (v_g) of 1.29 μm/h = 3.6 Å/s for $Al_{0.30}Ga_{0.70}As$ (0.9 μm/h for GaAs). Thus, significant surface migration is expected to occur at $T = 660$ °C.

To obtain a single differential equation for small $z_s - z_d$ and large $z_s - z_d$, the electric field given in Eqs. (8.49a) and (8.49b) is approximated by

$$\mathcal{E} = \left[\left(\frac{e}{\varepsilon}\,N_D^{2D}\right)^{-1} + \left(\frac{\phi_B}{z_s - z_d}\right)^{-1}\right]^{-1}, \tag{8.52}$$

which represents a lower limit of the true field. The differential equation then becomes

https://doi.org/10.1017/CBO9780511599828.011 Published online by Cambridge University Press

$$\frac{dz_d}{dt} = \frac{De}{kT}\left[\frac{\varepsilon}{eN_D^{2D}} + \frac{z_s - z_d}{\phi_B}\right]^{-1}, \tag{8.53}$$

with $z_s = v_s t$.

The surface electric field can be reversed in direction by appropriate background doping. Figure 8.18(b) shows the band diagram of a semiconductor with a n-type doping spike embedded into p-type background doping. The band diagram shows that the surface electric field is reversed in direction and reduced in magnitude. It is thus possible to screen and reduce the surface electric field by appropriate background doping.

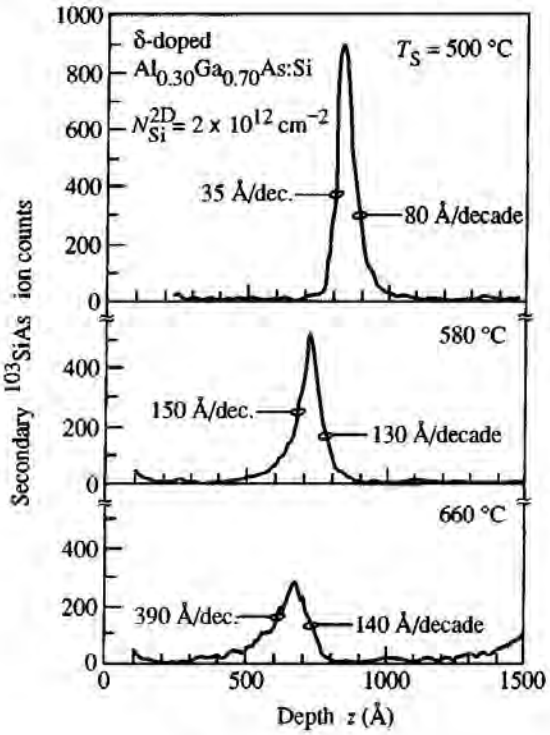


Fig. 8.19. Secondary ion mass spectrometry profile of Si in $Al_{0.30}Ga_{0.70}As$ grown at 500, 580 and 660 °C by molecular-beam epitaxy. Silicon was deposited during growth interruption to achieve a δ-function-like doping profile. SiAs with molecular weight 103 was used for detection.

The model of Fermi-level-pinning induced drift has been employed to explain experimental results on Si-doped $Al_{0.30}Ga_{0.70}As$ (Schubert et al., 1990a). Si-dopant profiles obtained from SIMS are shown in Fig. 8.19 for the three samples grown at 500, 580, and 660 °C. At a low growth temperature a sharp peak is observed. The slight asymmetric shape of the SIMS profile obtained at low growth temperature is due to the well-known 'knock-on' effect. As the growth temperature is increased, the profiles exhibit significant asymmetry. Surface

https://doi.org/10.1017/CBO9780511599828.011 Published online by Cambridge University Press

migration of dopants is evident from the profiles, especially at T_s = 660 °C. The steepnesses of the leading and the trailing slopes of the SIMS spectrum are evaluated in terms of the length in which the Si signal decreases by 1 order of magnitude. The leading slope increases from 35 Å/decade to 390 Å/decade, indicating the drift of impurities towards the surface. The trailing slope increases from 80 Å/decade to 140 Å/decade indicating diffusion of dopants, which is expected to be symmetric with respect to both sides of the doping spike.

Qualitatively the same, but quantitatively weaker redistribution of impurities towards the surface is observed for Si in GaAs. The smaller redistribution of impurities in GaAs is consistent with the smaller diffusion constant found in GaAs as compared to $Al_xGa_{1-x}As$.

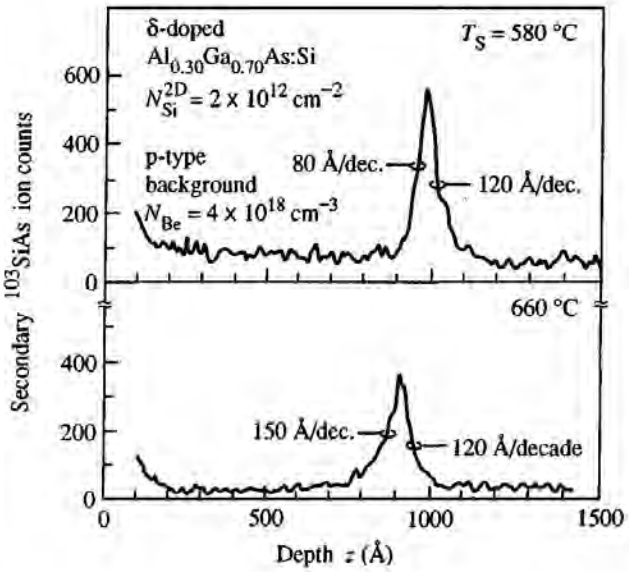


Fig. 8.20. Secondary ion mass spectrometry profile of Si in $Al_{0.30}Ga_{0.70}As$ grown at 580 and 660 °C. The epitaxial layer is also homogeneously doped with Be.

Fermi-level pinning at the semiconductor surface causes the doped layer to be depleted of free carriers and a localization of electrons in surface states. If the resulting dipole field is the driving force towards the surface, then this migration process can be reduced by screening the dipole field. Figure 8.20 shows two SIMS profiles in $Al_xGa_{1-x}As$ epitaxial samples with p-type Be background doping. The concentration of Be is chosen to be $N_A = 4 \times 10^{18}$ cm^{-3} in order to compensate for the Si dopants within 50 Å. Figure 8.20 reveals that the

https://doi.org/10.1017/CBO9780511599828.011 Published online by Cambridge University Press

segregation length is drastically reduced from 150 Å/decade to 80 Å/decade at a growth temperature of 580 °C. The decrease of the segregation length is attributed to the screening of the surface dipole caused by Fermi-level pinning. The trailing slope of the SIMS profile is changed insignificantly, indicating that diffusion and the 'knock-on' effect are not influenced by background doping. The SIMS profile for the sample grown at $T = 660$ °C shows the same qualitative trend as the sample grown at the intermediate temperature (see Figs. 8.19 and 8.20). The surface drift is reduced and the SIMS profile has a more symmetric shape, indicating that diffusion dominates the dopant redistribution. The experimental and theoretical results show that the surface migration process of Si in $Al_xGa_{1-x}As$ can be consistently explained by the model of Fermi-level-pinning induced drift of impurities. The model is consistent with the substrate temperature dependence of the impurity migration. Finally, the experimental results show that the migration can be reduced by appropriate background doping.

Further aspects of the surface migration mechanism are as follows. First, the magnitude of the redistribution scales with the diffusion coefficient as inferred from Eq. (8.53). Impurities with a large diffusion coefficient (such as Sn in GaAs) are therefore expected to redistribute more strongly towards the surface as compared to impurities with a small diffusion coefficient (such as Si in GaAs). Second, the Fermi-level-pinning model predicts a *net* displacement of impurities toward the surface. In fact, for sufficiently low growth rates, the impurity drift velocity can become comparable to the growth velocity; in this case, impurities drift along with the surface and remain in the vicinity of the surface. This is in contrast to the segregation model discussed in the previous section, in which no net displacement of impurities is expected. Third, the model of Fermi-level-pinning induced surface drift is a *general* model. Based on this model, *all* impurities in III–V semiconductors are expected to drift towards the surface.

The influence of the Fermi level at the surface on the incorporation has been considered previously by a number of groups (Casey et al., 1971; Zschauer and Vogel, 1971; Panish, 1973; Wolfe and Stillman, 1973; Wolfe and Nichols, 1977). In liquid-phase epitaxy, the incorporation of impurities at the liquid/solid interface is controlled by the equilibrium between the liquid and the crystal surface. The incorporation is therefore influenced by the position of the Fermi level at the growing surface rather than in the bulk of the crystal (Panish, 1973). The effect of Fermi-level pinning on the amphoteric behavior of Sn in GaAs was studied by Wolfe and Stillman (1973). They found that the amphoteric behavior of Sn can be explained by a surface-state density of 3×10^{11} cm^{-2}. Wolfe and Nichols (1977) explained thin p-type regions often observed at the (n-type)

https://doi.org/10.1017/CBO9780511599828.011 Published online by Cambridge University Press

epilayer/(n-type) substrate interface with the electric field associated with surface states and substrate doping. Surface states and substrate doping were believed to be the major cause of impurity gradients in epitaxial GaAs.

8.6 Impurity-induced layer disordering

Impurities have a profound effect on the self-diffusion of group-III elements and probably on group-V elements in III–V semiconductors. Laidig et al. (1981) found drastically increased Al–Ga diffusion in an AlAs/GaAs superlattice upon Zn diffusion. Zinc was diffused from a surface layer into the bulk. The interdiffusion of the group-III elements of the superlattice was found even at moderate temperatures of 600 °C.

The diffusion of group-III and group-V elements in III–V semiconductors is known as ***self-diffusion***. It is well known that the self-diffusion coefficient is very small in III–V semiconductors and that the corresponding activation energy for self-diffusion can be very high. For example, the Al–Ga interdiffusion activation energy was determined by Mei et al. (1987) in AlAs/GaAs structures to be $E_a = 4$ eV for doping concentrations $\gtrsim 5 \times 10^{17}$ cm^{-3}. Tan and Gösele (1988) measured the activation energy for group-III self-diffusion in undoped (near-intrinsic) GaAs and obtained $E_a = 6$ eV. The large activation energies demonstrate that self-diffusion is a rather unlikely process. The temperature dependence of the Ga self-diffusion coefficient was measured by Palfrey et al. (1981). For Ga diffusion from a Ga film on the surface of a GaAs crystal, the authors determined a diffusion coefficient of

$$D = 3.9 \times 10^{-5}\ \mathrm{e}^{-2.6\ \mathrm{eV}/kT}\ \mathrm{cm}^2/\mathrm{s}\ . \tag{8.54}$$

Note that the activation energy of 2.6 eV is much lower than the values obtained by Mei et al. as well as Tan and Gösele. However, a comparison is not straightforward since the diffusion experiments of Palfrey et al. were performed on non-stoichiometric material, i.e. GaAs with excess Ga. Furthermore, the residual impurity concentration in GaAs was probably different for the three reports. The self-diffusion of As in GaAs has been investigated by Palfrey et al. (1983) as well as by Goldstein (1961). The former group reports an activation energy of 3 eV for As self-diffusion in GaAs. In contrast, Goldstein estimates an activation energy of 10.2 eV for As self-diffusion in GaAs. Note that the two results are drastically different. Nevertheless, measurements by Palfrey et al. (1983) indicate that the As diffusion coefficient in GaAs is low, e.g. 5.2×10^{-16} cm^2/s at $T = 1000$ °C. It is thus well established that the self-diffusion coefficients in GaAs are very small under intrinsic conditions.

https://doi.org/10.1017/CBO9780511599828.011 Published online by Cambridge University Press

The self-diffusion in other III–V semiconductors is associated with a high activation energy as well. The activation energies for In and P diffusion in InP are 3.85 eV and 5.65 eV, respectively (Goldstein, 1961). In InAs, activation energies of 4.0 eV and 4.5 eV for In and As, respectively, were determined (Kato et al., 1969). Activation energies of 4.3 eV were determined for both In and Sb for self-diffusion in InSb (Kendall and Huggins, 1969). The above results confirm that self-diffusion in intentionally undoped III–V semiconductors is a relatively slow process.

The self-diffusion in III–V semiconductors is changed drastically at high impurity concentrations. The drastic change of self-diffusion is illustrated in Fig. 8.21 (Meehan et al., 1984). The figure shows an $Al_xGa_{1-x}As/GaAs$ superlattice that has been disordered on the left-hand side by Si diffusion. The right-hand side was masked by Si_3N_4 and, as a consequence, Si did not diffuse into the semiconductor. The superlattice is unaffected in this region by the annealing cycle of 10 h at 850 °C. Figure 8.21 illustrates that the inter-diffusion of group-III elements is strongly enhanced by impurity diffusion. Further experimental results have been summarized in an excellent review by Deppe and Holonyak (1988), which also summarizes experimental results on impurity-induced disordering by the donors Si, Ge, S, Sn, and Se as well as the acceptors Zn, Be, and Mg. Furthermore, disordering by (i) diffusion as well as (ii) implantation was described.

Next, we consider a physical model that accounts for increased self-diffusion in III–V semiconductors. As an example, we consider the group-III self-diffusion only and neglect group-V diffusion and follow the arguments of Deppe and Holonyak (1988). The self-diffusion of group-III lattice atoms must proceed through native defects of the crystal. Therefore, the self-diffusion rate will be dependent on the diffusion rate of the native defects, but since the concentration of native defects is typically much less than the concentration of group-III lattice atoms ($\cong 2 \times 10^{22}$ cm^{-3}), the group-III self-diffusion rate will also depend on the concentration of the requisite crystal defects. If we consider, for example, self-diffusion of the group-III atoms through group-III vacancies, then

$$D_{III} = f D_{V_{III}} [V_{III}] \tag{8.55}$$

where D_{III} is the group-III atom diffusion rate, $D_{V_{III}}$ is the group-III vacancy diffusion rate, V_{III} is a group-III vacancy, the brackets [ ] denote concentration, and the prefactor f contains information about the crystal structure (Manning, 1968) and the concentration of group-III lattice sites. Equation (8.55) shows that as $[V_{III}]$ increases so will D_{III}.

https://doi.org/10.1017/CBO9780511599828.011 Published online by Cambridge University Press

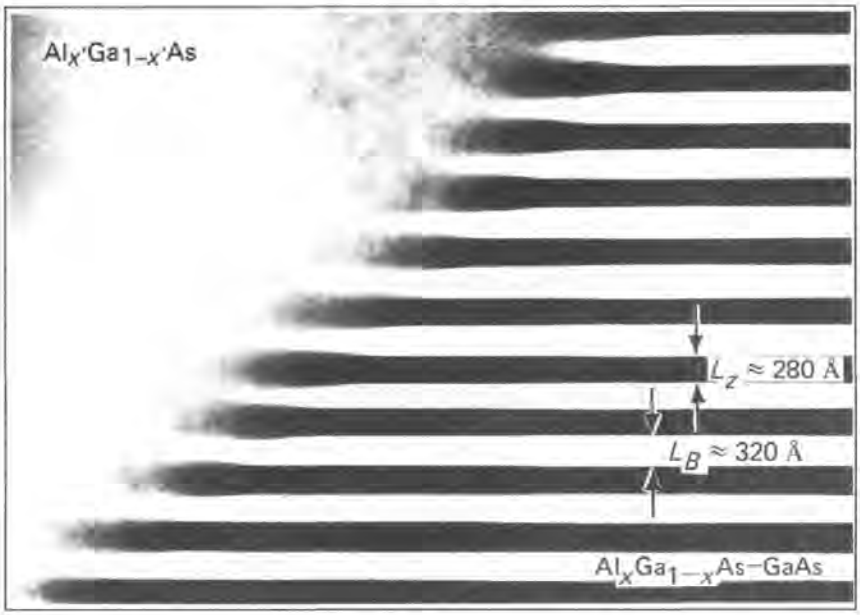


Fig. 8.21. Bright field transmission electron micrograph of a 40 - period $Al_{0.60}Ga_{0.40}As/GaAs$ superlattice ($L_B \approx 320$ Å, $L_z \approx 280$ Å) which has been disordered into bulk $Al_xGa_{1-x}As$ by Si diffusion (left side). The $Al_{0.60}Ga_{0.40}As/GaAs$ superlattice masked with Si_3N_4 has 'survived' the 850 °C (10 h) anneal (right side) (Meehan et al., 1984).

It has been known for a long time that if the point defects in a semiconductor possess various charge states, the equilibrium defect concentrations will depend on the crystal Fermi level (Longini and Greene, 1956). To illustrate further the influence of the Fermi level on the native defect concentration we consider the impurity–vacancy complex proposed by Laidig et al. (1982). They proposed that in the transfer of a Zn atom from a substitutional site to an interstitial site, an intermediate stage could occur, which consists of a complex formed by interstitial Zn and a group-III vacancy

$$Zn_i^+ + V_{III} \leftrightarrow (Zn_i V_{III})^+ \leftrightarrow Zn_{III}^- + 2h \qquad (8.56)$$

where Zn_i^+ and Zn_{III}^- are a (positively charged) interstitial Zn atom and a (negatively charged) substitutional Zn atom, respectively. We now consider the middle and right-hand side of Eq. (8.56) and recall that at equilibrium, the ratio of the concentrations of the initial and final products of the reaction is a constant, i.e.

https://doi.org/10.1017/CBO9780511599828.011 Published online by Cambridge University Press

$$\frac{[(Zn_i V_{III})^+]}{[Zn_{III}^-]\, p^2} = K \tag{8.57}$$

where p is the hole concentration and K is the equilibrium constant. The equation shows that the concentration of the Zn-vacancy complex increases with the square of the hole concentration, i.e. with the square of the Zn doping concentration. Since D_{III} is proportional to $[V_{III}]$ (see Eq. (8.55)), and $[V_{III}] \propto p^2$, it is clear that the group-III self-diffusion coefficient strongly increases with doping concentration. Thus, the occurrence of native defects which are required for self-diffusion and whose concentration depends on the doping concentration, is the basis for models on impurity-induced layer disordering. The influence of the Fermi level on the concentration of ionized lattice vacancies was first considered by Longini and Greene (1956) who explained the systematic differences between n- and p-type semiconductors with respect to lattice vacancy concentration, substitutional atom diffusion coefficients, and amphoteric impurity behavior.

Several other physical models were proposed to account for impurity-induced layer disordering which were summarized by Deppe and Holonyak (1988). Tan and Gösele (1987) assumed that both group-III and group-V vacancies can be charged either positively or negatively. They suggested that, in the case of p-type doping, group-III self-diffusion proceeds mainly because of positively charged group-III vacancies, while group-V diffusion proceeds because of positively charged group-V vacancies. Similarly, in the case of n-type doping group-III self-diffusion proceeds via negatively charged group-III vacancies and group-V diffusion via negatively charged group-V vacancies. Independently, at about the same time, Deppe et al. (1987) presented data showing that the diffusion of the Si impurity in GaAs is controlled in part by the crystal Fermi energy. Based on the dependence of the Si diffusion rate on the Fermi level and on the As vapor pressure over the crystal during annealing, Deppe et al. (1987) suggested that the Si diffusion, and the layer intermixing in $Al_xG_{1-x}As/GaAs$ quantum wells or superlattices that accompanies the Si diffusion, is due to donor vacancy complexes, $Si_{Ga} - V_{Ga}$. In related work, Kaliski et al. (1987) have presented experimental data on annealing of quantum wells containing either the donor Se or the acceptor Mg showing that for As-rich annealing conditions n-type quantum wells undergo considerable intermixing while p-type quantum wells remain stable. Under As-poor annealing conditions, the n-type quantum wells remain more stable while the p-type quantum wells undergo layer intermixing. Based on the fact that the layer intermixing depends on the type of doping (n or p) and As overpressure, the suggestion has been made that intermixing occurring in p-type

https://doi.org/10.1017/CBO9780511599828.011 Published online by Cambridge University Press

quantum wells under As-poor annealing conditions is due to group-III interstitials, while the intermixing occurring in n-type quantum wells under As-rich conditions is due to group-III vacancies (Kaliski, 1987). Devine et al. (1987) have independently suggested that layer disordering via Be diffusion in $Al_xGa_{1-x}As$/GaAs superlattices depends on group-III interstitials. Previously, Willoughby (1983) has suggested that interstitials are involved in $Al_xGa_{1-x}As$/GaAs superlattice disordered by Zn diffusion.

https://doi.org/10.1017/CBO9780511599828.011 Published online by Cambridge University Press

9

Deep centers

Deep centers are chemical impurities, native defects, or a combination of both, which have at least one energy level in the forbidden gap. The energy level or levels of deep centers are far removed from the conduction and valence band edges, which is in contrast to shallow impurities. The phenomenology of deep centers was discussed and analyzed in Chap. 2. In the present chapter, the characteristics of some specific deep centers will be summarized.

The *DX-center* is of primary technological importance in n-type $Al_xGa_{1-x}As$ devices such as transistors and lasers. The properties of this center have puzzled researchers for more than a decade. The *EL2 center* can cause undoped bulk-grown GaAs to be semi-insulating. The EL2 center is of importance for the growth of GaAs bulk crystals and for the production of substrates. *Hydrogen* can be used in two different ways to influence the electronic properties of III–V semiconductors. First, protons implanted into III–V semiconductors cause damage to the crystal; the damaged regions can trap carriers. Second, hydrogen can passivate acceptor as well as donor impurities. *Oxygen* is also used to render III–V semiconductors semi-insulating. *Chromium* and *iron* are deep impurities which are used to make GaAs and InP highly resistive. Both Cr and Fe are deep acceptors and compensate for residual shallow donors in the two semiconductors. They are used as intentional deep impurities in the bulk growth of GaAs and InP. Finally, rare-earth atoms such as Er, Pr, or Nd incorporated into semiconductors have energy levels which are not associated with either the conduction or valence band. Intra-impurity transitions of rare-earth impurities can be radiative. Such transitions are of interest for optoelectronic device applications.

https://doi.org/10.1017/CBO9780511599828.012 Published online by Cambridge University Press

9.1 DX-type centers

At the end of the 1970s it became clear that n-type $Al_xGa_{1-x}As$ with Al mole fractions of $0.2 \leq x \leq 0.4$ has very unusual properties as compared to GaAs. These properties include a large donor activation energy, a strong sensitivity of the conductivity on optical radiation, as well as large barriers to emission and capture. These anomalous properties, which are not expected from an effective-mass-like donor, led Lang et al. (1979) to the conclusion that the deep center involves a donor atom which forms a complex with another constituent. The authors therefore designated the center as a ***donor-complex*** or DX-center. Subsequently, this name became associated with the doping properties of the deep donor in n-type $Al_xGa_{1-x}As$.

The measurements of the free carrier concentration in n-type $Al_xGa_{1-x}As$ revealed a ***large thermal activation energy*** of the DX-center in Te-doped $Al_xGa_{1-x}As$ (Nelson, 1977; Lang and Logan, 1977), in Si-doped $Al_xGa_{1-x}As$ (Schubert and Ploog, 1984; Chand et al., 1984) as well as in $Al_xGa_{1-x}As$ doped with Se, Sn, etc. The large thermal ionization energy is evidenced by the dependence of the free carrier concentration on reciprocal temperature which is illustrated in Fig. 9.1 for Si-doped $Al_{0.25}Ga_{0.75}As$. The closed circles illustrate the electron concentration measured in the dark. The free electron concentration remains constant for temperatures below 150 K. The electron concentration increases at temperatures higher than 150 K indicating the thermal ionization of the deep donor center. Note that the ionization process continues even at room temperature, i.e. saturation of the free carrier concentration has not occurred even at $T = 300$ K. The increase of the carrier concentration at room temperature indicates that the DX-center has a large thermal activation energy. The saturation of the free carrier concentration at low temperatures ($T < 150$ K) was attributed to additional shallow donors which do not freeze out at low temperatures if the concentration of such shallow donors is sufficiently high (Schubert and Ploog, 1984). The authors evaluated the deep donor thermal activation energy and showed that the conventional formula frequently used to determine donor activation energies

$$n \propto \exp\left[-\frac{E_{dd}}{2kT}\right] \tag{9.1}$$

can *not* be used if shallow and deep donors co-exist in a semiconductor. Instead, they showed that the deep donor activation energy, E_{dd}, must be determined according to

https://doi.org/10.1017/CBO9780511599828.012 Published online by Cambridge University Press

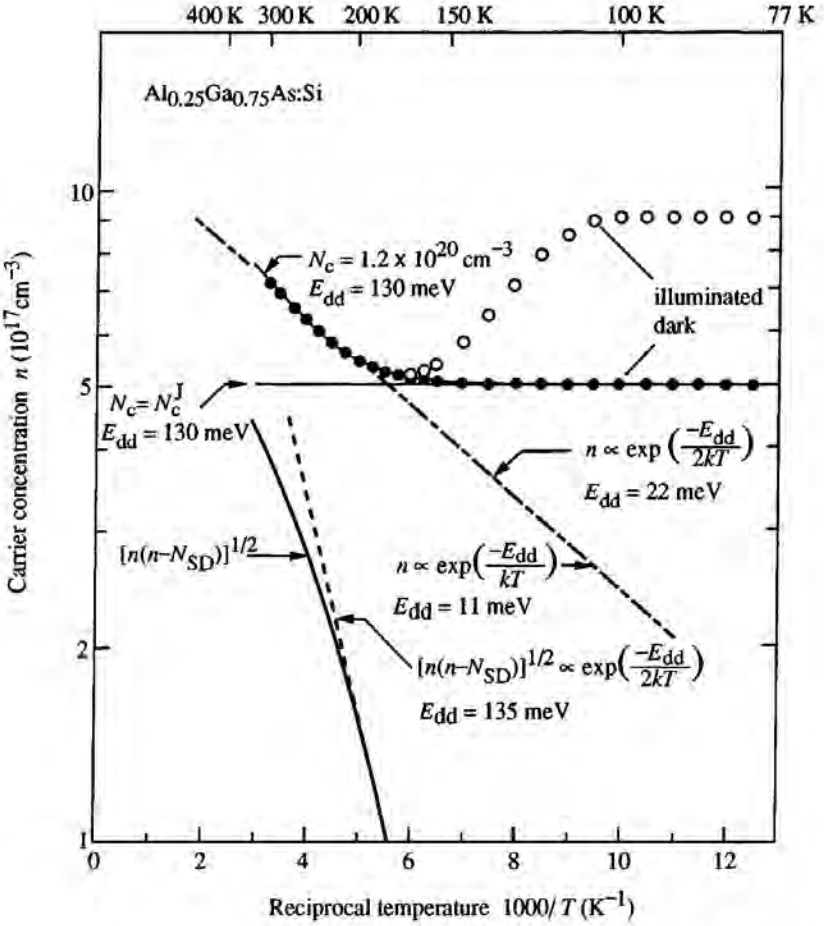


Fig. 9.1. Dependence of the Hall electron concentration in n-type $Al_{0.25}Ga_{0.75}As$:Si on inverse lattice temperature. Solid and open circles indicate experimental data measured in the dark and after illumination at low temperatures, respectively. The deep-donor thermal activation energy E_{dd} is evaluated by three methods. The simple relations $n \propto \exp(-E_{dd}/kT)$ and n $\propto$ $\exp(-E_{dd}/2kT)$ yield E_{dd} = 11 and 22 meV, respectively (dashed-dotted line). A more realistic value of E_{dd} = 135 meV is obtained using the relation $(n^2-nN_{SD})^{1/2} \propto \exp(-E_{dd}/2kT)$ at low temperature indicated by the dotted line. A simulation of the carrier concentration versus temperature in terms of Fermi–Dirac statistics yielding E_{dd} = 130 meV for the thermal activation energy of the deep donor (solid curve) coincides with the experimental data only if a density of states much larger than that of the Γ valley is used. The experimental data cannot be fitted to the experimental data by means of the lower joint density of states N_c^J.

https://doi.org/10.1017/CBO9780511599828.012 Published online by Cambridge University Press

$$\sqrt{n(n - N_{SD})} \propto \exp\left[-\frac{E_{dd}}{2kT}\right] \tag{9.2}$$

where N_{SD} is the shallow donor concentration ($N_{SD} = 5 \times 10^{17}$ cm^{-3} in Fig. 9.1). A deep donor thermal activation energy of $E_{dd} = 130$ meV was evaluated using this procedure.

The electronic properties of n-type $Al_xGa_{1-x}As$ change strongly as the Al mole fraction increases. Figure 9.2 shows the Hall carrier concentration of Si-doped n-type $Al_{0.32}Ga_{0.68}As$. Comparison with Fig. 9.1 yields that (i) the deep donor concentration has increased while (ii) the shallow donor concentration has decreased. Evaluation of the thermal activation energy yielded $E_{dd} = 135$ meV. Thus, the experimental results show that (i) the thermal activation energy of the deep DX-donor in n-type $Al_xGa_{1-x}As$ ($0.2 \leq x \leq 0.4$) is $E_{dd} \cong 130-140$ meV independent of the Al mole fraction, and (ii) that the relative concentration of deep DX-donors increases with Al mole fraction while simultaneously the shallow donor concentration decreases. Note that as a consequence of these properties, the free electron concentration at $T = 300$ K is *lower* than the Si impurity concentration. Several groups have interpreted the free electron concentration decrease as a lower ***doping-efficiency*** of n-type impurities in $Al_xGa_{1-x}As$ as compared to GaAs (see, for example, Ishibashi et al., 1982). The physical reason for the decreased carrier concentration at $T = 300$ K is the large thermal activation energy of the deep DX-donor which is much larger than kT at room temperature. Watanabe and Maeda (1984) independently came to the conclusion that shallow donors and DX-centers co-exist in Si-doped $Al_xGa_{1-x}As$. Evaluation of the shallow and deep donor concentrations yielded that the shallow donor concentration decreases at $x \cong 0.25$ while simultaneously the deep donor concentration increases. They further concluded that the change in Hall activation energy is a result of the changing concentration of the two types of donors.

A different interpretation of the thermal activation energy of deep DX-centers has been proposed by a number of groups (see, for example, Ishibashi et al., 1982; Chand et al., 1984). The authors evaluated the temperature dependent Hall concentration measurements using

$$n \propto \exp\left[-\frac{E_{dd}}{kT}\right] \tag{9.3}$$

and obtained deep donor activation energy that steeply increases from $E_{dd} \cong 10$ meV ($x = 0.20$) to $E_{dd} \cong 160$ meV ($x = 0.45$). Note, however, that even at small Al mole fractions ($x = 0.22-0.24$) where the donor energy is

https://doi.org/10.1017/CBO9780511599828.012 Published online by Cambridge University Press

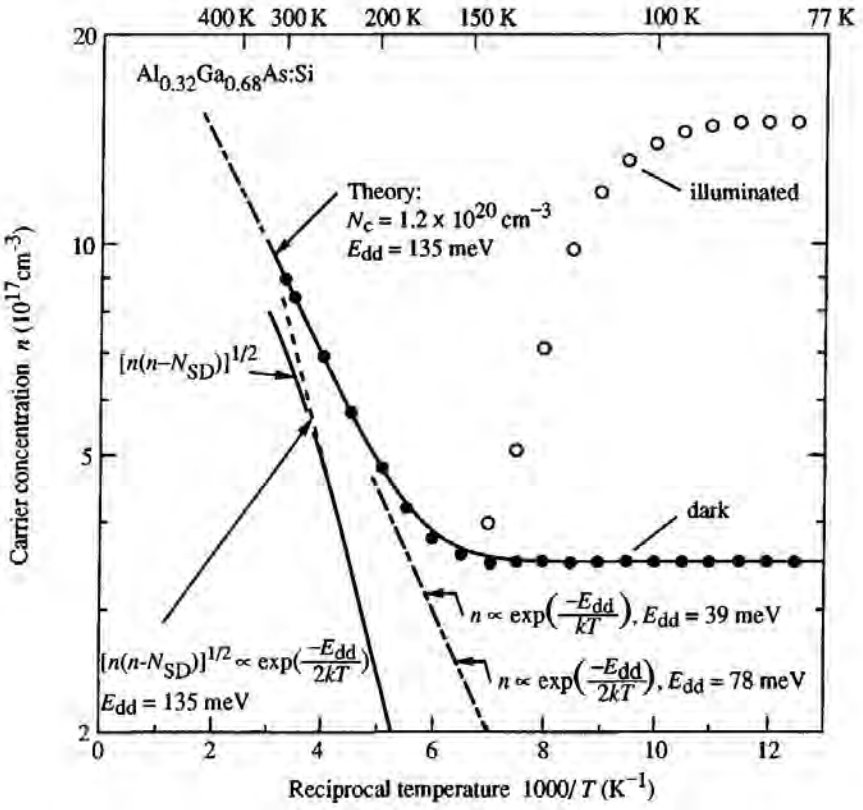


Fig. 9.2. Dependence of the Hall electron concentration in n-type $Al_{0.32}Ga_{0.68}As$:Si on inverse lattice temperature. Solid and open circles indicate experimental data measured in the dark and after illumination at low temperatures, respectively. The deep-donor thermal activation energy E_{dd} is evaluated by three methods. The simple relations $n \propto \exp(-E_{dd}/kT)$ and $n \propto \exp(-E_{dd}/2kT)$ yield E_{dd} = 39 and 78 meV, respectively (dashed-dotted line). A more realistic value of E_{dd} = 135 meV is obtained using the relation $(n^2-nN_{SD})^{1/2} \propto \exp(-E_{dd}/2kT)$ at low temperature indicated by the dotted line. A simulation of the carrier concentration versus temperature in terms of Fermi–Dirac statistics yielding E_{dd} = 135 meV for the thermal activation energy of the deep donor (solid curve) coincides with the experimental data only if a density of states much larger than that of the Γ valley is used.

supposedly shallow (10–20 meV), the ionization of the deep donor is not complete even at room temperature. The discrepancy between low activation energy but incomplete ionization at room temperature was not addressed by the authors.

Another key characteristic of DX-centers in $Al_xGa_{1-x}As$ is the ***persistent photo-conductivity*** (PPC) effect. Upon illumination of n-type $Al_xGa_{1-x}As$ at low temperature, the carrier concentration increases. The increase in carrier

https://doi.org/10.1017/CBO9780511599828.012 Published online by Cambridge University Press

337-TA-1366 RX-0255

concentration persists even after the illumination has been turned off. This phenomenon is known as persistent photoconductivity. The light used for illumination has a wavelength below the fundamental gap of $Al_xGa_{1-x}As$; band-to-band excitation is therefore excluded. The Hall carrier concentrations after illumination are shown in Figs. 9.1 and 9.2 by open circles. The carrier concentration remains high and does not decay to its dark value even hours or days after termination of the photoexcitation. The high PPC concentration can be quenched by heating the sample to a temperature >150 K as shown in Figs. 9.1 and 9.2. The kinetics of the quenching were first measured by Nelson (1977) at temperatures of 60–80 K in Te-doped $Al_xGa_{1-x}As$. The rate of the decrease of the carrier concentration increases at higher temperatures. The optical threshold energy for the PPC effect has been determined to be 0.85 eV ± 0.1 eV for Te-doped $Al_xGa_{1-x}As$ (Lang et al., 1979) and 1.0 eV ± 0.1 eV for Si-doped $Al_xGa_{1-x}As$ (Schubert et al., 1985). The large difference in thermal ionization energy and photoionization energy is well established for all n-type impurities in $Al_xGa_{1-x}As$. The large difference between thermal (≅0.1 eV) and optical (≅1 eV) activation energy cannot be explained by conventional, effective-mass-type impurity models. It is worthwhile to note that the PPC effect has deleterious consequences for semiconductor devices containing n-type $Al_xGa_{1-x}As$. Several efforts were undertaken to reduce or eliminate the PPC effect. Most notably, Baba et al. (1983) showed that the use of an AlAs/n-GaAs superlattice can eliminate PPC and improve the Si doping activation by a spatial separation of the Si impurities from the AlAs.

The model of ***large lattice relaxation*** has been successfully used to explain the peculiar properties of the DX-center in $Al_xGa_{1-x}As$ (Lang and Logan, 1977; Lang et al., 1979; Jaros, 1982). The concepts of *small* and *large* lattice relaxation are briefly reviewed in the following. The local structure of an impurity or defect generally depends on the electronic configuration of the center. That is, if the electronic configuration of a defect is changed, the structural configuration changes as well, i.e. the defect configuration relaxes. To illustrate the interdependence of the electronic and the structural configuration, we consider the hydrogen molecule as an example. The energy of the bonding and anti-bonding state of a hydrogen molecule is shown in Fig. 9.3(a). The distance between the two protons depends on the electronic state of the molecule, i.e. the total energy is minimized at different core distances for electrons occupying either the bonding or the anti-bonding state. This property results in a difference between absorption and emission energies for electronic transitions between the bonding and anti-bonding state. The difference in absorption and emission energies is known as the Franck–Condon shift. This shift can be explained by assuming that the two

https://doi.org/10.1017/CBO9780511599828.012 Published online by Cambridge University Press

RX-0255.382

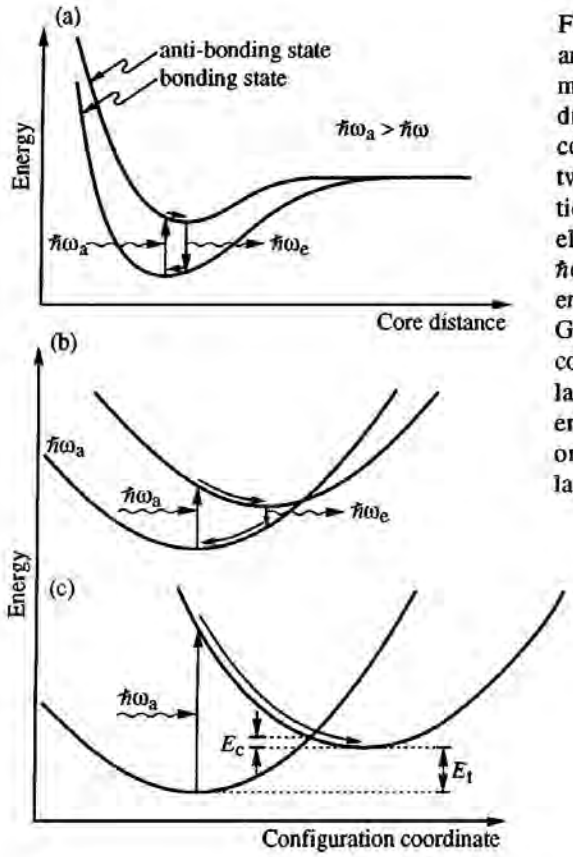


Fig. 9.3. (a) Bonding and antibonding state energy of a molecule as a function of distance between the two cores. The difference between the electronic absorption energy, $\hbar\omega_a$, and the electronic emission energy, $\hbar\omega_e$, is the Franck–Condon energy, $E_{FC} = \hbar\omega_a - \hbar\omega_e$. (b) Generalized configuration coordinate diagram for small lattice relaxation. (c) Generalized configuration coordinate diagram for large lattice relaxation.

nuclei do not move during the short time of the electronic transition due to the much heavier nuclear masses as compared to the electronic masses. Upon an electronic transition, the molecule 'slowly' moves to a new configuration, i.e. new core distance, vibrational frequency, etc. As a consequence, the emission energy, $\hbar\omega_e$, is smaller than the absorption energy, $\hbar\omega_a$ as illustrated in Fig. 9.3(a). The difference $\hbar\omega_a - \hbar\omega_e$ is called the ***Franck–Condon energy*** (see also Chap. 2).

The principle of small lattice relaxation is generalized in Fig. 9.3(b) which shows the defect energy for two electronic configurations as a function of the configuration coordinate. Without specifying the exact meaning of the configuration coordinate it is implied that the *structural* configuration of the impurity or defect is changed upon moving along the configuration coordinate. It is further frequently assumed that the total energy changes *quadratically* as the configuration is changed around the minimum energy position. This parabolic characteristic of the total defect energy is derived from Hooke's law. It is thus assumed that the elastic energy of the defect dominates. Note that the electronic

https://doi.org/10.1017/CBO9780511599828.012 Published online by Cambridge University Press

transitions between the two electronic states are allowed for the case of small lattice relaxation.

This situation is changed drastically for ***large lattice relaxations***. The configuration coordinate diagram corresponding to large lattice relaxation is shown in Fig. 9.3(c). The diagram shows two configurations of the defect. Excitation from the ground-state of the defect to the excited state requires a photon energy $\hbar\omega_a$. Once the defect has minimized its energy in the excited state, the defect *cannot return to the ground state* by means of an optical (i.e. 'vertical') transition. The excited state is thus a ***metastable state***. Note that the excited state is metastable only in the model of large lattice relaxation (Fig. 9.3c) but not for small lattice relaxation (Fig. 9.3b).

While optical transitions are always 'vertical' in the configuration coordinate diagram, thermally excited transitions need not be. During thermal excitation, the defect is displaced from its equilibrium position by vibrational energy. In order for the defect to return from the metastable state to the ground state, it must overcome the thermal capture barrier. The energy of the thermal capture barrier is denoted as E_c in Fig. 9.3(c). Let us estimate the probability of overcoming a capture barrier of $E_c = 200$ meV at a temperature of $T = 4.2$ K. The probability of thermally overcoming the barrier (per attempt) is given by $\exp(-E_c/kT)$ which amounts to 10^{-240}, which is zero for all practical purposes. The large lattice relaxation model can consistently explain the large difference of the thermal and the optical excitation energy. The thermal excitation energy (shown as E_t in Fig. 9.3c) is the difference between the energy minima of the two defect configurations which can be much smaller than the energy required for a vertical optical transition.

Lang and Logan (1977) and Lang et al. (1979) have successfully applied the model of large lattice relaxation to the DX-center in Te-doped n-type $Al_xGa_{1-x}As$. The schematic representation of the relevant energies of the DX-center and their representation in the configuration coordinate diagram are shown in Fig. 9.4(a) and (b) respectively. The authors determined the energies for Te-doped $Al_xGa_{1-x}As$ as follows: Optical excitation, $E_o = 850 \pm 100$ meV; thermal excitation, $E_t = 100 \pm 50$ meV; thermal emission, $E_e = 280 \pm 30$ meV; thermal capture, $E_c = 180 \pm 20$ meV. For Si-doped $Al_xGa_{1-x}As$ the energies can be summarized as follows (Schubert and Ploog, 1984; 1985; Chand et al., 1984; Watanabe et al., 1984; Mizuta et al., 1985; Künzel et al., 1983 and 1984): $E_o \cong 1$ eV, $E_t \cong 150$ meV, $E_e \cong 300$ meV, $E_c \cong 150$ meV. Other n-type impurities such as Se and Sn (see, for example, Tachikawa et al., 1984) have qualitatively similar but quantitatively slightly different characteristics than Te- and Si-doped $Al_xGa_{1-x}As$. Lang (1986)

https://doi.org/10.1017/CBO9780511599828.012 Published online by Cambridge University Press

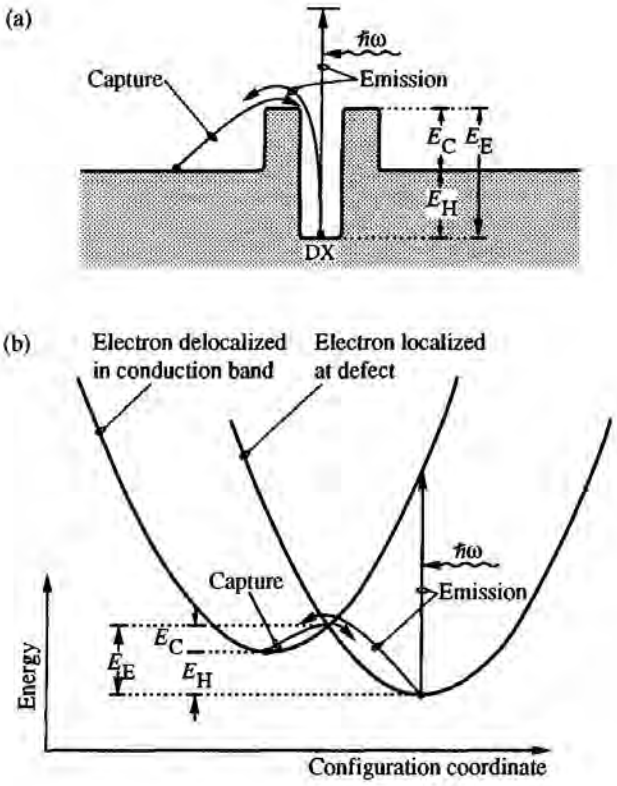


Fig. 9.4. (a) Energy barriers for transient capture (E_C), transient emission (E_E), Hall activation energy (E_H), and optical ionization energy for the DX-center in Te-doped $Al_xGa_{1-x}As$. (b) Schematic configuration coordinate diagram of the center (after Lang et al., 1979).

reviewed the energies of Se, Te, Si, and Sn donors in $Al_xGa_{1-x}As$ and S and Te donors in $GaAs_xP_{1-x}$.

Two atomic configurations were attributed to the unrelaxed and the relaxed state of the DX-center by Chadi and Chang (1988b, 1989), Zhang and Chadi (1990), and Chadi and Zhang (1991). The authors proposed that donors, e.g. a Si donor, can exist in two different configurations in $Al_xGa_{1-x}As$. One of the configurations is the simple substitutional donor which can be neutral or ionized. This configuration is shown for a Si donor on a cation site of $Al_xGa_{1-x}As$ in Fig. 9.5(a). In this normal substitutional site, the Si atom is 0.8 Å above the plane defined by any three adjacent As atoms. In the relaxed DX-configuration, the donor atom occupies an interstitial, threefold coordinated site. One of the four donor-arsenic bonds is broken as illustrated in Fig. 9.5(b). In this relaxed position, the Si atom is 0.2 Å below the plane defined by the three As atoms. The

https://doi.org/10.1017/CBO9780511599828.012 Published online by Cambridge University Press

Innoscience1366-00139058

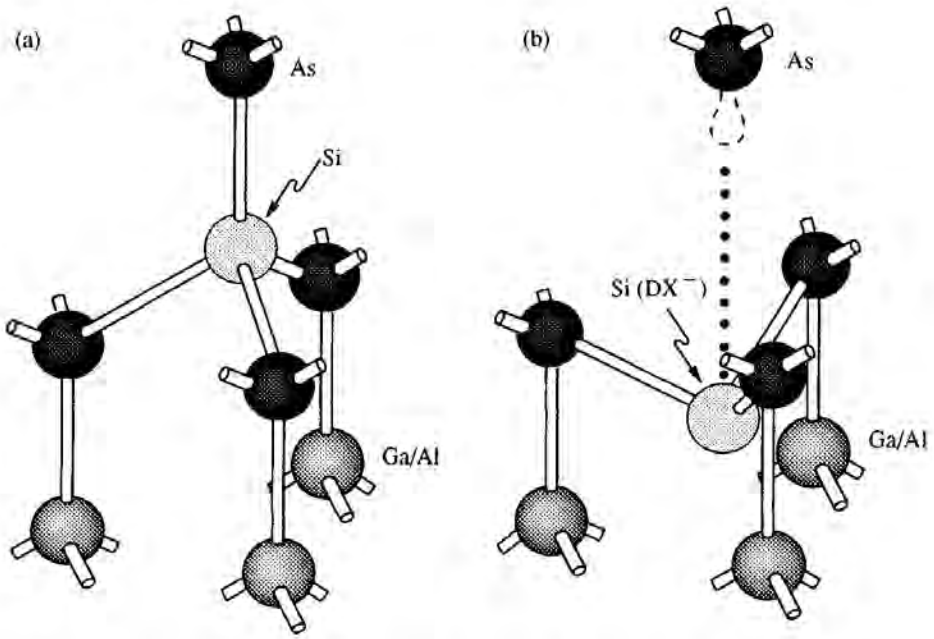


Fig. 9.5. (a) Substitutional Si donor on the cation site of an $Al_xGa_{1-x}As$ lattice. (b) DX-configuration of a Si donor in $Al_xGa_{1-x}As$. The Si donor occupies a threefold coordinated interstitial site and has three cations in its immediate vicinity.

total displacement of the Si is thus approximately 1.0 Å which is indeed a large displacement. Chadi and Chang (1988b) used ab initio self-consistent pseudopotential calculations to show that the DX-configuration is a stable configuration that is negatively charged by two electrons. The following reaction describes the transition from a substitutional donor to a DX-center

$$D^0 + e \leftrightarrow DX^- \tag{9.4a}$$

where D^0 and DX^- represent a neutral fourfold coordinated substitutional donor and a negatively charged DX-center, respectively. Thus, an ionized shallow donor can capture two electrons by assuming the DX-configuration, i.e.

$$D^+ + 2e \leftrightarrow DX^- . \tag{9.4b}$$

The capture of two electrons by the DX-center is supported by experiments of Fujisawa et al. (1990). The authors showed by co-doping of $Al_xGa_{1-x}As$ with Si and Ge that the number of electrons trapped by Ge impurities exceeds the number of Ge impurities, which favors a negative charge state of the DX-center. In contrast, a one-electron ground state of the DX-center has been concluded by

https://doi.org/10.1017/CBO9780511599828.012 Published online by Cambridge University Press

Khachaturyan et al. (1989). From magnetic susceptibility measurements on epitaxial $Al_xGa_{1-x}As$ doped with Si and Te, the authors propose that DX is a paramagnetic center. Further support of the DX-model of Chadi and Chang was obtained from the resolution of several different DX-levels (Kaniewska and Kaniewski, 1985; Takikawa and Ozeki, 1985; Baba et al., 1989; Mooney et al., 1991) which can be attributed to a different local environment of the DX-center. As shown in Fig. 9.5(b), the displaced donor atom is surrounded by three cations (Al or Ga). Depending on the Al mole fraction of the semiconductor, the three cations can include 0, 1, 2, or 3 Al atoms. Thus, four distinct local environments exist which are expected to be reflected in the signature of the DX-center. Four distinct levels of the DX-center have indeed been observed by Baba et al. (1989) which lends further support to the DX-model proposed by Chadi and Chang.

The two configurations of Chadi and Chang also explain the phenomenon of PPC. If the negatively charged DX-center is photoionized, it assumes a neutral state. This state (DX^0) is *unstable* and has an energy 1.3 eV higher than the neutral substitutional Si donor. The Si donor therefore assumes the substitutional D^0 configuration. At sufficiently low temperatures, the Si cannot assume the negatively charged DX^--configuration due to the large capture barrier. The ability to explain the PPC effect lends support to the model of large lattice relaxation. Models proposing small lattice relaxation (see e.g. Mizuta et al., 1985; Mizuta and Kitano, 1987; Mizuta and Mori, 1988) cannot explain the PPC effect observed experimentally. Theoretical and experimental aspects of the DX-center in $Al_xGa_{1-x}As$ and in GaP_xAs_{1-x} were reviewed by Wolford (1991). Further reviews on the DX-center were given by Jaros (1982), Mooney (1990), and Theis (1990).

The reaction describing the formation of the DX-center (see Eq. (9.4)) can also be written as

$$2D^0 \rightarrow D^+ + DX^- \,. \tag{9.5}$$

In n-type $Al_xGa_{1-x}As$, this reaction is strongly exothermic due to the low energy of the DX^- configuration. Donor centers for which Eq. (9.5) is exothermic are called ***negative-U centers***, where U is the effective electron–electron correlation energy of the two centers. The two major contributions to the electron–electron correlation energy are (i) the repulsive coulombic energy of the two electrons and (ii) the lattice distortion energy (Street and Mott, 1975). If the lattice distortion energy more than compensates for the electron repulsion, a *negative* effective correlation energy results. Since such a negative effective correlation energy applies to the DX-center, it is frequently referred to as a negative-U center.

https://doi.org/10.1017/CBO9780511599828.012 Published online by Cambridge University Press

The symmetry of the DX-center in Te-doped $Al_xGa_{1-x}As$ was investigated by Peale et al. (1992a, 1992b) in terms of absorption spectroscopy of the DX-center. The authors used polarized light incident along various symmetry axes for excitation of the DX-center. They found no significant effect for different polarization directions (absence of dichroism) and concluded that either the dipole matrix elements of the DX-center are accidentally very isotropic, or that more likely there is *no* large symmetry-lowering distortion at this center. The absence of a symmetry-lowering distortion of the DX-center is in conflict with the broken-bond model of Chadi and Chang. Subsequently, Chadi (1992) proposed a new model in which substitutional donors in $Al_xGa_{1-x}As$ have two distinct negatively charged DX-like deep-donor states. The first state has a broken-bond configuration while the second arises from a symmetric 'breathing mode' relaxation around the impurity. The latter breathing mode is a symmetric radially outward displacement of its four nearest-neighbors. Chadi (1992) proposed that the absence of dichroism, which has been observed experimentally, is consistent with the tetrahedrally symmetric breathing mode configuration of substitutional donors.

9.2 The EL2 defect

The EL2 defect has had a colourful history. It is the history of the dominant defect in GaAs which has been identified to be most probably the As-antisite defect, As_{Ga}, i.e. a native defect with no other constituents. As a complicating feature, the EL2 defect exhibits metastability due to lattice relaxation which is very similar to the metastability of the DX-center discussed in the previous section. The EL2 center is instrumental in rendering semi-insulating nominally undoped GaAs bulk crystals grown by the Czochralski technique. The name 'EL2' is due to Martin et al. (1977) who analyzed and classified many deep levels in GaAs.

The deep level transient spectroscopy (DLTS) signal of undoped n-type GaAs grown by organometallic vapor-phase epitaxy (OMVPE) is shown in Fig. 9.6 as a function of temperature (Samuelson et al., 1981). The DLTS spectrum reveals a major signal at $T = 390$ K which is the dominant defect level in GaAs. The negative amplitude of the DLTS signal indicates that the level is an electron trap. This dominant deep level is called 'EL2' or 'O-level' in the literature. For the spectrum shown in Fig. 9.6, the concentration of the EL2 level is approximately 1.25×10^{14} cm^{-3}. For VPE-grown GaAs, the concentration of the EL2 level varies between 10^{13} and 10^{16} cm^{-3} (Wagner et al., 1980; Ozeki et al., 1979). In bulk GaAs grown by the Czochralski technique, the EL2 defect can have similar concentrations. Holmes et al. (1982) showed for bulk GaAs that the EL2 defect

https://doi.org/10.1017/CBO9780511599828.012 Published online by Cambridge University Press

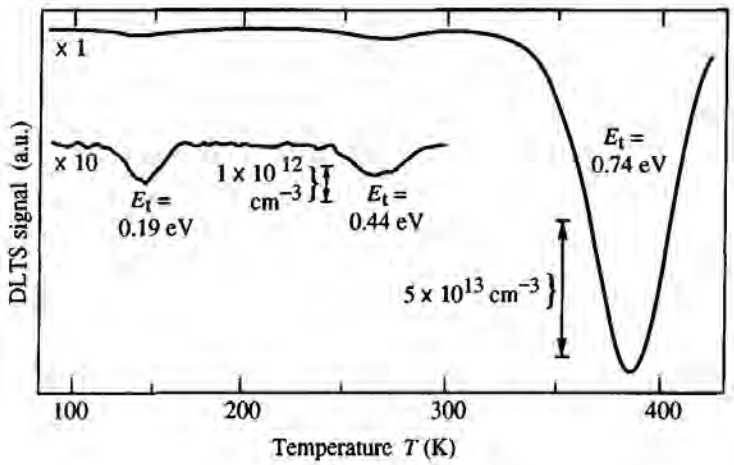


Fig. 9.6. Typical DLTS spectrum of unintentionally doped n-type GaAs grown by organometallic vapor-phase epitaxy (after Samuelson et al., 1981).

concentration varies between 5×10^{15} cm^{-3} and 1.7×10^{16} cm^{-3} depending on the As atom fraction in the melt. The EL2 level is particularly low in GaAs grown by molecular-beam epitaxy (MBE) under optimized growth conditions where the EL2 concentration is below 10^{13} cm^{-3}. Evaluation of the activation energy of the dominant deep donor yields $E_{dd} = 0.74$ eV below the conduction band edge (Samuelson et al., 1981). Evaluation of the ionization energy by other groups yielded $E_{dd} = 0.72...0.82$ eV. Figure 9.6 also exhibits DLTS signals at $T = 140$ K and $T = 270$ K. The concentration of these two levels is approximately 10^{12} cm^{-3}, i.e. much lower than the EL2 defect. The two low-concentration levels will not be further discussed.

The EL2 defect is, as will be shown later, a double donor which has significant technological importance for the growth of semi-insulating (SI) GaAs. GaAs bulk crystals grown by the liquid encapsulated Czochralski (LEC) technique contain a range of chemical impurities including Mn, Fe, B, C, Si, and S (Holmes et al., 1982). The dominant residual impurity is the shallow acceptor C with a concentration in the 10^{15} cm^{-3} range. If no deep traps were present in LEC-grown GaAs, the residual conductivity would be p-type with a resistivity of 0.1 to 10 Ω cm. However, many applications require resistivities of the substrate $> 10^7$ Ω cm, i.e. semi-insulating substrates. The occurrence of the EL2 defect allows one to obtain highly resistive GaAs for sufficiently high concentrations of EL2. The EL2 donor level located approximately 0.75 eV below the conduction band edge compensates for the shallow C acceptor impurities. For $N_{EL2} > N_C$, a

https://doi.org/10.1017/CBO9780511599828.012 Published online by Cambridge University Press

fraction of the EL2 centers (i.e. N_C/N_{EL2}) will be ionized, while the remaining EL2 centers will be neutral (the ionization energy of 750 meV is too large for a thermal ionization process at room temperature). As a consequence, the Fermi level is pinned at the (upper) EL2 level which is approximately in the middle of the GaAs band gap. As a result, GaAs with sufficiently high concentration of EL2 has ***near-intrinsic*** characteristics.

Holmes et al. (1982) showed that the EL2 concentration can be controlled during LEC growth via the As/Ga composition in the melt. For their specific experimental conditions they obtained GaAs with p-type conductivity for an atomic As concentration below 0.475. For As concentrations above 0.475 the GaAs was semi-insulating. The dependence suggests that the EL2 defect is As related, e.g. an As_{Ga} antisite defect. For high As/Ga ratios, the concentration of EL2 defects increases which compensates the shallow acceptors. At low As/Ga ratios, the shallow C acceptor impurities are not fully compensated leading to residual p-type conductivity of the substrates. An increasing EL2 concentration with increasing V/III ratio was also found by Miller et al. (1977), Ozeki et al. (1979), Wagner et al., (1980) and Samuelson et al., (1981). The latter authors found a dependence of $N_{EL2} \propto p_{AsH_3}^{0.5}$.

The EL2 defect has been considered originally to be related to oxygen in GaAs. Increasing the partial pressure of oxygen in the ampoule (Ainslie et al., 1962) or adding Ga_2O_3 to the melt (Fertin et al., 1967) during GaAs growth by the horizontal Bridgman technique results in a drastic change of the electrical properties of the as-grown GaAs. The deep oxygen level was thought to compensate shallow impurities (Allen, 1960; Haisty et al., 1962). However, it was shown later on that the deep EL2 level is probably not related to oxygen (Wagner et al., 1980; Huber et al., 1979). Furthermore, oxygen contamination became a less severe problem due to the increased purity of source materials and the employment of chemically inert materials in growth reactors.

Among the many specific models proposed for the EL2 defect there are only two models that are directly supported by spectroscopic evidence. These are the isolated As_{Ga} antisite defect and the $As_{Ga} - As_i$ antisite–interstitial pair (Kaufman, 1989). At present, the As antisite defect, As_{Ga}, is considered to be the most probable physical origin for the EL2 center. Several groups have unequivocally established that the EL2 concentration increases with the partial pressure of the As precursor or the As mole fraction in the bulk (see, for example, Samuelson et al., 1981, Holmes et al., 1982, and references therein). Furthermore, Weber (1985, 1991) and Muszalski et al. (1991) showed that unusually high (up to 10^{20} cm^{-3}) concentrations of the EL2 defect are obtained in *GaAs grown at very low temperatures* by MBE. Such low growth temperatures

https://doi.org/10.1017/CBO9780511599828.012 Published online by Cambridge University Press

are well known to yield non-stoichiometric, As-rich, GaAs. The non-stoichiometry is due to the lack of As reevaporation from the growing GaAs layer. (These growth conditions do not fulfill the three-temperature-criterion formulated by Guenter (1958) for stoichiometric growth of GaAs). As a result, an abundance of As_{Ga} defects are formed in GaAs grown at low temperatures.

It has also been argued that the EL2 defect could be related to an As antisite and As interstitial pair, $As_{Ga} - As_i$, or other As_{Ga}-related defects (Spaeth et al., 1990). However, several observations do not support the hypothesis of an $As_{Ga} - As_i$ pair. First, thermal treatment of GaAs containing the EL2 defect revealed that the EL2 defect is relatively stable at temperatures of 800 – 900 °C. Makram-Ebeid et al. (1982) compared the stability of EL2 with Cr in GaAs. If one component of the EL2 were an interstitial As, As_i, the As_i would be expected to diffuse rapidly due to its interstitial position. However, such a rapid diffusion has not been observed. Furthermore, Baraff et al. (1988) investigated the $As_{Ga} - As_i$ pair defect in GaAs using electronic structure calculations. They found no plausible mechanism for binding the two components of the pair to each other. If there is indeed no plausible binding mechanism, the probability of the occurrence of $As_{Ga} - As_i$ pairs is much smaller than the experimentally observed EL2 concentrations. The authors also predicted an effective-mass-like shallow level for the $As_{Ga} - As_i$ pair which has not been found experimentally.

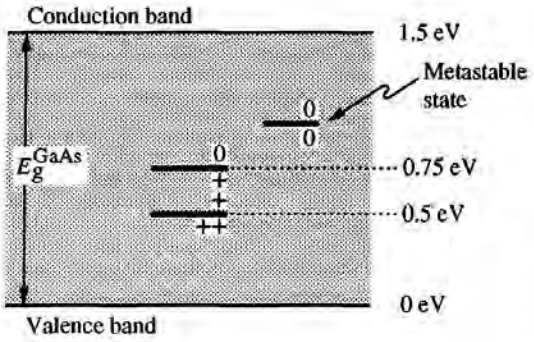


Fig. 9.7. Energy levels of the EL2 defect within the GaAs band gap. The EL2 defect has two donor levels at 0.5 eV and 0.75 eV above the valence band edge; the defect also has a metastable neutral level originating from a defect configuration with large lattice relaxation.

The schematic scheme of the electronic levels of the EL2 defect is shown in Fig. 9.7. The As has two excess electrons if occupying a Ga site, i.e. is a double donor. The lowest donor level is 0.5 eV above the top of the valence band. This donor level is usually not observed in DLTS measurements since it requires very high temperatures (>> 300 K) to be ionized. Evidence for the lowest EL2 donor level is obtained from luminescence and luminescence excitation spectroscopy

https://doi.org/10.1017/CBO9780511599828.012 Published online by Cambridge University Press

which reveal EL2 related bands at 0.63 eV and 0.68 eV (Tajima, 1987; Tajima et al., 1987). The second donor level is approximately 0.75 eV above the valence band edge. In semi-insulating GaAs, the Fermi level is pinned at this level. The EL2 defect has also a third level which has metastable properties. The metastable level has a neutral charge state; its properties will be discussed below.

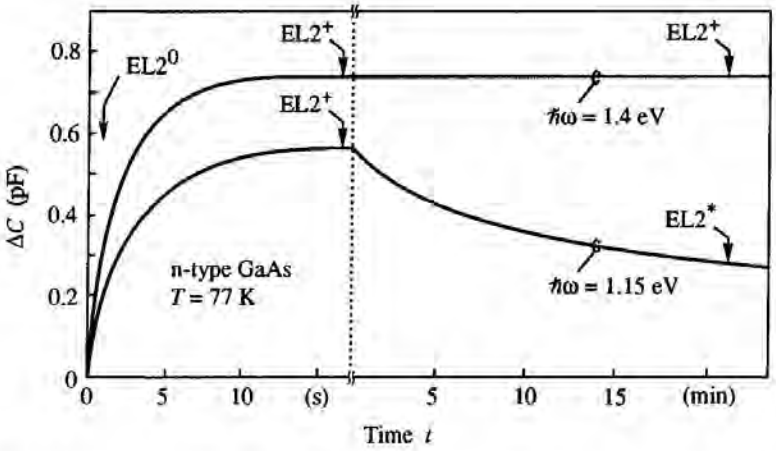


Fig. 9.8. Typical photocapacitance transients at 77 K for n-type GaAs containing the EL2 defect. Initially the EL2 defects are in the neutral ($EL2^0$) state. After illumination with $\hbar\omega$ = 1.15 eV and 1.4 eV, the defects assume an ionized state ($EL2^+$). Long illumination with $\hbar\omega$ = 1.15 eV quenches the capacitance indicating that the defect assumes again the initial neutral (metastable) state (after Vincent and Bois, 1978).

One of the key features of the EL2 defect is its metastability which has complicated the understanding of the defect. The metastability of the EL2 manifests itself at low temperatures in the following way. Upon photoexcitation the characteristic features associated with the EL2 disappear. These features include luminescence bands, absorption bands and electrical activation. The metastable characteristics of the EL2 were postulated based on the photocapacitance characteristics of GaAs shown in Fig. 9.8 (Vincent and Bois, 1978). The capacitance of an n-type GaAs sample with a Schottky contact is measured during illumination with different photon energies. Initially, all EL2 centers are in a neutral state ($EL2^0$). Upon illumination with $\hbar\omega$ = 1.15 or 1.4 eV, the EL2 level becomes ionized ($EL2^+$) which results in an increase of the capacitance. Certainly, several transitions compete in the illumination process including EL2-to-CB and VB-to-EL2 excitation. That is, at sufficiently high illumination intensities the major fraction of EL2 is ionized while a small fraction

https://doi.org/10.1017/CBO9780511599828.012 Published online by Cambridge University Press

is temporarily in a neutral state. Illumination with $\hbar\omega = 1.4$ eV yields a steady-state capacitance change while illumination with $\hbar\omega = 1.15$ eV yields a surprising result. The change of the capacitance decreases and approaches the initial capacitance value as shown in Fig. 9.8. The decrease of the capacitance can be explained *only if the final charge state of the EL2 is the same as the initial state*. Therefore, the final state, which is called EL2*, must be neutral. Furthermore, the final state is *metastable* since the center cannot be ionized any more. The experiment shown in Fig. 9.8 can be repeated only after the sample is heated to higher temperatures and cooled down again. In the interpretation of their experiments, Vincent and Bois (1978) assumed that the EL2 center undergoes an optically induced transition to the metastable EL2* state. They assumed that the transition does occur for photoexcitation at 1.15 eV but not for 1.4 eV.

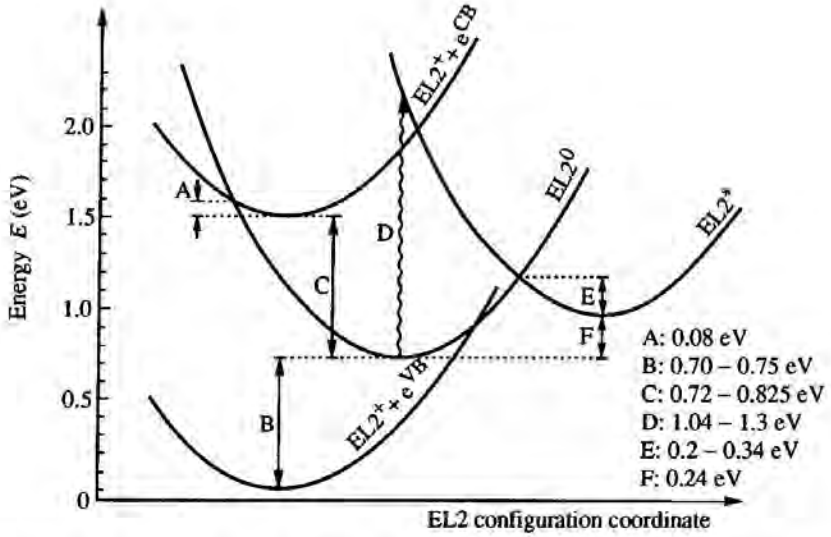


Fig. 9.9. Configuration coordinate diagram for the EL2 defect in the normal and the lattice-relaxed, metastable state. In the normal state the electron can be in the valence band ($EL2^+ + e^{VB}$), localized at the defect ($EL2^0$), or in the conduction band ($EL2^+ + e^{CB}$). The second donor level of the EL2 defect (0.5 eV above the VB, see Fig. 9.7.) is not shown (after Vincent and Bois, 1978).

The metastable state of the EL2 was further modeled using the configuration coordinate diagram (Vincent and Bois, 1978). A configuration coordinate diagram for the EL2 center is shown in Fig. 9.9, which shows the neutral state, $EL2^0$, the metastable state EL2*, and the singly ionized state, $EL2^+ + e^{CB}$ or $EL2^+ + e^{VB}$. Note that the lower donor level, $EL2^{++}$, is not shown since it is

https://doi.org/10.1017/CBO9780511599828.012 Published online by Cambridge University Press

irrelevant for the photocapacitance experiments discussed here. The lower donor level can be considered to be always occupied at sufficiently low photoexcitation intensities. Transition 'C' is the thermal ionization of the upper EL2 donor level; transition 'D' is the optical transition from the neutral state, $EL2^0$, to the metastable state, EL2*. In order to relax from EL2* to $EL2^0$, the energy barrier 'E' needs to be overcome. Since the energy barrier 'E' is on the order of 200–340 meV, this transition cannot occur at low temperatures, i.e. the center remains in the metastable EL2* configuration.

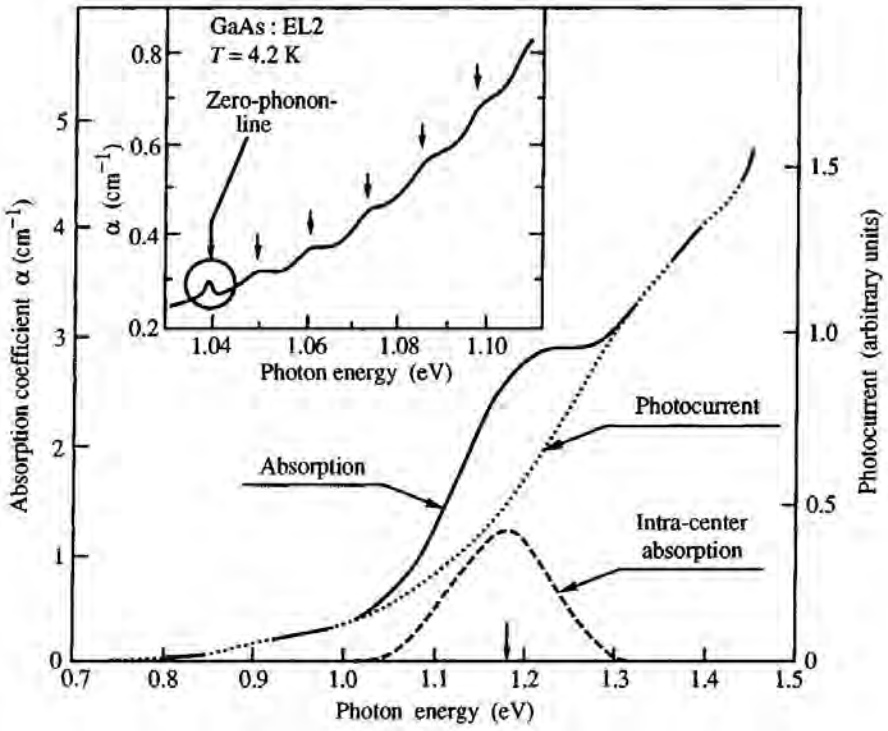


Fig. 9.10. Absorption coefficient and photocurrent versus photon energy for n-type GaAs containing the EL2 defect with a concentration of $2 \times 10^{16} cm^{-3}$. The inset shows the EL2 zero-phonon-line intra-center transition and five phonon replicas (after Kaminska, 1984).

Further evidence for the photon-induced $EL2^0$ to EL2* transition was obtained from absorption measurements which revealed the signature of the 1.15 eV intra-center transition (Kaminska et al. 1983) in n-type GaAs. A typical absorption measurement for GaAs containing the EL2 defect is shown in Fig. 9.10 (Kaminska, 1984; Dischler et al., 1986). After the sample is cooled in the dark, the absorption measurement reveals an absorption band starting at

https://doi.org/10.1017/CBO9780511599828.012 Published online by Cambridge University Press

337-TA-1366 RX-0255

energies of 0.8 eV (solid line). The absorption band is completely bleached after sufficiently long illumination with $\hbar\omega = 1.18$ eV (dashed lines). The intra-center transition has its zero-phonon line at $\hbar\omega = 1.04$ eV as shown in the inset. Phonon replicas are observed at energies 11, 22, 33, ... meV higher than the zero-phonon line (Kaminska et al. 1983). The authors showed that intra-center absorption occurs at energies ranging from 1.04 eV to 1.3 eV with a peak absorption occurring at approximately 1.18 eV. Figure 9.10 also shows the photocurrent signal which is due to electronic transitions creating free electrons or holes. Comparison of the absorption signal with the photocurrent signal reveals that the intra-center absorption (i.e. absorption minus photocurrent) is a significant fraction of the overall absorption. The background absorption at $E > 0.8$ eV is probably due to EL2-to-CB and VB-to-EL2 excitations. The band-to-EL2 transitions have been shown to be much stronger than the $EL2^0$-to-EL2* transition (see, for example, Kaufmann, 1989; Baraff, 1992).

Previous theoretical studies on the electronic structure of the As_{Ga} antisite defect in GaAs revealed that the As_{Ga} defect has three bound states of A_1 symmetry, one of which falls deep into the fundamental gap and is occupied by two electrons in the neutral state of the defect (Bachelet et al., 1983). This A_1 state can also be occupied by a single electron resulting in a positively charged defect. The energy levels of the gap A_1 state of the defect were calculated to be $E_1 \equiv 0.8$ eV (++/+) and $E_2 \equiv 1.1$ eV (+/0) above the valence band edge and are about 0.3 eV higher than the experimental values for the EL2 defect (see Fig. 9.14). The energy separation between the two levels ($E_2 - E_1$), however, agrees well with experimental results. The A_1 symmetry of the gap state designates a *spherically symmetric* state (see, for example, Cotton, 1971). The A_1 states thus have the symmetry of the hydrogenic ls orbital. The calculations of Bachelet et al. also revealed an additional state of T_2 symmetry which is resonant with the conduction band. The T_2 symmetry designates a state that is invariant for 90° rotations in the planes of a cartesian coordinate system. Thus, the T_2 state has the same symmetry as atomic p orbitals.

The fine structure of the zero-phonon line of the $EL2^0$-to-EL2* transition was studied under uniaxial stress in order to assess the symmetry of this transition. Kaminska et al. (1985) and Bergman et al. (1988) showed that the transition is consistent with the symmetry of a $A_1 \rightarrow T_2$ transition at a defect with overall tetrahedral (T_d) symmetry. On this basis Kaminska et al. concluded that the EL2 is the As_{Ga} antisite defect. The tetrahedral symmetry of the EL2 defect was confirmed by Nissen et al. (1990, 1991) using photoluminescence studies under uniaxial stress. The authors used a transition from the conduction band to the A_1 midgap level of the As_{Ga}. No splitting was found under uniaxial stress, indicating

https://doi.org/10.1017/CBO9780511599828.012 Published online by Cambridge University Press

RX-0255.395

that there was no orientational degeneracy to be lifted, and as a consequence, that there could be no defect closely attached to the As_{Ga}.

A remarkable microscopic physical model for the EL2 defect was proposed by Chadi and Chang (1988a) and independently by Dabrowski and Scheffler (1988, 1989) using self-consistent total energy calculations of the As_{Ga} defect. The calculations showed that, immediately after an $A_1 \rightarrow T_2$ transition at the neutral isolated As_{Ga}, the total energy of the system would be somewhat greater than the energy of a strongly distorted configuration. In this strongly distorted configuration, one of the four As–As bonds of the central As_{Ga} atom is broken and the As_{Ga} atom moves along a ⟨111⟩ direction into an interstitial position 0.29Å below the plane of its three remaining As neighbors. The other As atom whose bond was broken, remains in its original position. Thus, the distorted configuration gives rise to two threefold coordinated As atoms with different local environments. The As_{Ga} defect may spontaneously relax into this configuration, which was shown to exhibit metastability, after an optically induced $A_1 \rightarrow T_2$ transition. The normal configuration (fourfold coordinated or tetrahedral symmetry) and of the metastable configuration (threefold coordinated, interstitial As with broken bond) of the As_{Ga} antisite defect have a strong similarity to the D^0 and DX^- configuration of the DX center. To visualize the similarity it is useful to reinspect Fig. 9.5. If the Si atom in Fig. 9.5(a) is replaced with an As atom, the regular As_{Ga} antisite defect is obtained. The metastable configuration of the EL2 defect is obtained, if the Si (DX^-) atom in Fig. 9.5(b) is replaced by a As atom. In the metastable position, the As is approximately 0.3 Å below the plane of its three remaining As neighbors. The normal position of the As is approximately 0.9 Å above the plane. Thus, the As atom moves 1.2 Å along the ⟨111⟩ direction, away from its 'ideal' Ga substitutional position, and breaks one of its bonds by stretching it to ≅ 3.6 Å (Chadi and Chang, 1988a). The breaking of the As–As bond may be understood as the placement of an electron in the antibonding state of the As_{Ga} donor defect and thereby weaken one of the existing bonds so much that the defect atom would move, breaking the bond holding it in place (Baraff, 1992). Note that the DX-configuration is negatively charged (DX^-), whereas the As in the same interstitial position is neutral. Thus, the normal-to-metastable transition is a neutral-to-neutral state transition. This feature of the center is in agreement with the experimental photocapacitance measurements shown in Fig. 9.8 which indicate that the $EL2^0 - EL2^*$ transition does not involve a change in charge state.

The physical and electronic properties of the EL2 center have been reviewed by Weber (1985), Martin and Makram-Ebeid (1986), Kaufmann (1989), and Baraff (1992).

https://doi.org/10.1017/CBO9780511599828.012 Published online by Cambridge University Press

9.3 Hydrogen

Hydrogen is not an electrically active substitutional impurity in III–V semiconductors. That is, if hydrogen were incorporated in an intrinsic, undoped semiconductor, the electronic properties of the semiconductor would not be changed by the hydrogen incorporation. However, hydrogen strongly interacts with shallow donor and acceptor impurities in III–V semiconductors. Hydrogen can neutralize such shallow impurities and consequently change the electronic properties of III–V semiconductors dramatically. In addition, hydrogen implantation creates defects which can significantly change the conductivity of the semiconductor. For example, semi-insulating characteristics of GaAs with resistivities exceeding $10^7\,\Omega$ cm can be achieved by implantation of hydrogen. As a result, hydrogen is of significant technological importance for III–V device technology.

The two major methods of hydrogen incorporation are (i) by diffusion at relatively low temperatures and (ii) by implantation of H ions (protons). The resulting characteristics of the semiconductor strongly depend on the method by which hydrogen is incorporated. Therefore, the following sections are devoted to characteristics of semiconductors with hydrogen being incorporated by different methods, namely incorporated by *diffusion* (Sect. 9.3.1) and incorporated by *implantation* (Sect. 9.3.2). Other methods for hydrogen incorporation such as electrochemical techniques (Seager, 1991) will not be discussed. A final section (Sect. 9.3.3) is dedicated to the influence of residual hydrogen during *growth* by molecular-beam epitaxy.

9.3.1 Hydrogen incorporation by diffusion

Hydrogen can be incorporated from a H surface population into the bulk of the semiconductor by means of diffusion. Atomic (H) and molecular (H_2) hydrogen surface populations can be generated by a low pressure (0.1 to 100 Torr) glow-discharge, direct current (dc) or radio-frequency (rf) plasma reactor (Seager and Ginley, 1982). In the direct current type reactor, the semiconductor serves as the cathode resulting in a positive proton current towards the semiconductor. Proton current densities in the range of several mA/cm^2 impinge on the semiconductor surface at applied biases of few hundred volts. The voltage drop occurs in the cathode near region (Boenig, 1982) resulting in a substantial kinetic energy of protons which may lead to some H^+-ion damage in the surface near region of the semiconductor. Furthermore, electric field inhomogeneities may lead to H^+ current inhomogeneities, which in turn lead to a non-uniform H distribution.

Some of the above mentioned disadvantages are avoided in radio-frequency plasma reactors in which the sample is mounted 'downstream'. The

https://doi.org/10.1017/CBO9780511599828.012 Published online by Cambridge University Press

'downstream' configuration of the sample implies that the sample is spatially removed from the radio-frequency generator (see, for example, Pearton et al., 1987a). The 'downstream' formation effectively eliminates the direct bombardment damage discussed above. The lack of exposure to a high electric field also reduces the non-uniformity of the hydrogen surface population discussed above.

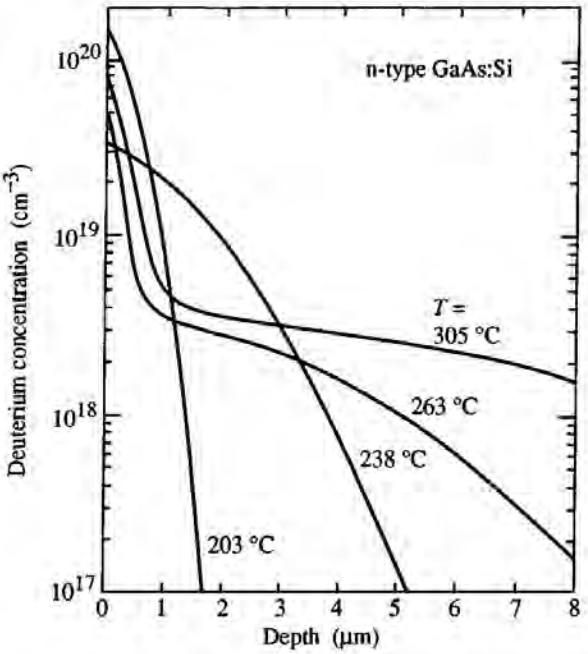


Fig. 9.11. Deuterium concentration profiles in bulk n-type GaAs:Si after exposure to a radio-frequency deuterium plasma (with power density of 0.2 W/cm^2) for 90 min at different temperatures (after Chevallier et al., 1991).

The deuterium (D) concentration as a function of depth for a 90 min exposure of GaAs to a radio-frequency D plasma is shown in Fig. 9.11 (Chevallier et al. 1991). The GaAs samples were heated to different temperatures resulting in markedly different D distributions. The authors showed that the D profiles can be fitted well by the erfc-function. The good fit indicates that the diffusion mechanism follows fickian laws. The fit further indicates that regular diffusion is the dominant mechanism by which D is incorporated into the semiconductor. At a temperature of 240 °C, the authors estimated the diffusion constant to be 3×10^{-12} cm^2/s. The temperature dependence of the hydrogen diffusion constant has been described by Chevallier et al. (1991) according to

https://doi.org/10.1017/CBO9780511599828.012 Published online by Cambridge University Press

$$D = D_0 \exp(-E_a/kT) , \tag{9.6}$$

with $D_0 = 115$ cm^2/s and $E_a = 1.38$ eV. Note that the diffusion coefficient of H and D are many orders of magnitude higher as compared to substitutional impurities such as Si, Be, Sn, etc. The large diffusion coefficient of H indicates that the diffusion mechanism of H and D in GaAs is a very rapid one such as interstitial diffusion. Interstitial diffusion is indeed expected for H and D as the small size of these atoms allows them to easily propagate via interstitial sites. It is finally important to note that the deuterium diffusion coefficient (and probably also the hydrogen diffusion coefficient) depends on the doping concentration. Pearton et al. (1987b) showed that the deuterium diffusion coefficient increases as the intentional donor concentration decreases. This dependence indicates either some kind of donor–hydrogen interaction which hinders the propagation of H and D in the semiconductor crystal or else a charge-state dependence, i.e. that the ionized H diffuses more easily than does the neutral H.

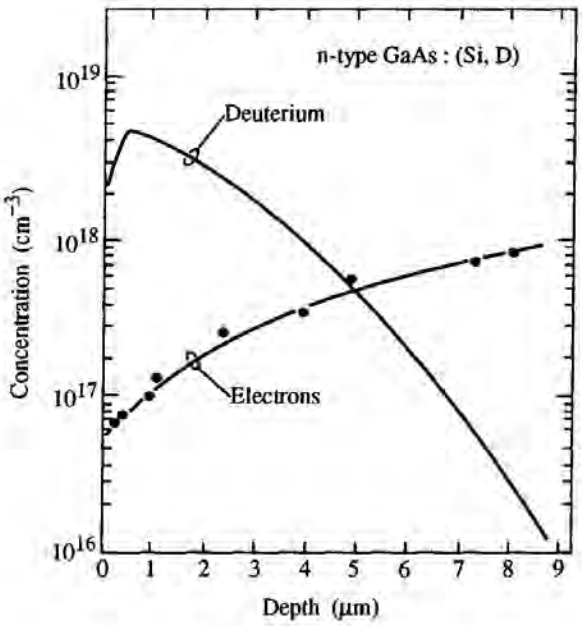


Fig. 9.12. Deuterium and free carrier concentration in n-type GaAs:Si exposed to a deuterium plasma at 250 °C for 90 min. The decreasing deuterium concentration in the near surface region is attributed to deuterium out-diffusion during sample cooling after plasma exposure (after Chevallier et al., 1986).

The donor–hydrogen or donor–deuterium interaction is further illustrated in Fig. 9.12 which shows the free electron concentration and the deuterium concentration versus depth (Chevallier et al., 1986). The deuterium was incorporated by exposing the sample to a radio-frequency deuterium plasma for 90 min at 250 °C. Before plasma exposure, the carrier concentration did not depend on depth. Figure 9.12 reveals that the free electron concentration clearly

https://doi.org/10.1017/CBO9780511599828.012 Published online by Cambridge University Press

decreases with increasing deuterium concentration. This result indicates that hydrogen ***passivates*** or ***neutralizes*** shallow donors in semiconductors. The passivation process for Si donors can be written as (Chevallier et al., 1991)

$$H^0 + Si^+ + e \leftrightarrow Si-H \tag{9.7}$$

where H^0 represents a neutral hydrogen atom.

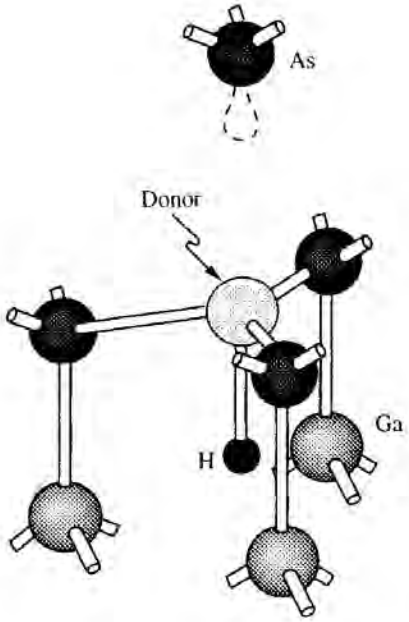


Fig. 9.13. Schematic representation of the group-IV donor–hydrogen complex with hydrogen in the AB site.

The commonly accepted atomic model for donor passivation by hydrogen is shown in Fig. 9.13. The substitutional Si atom is fourfold coordinated. The hydrogen is in an interstitial (AB) site and bound to the Si donor. One of the original Si–As bonds is broken leaving the As atom opposite the hydrogen atom with a lone pair of electrons. The electron count of the Si–H complex yields that the complex is neutral, i.e. H has passivated the donor atom.

Unambiguous information on the Si–H bond was obtained from local vibrational modes (LVM) of hydrogen bound to Si isotopes which clearly demonstrated the existence of the H–Si bond (Pajot et al., 1988b). The authors proposed that hydrogen is located in an antibonding position along a trigonal axis and that the Si is fivefold coordinated. However, Briddon and Jones (1989) subsequently showed that the fivefold coordination of Si is not stable. Large cluster calculations revealed that the Si–As bond opposite the hydrogen (see Fig. 9.13) is broken and that the Si is fourfold coordinated. The additional

https://doi.org/10.1017/CBO9780511599828.012 Published online by Cambridge University Press

electron provided by the donor forms a lone pair with the dangling bond of the threefold coordinated As atom.

Although the atomic model shown in Fig. 9.13 has been verified for Si–H in GaAs, it is generally assumed that the model also applies to other donor impurities in III–V semiconductors. Experimentally, passivation of donors by hydrogen has been found for a large number of donors including Si, Ge, Sn, S, Se, and Te (Pearton et al., 1986). In addition, the activation energy for the recovery of the electrical activity, i.e. the dissociation of the donor–hydrogen bond, was found to be proportional to the donor–hydrogen bond strength. This interdependence further supports the model in which the hydrogen is directly bound to the donor atom. Note that hydrogen also passivates group-VI donors (S, Se, Te). A definite atomic model for the passivation of group-VI donors by hydrogen atoms has not yet been developed.

Hydrogen diffuses out of hydrogenated semiconductors, if the samples are heated to sufficiently high temperatures, typically larger than 400 °C. The original conductivity of hydrogenated samples can be restored by such an annealing cycle. McCluskey et al. (1989) showed that 100% of the original conductivity of a Si-doped GaAs sample can be restored upon heating to 400 °C for 5 min. The Si-doped layer was buried 3 μm deep below the surface. Previous hydrogen plasma exposure of the sample reduced the free carrier concentration to 1/3 of its original concentration. The annealing experiments also indicate that hydrogen does not favour incorporation into III–V semiconductors at temperatures exceeding approximately 400 °C.

Hydrogen also passivates shallow ***acceptors*** in III–V semiconductors. The atomic model for the substitutional group-II acceptor is shown in Fig. 9.14. The hydrogen atom is bound to an arsenic atom and occupies a BC-site between the (Be) acceptor impurity and the arsenic neighbors. The hydrogen atom thus satisfies the electron pair requirement of the arsenic neighbor. The entire hydrogen-impurity complex is neutral, i.e. hydrogen passivates the acceptor. To date, the atomic model shown in Fig. 9.14 is generally assumed not to be restricted to Be but to apply to all substitutional group-II acceptors.

Originally, the atomic model shown in Fig. 9.14 was shown to be valid for substitutional Be impurities. The Be–H complex has been studied by local vibrational mode (LVM) spectroscopy (Nandhra et al., 1988). The use of uniaxial stress during LVM spectroscopy allows one to lift orientational degeneracies and identify the symmetry of the complex. Low-temperature LVM measurements showed that the As–H bonds are aligned along the trigonal axis (Stavola et al., 1989). Although the measurements did not reveal if the hydrogen occupies the BC or the AB position, it is now commonly assumed that it occupies the BC site.

https://doi.org/10.1017/CBO9780511599828.012 Published online by Cambridge University Press

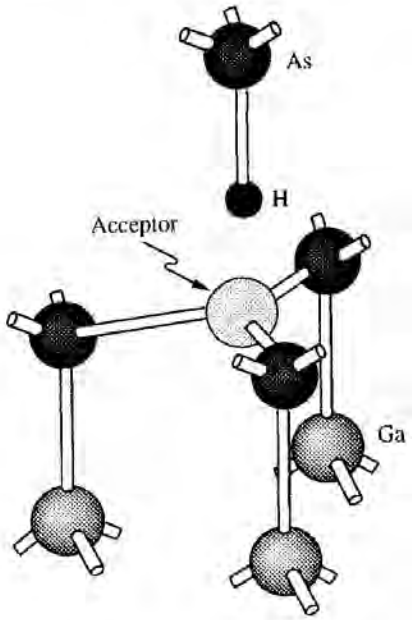


Fig. 9.14. Schematic representation of the group-II acceptor–hydrogen complex with hydrogen in the BC site.

The hydrogen BC site was originally proposed by Pankove et al. (1985) and has been confirmed by cluster calculations (Briddon and Jones, 1989).

Finally, hydrogen can also passivate group-IV acceptors such as C or Ge. Chevallier et al. (1988) proposed an atomic model in which the hydrogen is bound to the group-IV acceptor and is in a BC position between the group-IV acceptor and one of its group-III neighbors.

9.3.2 Hydrogen incorporation by implantation

Hydrogen implantation is a process that is widely used to render III–V semiconductors highly resistive. *Semi-insulating* properties with resistivities $\leq 10^7$ Ω cm can be achieved by hydrogen implantation as well. The implantation process allows one to choose the implantation depth which provides high flexibility to tailor the electrical properties of thin films.

The result of hydrogen implantation, which is frequently termed *proton* implantation, is twofold. First, high-energy protons create ***defects*** along their implantation path. These defects include point defects such as interstitials, vacancies, antisite defects, etc. Such defects commonly have levels within the fundamental gap which can trap free carriers. The semiconductor thus becomes highly resistive. Note that this mechanism is irrelevant if hydrogen is introduced by diffusion (see Sect. 9.3.1). Diffusion is an equilibrium process and usually does not introduce point defects. Second, hydrogen forms complexes with donor

https://doi.org/10.1017/CBO9780511599828.012 Published online by Cambridge University Press

and acceptor impurities (see Sect. 9.3.1). As a consequence, the impurities are neutralized and the free carrier concentration is reduced. Note that this second mechanism is the only relevant mechanism if hydrogen is introduced by diffusion. However, at typical implantation energies, the shallow impurity passivation by hydrogen is a minor contribution to the overall change of the electrical characteristics of the semiconductor.

The simplest defects created during hydrogen ion implantation are Frenkel pairs, consisting of a vacancy and the displaced lattice atom. More complex defects such as divacancies, trivacancies, clusters of vacancies, clusters of interstitials, clusters involving an impurity, and others can also be created (Corbett, 1971). Line defects such as dislocations caused by an accumulation of point defects are common in implanted material (Pearton, 1990). The total number of atoms displaced by an incoming ion is given by (Kinchin and Pease, 1955)

$$N_d \equiv E_n/2E_d \tag{9.8}$$

where E_n is the total energy loss of implanted ions in nuclear collisions, and E_d is the displacement energy for a lattice atom. The displacement energy is approximately 15–20 eV in GaAs and has similar values in other III–V semiconductors. Note that E_n is usually much smaller than the primary ion energy. This is because most of the energy loss of primary ions is due to electronic collisions (i.e. collision of ions with the electron shell of lattice atoms) rather than nuclear collisions. In an example, Pearton (1990) estimated that a 200 keV H^+ ion creates about nine displaced atoms.

Experimental investigations on the defect creation in III–V semiconductors upon ion implantation confirmed the formation of a multitude of point defects (Wesch et al., 1989). The study revealed that amorphization of the semiconductor occurs via homogeneous defect nucleation. The authors further showed that the creation and annihilation of a defect depends strongly on the implantation temperature. 'Hot' implants, i.e. implantation at elevated target temperatures, tend to result in less defects due to the annihilation during the implantation process, e.g. the recombination of Frenkel defects. Tell et al. (1990) reported enhanced diffusion of Si impurities in GaAs subjected to H ion implantation. The increase in the Si diffusion coefficient was found to be as large as one order of magnitude. The enhanced diffusivity of Si in GaAs was attributed to enhanced defect concentration in the implanted material.

Hydrogen distributions obtained by implantation in GaAs and InP at different implantation energies are shown in Fig. 9.15. The distributions are calculated using the 'TRIM '91' computer code (Ziegler et al., 1991). The hydrogen atom

https://doi.org/10.1017/CBO9780511599828.012 Published online by Cambridge University Press

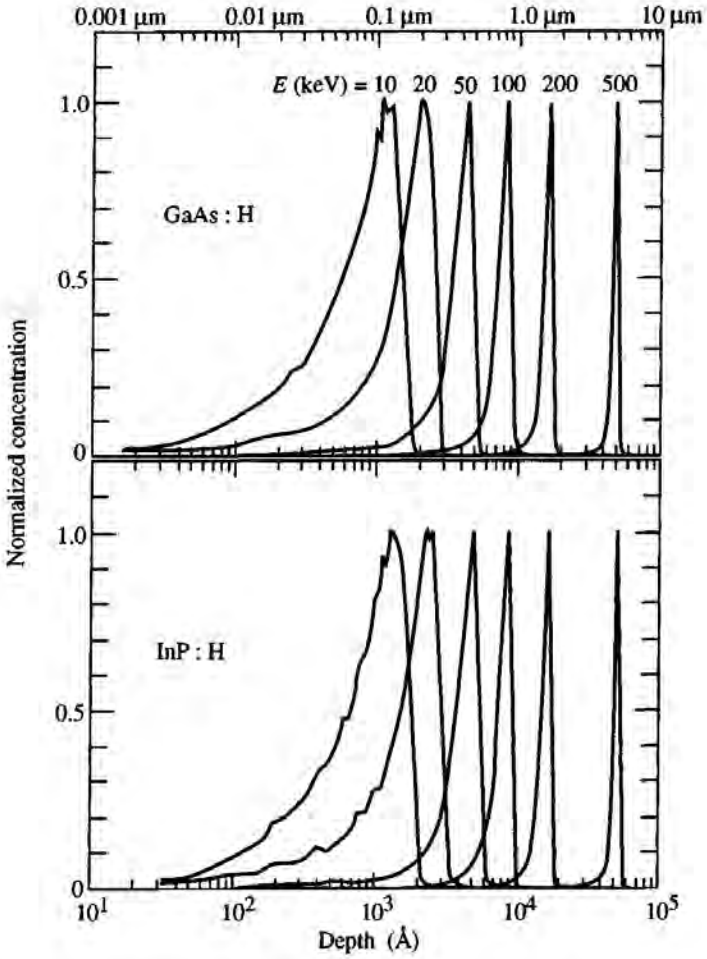


Fig.9.15. Concentration of implanted hydrogen versus depth in GaAs and InP for different implantation energies (calculated with TRIM '91 code).

distribution shown in Fig. 9.15 does not represent the distribution of defects in the crystal. It is evident that defects are created along the path of the atom, i.e. the defect concentration is higher than the hydrogen atom concentration in the near-surface region.

Pearton (1990) reported a quantitative comparison between the hydrogen ion concentration and the defect concentration in GaAs implanted with 200 keV protons. The comparison of hydrogen atom concentration and defect concentration is shown in Fig. 9.16. The two concentrations exhibit a qualitatively similar dependence. However, the damage distribution is closer to the surface than the ion distribution. The damage profile shown in Fig. 9.16 was

https://doi.org/10.1017/CBO9780511599828.012 Published online by Cambridge University Press

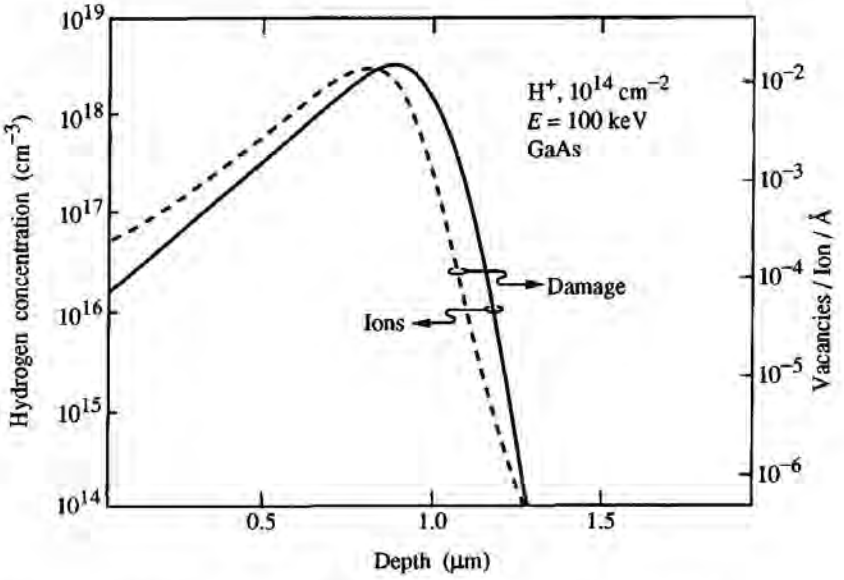


Fig. 9.16. Hydrogen atom distribution and damage distribution for E = 100 keV proton implantation in GaAs (after Pearton, 1990).

obtained from Monte Carlo calculations of energy deposition given up in atomic stopping processes, or equivalently, of vacancy production per incoming ion.

Post-implantation annealing of n^+-GaAs:Si implanted with hydrogen was studied by Zavada et al. (1985, 1988). The authors described the redistribution of hydrogen during the thermal annealing process by a diffusion constant whose temperature dependence was described by

$$D = D_0 \exp(-E_a/kT) , \tag{9.9}$$

with $D_0 = 1.5 \times 10^{-5}$ cm^2/s and an activation energy of $E_a = 0.62$ eV. The activation energy of 0.62 eV is much smaller than the activation energy for hydrogen diffusion without previous implantation (see Eq. (9.6)) which indicates that the defects created in the implantation process facilitate the diffusive motion of hydrogen.

Post implantation annealing of hydrogen-implanted III–V semiconductors has several consequences. First, hydrogen spatially redistributes as discussed above. Second, hydrogen–impurity complexes are formed at moderate annealing temperatures (200–500 °C). The formation of Si–H complexes in GaAs has been established by infra-red absorption spectroscopy (Pajot et al., 1988a). Third, at high temperatures (T > 500 °C) hydrogen diffuses strongly and eventually

https://doi.org/10.1017/CBO9780511599828.012 Published online by Cambridge University Press

diffuses out of the semiconductor. The hydrogen–impurity bond is easily broken at such high temperatures. Fourth, defects created during the implantation process can be annealed out at sufficiently high temperatures. As a result, the conductivity of the semiconductor increases; for appropriate annealing conditions, the original conductivity of the semiconductor can be restored with a near 100% efficiency.

The possibility of rendering III–V semiconductors semi-insulating by hydrogen implantation made this technique very attractive for device applications. Steeples et al. (1980) showed that resistivities of $> 10^7\ \Omega$ cm can be achieved in GaAs by proton implantation. Previously, proton bombardment was shown to be very efficient for pn-junction devices and Schottky contact isolation (Foyt et al., 1969). Proton implantation has also been used for optical waveguide formation (Garmire et al., 1972) and for laser fabrication (Van der Ziel et al., 1981). More recently, continuous wave operation was achieved in AlGaAs/GaAs quantum well lasers (Jackson et al., 1988), GaInAsP/InP buried ridge lasers (Kazmierski et al., 1989), and in AlGaAs/GaAs vertical cavity lasers (Tu et al., 1992) using proton implantation.

9.3.3 Role of hydrogen during growth

The quality of epitaxial crystals grown by molecular-beam epitaxy can be improved by introducing *atomic* hydrogen into the growth chamber. The improvement has been reported by several groups (see, for example, Calawa, 1978; Bachrach and Bringans, 1983; Sugiura et al., 1986; Pao et al., 1986; Kopev et al., 1989). However, the improvement is not due to the incorporation of hydrogen into the semiconductor but rather to chemical reactions of hydrogen with other residual gases in the growth chamber.

Several epitaxial growth systems have large quantities of H and H_2 in the reaction chamber. These growth techniques include GSMBE, OMVPE, and CBE. Hydrogen is introduced in these techniques via PH_3, AsH_3, or as a carrier gas. Hydrogen has also been intentionally introduced during molecular-beam epitaxial growth, i.e. a technique that usually neither requires nor generates hydrogen during growth. The hydrogen has been introduced either as molecular hydrogen (Calawa, 1978) or as dissociated hydrogen atoms (Bachrach and Bringans, 1983). However, H cannot be detected in the epitaxial layers by common analytical techniques such as secondary ion mass spectrometry if the growth temperature is ≥ 400 °C. That is, hydrogen is not incorporated effectively at typical epitaxial growth temperatures.

The main advantage of hydrogen introduction during molecular-beam epitaxial growth is the chemical reaction of hydrogen with residual gases in the

https://doi.org/10.1017/CBO9780511599828.012 Published online by Cambridge University Press

growth chamber. It has been pointed out (Calawa, 1978) that carbon (including CO and CO_2) and oxygen are contaminants in GaAs and other semiconductors. These residual contaminants are present in sufficient abundance to dope films in the $10^{13} - 10^{14}$ cm^{-3} range. For example, an impurity with a unity sticking coefficient and a partial pressure of about 10^{-12} Torr at the substrate surface would result in a concentration of unwanted impurities of 10^{17} cm^{-3} (Calawa, 1978). Both carbon and oxygen are electrically active impurities in GaAs which degrade the quality of the material. Because hydrogen is highly reactive with carbon and oxygen, the presence of H_2 and H during growth can be expected to affect the incorporation of these two impurities.

An improvement of the transport characteristics of GaAs has indeed been found experimentally upon introduction of hydrogen. Calawa (1978) found a reduction of the residual carrier concentration by a factor of 2 and a significant increase in carrier mobility. The author also found a type conversion from p-type to n-type upon hydrogen introduction. Pao et al. (1986) found similar improvements; in addition, a dramatic reduction in deep electron trap concentration was found. Kopev et al. (1989) reported a decrease in the density of oval defects in GaAs upon the introduction of hydrogen. Oval defects were attributed to GaO and Ga_2O_3 on the crystal surface; both types of oxides were reduced in density upon hydrogen introduction.

The incorporation of H into GaAs:C during epitaxial growth by CBE and OMVPE was analyzed by Stavola et al. (1991). Hydrogen was found to incorporate from the organometallic sources used as group-III precursors, from hydrides used as group-V precursors, and even from forming gas (15% H_2, 85% N_2) used as an annealing ambient. Hydrogen was found to readily incorporate into GaAs at growth temperatures $\leq$ 500 °C which resulted in a passivation of 5–50% of the C impurities. Post-growth annealing at 550 °C for 60 s in an inert ambient (He) was sufficient to dissociate the C–H complexes and electrically activate the C acceptors.

9.4 Chromium, iron, and oxygen

Compound semiconductors can be intentionally doped with deep impurities in order to render the semiconductor highly resistive. The ionization energy of such deep impurities is much larger than the thermal energy, kT, at room temperature. Deep impurities are therefore not thermally ionized at room temperature. Furthermore, shallow impurities can be compensated with deep centers yielding very low free carrier concentrations. Consider, for example a semiconductor with a shallow donor concentration N_D and a deep acceptor concentration N_A, with $N_A > N_D$. Electrons originating from the shallow donors will occupy the deep

https://doi.org/10.1017/CBO9780511599828.012 Published online by Cambridge University Press

acceptor states rather than conduction band states. Since $N_A > N_D$, only a fraction of the deep acceptor states are occupied. As a result, the Fermi level is pinned at the deep acceptor level. Thus, intentional doping with deep impurities can drastically reduce the free carrier concentration.

If the energy level of a deep impurity is at or near the intrinsic Fermi level, i.e. in the vicinity of the middle of the forbidden gap, the free carrier concentration equals the intrinsic carrier concentration. The intrinsic carrier concentration is very small, e.g. $n_i \cong 10^7$ cm^{-3} in GaAs. Such low concentrations cannot be achieved by conventional methods, since the unintentional background impurity concentration usually exceeds the intrinsic concentration by many orders of magnitude. It is thus desirable that intentional deep impurities have an energy level close to the middle of the forbidden gap of the semiconductor.

The energy levels of chromium (Cr) and iron (Fe) in GaAs and InP are shown in Fig. 9.17. The energy levels closest to the midgap position are the Cr acceptor level in GaAs and the Fe acceptor level in InP. The lowest free carrier concentrations are indeed achieved with Cr-doped GaAs and Fe-doped InP.

Semi-insulating substrate materials are of technological importance for device isolation purposes. Materials with resistivities exceeding 10^7 Ω cm are called ***semi-insulating***. Semi-insulating GaAs and InP can be obtained by means of doping with Cr and Fe, respectively, in order to compensate for shallow donor impurities. In addition, semi-insulating materials can also be grown by selecting growth conditions that favor the formation of native defects which in turn can trap free carriers. Highly resistive properties of GaAs (see Sect. 9.2) and InP (Hofmann et al., 1989) have been demonstrated *without* intentional doping. The EL2 defect has been identified as causing the highly resistive characteristic in GaAs. In InP, the relevant center causing high resistivity has not yet been identified.

9.4.1 Chromium (Cr)

Chromium is a deep acceptor in III–V semiconductors. In GaAs, the Cr acceptor energy is 0.79 eV above the valence band edge as shown in Fig. 9.17. The level is very close to the midgap position in GaAs which makes Cr an ideal impurity for the growth of semi-insulating GaAs. In InP, the Cr acceptor energy is 0.96 eV above the valence band edge which is not particularly close to the InP midgap position. Furthermore, Cr has a much lower solid solubility in InP than in GaAs, which necessitates very high purity starting material of InP to achieve high resistivity (Mullin et al., 1971). Chromium is therefore not used in InP to render the material semi-insulating.

Chromium has been widely used in bulk GaAs grown by the Czochralski

https://doi.org/10.1017/CBO9780511599828.012 Published online by Cambridge University Press

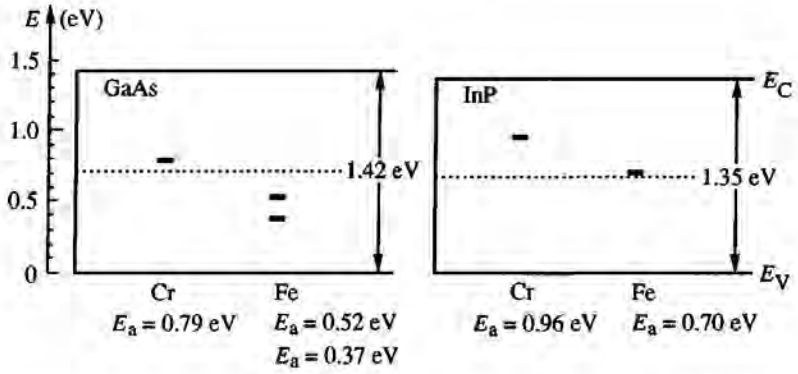


Fig. 9.17. Acceptor levels of Cr and Fe in GaAs and InP measured from the top of the valence band.

technique (see, for example, Lindquist, 1977). Residual n-type conductivity is obtained in GaAs grown in a quartz (SiO_2) crucible. The n-type conductivity results from Si impurities that are incorporated from the quartz walls into the bulk GaAs. Si impurities have typical concentrations in the low 10^{16} cm^{-3} range in such unintentionally doped GaAs. In order to compensate for the n-type conductivity, Cr is added to the melt at a concentration of typically 5×10^{16} cm^{-3}. The Cr concentration is thus higher than the shallow donor concentration which yields a complete compensation of the shallow donors. Cr-doped GaAs is also grown by the liquid encapsulated Czochralski (LEC) technique which has several advantages over the regular Czochralski technique without an encapsulant (Müller, 1987).

Cr-doped GaAs has also been grown by other bulk growth techniques such as the gradient freeze method. Orito et al. (1984) achieved resistivities exceeding 10^8 Ω cm in Cr-doped GaAs grown by this method. Silicon was found to be the dominant shallow impurity in nominally undoped GaAs. The residual Si concentration ranged between 2×10^{15} and 2×10^{16} cm^{-3}. The Cr concentration in the GaAs ranged between 1×10^{16} and 4×10^{16} cm^{-3} and increased with growth time due to Cr segregation effects.

Cr-doped GaAs grown by the horizontal Bridgman and the LEC technique have been compared by Miyazawa and Nanishi (1983). The authors found that the horizontal Bridgman grown material has an inhomogeneous distribution of electrical properties even at relatively low Cr concentrations in the melt. The LEC-grown material was found to be more uniform and suited for use in GaAs integrated circuit fabrication.

https://doi.org/10.1017/CBO9780511599828.012 Published online by Cambridge University Press

Innoscience1366-00139082

A major drawback of Cr-doped GaAs is the Cr diffusion and redistribution during high-temperature processing and during epitaxial growth. The redistribution of Cr has been discussed in Chap. 8. Redistribution effects can lead to non-uniform electrical characteristics of a wafer which in turn can affect device parameters such as the threshold voltage of an injection laser. Therefore, Cr-doped GaAs substrates are infrequently used at the present time. Instead, ***undoped, semi-insulating GaAs*** substrates grown by the LEC technique constitute the major part of the present GaAs substrate market. The semi-insulating electrical characteristic of the undoped GaAs substrate is due to the native EL2 defect (see Sect. 9.2) which compensates residual shallow impurities.

The electrical characteristics of undoped GaAs grown by the LEC technique have been investigated by Matsumura et al. (1983). The authors showed that the resistivity and the dislocation density are correlated. A low dislocation density was found in the highly resistive areas of the GaAs wafer. They found undoped semi-insulating GaAs superior over Cr-doped GaAs due to the lack of inhomogeneities and non-uniformities induced by Cr redistribution.

9.4.2 Iron (Fe)

Iron (Fe) is a deep acceptor in III–V semiconductors. In InP, the Fe acceptor energy is 0.70 eV above the valence band edge as shown in Fig. 9.17 (Iseler, 1979). The Fe level is very close to the midgap position in InP which makes it an ideal impurity for the growth of semi-insulating InP. In GaAs, the Fe acceptor energies are 0.52 and 0.37 eV above the valence band edge which is not particularly close to the GaAs midgap position. Iron is therefore not used in GaAs to render the semiconductor semi-insulating.

Fe-doped InP has semi-insulating properties with resistivities as high as 4.6×10^7 Ω cm (Kim et al., 1986). The authors also investigated the variations of the resistivities across 5 cm InP substrates. A V-shaped pattern of the resistivity was found along the $\langle 011 \rangle$ and the $\langle 01\bar{1} \rangle$ axes. The Hall mobilities on the wafers were 1700–3000 cm^2/V s. The low electron mobility was attributed to neutral impurity scattering.

Iron doping has been used for the growth of semi-insulating InP bulk crystals using the LEC technique (Shimakura et al., 1989), modified LEC techniques (Oda et al., 1991), the horizontal Bridgman technique (Kainosho et al., 1990), the vertical gradient freeze (VGF) technique (Monberg et al., 1987) and an improved Bridgman technique called electrodynamic gradient (EDG) technique (Monberg et al., 1988). All of these bulk crystal growth techniques allow one to obtain InP:Fe with semi-insulating electrical characteristics. The highest resistivities achieved exceed 10^8 Ω cm (Oda et al., 1991). The deep Fe acceptor impurities

https://doi.org/10.1017/CBO9780511599828.012 Published online by Cambridge University Press

compensate for shallow donor impurities in InP. The dominant shallow donor impurity in bulk InP was found to be Si, which incorporates into the polycrystalline starting material from quartz boats and quartz ampoules (Oda et al., 1990). The Si-impurity concentration is typically in the low 10^{15} cm^{-3} range in nominally undoped single crystal InP. Consequently, a typical Fe concentration in the mid to high 10^{15} cm^{-3} is required in order to compensate for the shallow donors.

Iron has been used as a dopant during epitaxial growth to obtain highly resistive InP. Long et al. (1984) reported resistivities as high as 2×10^8 Ω cm for Fe-doped InP grown by organometallic vapour-phase epitaxy. A gaseous Fe doping precursor is required for the growth process. Long et al. (1984) used $Fe(CO)_5$ (pentacarbonyl iron) and $Fe(C_5H_5)_2$ (ferrocene) as precursors. Ferrocene is a solid at room temperature with a relatively low vapour pressure of 1.16 Pa (Speier et al., 1986).

Epitaxial Fe-doped InP has been used in semiconductor device structures such as transistors and lasers. Temkin et al. (1988) demonstrated $Ga_{0.47}In_{0.53}As/InP$ heterostructure field-effect transistors which employed Fe-doped InP as the gate insulator. The gate metallization was deposited directly on the epitaxially grown InP:Fe layer. Excellent extrinsic transconductances of 560 mS/mm were obtained on transistors with a 1.2 μm long gate (Chen et al., 1989). A device transit frequency of 24 GHz was extrapolated from the measurements. Fe-doped InP is also used as current blocking layer in semiconductor lasers emitting at $\lambda = 1.3$ μm using ferrocene as doping precursor (Dutta, 1989).

Iron impurities redistribute themselves during epitaxial growth and during post-growth processing (see, for example, Oberstar et al., 1981). The redistribution of Fe has been discussed in further detail in Chap. 8. Such Fe redistribution can be detrimental to semiconductor devices. In order to avoid Fe redistribution effects, it is desirable to grow ***undoped, semi-insulating InP***. Klein et al. (1986) showed that highly resistive InP can be obtained from nominally undoped starting material by annealing. The authors obtained a resistivity of 3.6×10^5 Ω cm by using an annealing temperature of 900–940 °C and a phosphorus overpressure of 6 bar. Undoped InP with semi-insulating characteristics, i.e. $>10^7$ Ω cm, was reported by Hofmann et al. (1989). The high resistivity was obtained by annealing the InP in an ampoule at 900–950 °C. Phosphorus heated to 460–480 °C was located in the same ampoule. The duration of the annealing process was 80 hours. The authors attributed the semi-insulating characteristic of the InP to a deep acceptor with a concentration $<5 \times 10^{15}$ cm^{-3}. The microscopic physical nature of the deep acceptor remains unknown.

https://doi.org/10.1017/CBO9780511599828.012 Published online by Cambridge University Press

9.4.3 Oxygen

Oxygen (O) has been intentionally incorporated into III–V semiconductors during crystal growth (Ainslie et al., 1962) or by ion implantation (Favennec, 1976; Devenaud and Favennec, 1979). As a result, highly resistive materials have been obtained. The highest resistivities obtained in GaAs:O exceed 10^8 Ω cm. Originally, O impurities in GaAs were thought to create deep donor states at an energy of 0.75 eV below the conduction band edge (Gooch et al., 1961). This level has been labeled as the EL2 center and it was generally assumed that O impurities were the microscopic origin of the EL2 center (see Sect. 9.2). However, attempts to deliberately create the 0.75 eV trap in GaAs by intentional incorporation of Ga_2O_3 during epitaxial growth proved unsuccessful (Otsubo et al. 1973; Lang and Logan, 1975). Clear evidence that O is not related to the EL2 defect was obtained from combined secondary ion mass spectrometry (SIMS) and deep level transient spectroscopy (DLTS) experiments on GaAs grown by the Bridgman technique (Huber et al., 1979). Even at the present time it is not clear which states are created by O in GaAs.

Implantation of O into GaAs yields semi-insulating material regardless of the original conductivity type. Resistivities of $10^7 - 10^8$ Ω cm were obtained from n-type and p-type GaAs implanted with O (Von Neida et al., 1989; Pearton, 1990). The high resistivity persists even after annealing at moderate temperatures (e.g. 500 °C). This result shows that O in GaAs does not create just a single level in GaAs such as a deep donor level or a deep acceptor level. In order to compensate shallow donors *and* shallow acceptors, O must create several states within the fundamental gap, or alternatively, form different complexes in GaAs which have one or several trap levels.

Oxygen is frequently implanted into GaAs for device isolation purposes. In addition to the highly resistive character of O-implanted GaAs, oxygen is more stable than hydrogen (see previous section). While the defects created by H implantation can be annealed out at moderate temperatures (e.g. 500 °C), oxygen and oxygen-related complexes are much more stable in GaAs. Annealing of GaAs:O at 500 °C does not restore the original conductivity of intentionally doped GaAs (Pearton, 1990). However, annealing of O-implanted GaAs at higher temperatures of 700–900 °C decreases the resistivity drastically for Zn-, Mg-, Cd-, Si-, and S-doped material. The decrease of the resistivity suggests that the O-induced damage is annealed out. For Be-doped GaAs implanted with O, the resistivity did not decrease substantially. Pearton (1990) proposed that Be–O complexes such as $Be_{Ga} - O_{As}$ may cause the lack of conductivity recovery upon annealing.

https://doi.org/10.1017/CBO9780511599828.012 Published online by Cambridge University Press

The role of O in GaP is well understood and has been reviewed by Dean (1986). The state introduced by O into the gap of GaP is a donor level located 0.4 eV below the conduction band edge. Low temperature (77 K) luminescence measurements revealed the existence of an 1.96 eV luminescence band whose intensity strongly increases under O-rich crystal growth conditions (Gershenzon and Mikulyak, 1962). The authors concluded that the 1.96 eV luminescence band originates from a donor-to-valence-band transition and that the microscopic origin of the donor probably is O occupying a substitutional P site. The O donor energy was estimated to be 0.4 eV, since the luminescence transition (1.96 eV) occurred 0.4 eV below the band gap energy (E_g = 2.36 eV) at T = 77 K. Oxygen in GaP also has technological importance. GaP is an indirect semiconductor with a very low electroluminescence efficiency. Incorporation of small amounts of O increases the luminescence efficiency drastically. The emission from GaP:O is in the visible part of the spectrum and has a green colour.

9.5 Rare-earth impurities

Lanthanides and actinides are rare-earth elements with incompletely filled 4f and 5f electron shells. The partially filled 4f electron shell of lanthanides is surrounded by closed $5s^2$ and $5p^6$ shells shells. If III–V semiconductors are doped with rare-earth atoms, the outer s and p shells effectively screen the inner 4f shell from the crystalline environment of the host. Radiative transitions can occur between 4f orbitals of lanthanides. The energy of intra-4f-shell transitions is nearly independent of the host semiconductor due to the screening of the 4f electron shells by the outer electrons. As a consequence, the intra-4f-shell transitions are spectrally pure and exhibit narrow linewidths that are only weakly (inhomogeneously) broadened by the host semiconductor. Furthermore, the energy of the intra-4f-shell transitions is independent of temperature due to the atomic nature of the transitions.

Doping of III–V semiconductors with lanthanides is motivated by the possibility of sharp emission lines whose energies are independent of temperature. Such doped structures are potentially useful for LEDs and lasers. Rare-earth impurities used for doping include Praseodymium (Pr), Neodymium (Nd), Erbium (Er), and Ytterbium (Yb) (Ennen and Schneider, 1985). Examples are Yb in InP (Zakharenkov et al., 1981), Yb in GaAs (Ennen et al., 1983a), Yb in GaP (Kasatkin et al., 1981a), Er in GaAs (Klein et al., 1991), Er in GaP and InP (Ennen et al., 1983b), Pr in GaP (Kasatkin et al., 1981b). Of special interest is the lanthanide Er which emits at a wavelength of approximately 1.55 μm. This corresponds to the wavelength of minimum loss in silica fibers. Er is also used for doping silica fibers (Miniscalco, 1991). Such Er-doped fibers serve as

https://doi.org/10.1017/CBO9780511599828.012 Published online by Cambridge University Press

distributed optical amplifiers.

It has been assumed that Er is threefold positively charged (Er^{3+}) and occupies cation sites in III–V semiconductors (Ennen and Schneider, 1985). The electronic intra-$4f^{11}$-shell transition is then $^4I_{13/2} \rightarrow {}^4I_{15/2}$. More recently, a study on Er-ion-implanted GaAs showed that Er can exist in a number of different configurations including Er^{2+}, Er^{3+}, tetrahedrally symmetric interstitial sites, and as complexes of interstitial Er with defects or impurities (Klein et al., 1991). The study also found that the Er^{3+} photoluminescence line is comprised of a superposition of lines from different Er sites.

The luminescence intensity of rare-earth-doped III–V semiconductors is highest at low temperatures. The luminescence yield strongly decreases at higher temperatures, e.g. at room temperature. This phenomenon is known as *temperature quenching* of the luminescence. Taguchi et al. (1992) showed that the temperature quenching of the luminescence in Yb-doped InP is due to transfer to energy from the excited Yb atom back to an electronic excitation of the InP. The authors argued that electron–hole pairs created in InP by above-bandgap illumination excite the Yb atom via an intermediate bound excitonic state. At high temperatures, the intermediate excitonic state is formed by deexcitation of Yb atoms. Furthermore, the luminescence of rare-earth-doped III–V semiconductors does not increase linearly with the rare-earth concentration. At high concentrations, the luminescence intensity decreases, which is known as *concentration quenching* of the luminescence. The concentration quenching is probably due to the formation of complexes and pairs involving the rare-earth ions.

https://doi.org/10.1017/CBO9780511599828.012 Published online by Cambridge University Press

10

Doping in heterostructures, quantum wells, and superlattices

This chapter is devoted to the role of impurities in semiconductor structures which consist of different types of semiconductor materials. Semiconductor heterostructures, quantum wells and superlattices are structures in which the individual layers have spatial dimensions comparable to the carrier de Broglie wavelength. As a consequence, quantum effects cannot be neglected in such small semiconductor structures. Furthermore, the spatial dimensions of such structures can be comparable to the Bohr radius of impurities. As a consequence, the characteristics of impurities, e.g. ionization energy and wave function, are changed. The area of quantum semiconductor physics has gained much interest since the 1970s. The physical properties of several semiconductor quantum structures are closely related to the doping and to residual impurities in such structures. Among these structures are selectively doped heterostructures, doping superlattices, doped quantum wells, and doped quantum barriers, which will be discussed in this chapter.

10.1 Selectively doped heterostructures

Selectively doped heterostructures are structures which consist of a doped wide-gap semiconductor and an undoped narrow-gap semiconductor. Selectively doped heterostructures were first realized by Stormer et al. (1978) and Dingle et al. (1978) in an attempt to reduce scattering of carriers by ionized impurities. The electron mobilities obtained in $Al_xGa_{1-x}As/GaAs$ heterostructures at low temperatures can exceed 10^7 cm^2/V s (Pfeiffer et al., 1989a).

The band diagram of a selectively doped n-type heterostructure is shown in Fig. 10.1. The structure consists of a doped wide-gap semiconductor (left side of

https://doi.org/10.1017/CBO9780511599828.013 Published online by Cambridge University Press

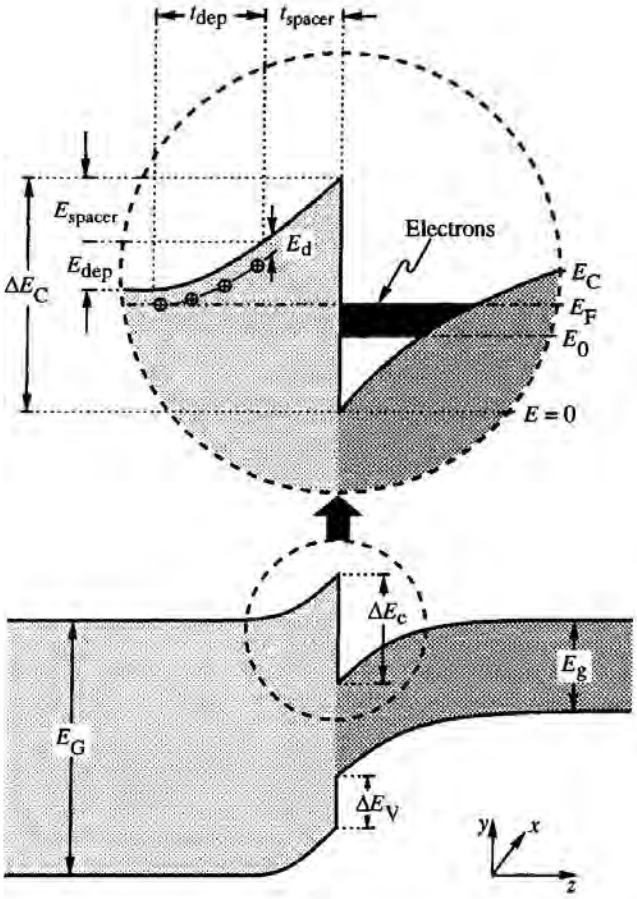


Fig. 10.1. Band diagram of a selectively doped heterostructure consisting of a doped wide-gap semiconductor and an undoped narrow-gap semiconductor. Due to the lower conduction band energy, electrons transfer from their parent donors to the narrow-gap semiconductor.

Fig. 10.1) and an undoped narrow-gap semiconductor (right side of Fig. 10.1). Since the conduction band edge of the narrow-gap semiconductor is assumed to be lower in energy, electrons originating from donors in the wide-gap semiconductor transfer to the narrow-gap semiconductor. The transferred electrons form a quantized, two-dimensional electron gas (2DEG) located at the interface. The two-dimensional character of the electron gas as well as the quantization of motion of the electrons in the z-direction (see Fig. 10.1) was demonstrated by Stormer et al. (1979). Electrons are spatially separated from their parent ionized impurities. As a consequence, ionized impurity scattering is reduced in such heterostructures as compared to a doped bulk semiconductor. The electron mobility is especially enhanced at low temperatures where ionized

https://doi.org/10.1017/CBO9780511599828.013 Published online by Cambridge University Press

impurity scattering is the dominant scattering mechanism. At room temperature, the mobility enhancement is moderate due to the dominance of phonon scattering.

10.1.1 The electron density

The two-dimensional (2D) electron density of the electron gas at the interface of the two semiconductors is determined by two driving forces. First, electrons transfer from their parent donor states to the narrow-gap semiconductor due to the availability of states at lower energy. Second, an electric dipole field is created by the electron transfer whose charges consists of the depleted donor layer in the wide-gap semiconductor and the electron gas in the narrow-gap material. The transfer of electrons continues until the Fermi level of the electron gas coincides with the donor energy in the neutral region of the wide-gap semiconductor.

The calculation of the electron density of a selectivity doped heterostructure is most conveniently done by considering the energies of the electron states involved. The detailed conduction-band diagram of a selectively doped heterostructure is shown in Fig. 10.1. As an example, we consider an $Al_xGa_{1-x}As/GaAs$ heterostructure consisting of a doped $Al_xGa_{1-x}As$ region, an undoped $Al_xGa_{1-x}As$ spacer, and an undoped GaAs narrow-gap region. The purpose of the undoped $Al_xGa_{1-x}As$ spacer is to further spatially separate the free electrons from their parent ionized impurities. This separation was shown to further increase the electron mobility (Stormer et al., 1981c). We now consider the different energies involved in the heterostructure.

(i) Donor ionization energy, E_d: The thermal ionization energy of the shallow donor in GaAs and $Al_xGa_{1-x}As$ is approximately 5 meV. At low temperatures, the Fermi level coincides with the donor level in the undepleted $Al_xGa_{1-x}As$ side of the heterostructure.

(ii) Depletion energy, E_{dep}: Assuming a three-dimensional (3D) doping concentration N_D, the 2D density of transferred electrons is given by

$$n_{2DEG} = N_D \, t_{dep} \tag{10.1}$$

where t_{dep} is the (unknown) thickness of the depletion region. Any residual acceptor concentration is neglected. The magnitude of the electric field at the end of the depletion region can be obtained from Gauss's law

$$\mathcal{E} = \frac{e}{\varepsilon} N_D \, t_{dep} = \frac{e}{\varepsilon} n_{2DEG} \, . \tag{10.2}$$

The energy drop in the depletion region is then given by

https://doi.org/10.1017/CBO9780511599828.013 Published online by Cambridge University Press

$$E_{\text{dep}} = \frac{1}{2} e\,\mathcal{E}\,t_{\text{dep}} = \frac{e^2}{2\varepsilon}\,\frac{n_{2\text{DEG}}^2}{N_{\text{D}}}\,. \tag{10.3}$$

In the case of $N_{\text{D}} \to \infty$, i.e. for δ-doping, the depletion region thickness and energy drop approach zero, i.e. $t_{\text{dep}} \to 0$ and $E_{\text{dep}} \to 0$.

(iii) Spacer energy, E_{spacer}: The energy drop in the spacer region is given by

$$E_{\text{spacer}} = e\mathcal{E}\,t_{\text{spacer}} = \frac{e^2}{\varepsilon}\,n_{2\text{DEG}}\,t_{\text{spacer}} \tag{10.4}$$

where t_{spacer} is the thickness of the spacer region.

(iv) Conduction band discontinuity, ΔE_{c}: The conduction band discontinuity is a materials parameter. For the material system $Al_xGa_{1-x}As/GaAs$ the conduction band discontinuity is given by

$$\Delta E_{\text{c}} \cong \frac{70}{100}\,\Delta E_{\text{g}} = \frac{70}{100}\,1.247\text{eV}\,x_{\text{Al}} \tag{10.5}$$

where it is assumed that 70% of the bandgap discontinuity occurs in the conduction band. The factor 1.247 eV x_{Al} expresses the change of the $Al_xGa_{1-x}As$ band gap with Al mole fraction (Casey and Panish, 1978). For a 32% Al mole fraction, the conduction band discontinuity calculated from Eq. (10.5) equals 279 meV.

(v) Subband energy, E_0: The ground-state energy of the triangular well can be conveniently obtained by a variational calculation using the trial function

$$\psi(z) = A\,z\,e^{-\alpha z} \tag{10.6}$$

where α is the trial parameter and A is a normalization parameter. The wave function vanishes at $z = 0$, i.e. at the interface, as schematically shown in Fig. 10.2. The wavefunction decays exponentially in the triangular GaAs side of the barrier. The normalization condition $\langle\psi|\psi\rangle = 1$ yields the normalization constant $A = 2\alpha^{3/2}$ and thus the normalized wave function

$$\psi(z) = 2\alpha^{3/2}\,z\,e^{-\alpha z} \tag{10.7}$$

which is also called the Fang–Howard wave function (Fang and Howard, 1966).

Calculation of the energy expectation value for this wave function yields

https://doi.org/10.1017/CBO9780511599828.013 Published online by Cambridge University Press

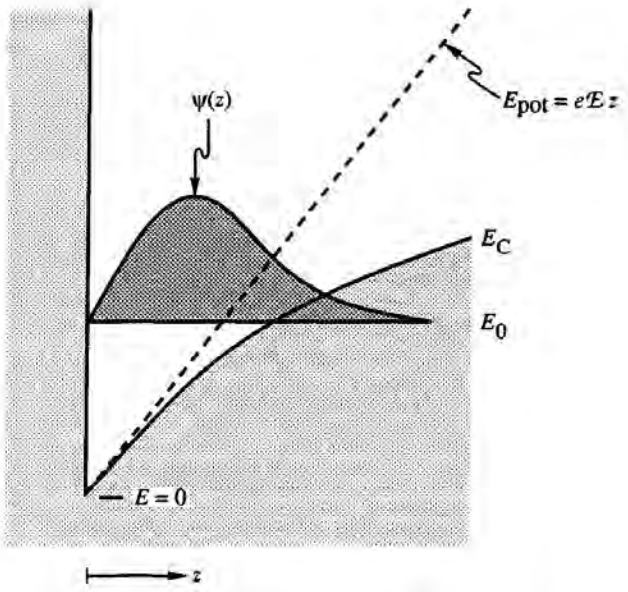


Fig. 10.2. Fang–Howard wave function, $\psi(z) \propto z \exp(-\alpha z)$, at the interface of an $Al_xGa_{1-x}As/GaAs$ heterostructure.

$$\langle E \rangle = \langle \psi | H | \psi \rangle$$

$$= \left\langle \psi \left| -\frac{\hbar^2}{2m^*} \frac{\partial^2}{\partial z^2} + E_{pot}(z) \right| \psi \right\rangle$$

$$= e\mathcal{E}\frac{3}{2\alpha} + \frac{\hbar^2}{2m^*}\alpha^2 \qquad (10.8)$$

where the potential energy $E_{pot}(z) = e\mathcal{E}z$. Minimizing the expectation value of the energy yields the trial parameter α according to

$$\alpha = \left(\frac{3}{2} e\mathcal{E} \frac{m^*}{\hbar^2} \right)^{1/3} . \qquad (10.9)$$

Insertion of the trial parameter α into Eq. (10.8) yields the ground-state energy of the triangular potential well

https://doi.org/10.1017/CBO9780511599828.013 Published online by Cambridge University Press

$$E_0 = \langle E \rangle_{\min} = \frac{3}{2}\left[\frac{3}{2} e\mathcal{E} \frac{\hbar}{\sqrt{m^*}}\right]^{2/3} \tag{10.10}$$

which can also be expressed in terms of the 2D electron density

$$E_0 = \frac{3}{2}\left[\frac{3}{2} \frac{e^2}{\varepsilon} n_{2\mathrm{DEG}} \frac{\hbar}{\sqrt{m^*}}\right]^{2/3} . \tag{10.11}$$

(vi) Degeneracy energy of 2DEG, $E_F - E_0$. Due to the finite density of states, the Fermi level increases above the ground-state energy E_0 at high free carrier densities. The energy $E_F - E_0$ is obtained as

$$E_F - E_0 = n_{2\mathrm{DEG}}/\rho_{\mathrm{DOS}}^{2\mathrm{D}} \tag{10.12}$$

where $\rho_{\mathrm{DOS}}^{2\mathrm{D}}$ is the two-dimensional density of states given by $\rho_{\mathrm{DOS}}^{2\mathrm{D}} = m^*/\pi\hbar^2$. The equation is valid for degenerate electron systems, where the Fermi–Dirac distribution can be approximated by a step function. The corresponding equation for the non-degenerate limit is given in Chap. 3.

The total energy balance of the heterostructure can be written as (see Fig. 10.1 for illustration)

$$E_d + E_{dep} + E_{spacer} + E_0 + (E_F - E_0) = \Delta E_c \tag{10.13}$$

where it is assumed that the Fermi energy is the same on both sides of the interface, i.e. the system is in electronic equilibrium. All the energies in Eq. (10.13) can be expressed as a function of $n_{2\mathrm{DEG}}$ which is then the only variable in the equation. It is not possible to explicitly solve the equation for $n_{2\mathrm{DEG}}$. However, the solution for $n_{2\mathrm{DEG}}$ can be easily obtained by an iterative process.

Fully self-consistent calculations of the electron density in selectively doped heterostructures have been reported in the literature (Ando, 1982a and 1982b; Stern and Das Sarma, 1984; Vinter, 1984). In such self-consistent calculations, the Schrödinger and Poisson equations are solved in an iterative process and many-body effects may be taken into account. Nevertheless, the results obtained from the approximate calculation described above compare favorably with the much more elaborate self-consistent calculations. In self-consistent calculations, the solution of Poisson's equation is straightforward whereas the accurate solution of Schrödinger's equation is more elaborate. Therefore, several groups used approximate solutions of the Schrödinger equation, including the variational solution (Stern, 1983; Fang and Howard, 1966) and the WKB approximation (Ando, 1985).

https://doi.org/10.1017/CBO9780511599828.013 Published online by Cambridge University Press

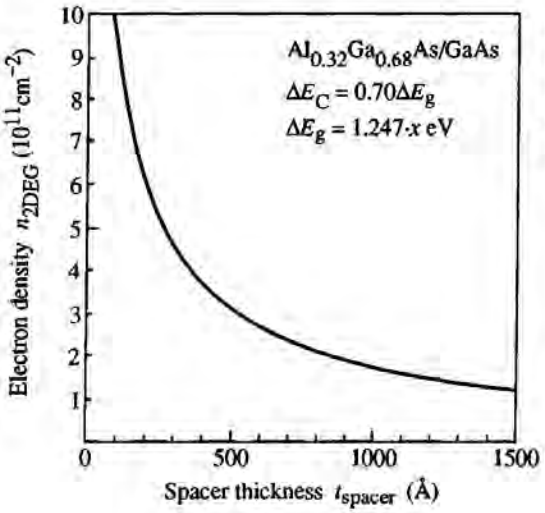


Fig. 10.3. Calculated electron density in selectively doped $Al_xGa_{1-x}As/GaAs$ heterostructures as a function of spacer thickness, t_{spacer}.

As an example, the carrier density of the 2DEG calculated from Eq. (10.13) is shown in Fig. 10.3 as a function of the spacer thickness. The Al mole fraction used is $x = 32\%$ which leads to a conduction band discontinuity of $\Delta E_c = 279$ meV. Other parameters used are $\varepsilon/\varepsilon_0 = \varepsilon_r = 13.1$ and $m^* = 0.067m_0$. The structure is assumed to be δ-doped which results in a zero depletion energy $E_{dep} = 0$. Figure 10.3 reveals that the electron density decreases for large spacer thicknesses. The electron density can also be calculated for different doping concentrations, N_D, which enter E_{dep} in Eq. (10.13). The values of n_{2DEG} are lower for homogeneous doping as compared to the δ-doped case shown in Fig. 10.3. Delta-doped heterostructures were shown to have higher electron densities (Schubert et al., 1987b) as well as higher electron mobilities (Schubert et al., 1989b) as compared to their homogeneously doped counterparts.

10.1.2 The electron mobility

In bulk semiconductors, the dominant scattering mechanism at low temperatures is ionized impurity scattering, which is strongly reduced in selectively doped heterostructures. The spatial separation of electrons from their parent ionized impurities reduces ionized impurity scattering making possible electron mobilities exceeding 10^6 cm^2/V s at low temperatures. In order to elucidate the mobility enhancement we will first discuss the role of impurity scattering in bulk semiconductors.

Ionized impurity scattering in semiconductors is governed by the same physical principles as Rutherford scattering. In both scattering processes the

https://doi.org/10.1017/CBO9780511599828.013 Published online by Cambridge University Press

trajectory of a charged particle is diverted by the interaction with another charged particle. The coulombic interaction of two charged particles is strongest for a small distance between the interacting particles and a long interaction time. Such a long interaction time is given for slowly moving electrons, that is for a non-degenerate carrier gas at low temperatures. The low-temperature mobility is therefore a measure of the impurity and defect content in non-degenerately doped semiconductors.

The mobility due to ionized impurities was calculated by Conwell and Weisskopf (1950) and later by Brooks and Herring (Brooks, 1955). A review on ionized impurity scattering was given by Chattopadhyay and Queisser (1981). While Conwell and Weisskopf (CW) used unscreened Coulomb potentials, i.e. $V = e/4\pi\varepsilon r$, Brooks and Herring (BH) used screened Coulomb potentials, i.e. $V = (e/4\pi\varepsilon r)e^{-\lambda r}$, where λ is the inverse screening length.

The ionized impurity mobility in the Conwell–Weisskopf approximation is given by

$$\mu_{CW} = \frac{128\sqrt{2\pi}\,\varepsilon^2 (kT)^{3/2}}{N_{II}\, e^3 \sqrt{m}} \left[\ln\left(1 + \frac{(12\pi\varepsilon kT^2)}{N_{II}^{2/3}\, e^4}\right)\right]^{-1} \qquad (10.14)$$

where N_{II} is the concentration of ionized impurities.

The Brooks–Herring approach, which includes the screening of impurities by free carriers, yields for the ionized impurity mobility

$$\mu_{BH} = \frac{128\sqrt{2\pi}\,\varepsilon^2 (kT)^{2/3}}{N_{II}\, e^3 \sqrt{m}} \left[\ln(1 + \beta_{BH}^2) - \frac{\beta_{BH}^2}{1 + \beta_{BH}^2}\right]^{-1} . \qquad (10.15)$$

The parameter β_{BH} is given by

$$\beta_{BH} = 2\,\frac{m}{\hbar}\left(\frac{2}{m} 3kT\right)^{1/2} r_D \qquad (10.16)$$

where $r_D = (\varepsilon kT/e^2 n)^{1/2}$ is the Debye screening length, and n is the free carrier concentration. For degenerately doped semiconductors, the Debye screening length must be replaced by the Thomas–Fermi screening length and the thermal energy must be replaced by the Fermi energy.

Both the CW and the BH approach predict a temperature dependence of

$$\mu \propto T^{3/2} , \qquad (10.17)$$

i.e. an increasing mobility with temperature. For a non-degenerate semiconductor the experimental mobility indeed approaches zero for $T \to 0$. In *degenerately*

https://doi.org/10.1017/CBO9780511599828.013 Published online by Cambridge University Press

doped semiconductors, the Fermi velocity is larger than the thermal velocity at sufficiently low-temperatures and the mobility is expected to remain constant in the low-temperature regime. Note that a qualitative discrepancy exists between the CW and the BH approximation with regard to their density dependence. While the CW-mobility decreases continuously at high concentrations, the BH-mobility first decreases with impurity density but then increases again at very high impurity concentrations (Seeger, 1982). The increase in the BH-mobility is due to screening of the ionized impurity potentials.

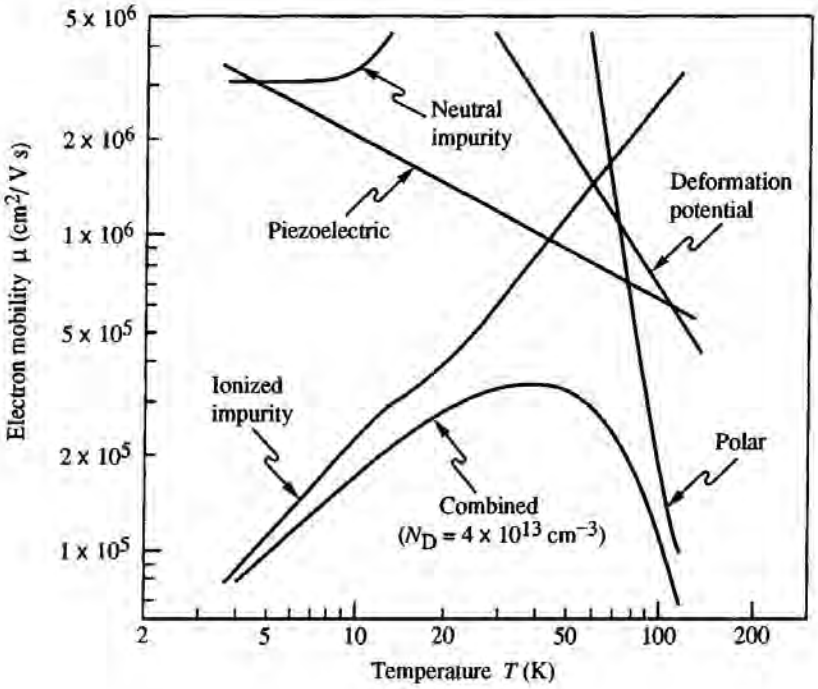


Fig. 10.4. Calculated electron mobilities due to different scattering mechanisms and combined mobility inferred from Matthiessen's rule in high purity GaAs ($N_D = 4 \times 10^{13}$ cm^{-3}) as a function of temperature (after Wolfe et al., 1970).

The calculated electron mobility in moderately doped bulk n-type GaAs is shown in Fig. 10.4 (Wolfe et al. 1970). In addition to ionized impurity scattering, neutral impurity, piezoelectric, deformation potential, and polar phonon scattering are shown. The combined mobility is also included and is obtained from the sum of the individual scattering mechanisms according to $\mu^{-1} = \sum_i \mu_i^{-1}$ (Matthiessen's rule).

https://doi.org/10.1017/CBO9780511599828.013 Published online by Cambridge University Press

The major scattering mechanisms in selectively doped $Al_xGa_{1-x}As$/GaAs heterostructures were reviewed by Stormer (1983) and are given by bulk and interface phonon-scattering, alloy scattering in the $Al_xGa_{1-x}As$, neutral and ionized impurity scattering in the GaAs (unintentional impurities), remote impurity scattering (intentional impurities), interface roughness scattering, intersubband scattering, and real-space scattering. In the following, the scattering mechanisms will be discussed.

(1) Scattering by bulk phonons and interface phonons occurs at all finite lattice and electron temperatures. However, since the two materials $Al_xGa_{1-x}As$ and GaAs are very similar in density and dielectric constant, interface phonons are weak and electron scattering via these phonons is negligible. Calculations of the scattering rate due to bulk phonons show similar scattering rates for bulk material and heterostructures (Price 1981, 1984a, 1984b; Hess, 1979). Scattering by optical phonons dominates the mobility in selectivity doped heterostructures at temperatures ≥ 100 K. Above this temperature the mobility in selectivity doped heterostructures coincides with the mobility in high-purity GaAs.

(2) Alloy scattering due to random distribution of Al and Ga in the alloy $Al_xGa_{1-x}As$ is a minor scattering mechanism in selectively doped heterostructures. The random cation distribution leads to potential fluctuations which scatter charge carriers. The penetration of the electron wave function into the $Al_xGa_{1-x}As$ is small (note that the penetration in the Fang–Howard wave function is assumed to be zero). Consequently, the scattering due to alloy fluctuations plays a minor role. Alloy scattering in bulk semiconductors increases with the Al mole fraction and reaches a maximum at $x = 0.5$. Experimental reports of the mobility in selectively doped heterostructures suggested an increase of the mobility with Al mole fraction (Stormer et al., 1981a) as well a decrease of the mobility (Drummond et al., 1982). The optimum Al content for selectively doped heterostructures was reported to be $x = 32\%$ (Pfeiffer, 1990).

(3) Neutral and ionized unintentional impurities in the undoped GaAs and $Al_xGa_{1-x}As$ layer contribute to the scattering in selectively doped heterostructures. However, the scattering by neutral impurities is much weaker than the scattering by ionized impurity atoms due to the lack of Coulomb charge. The background concentration in the undoped GaAs can be in the low 10^{13} cm^{-3} range. Higher background concentrations (e.g. 10^{16} cm^{-3}) were demonstrated to reduce the electron mobility drastically

https://doi.org/10.1017/CBO9780511599828.013 Published online by Cambridge University Press

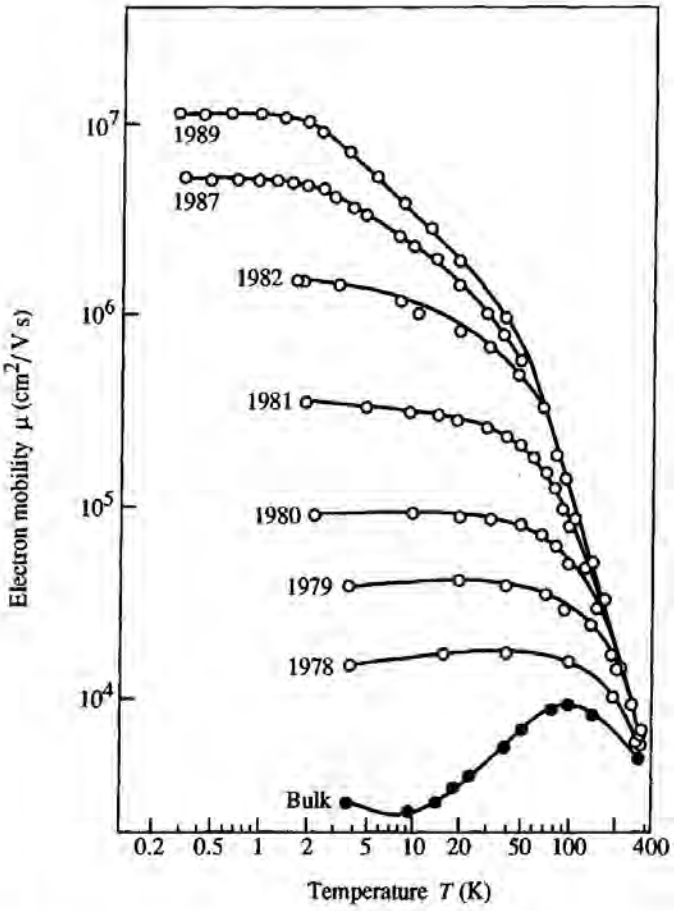


Fig. 10.5. Electron mobilities in selectively doped $Al_xGa_{1-x}As/GaAs$ heterostructures (open circles) as a function of temperature for different years. The mobility of bulk GaAs ($N_D = 2 \times 10^{17}$ cm^{-3}, solid circles) is shown for comparison (Pfeiffer et al., 1989a).

(Drummond et al., 1981a).

(4) Remote impurity scattering occurs due to the Coulomb potentials of the intentional dopants in the $Al_xGa_{1-x}As$. Remote impurity scattering can be reduced by increasing spacer thicknesses, i.e. be moving the impurities further away from the electron gas. However, the increasing spacer thickness reduces the electron density (as shown in Fig. 10.3), which again results in a lower mobility due to a reduction in screening. Remote ionized impurity scattering dominates the mobility for small spacer thicknesses ($t_{spacer} < 300$ Å). On the other hand, remote ionized impurity scattering becomes irrelevant for very large spacer thicknesses. The highest

https://doi.org/10.1017/CBO9780511599828.013 Published online by Cambridge University Press

337-TA-1366 RX-0255

mobilities are obtained with spacer thicknesses on the order of 600 Å – 700 Å (Harris et al., 1986; Pfeiffer et al., 1989b). Remote impurity scattering in non-degenerate systems has the $\mu \propto T^{3/2}$ dependence. In a highly degenerate system, the Fermi velocity is larger than the thermal velocity. Furthermore, the Fermi velocity is independent of temperature. As a consequence, the mobility saturates at low temperatures. Walukiewicz et al. (1984) showed that for typical electron densities the mobility is temperature-independent for $T < 50$ K. However, for very high mobility samples the temperature range of constant mobility is shifted towards lower temperatures (see Fig. 10.5).

(5) Interface roughness scattering occurs due to the roughness of the interface between the $Al_xGa_{1-x}As$ layer and the GaAs. The roughness of the interface depends on the growth conditions such as the growth temperature and the growth interruption time at the interface. Using 120 s growth interruptions at an $Al_xGa_{1-x}As$/GaAs interface smooth islands of several 100 Å diameter can be obtained (Kopf et al., 1991). Nevertheless, even the existence of monolayer flat islands with a diameter of several hundred ångströms does not necessarily imply a reduction of interface roughness scattering: The Fermi wavelength is approximately 350 Å (at $n_{2DEG} = 5 \times 10^{11}$ cm^{-2}), i.e. comparable to the island sizes achievable by growth interruptions. The lateral correlation length of interface roughness in MBE grown GaAs/AlAs quantum wells was investigated by Noda et al. (1991) using mobility measurements. Lateral correlation lengths as large as 300 Å were deduced.

(6) Intersubband scattering becomes relevant at either sufficiently high temperatures or at high densities at which a second subband becomes populated. In selectively doped $Al_xGa_{1-x}As$/GaAs heterostructures, the second subband becomes populated at an electron density of $6 \times 10^{11} - 7 \times 10^{11}$ cm^{-2} (Ando and Mori, 1979). Intersubband scattering does not open a new scattering channel (instead, all the above scattering mechanisms can contribute) but represents an increase in scattering probability due to an increase in phase space. At low temperatures when the second subband of the 2DEG becomes populated, quasi-elastic scattering can occur from one subband to the other giving rise to a sudden drop in mobility (Stormer, 1983). The drop in mobility due to intersubband scattering was estimated theoretically (Mori and Ando, 1980) and measured experimentally to be as large as 30% (Stormer et al., 1981a,b).

https://doi.org/10.1017/CBO9780511599828.013 Published online by Cambridge University Press

RX-0255.426

337-TA-1366 RX-0255

(7) Real-space transfer scattering can occur at very high electric fields and is due to the transfer of electrons from the GaAs channel to the $Al_xGa_{1-x}As$ layer. The mobility in the $Al_xGa_{1-x}As$ is much lower than in the GaAs layer due to alloy scattering. As a result, the mobility is expected to drop dramatically at the onset of this transfer. Hess et al. (1979) who considered real-space transfer in semiconductor heterostructures concluded that negative differential conductivity can occur due to this transfer.

The electron mobility in $Al_xGa_{1-x}As/GaAs$ heterostructure is shown in Fig. 10.5 as a function of temperature for the years 1978 through 1989 (Pfeiffer et al., 1989a). The improvement of the mobility over the years reflects (i) the introduction of a spacer layer, (ii) improved vacuum in the MBE process, (iii) use of δ-doping, (iv) higher purity sources, and (v) improved substrate quality and preparation.

10.2 Doping aspects of selectively doped heterostructures

The distribution and concentration of dopants in selectively doped heterostructures determines many of its transport properties. To achieve, for example, high mobilities, thick spacer layers are required in order to minimize remote ionized impurity scattering. To achieve, for example, high electron densities, high doping concentrations are required. In this section, the ***optimum dopant distribution*** for (i) maximum electron density in heterostructures and (ii) maximum electron mobility in heterostructures is analyzed. Furthermore, the differences in ***normal*** and ***inverted heterostructures*** will be discussed. The properties of normal heterostructures ($Al_xGa_{1-x}As$ grown on top of GaAs) are different from inverted heterostructures (GaAs grown on top of $Al_xGa_{1-x}As$). The differences are mainly due to the different doping distributions in the structures.

10.2.1 Heterostructures with maximum electron density

High electron densities in selectively doped heterostructures are most desirable for field-effect transistors. The transconductance (amplification) of field-effect transistors increases with the electron density. The electron density increases with decreasing spacer thickness and reaches a maximum for zero spacer thickness. The effect of different doping distributions on mobility must be studied in samples with the *same spacer thickness.*

The conduction band diagram of two selectively doped heterostructures with the same spacer thickness is shown in Fig. 10.6. The figure depicts (a) a δ-doped and (b) a homogeneously doped heterostructure, respectively. The δ-doped heterostructure can be considered to be the limit of homogeneous doping for

https://doi.org/10.1017/CBO9780511599828.013 Published online by Cambridge University Press

RX-0255.427

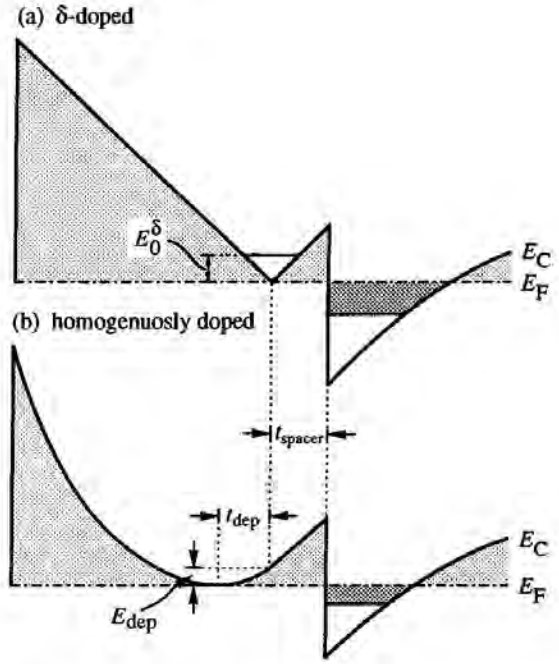


Fig. 10.6. Conduction band diagram of (a) a δ–doped and (b) a homogeneously doped heterostructure. The thickness of the undoped spacer region is the same in both heterostructures. The selectively δ-doped heterostructure yields the highest densities of the two-dimensional electron gas.

$N_D \rightarrow \infty$. This suggests that δ-doping results in the highest electron density. The thickness of the depletion region, t_{dep}, and the associated energy drop (see Eq. 10.3), E_{dep}, approach zero in the limiting case of δ-doping. In order to maximize the free carrier concentration, the terms on the left-hand side of Eq. (10.13) need to be minimized whereas the term on the right-hand side of Eq. (10.14) (i.e. ΔE_c) needs to be maximized. Delta-doping eliminates the term 'E_{dep}' and therefore maximizes the free carrier concentration of the heterostructure.

Delta-doped heterostructures have another advantage over their homogeneously doped counterparts: Due to the narrow V-shaped potential well generated by δ-doping in the $Al_xGa_{1-x}As$, size-quantization occurs also in the $Al_xGa_{1-x}As$ (Schubert et al., 1987b). The quantization energy, E_0^δ, increases the energy of the lowest electron state in the $Al_xGa_{1-x}As$. As a consequence, the difference in energy between the $Al_xGa_{1-x}As$ and the GaAs is enhanced which results in a further transfer of electrons into the narrow-gap GaAs layer. Size quantization in the homogeneously doped heterostructure is smaller or may not

https://doi.org/10.1017/CBO9780511599828.013 Published online by Cambridge University Press

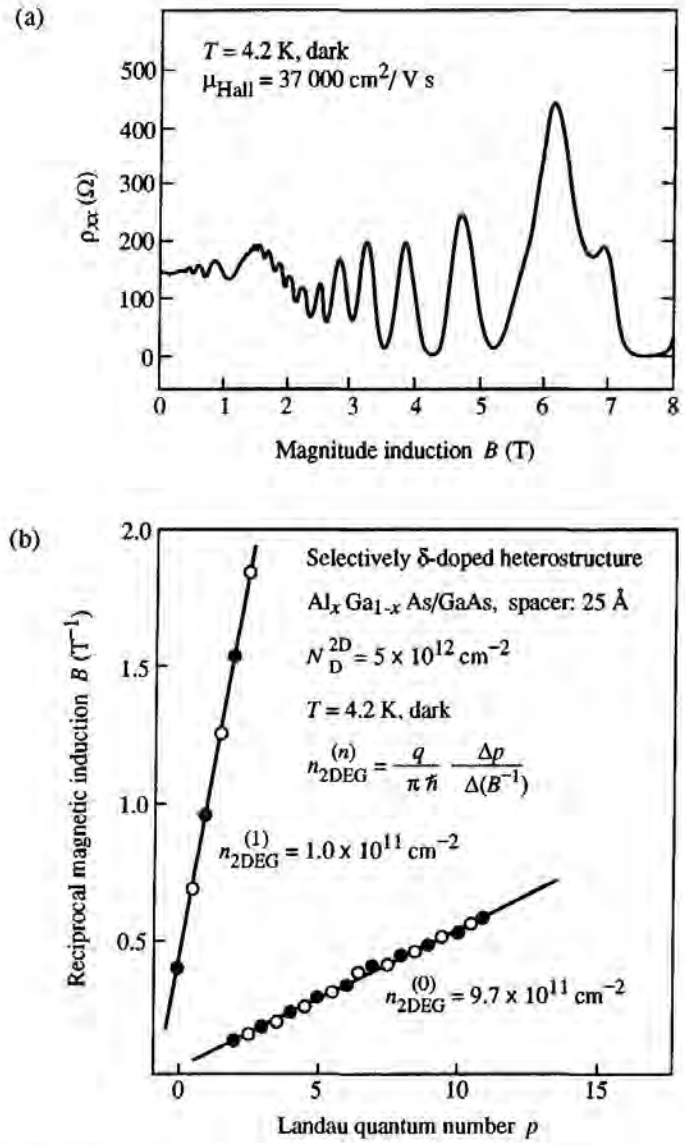


Fig. 10.7. (a) Low-temperature magnetoresistance of a selectively δ-doped heterostructure. (b) Evaluation of the two distinct periods of the Shubnikov–de Haas oscillation yields a concentration of 9.7×10^{11} and 1×10^{11} cm^{-2} for the lowest and first excited subband, respectively.

occur at all at low doping concentrations (Vinter, 1983).

The highest electron densities in $Al_xGa_{1-x}As/GaAs$ are obtained in δ-doped heterostructures. The measured densities exceed 10^{12} cm^{-2} (Schubert et al., 1987b) even at low temperatures. Magnetoresistance measurements of a selectively δ-doped heterostructure are shown in Fig. 10.7. The oscillations of the

https://doi.org/10.1017/CBO9780511599828.013 Published online by Cambridge University Press

337-TA-1366 RX-0255

magnetoresistance are called Shubnikov–de Haas oscillations and are due to additional quantization of the energy levels in the magnetic field. The oscillations are periodic in $1/B$. Two clearly distinct periods of the oscillation are observed in Fig. 10.7. The two periods are due to two electronic subbands that are occupied at low temperatures. The concentrations within the two subbands can be evaluated by plotting the Landau quantum numbers of the minima (solid circles) and maxima (open circles) versus reciprocal magnetic field, as shown in Fig. 10.7(b). The slope of this plot yields the concentrations of 9.7×10^{11} cm^{-2} and 1×10^{11} cm^{-2} for the lowest and first excited subbands, respectively. The total concentration is $n_{2DEG} = 1.07 \times 10^{12}$ cm^{-2} at low temperatures. The corresponding mobility is $\mu = 37\,000$ cm^2/V s. At room temperature, a concentration of $n_{2DEG} = 1.7 \times 10^{12}$ cm^{-2} and a mobility of 8900 cm^2/V s have been obtained from Hall measurements on the same sample.

High densities of the electron gas are advantageous in selectively doped heterostructure transistors. High electron densities result in high transconductances, i.e. high amplification of transistors (Mimura, 1983).

10.2.2 Heterostructures with maximum mobility

The doping distribution influences the carrier mobility via remote impurity scattering. It is an interesting question which doping configuration minimizes remote impurity scattering and results in the highest mobilities. In order to compare different doping configurations it is necessary to compare configurations which result in the *same carrier density*. This restriction is necessary since the carrier mobility depends on the carrier density.

Two different doping distributions which result in the same electron-gas density are shown in Fig. 10.8. The centroid of the two doping distributions has the same distance z_c from the interface. If the thickness of the doped layer, z_d, is reduced and simultaneously the doping concentration, N_D, is increased such that the product is a constant ($z_d N_D = \text{const} = n_{2DEG}$), the free carrier concentration, n_{2DEG}, remains constant as well. It can be easily verified from Poisson's equation that such doping distributions result in the *same* potential and the *same* electric field at the interface, i.e. in the same free carrier density.

In order to estimate the effect of remote ionized impurity scattering, Schubert et al. (1989b) calculated the potential fluctuations occurring at the interface due to random doping impurity distribution. The authors found that potential fluctuations are minimized if the thickness of the doping distribution approaches zero, i.e. for δ-doping in the $Al_xGa_{1-x}As$. The minimization of potential fluctuations is equivalent to a maximization of remote ionized impurity mobility, since the scattering matrix element is proportional to the magnitude of the

https://doi.org/10.1017/CBO9780511599828.013 Published online by Cambridge University Press

RX-0255.430

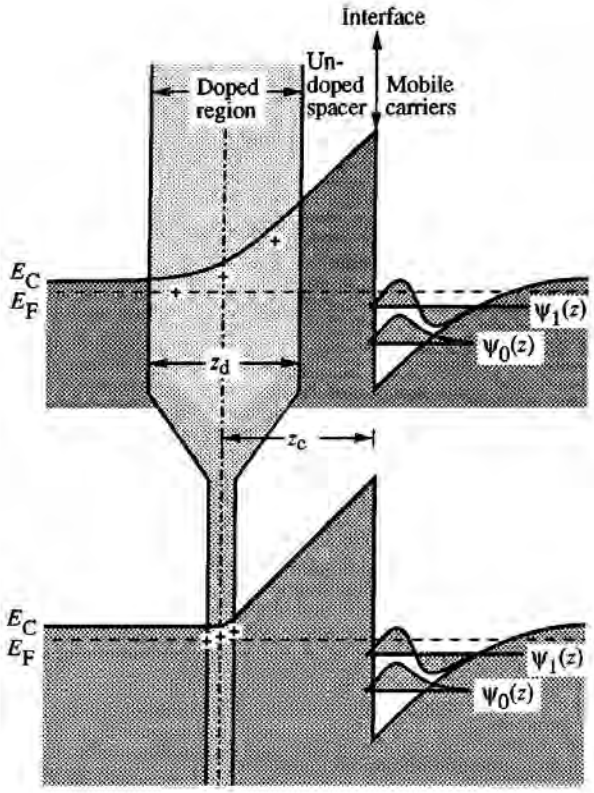


Fig. 10.8. Schematic illustration of the conduction band diagram of a selectively doped heterostructure for different doped layer thicknesses and doping concentrations. The free carrier density remains constant upon changing the doped layer thickness.

scattering potential. The electron mobility monotonically decreases with a decreasing magnitude of the potential fluctuations. This monotonical relationship is valid even in the presence of screening.

Experimental Hall mobilities (left ordinate) and carrier densities (right ordinate) of selectively doped heterostructures with different thicknesses of the doped region are shown in Fig. 10.9. The thickness of the doped region, z_d, is changed, while the distance of the doped region centroid, z_c, remains constant as shown in the inset. The electron mobilities at 4.2 K range between 860 000 $cm^2/V\ s$ for $z_d = 800$ Å and $4.53 \times 10^6\ cm^2/V\ s$ for $z_d \to 0$ Å. Mobilities are measured in the dark after illumination. Electron mobilities increase as z_d decreases (see Fig. 10.9) with the highest mobilities obtained as z_d approaches zero. The mobility follows the qualitative trend predicted by the theoretical model.

https://doi.org/10.1017/CBO9780511599828.013 Published online by Cambridge University Press

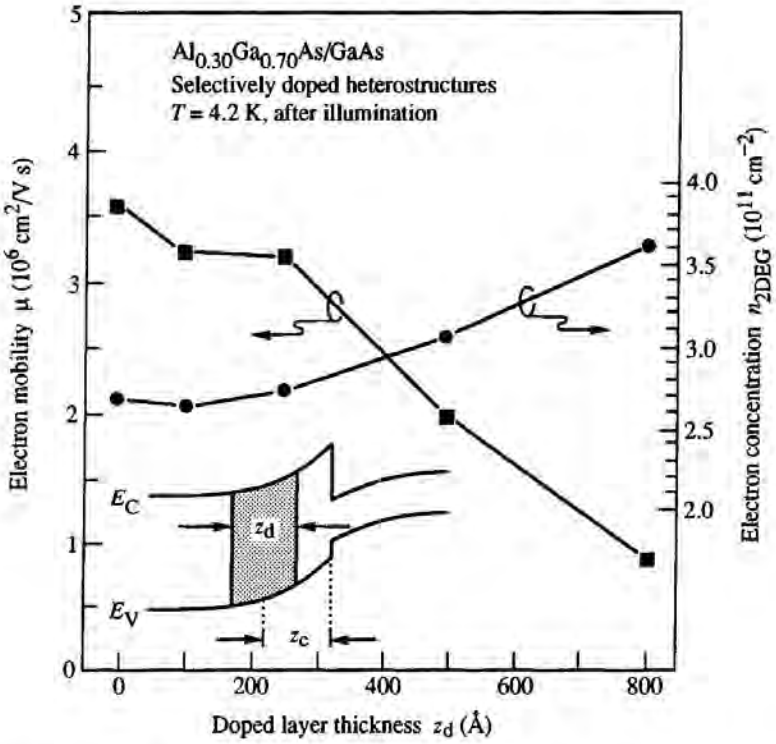


Fig. 10.9. Electron mobility (left ordinate) and electron density (right ordinate) versus doped layer thickness, z_d, of selectively doped heterostructures grown by molecular-beam epitaxy. Samples were grown with z_d = 0, 100, 250, 500, and 800 Å, with z_c = 400 Å = constant. The densities and mobilities were measured after illumination. The values measured before illumination are typically 15–35% lower but follow the same qualitative trend.

Figure 10.9 further illustrates the carrier density as a function of the doped layer thickness. An increase of n_{2DEG} is observed as z_d increases, which is not expected if only shallow donors are taken into account. A probable cause for this increase is the coexistence of shallow and deep donors in the $Al_xGa_{1-x}As$: As z_d increases, more deep donors are elevated above the Fermi level in the doped region close to the interface, as illustrated in Fig. 10.8. Consequently, the deep donors nearest the interface become ionized and the mobile carrier density is enhanced. This concentration enhancement is expected for carriers in the dark. It is maintained even after illumination in samples with large z_d, due to photoionization of deep donors close to the interface.

In addition to remote donors in the $Al_xGa_{1-x}As$, unintentional shallow and deep impurities in the vicinity of the interface reduce the carrier mobility. The influence of any such static imperfection is reduced by screening. The mobility

https://doi.org/10.1017/CBO9780511599828.013 Published online by Cambridge University Press

increases with concentration according to the relation $\mu \propto n^{\beta}_{2DEG}$ with $0.5 < \beta < 1.5$ (Pfeiffer et al., 1989a, Price, 1984a and 1984b). Thus, the decrease of mobility with increasing z_d (see Fig. 10.9) would be even more pronounced, if n_{2DEG} were independent of z_d.

Free carriers at the interface are scattered by (i) remote ionized dopants as well as by (ii) unintentional background impurities in the narrow-gap semiconductor. Scattering by remote impurities is reduced for large spacer thicknesses. However, large spacer thicknesses reduce the carrier density *and* therefore the carrier mobility since $\mu \propto n^{\beta}_{2DEG}$. Furthermore, scattering by background impurities becomes more relevant at low carrier densities due to less efficient screening of background impurities. Thus, ionized impurity scattering dominates at low temperatures for small spacer thicknesses (remote intentional impurities) as well as for large spacer thicknesses (unintentional background impurities). The maximum mobility is achieved for intermediate spacer thicknesses (Harris et al., 1986; Pfeiffer et al., 1989b). At low background impurity concentrations of 2×10^{13} cm^{-3}, the maximum mobility was obtained at a spacer thickness of 750 Å (Pfeiffer et al., 1989b).

10.2.3 The inverted interface problem

Inverted heterostructures are known to yield much lower mobilities as compared to regular heterostructures. ***Regular heterostructures*** are heterostructures which have the doped $Al_xGa_{1-x}As$ grown on top of the GaAs. ***Inverted heterostructures*** are heterostructures which have the undoped GaAs grown on top of the doped $Al_xGa_{1-x}As$. Experimental results of electron mobilities indicated that the mobilities are much lower in inverted heterostructures as compared to regular heterostructures (Drummond et al., 1981b). Despite a wide variety of growth conditions and different designs of inverted heterostructures, the mobilities in such inverted structures are significantly lower than in their regular counterparts (Cho et al., 1988).

The low mobilities obtained in inverted heterostructures have been attributed to the microscopically rough surface morphology of $Al_xGa_{1-x}As$ (see, for example, Alexandre et al., 1985) and to dopant segregation from the doped $Al_xGa_{1-x}As$ into the GaAs channel region. The problem of dopant segregation is illustrated in Fig. 10.10, which shows a GaAs quantum well embedded in two $Al_xGa_{1-x}As$ barriers. The $Al_xGa_{1-x}As$ barriers are δ-doped 400 Å below and above the quantum well interface. The secondary ion mass spectrometry (SIMS) profile of the Si dopants of the quantum well is also shown in Fig. 10.10. The figure illustrates (i) a pronounced Si tail towards the growth surface and (ii) a shift of the Si peak concentration towards the surface.

https://doi.org/10.1017/CBO9780511599828.013 Published online by Cambridge University Press

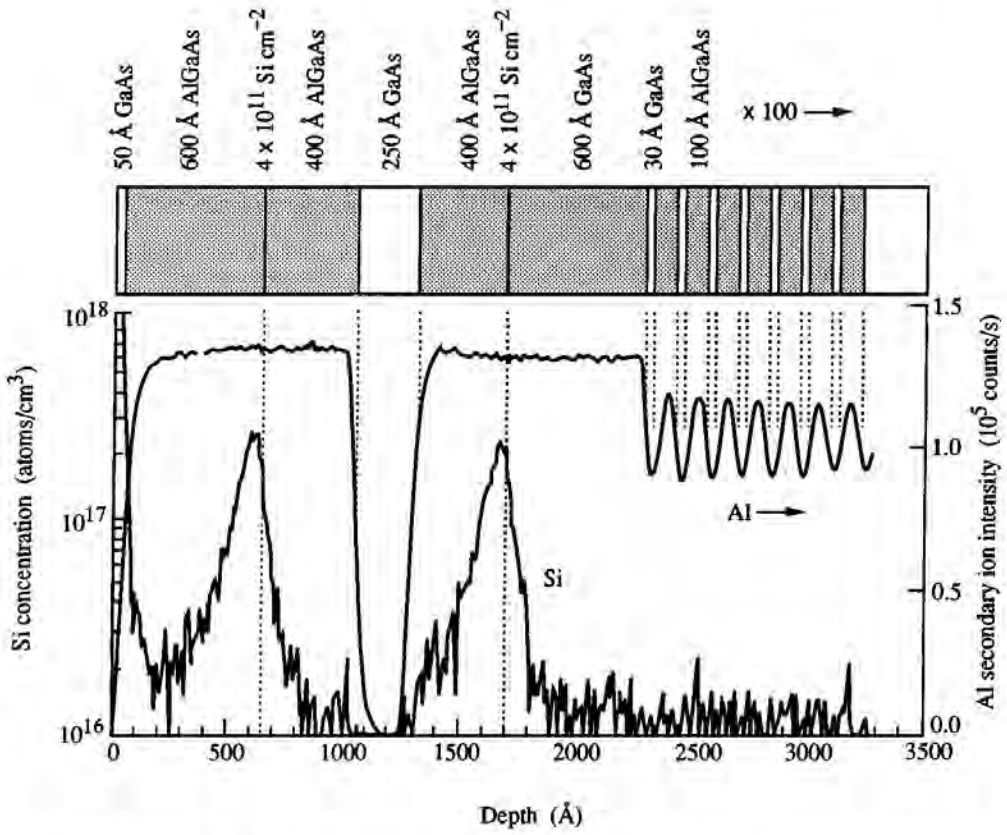


Fig. 10.10. Si and Al secondary ion mass spectrometry (SIMS) profile of an $Al_xGa_{1-x}As/GaAs$ quantum well structure δ-doped on both sides of the GaAs well.

The movement of Si along with the growing surface (see Chap. 8 for further discussion) results in an effectively increased spacer thickness for regular structures and an effectively decreased spacer thickness for inverted structures as compared to the nominal spacer thickness. As a consequence, the densities of the two-dimensional electron gas is expected to be higher for inverted structures as compared to the nominal spacer thickness. The electron concentrations of regular and inverted heterostructures are shown in Fig. 10.11 as a function of the nominal spacer thickness. The inverted heterostructure has a higher electron density as compared to the regular heterostructure for the same nominal spacer thickness (Pfeiffer et al., 1991).

In order to achieve comparable mobilities in inverted heterostructures, a larger spacer thickness must be used in order to compensate for the Si migration towards the surface. The mobilities of regular and inverted $Al_xGa_{1-x}As/GaAs$

https://doi.org/10.1017/CBO9780511599828.013 Published online by Cambridge University Press

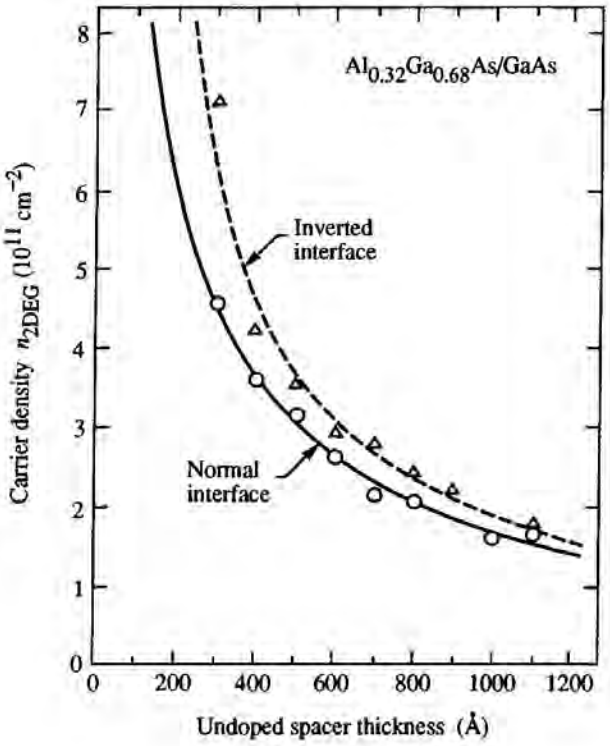


Fig. 10.11. Electron densities measured at 4.2 K after illumination of normal and inverted selectively doped quantum well structures as a function of spacer thickness. Circles and triangles are experimental values. The solid curve is calculated. The dashed curve is a fit to the experimental data obtained by shifting the solid curve to the right by 130 Å.

heterostructures are shown in Fig. 10.12 as a function of the nominal spacer thickness. The electron mobility of the inverted structure reaches its maximum of 2.4×10^6 cm^2/V s at a nominal spacer thickness of 800 Å. The regular heterostructure reaches maximum mobility at a smaller nominal spacer thickness of 700 Å.

The Si migration problem in inverted heterostructures can only be partly solved by the increased spacer thickness. The SIMS profile of Fig. 10.10 also shows an *exponential tail* of the Si concentration towards the semiconductor surface. This tail extends into the undoped GaAs channel region. Any unwanted impurities in the undoped GaAs channel region have a deleterious effect on the electron mobility. Such residual impurities in the GaAs channel region lower the electron mobility in the optimized inverted heterostructure. As a result, the electron mobility in the inverted structure is lower as compared to the regular structure (see Fig. 10.12).

10.3 Doping superlattices

Semiconductor doping superlattices are structures which contain alternately n-type and p-type doped regions. Different from compositional superlattices,

https://doi.org/10.1017/CBO9780511599828.013 Published online by Cambridge University Press

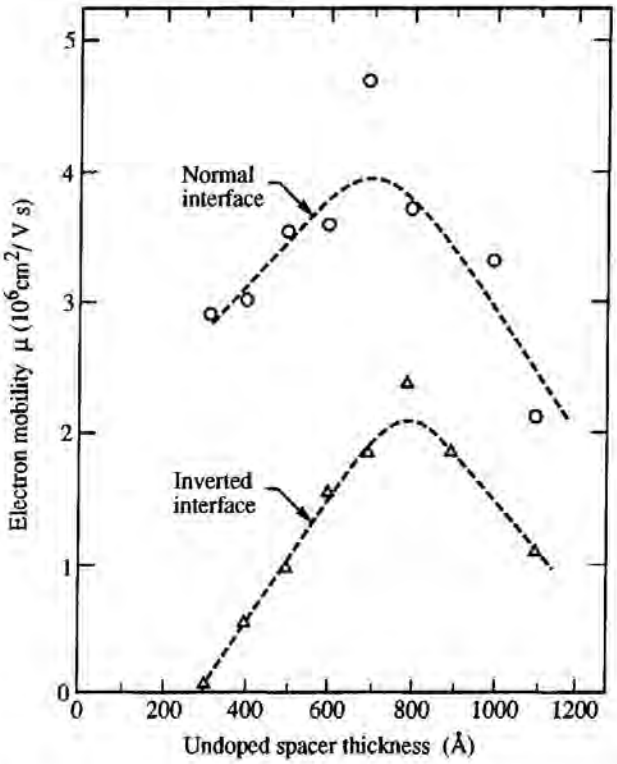


Fig. 10.12. Electron mobilities measured at 4.2 K in the dark after exposure to light for normal and inverted selectively doped quantum well structures whose carrier densities are plotted in Fig. 10.11.

doping superlattices contain only one semiconductor material. They are periodic with typically 10–100 periods. Consider a doping superlattice which has the same doping concentration in the n- and p-type regions. For sufficiently closely spaced doping regions electrons from donors recombine with acceptors; the entire doping superlattice is then depleted of free carriers. The periodic positive and negative charge (due to the ionized donors and acceptors) results in a potential modulation of the conduction and valence band.

The periodic potential, which is called the superlattice potential, gives rise to a number of unique properties not found in any other modulated semiconductor structure. Among the intriguing properties of doping superlattices are (1) a reduced energy gap of the superlattice compared with the (undoped) host semiconductor; (2) an enhanced carrier lifetime for radiative recombination; and (3) the tunability of the superlattice energy gap by the excitation intensity. These

https://doi.org/10.1017/CBO9780511599828.013 Published online by Cambridge University Press

unique properties can be utilized in semiconductor devices such as tunable light-emitting diodes, lasers, and light-intensity modulators.

The general concept of doping superlattices was first proposed by Esaki and Tsu (1970). These authors envisioned two possibilities to periodically modulate the conduction and valence band potential of a semiconductor, namely by (i) alternating n- and p-type doping as well as by (ii) periodically changing the semiconductor materials (compositional superlattice). They predicted novel electronic properties of such superlattices including negative differential conductivity for transport along the superlattice growth direction.

The present section on doping superlattices focuses on δ-doped doping superlattices. Such δ-doped doping superlattices have a higher potential modulation, shorter periods, and reduced potential fluctuations (due to random impurity distribution) as compared to their homogeneously doped counterparts (Schubert et al., 1985, 1988a and 1988b). Furthermore, quantum-confined interband transitions were observed in δ-doped doping superlattices but not in homogeneously doped superlattices.

The doping profile of the doping superlattices discussed here consist of a train of alternating n-type and p-type δ-functions. Such a doping profile is shown in Fig. 10.13(a) along with its mathematical expression. If the period of the superlattice, z_p, is sufficiently small, electrons originating from donors recombine with acceptors. If the donors and acceptors have the same density (and all of them are ionized) there are no excess carriers of extrinsic origin and the superlattice is depleted from free carriers.

The dominant charges in a doping superlattice under thermal equilibrium conditions are impurity charges. The schematic band diagram of a doping superlattice is shown in Fig. 10.13(b) along with the electron and hole wave functions of the superlattice. Also shown is a schematic optical absorption transition from the top heavy-hole subband to the lowest conduction subband. The band diagram of δ-doped doping superlattices has the shape of a sawtooth. Such doping superlattices are therefore also called ***sawtooth superlattices***. Inspection of the transition energy reveals that it is smaller than the fundamental gap energy of the host semiconductor. That is, doping superlattices allow one to *extend the gap of any semiconductor to lower energies*, which is an intriguing feature. For example, a GaAs doping superlattice can be used as a light-detecting or light-emitting device at $\lambda > 0.87$ μm, i.e. below the fundamental gap of the GaAs host lattice.

This suggests that the energy gap of a doping superlattice be defined as the energy between the lowest conduction subband and the highest valence subband. Assuming a degenerate valence band of the host semiconductor at $k = 0$, heavy

https://doi.org/10.1017/CBO9780511599828.013 Published online by Cambridge University Press

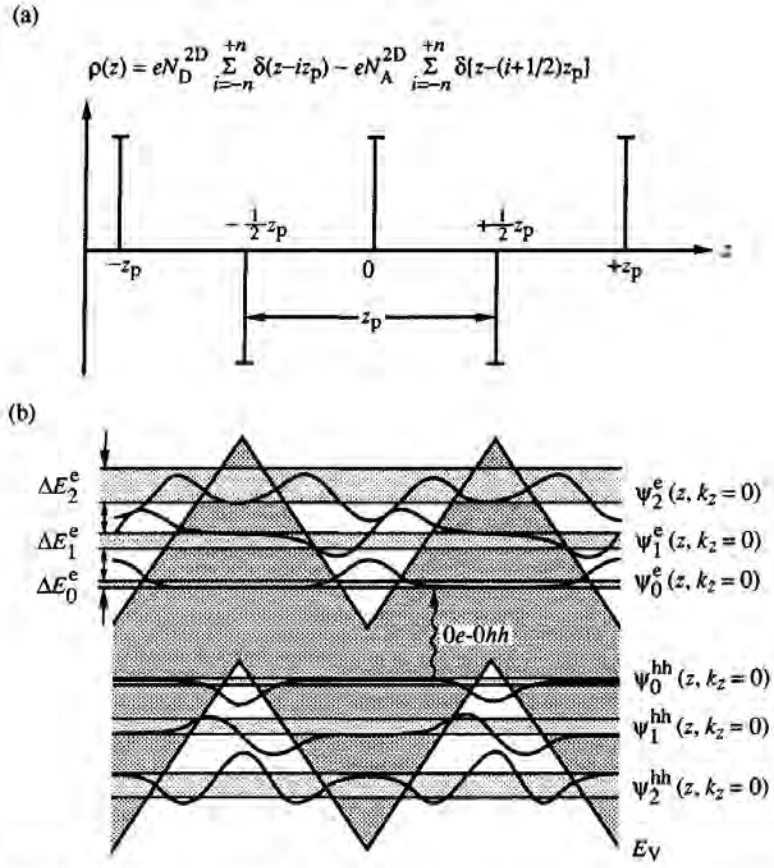


Fig. 10.13. (a) Doping profile of a δ-doped doping superlattice consisting of a train of alternate n-type and p-type δ-functions . (b) Schematic band diagram and wave functions of the δ-doped doping superlattice. The wave functions $\psi_n(z)$ are shown for $k_z = 0$. Minibands have a width of ΔE_n.

as well as light-hole subbands are formed. We define the superlattice energy gap, E_g^{SL}, as

$$E_g^{SL} = E_g - eV_z + E_0^e + E_0^{hh} \tag{10.18a}$$

where the amplitude of the superlattice modulation is given by

$$V_z = \frac{1}{4}\frac{eN^{2D}}{\varepsilon} \tag{10.18b}$$

and N^{2D} is the (donor and acceptor) impurity density. The lowest subband energies for electrons and heavy holes, E_0^e and E_0^{hh}, are given by (Schubert, 1990)

https://doi.org/10.1017/CBO9780511599828.013 Published online by Cambridge University Press

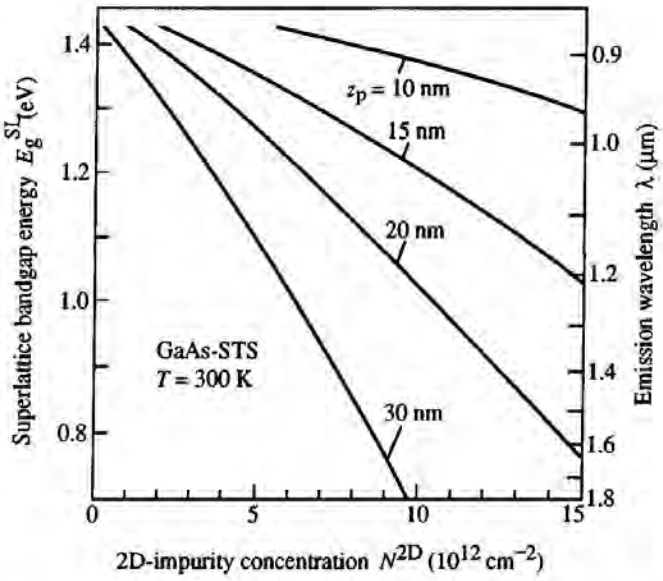


Fig. 10.14. Energy gap and emission wavelength of a sawtooth superlattice as a function of doping densitiy and period. The energy gap has values *smaller* than the gap of the GaAs host lattice.

$$E_0 = \frac{3}{10}\left[\frac{9^2}{2}\right]^{1/3}\left[\frac{e^2\hbar^2\mathcal{E}^2}{2m^*}\right]^{1/3} \tag{10.19}$$

where m^* is the electron or heavy-hole effective mass. The superlattice bandgap energy is shown in Fig. 10.14 for a GaAs doping superlattice. The superlattice band gap decreases with increasing doping concentration and period. That is, doping superlattice have an effective energy gap that is smaller as compared to the host semiconductor.

The concept of generating a periodic potential by means of ionized impurities was proposed by Esaki and Tsu (1970). Novel properties such as negative differential conductivity were postulated in such doping superlattices. Shortly after the initial proposal of doping superlattices, published work was exclusively of a theoretical nature (Romanov, 1972; Romanov and Orlov, 1973; Döhler, 1972a and 1972b). Experimental work started in the 1980s and included the observation of the tunability of the energy gap in doping superlattices (Döhler et al., 1981). Extended reviews on homogeneously doped and δ-doped doping superlattices have become available (Ploog and Döhler, 1983; Döhler, 1986; Schubert, 1990).

https://doi.org/10.1017/CBO9780511599828.013 Published online by Cambridge University Press

337-TA-1366 RX-0255

Quantum-confined interband transitions were readily observed in the compositional $Al_xGa_{1-x}As/GaAs$ superlattices. However, quantum-confined interband transitions were not observed in homogeneously doped superlattices. Doping superlattices which were grown using the δ-doping technique resulted in a dramatic improvement of their optical properties. Quantum-confined optical interband transitions were observed for the first time in absorption spectroscopy (Schubert et al., 1988b) as well as in photoluminescence spectroscopy (Schubert et al., 1989a).

The improved δ-doped doping superlattice structure consists of a train of alternating n-type and p-type δ-doping sheets separated by intrinsic (undoped) layers. A periodic n-i-p-i sequence results, whose band diagram consists of linear sections. The δ-doped superlattice has several important advantages over the homogeneously doped structure including (i) larger superlattice modulation, (ii) the feasibility of shorter periods, and (iii) the minimization of potential fluctuations (Schubert et al., 1988a).

Optical transitions in δ-doped doping superlattices are not governed by the 'conventional' selection rules. The 'conventional' selection rules apply to compositional quantum wells with the quantum states $n = 0, 1, 2, \ldots$ and allow interband transitions (in the absence of electric fields) only if $\Delta n = 0$. For example, an $n = 0$ conduction subband electron can recombine with a $n = 0$ valence subband hole. In doping superlattices, the selection rules are fundamentally different. That is, the optical dipole matrix elements are finite and non-zero for all transitions. The matrix element involves an initial and final state which have an exponentially decaying part and a spatially oscillating part, yielding a finite, non-zero transition probability for all transitions. This property of doping superlattices is in contrast to compositional superlattices where 'conventional' selection rules do apply.

The GaAs doping superlattice epitaxial layers discussed here were grown by gas-source molecular-beam epitaxy on undoped semi-insulating GaAs substrates. The growth temperature was kept below $T = 550$ °C to avoid diffusion of n-type (Si) and p-type (Be) impurities. The design parameters of the superlattice include a period of $z_p = 150$ Å and a two-dimensional doping density of $N_D^{2D} = N_A^{2D} = 1.25 \times 10^{13}$ cm^{-2}. The samples have 10 periods of 20 dopant sheets separated by $\frac{1}{2}z_p = 75$ Å. The samples have a closely balanced impurity concentration, i.e., $N_D^{2D} \cong N_A^{2D}$. Such a balance is essential, because its absence would blue-shift the absorption edge (Burstein–Moss shift). Absorption measurements were performed on polished, 0.25-cm^2 samples using a dual-beam Perkin–Elmer Model 330 spectrophotometer and a variable-temperature cold-finger cryostat.

https://doi.org/10.1017/CBO9780511599828.013 Published online by Cambridge University Press

RX-0255.440

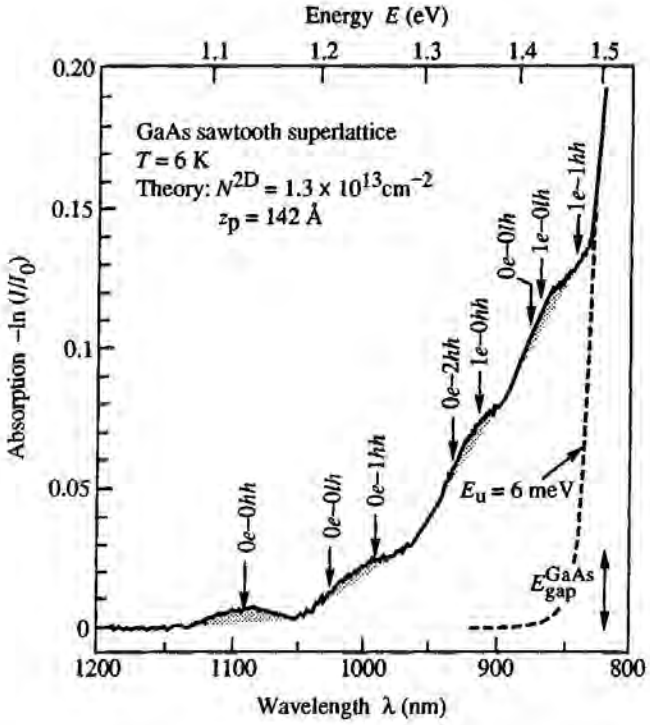


Fig. 10.15. Optical interband absorption spectrum of a GaAs sawtooth superlattice at $T = 6$ K. Theoretical transition energies are indicated by arrows. The lowest electron to lowest heavy hole transition is denoted as 0*e*–0*hh*. The parameters used for the calculation are a period of 142 Å and a dopant concentration of 1.3×10^{13} cm^{-2}. The energy gap of the substrate is marked by a double arrow. The absorption tail of the substrate is characterized by an Urbach-tail energy of $E_U = 6$ meV.

Absorption spectra on GaAs sawtooth doping superlattices measured at $T = 6$ K are shown in Fig. 10.15. The gap energy of the undoped GaAs substrate corresponds to a wavelength of $\lambda = 820$ nm and is shown by a double arrow. The substrate absorbs light at energies slightly below the fundamental gap; this absorption of bulk material is known as the *Urbach tail* (Urbach, 1953). The corresponding Urbach-tail energy is $E_U = 6$ meV for undoped GaAs samples. A typical absorption spectrum of an undoped GaAs sample is shown as a dashed curve in Fig. 10.15.

The absorption spectrum shown in Fig. 10.15 shows strong absorption up to 400 meV below the fundamental gap of the GaAs host lattice. The striking aspect of the absorption spectrum are four distinct features: an absorption maximum (peak) at $\lambda = 1090$ nm and three shoulders at wavelengths of $\lambda = 1000$, 920,

https://doi.org/10.1017/CBO9780511599828.013 Published online by Cambridge University Press

337-TA-1366 RX-0255

and 865 nm. The structure can be attributed to transitions between quantum-confined states in the valence and conduction band. Such quantum-confined interband transitions have not been observed in homogeneously doped doping superlattices. Furthermore, the absorption does not increase monotonically with energy, but has a clear *peak* at $\lambda = 1090$ nm. Unlike the absorption spectrum shown in Fig. 10.15, the joint density of states increases *monotonically* with energy. The occurrence of such an absorption peak indicates excitonic or electron–hole correlation effects.

The formation of excitons necessitates a deeper understanding of the physical properties of doping superlattices. Electron–hole separation naturally hinders the formation of excitons. However, the absorption peak shown in Fig. 10.15 elucidates exciton formation in sawtooth superlattices with appropriate design parameters. Furthermore, excitonic absorption increases the absorption coefficient by several orders of magnitude over nonexcitonic absorption.

Proetto (1990) calculated properties of the ground state exciton in a sawtooth superlattice structure using a variational wave function. He calculated the exciton binding energy as a function of the superlattice period and the dopant density. This calculation revealed that the binding energy is of a similar magnitude (e.g. $E_b = 6$ meV for a period of 100 Å) as compared to bulk GaAs, despite the spatial separation of electrons and holes.

The built-in electric field in the sawtooth superlattice is given by $\mathcal{E} = eN^{2D}/2\varepsilon$ which is equal to $\mathcal{E} \gtrsim 5 \times 10^5$ V/cm. At such high fields, excitonic absorption is not observable in homogeneous semiconductors or square-shaped quantum wells due to a field-induced ionization of excitons. In contrast to homogeneous semiconductors or square-shaped quantum wells, the sawtooth structure, despite the presence of an extremely high field, opposes a field-induced separation of carriers over more than half a superlattice period. Thus, electron–hole correlation effects can be observed even at field strengths exceeding 10^5 V/cm. Excitonic enhancement of the absorption can, however, occur in doping superlattices, only if the spatial electron–hole separation (which is approximately $\frac{1}{2}z_p$ for $n = 0$ states) is smaller than the electron–hole interaction length (excitonic diameter). This condition is indeed satisfied for samples with $\frac{1}{2}z_p = 75$ Å. Excitonic enhancement of the absorption has not been observed in doping superlattices with $z_p >> a_B^*$.

We next compare the experimental absorption data with theoretical transition energies. The arrows shown in Fig. 10.15 are calculated energies of quantum-confined transitions. The lowest electron ($n = 0$) to lowest heavy-hole ($n = 0$) transition is referred to as the $0e$–$0hh$ transition. There is good agreement between calculated quantum-confined transition energies and experimental ones

https://doi.org/10.1017/CBO9780511599828.013 Published online by Cambridge University Press

RX-0255.442

over a wide range of energies. For the calculation, a period of $z_p = 142$ Å and a doping density of $N_D^{2D} = N_A^{2D} = 1.3 \times 10^{13}$ cm^{-2} were used.

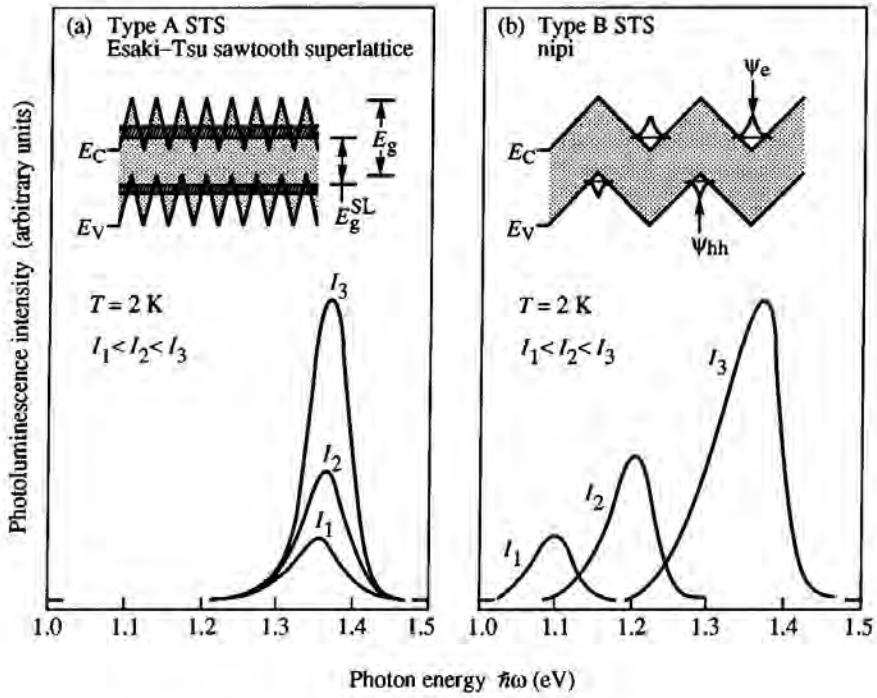


Fig. 10.16. Low-temperature photoluminescence spectra on (a) short-period (Type A) sawtooth superlattices and (b) long-period (Type B) sawtooth superlattices at three different excitation intensities. The emission wavelength is constant for the type A superlattice, whereas it is tunable for the type B superlattice.

The optical properties of doping superlattices strongly depend on the period of the superlattice. Doping superlattices with short and long periods are displayed schematically in the inset of Fig. 10.16(a) and (b), respectively. In short-period (or Type A) sawtooth doping superlattices, the barriers between adjacent quantum wells are thin (e.g. 100 Å) and coupling between adjacent wells becomes significant. Furthermore, the overlap between electron and hole wave function is largest for short-period doping superlattices. Long-period (or Type B) doping superlattices have thick barriers between adjacent quantum wells (e.g. 600 Å) which results in negligible tunneling between adjacent quantum wells. The long period also results in negligible overlap between electron and hole wave functions, i.e. long recombination lifetimes of carriers.

https://doi.org/10.1017/CBO9780511599828.013 Published online by Cambridge University Press

Drastic differences in the optical properties of long-period and short-period doping superlattices were found in low-temperature photoluminescence experiments (Schubert et al., 1987a). The photoluminescence spectra of a short-period and a long-period doping superlattice are shown in Fig. 10.16(a) and (b) respectively. The periods of the superlattices are 150 Å and 600 Å. The doping density is 1×10^{13} cm^{-2} for both types of superlattices. The photoluminescence spectrum shown in Fig. 10.16(a) reveals an emission peak energy at 1.37 eV. Note that the emission energy is smaller than the energy gap of GaAs, which is $E_g = 1.512$ eV at low temperatures. Three different excitation intensities $I_1 < I_2 < I_3$ are used for excitation. The peak energy of the spectra slightly shifts to higher energies with increasing excitation intensity. However, the shift is very small, if compared to the width of the spectra. Thus, an approximately constant peak energy as a function of excitation intensity is found in short-period doping superlattices.

Strong tunability is found in long-period doping superlattices as shown in Fig. 10.16(b). The wavelength is continuously tunable from 1.1 eV to 1.4 eV. The tuning range is larger than the full-width half-maximum of the luminescence line and confirms earlier observations of tunability in doping superlattices (Ploog and Döhler, 1983).

Clearly resolved quantum-confined interband transitions in photoluminescence spectra are shown in Fig. 10.17. The samples have a balanced donor and acceptor density of 1.25×10^{13} cm^{-2} and a period of 150 Å. Three photoluminescence peaks are observed at $\lambda \cong 0.98$, 1.02, and 1.09 μm. Furthermore, a shoulder is observed at the high-energy side of the spectrum at $\lambda \cong 0.95$ μm. The luminescence peaks can be attributed to transitions between quantum-confined conduction and valence band states. The assignment of luminescence peaks is confirmed by calculated transition energies and the comparison with experimentally observed peak energies. A very good fit between experimental and calculated peak energies is obtained by using $N^{2D} = 1.3 \times 10^{13}$ cm^{-2} and $z_p = 142$ Å. Five transitions can be identified, namely due to $0e \rightarrow 0hh$, $0e \rightarrow 0lh$, $0e \rightarrow 1hh$, $0e \rightarrow 2hh$, and $1e \rightarrow 0hh$ transitions.

The photoluminescence spectrum of Fig. 10.17 displays not only the *lowest* transition but also transitions via excited states, e.g., the $0e \rightarrow 1hh$ transition. Furthermore, excited-state transitions (e.g., $0e \rightarrow 0lh$ or $0e \rightarrow 1hh$) are more intense than the ground-state ($0e \rightarrow 0hh$) transition. The light-hole transition is stronger than the heavy-hole transition, even though the density of states of the light-hole subband is much smaller (approximately a factor of $m^*_{hh}/m^*_{lh} \cong 7$). Characteristics of the photoluminescence spectrum can be consistently explained

https://doi.org/10.1017/CBO9780511599828.013 Published online by Cambridge University Press

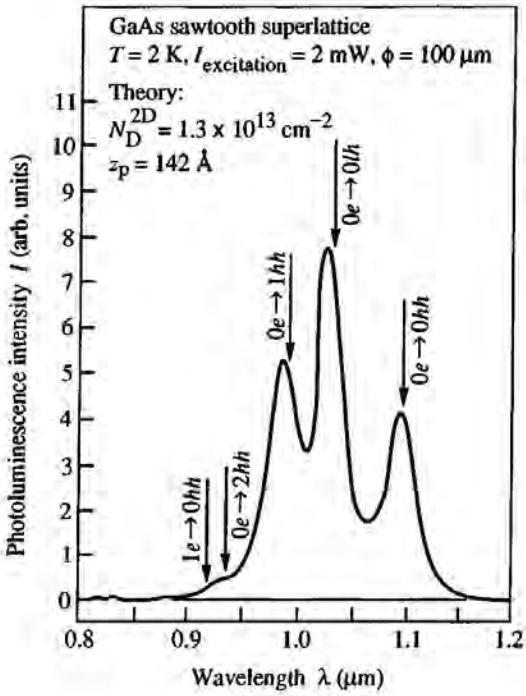


Fig. 10.17. Low-temperature photoluminescence spectrum of a sawtooth doping superlattice. The arrows indicate theoretical transition energies calculated for a superlattice period of $z_p = 142$ Å and a doping density of $N_D^{2D} = N_A^{2D} = 1.3 \times 10^{13}$ cm^{-2}.

in terms of the unique energy dependence of the oscillator strength of the sawtooth structure (Schubert et al., 1989a).

The photoluminescence line shape in semiconductors and semiconductor quantum-well structures can usually be determined by the product of the joined density of states and the thermal distribution of carriers. The latter is frequently modeled in terms of a Boltzmann distribution and a carrier temperature. The carrier temperature depends on the photoluminescence excitation intensity and is typically in the range $10 \leq T_C \leq 50$ K at a lattice temperature of $T_1 = 2$ K. The transition-matrix element depends weakly on energy in homogeneous semiconductors or compositional semiconductor quantum wells. In contrast, the oscillator strength increases exponentially with energy in the sawtooth superlattice. Thus, the oscillator strength has an opposite dependence on energy, as compared to the thermal distribution. Consequently, transitions from excited states can be observed in the sawtooth structure, even though they are sparsely populated.

10.4 Impurities in quantum wells and quantum barriers

Impurities located in *quantum wells* have different characteristics as compared to impurities in the bulk. The change in impurity characteristics is due to the

https://doi.org/10.1017/CBO9780511599828.013 Published online by Cambridge University Press

quantum well potential which confines the electron (hole) in addition to the Coulomb potential of the shallow impurity. The effect of the quantum well potential is significant, if the quantum well width is on the order of or smaller than the Bohr radius of the impurity. The change in impurity characteristics include the impurity wave function and the impurity binding energy. In this section, the properties of shallow impurities located in quantum wells are discussed. More recently, structures with impurities located in *quantum barriers* have been demonstrated and these are also included here.

Electrons and holes are bound to hydrogenic impurities by means of the attractive Coulomb potential given by

$$V(r) = \frac{e}{4\pi\varepsilon r} \tag{10.20}$$

where the spherical coordinate r is the distance from the impurity. The wave function of the bound states of the Coulomb potential can be obtained from the Schrödinger equation. In bulk semiconductors, shallow hydrogenic impurities can be adequately described within the effective-mass approximation (see Chap. 1). The effective-mass Hamiltonian operator of a coulombic potential is given by

$$H = -\frac{\hbar^2}{2m^*}\nabla^2 - \frac{e^2}{4\pi\varepsilon r}. \tag{10.21a}$$

If the band structure is isotropic and non-degenerate and if the dispersion relation is parabolic, then the Schrödinger equation reduces to the hydrogen problem. In spherical coordinates it is given by (Kohn, 1957)

$$\left(\frac{p^2}{2m^*} - \frac{e^2}{4\pi\varepsilon r}\right)\psi(r) = E\psi(r) \tag{10.21b}$$

where p is the particle momentum, m^* is the carrier effective mass, and ε is the permittivity of the material. The solution of the equation with the lowest energy, i.e. the 1s hydrogenic wave function is given by

$$\psi_{1s}(r) = \frac{1}{\sqrt{\pi a_B^{*3}}}\exp(-r/a_B^*) \tag{10.22}$$

where a_B^* is the effective Bohr radius

$$a_B^* = \frac{4\pi\varepsilon\hbar^2}{m^* e^2} = 0.529\text{Å}\,\frac{\varepsilon}{\varepsilon_0}\,\frac{m_0}{m^*} \tag{10.23}$$

in which 0.529 Å is the hydrogen atom Bohr radius. For GaAs, the effective

https://doi.org/10.1017/CBO9780511599828.013 Published online by Cambridge University Press

Bohr radius for donors is $a_B^* = 103$ Å. The binding energy of the lowest state is given by

$$E_{Ryd} = \frac{m^* e^4}{32\pi^2 \varepsilon^2 \hbar^2} = 13.6 \text{ eV} \frac{\varepsilon_0^2}{\varepsilon^2} \frac{m^*}{m_0} \tag{10.24}$$

where 13.6 eV is the Rydberg energy. For GaAs, the effective Rydberg energy is $E_{Ryd} = 5.31$ meV.

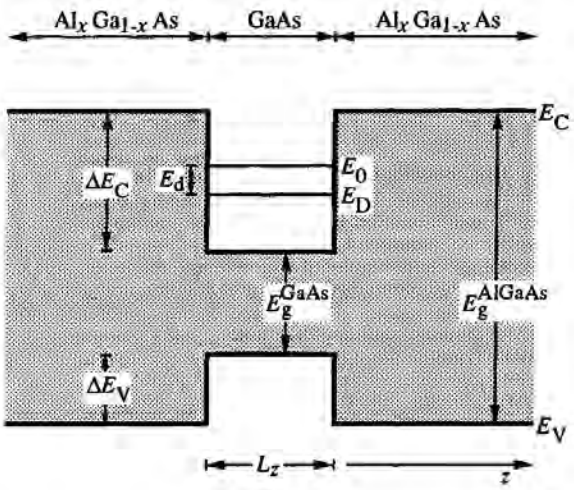


Fig. 10.18. Schematic band diagram of an $Al_xGa_{1-x}As/GaAs$ quantum well structure. A donor level (E_D) and the lowest subband level (E_0) are separated by the donor ionization energy (E_d).

Impurity characteristics change if the impurity is located in a quantum well. Furthermore, since quantum well structures lack translational invariance the binding energy and the wave function depend on the position of the impurity in the well. A schematic energy level scheme of a quantum well with a donor impurity is shown in Fig. 10.18. The energy of the lowest state in the well is denoted by E_0. An impurity provides an additional confining potential. As a consequence, the donor energy is *below* the lowest conduction subband. The donor ionization energy, E_d, is defined as the difference between the lowest conduction subband energy and the donor energy in analogy to bulk impurities. The evolution of the impurity wave function with quantum well thickness was discussed by Bastard (1981) and is schematically shown in Fig. 10.19 for different well widths and different impurity positions in the well. For thick wells ($L_z >> a_B$) the Coulomb potential is the dominant confining potential. In this

https://doi.org/10.1017/CBO9780511599828.013 Published online by Cambridge University Press

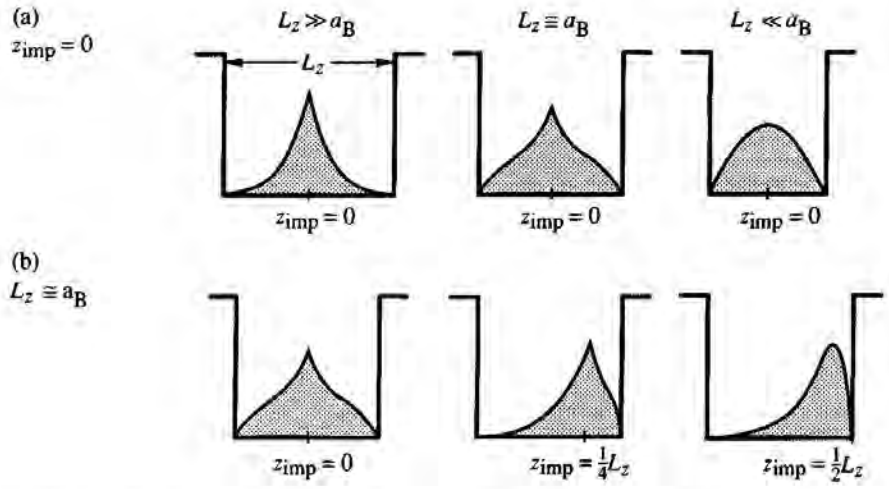


Fig. 10.19. Schematic illustration of the wave function of an electron bound to a hydrogenic impurity for (a) different quantum well width and (b) different positions of the impurity in the quantum well.

case, the impurity wave function is similar to the impurity wave function in the bulk. For thin wells ($L_z << a_B$), the quantum well potential is the dominant confining potential. In this case, the impurity wave function is similar to the free quantum-confined state. Figure 10.19 also reveals that the impurity wave function (and therefore also its energy) depends on the impurity position.

In order to calculate the energy and the wave function of the impurity in a quantum well, the quantum well potential must be included in the Hamiltonian operator. The Hamiltonian of Eq. (10.21a) needs to be modified according to

$$H = -\frac{\hbar^2}{2m^*}\nabla^2 - \frac{e^2}{4\pi\varepsilon r} + eV(z) \qquad (10.25a)$$

where

$$eV(z) = \begin{cases} 0 & \text{for } z \text{ in the well} \\ \Delta E_c & \text{for } z \text{ in the barrier} . \end{cases}$$

Note that both m^* and ε can in principle be different in the well and the barrier material. For an isotropic and parabolic band, the Hamiltonian can be written as

https://doi.org/10.1017/CBO9780511599828.013 Published online by Cambridge University Press

$$H = \frac{p_x^2 + p_y^2}{2m^*} + \frac{p_z^2}{2m^*} - \frac{e^2}{4\pi\varepsilon\sqrt{x^2 + y^2 + (z - z_{\text{imp}})^2}} + eV(z) \tag{10.25b}$$

where x and y are the in-plane coordinates and z is the coordinate normal on the quantum well plane.

An approximate solution of the hydrogenic impurity in a quantum well with a thickness L_z was given by Bastard (1981). The author employed a variational method to solve Schrödinger's equation and used the envelope trial function

$$\psi(x,y,z) = A\cos(kz)\exp[(1/\lambda)\sqrt{x^2+y^2+(z-z_{\text{imp}})^2}] \tag{10.26}$$

where A is a normalization constant, λ is the trial parameter, and $k = \pi/L_z$. The wave function vanishes at the boundaries of the well, i.e. tunneling into the barriers is neglected. Thus, the trial function of Eq. (10.26) is strictly valid only for a quantum well with infinitely high barriers.

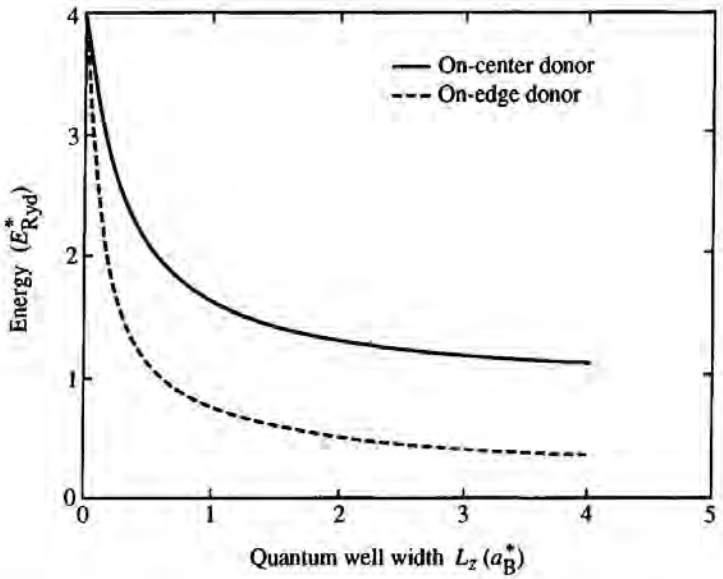


Fig. 10.20. Binding energy for a hydrogenic impurity located at the center or edge of a quantum well as a function of the quantum well thickness. For GaAs, the energy and length units are $E^*_{\text{Ryd}} = 5.31$ meV and $a^*_{\text{B}} = 103$ Å, respectively (after Bastard, 1981).

The energy obtained from the trial function is the energy of the donor ground state relative to the bottom of the quantum well which was defined as $E = 0$. It is instructive to measure the donor ground-state energy relative to the lowest

https://doi.org/10.1017/CBO9780511599828.013 Published online by Cambridge University Press

conduction subband. This energy can be obtained by using the same trial function (Eq. (10.26)) but by omitting the Coulomb term in the Hamiltonian operator (Eq. (10.25)) (Masselink et al., 1986). The calculated donor ground-state energy relative to the lowest conduction subband is shown in Fig. 10.20 for donors in the center (solid line) and at the edge (dashed line) of the quantum well (Bastard, 1981). The donor ionization energy equals E_{Ryd} in the bulk limit ($L_z >> a_{\mathrm{B}}$). With decreasing quantum well thickness, the donor binding energy increases. The increase is due to the fact that the wave function is further localized at the site of the donor atom where the electron experiences a lower potential energy. For infinitely small quantum well thicknesses, the problem reduces to the two-dimensional hydrogen atom. The donor binding energy is then $E_{\mathrm{d}}^{\mathrm{2D}} = 4\ E_{\mathrm{Ryd}}$. The Bohr radius of the two-dimensional hydrogen atom equals $a_{\mathrm{B}}^{\mathrm{2D}} = \frac{1}{2}\ a_{\mathrm{B}}$ (Bastard et al., 1982). Donors located on the edge of the quantum well have a smaller binding energy except for the two-dimensional limit $L_z \rightarrow 0$. The overlap of the electron wave function (Eq. (10.26)) with the on-edge donor is smaller, which results in a smaller binding energy as shown in Fig. 10.20.

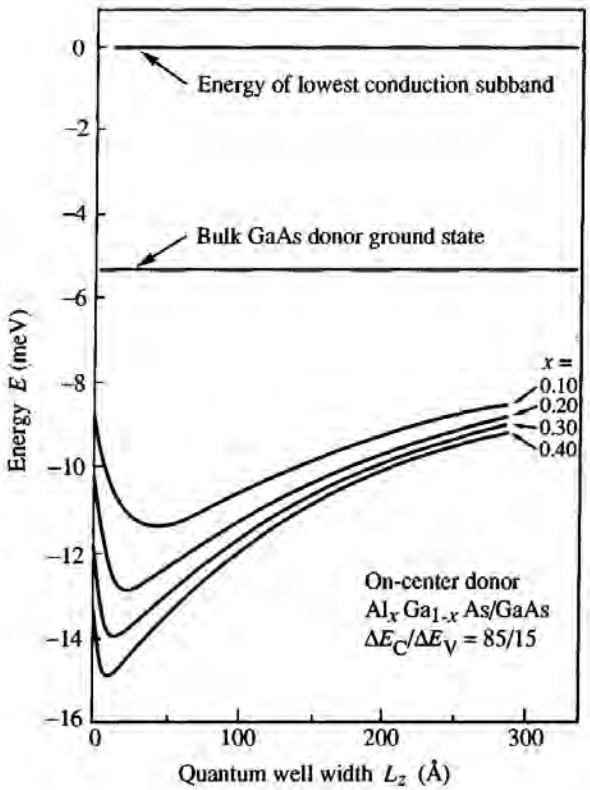


Fig. 10.21. Calculated donor binding energy in $Al_xGa_{1-x}As/GaAs$ quantum wells as a function of well widths (after Mailhiot et al., 1982b).

https://doi.org/10.1017/CBO9780511599828.013 Published online by Cambridge University Press

The simple model of Bastard (1981) has been subsequently refined by Mailhiot et al. (1982a and b) and by Greene and Bajaj (1983). The authors took into account (i) the finite barrier height of an $Al_xGa_{1-x}As/GaAs$ quantum well, (ii) the different effective mass in $Al_xGa_{1-x}As$ and GaAs, and (iii) the different dielectric constant of the two materials. The calculated on-center donor energy relative to the edge of the lowest conduction subband is shown in Fig. 10.21 (Mailhiot et al., 1982b). The donor binding energy increases with decreasing quantum well thickness, reaches a maximum at a small well thickness and finally decreases again for very small quantum well thicknesses. In the two limits, $L_z \to \infty$ and $L_z \to 0$, the donor binding energy is given by the GaAs and $Al_xGa_{1-x}As$ donor binding energy, respectively. In the intermediate range ($0 < L_z < a_B$) the binding energy reaches a maximum because the impurity wave function is compressed at the location of the donor atom by the quantum well potential. The localization of the wave function at the location of the impurity atom results in an increase of the donor binding energy.

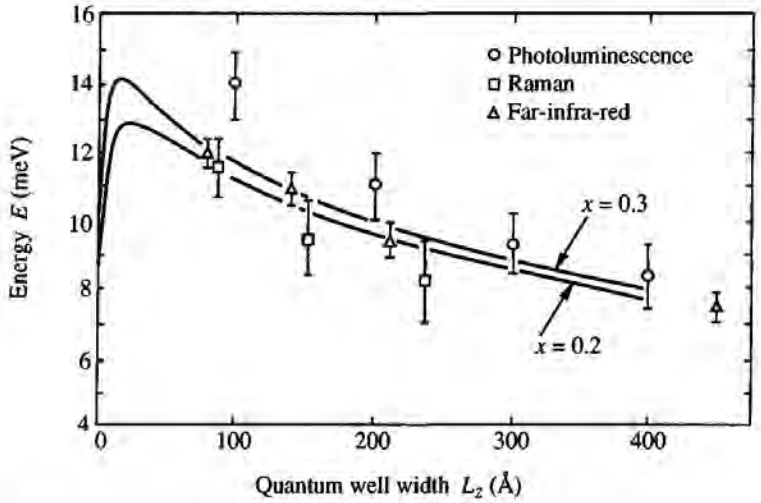


Fig. 10.22. Calculated binding energies for hydrogenic donors in $Al_xGa_{1-x}As/GaAs$ quantum wells for two different Al mole fractions along with experimental data obtained through photoluminescence, Raman, and far-infra-red absorption measurements (after Masselink et al., 1986).

A comparison between calculated and measured donor binding energies in $Al_xGa_{1-x}As/GaAs$ quantum wells is shown in Fig. 10.22 (Masselink et al., 1986). The experimental data were obtained from photoluminescence, Raman, and far-infra-red spectroscopy. The calculated donor binding energies agree with

https://doi.org/10.1017/CBO9780511599828.013 Published online by Cambridge University Press

nearly all measured data within the experimental error. A comparison of experimental and calculated donor and acceptor binding energies was also made by Greene and Bajaj (1985b). The authors found only minor discrepancies between theory and experiment.

The effect of a non-parabolic dispersion relation in the conduction band on hydrogenic donors in quantum wells has been investigated by Chandhuri and Bajaj (1984). The effect of non-parabolicity was included by using an energy-dependent effective mass obtained from the $\vec{k}\cdot\vec{p}$ approximation. The authors found a small increase in donor binding energies upon inclusion of non-parabolicity. The increase was observed for all values of L_z. Excited states of hydrogenic impurity centers and the effect of magnetic fields were analyzed by Greene and Bajaj (1985a, 1988). The authors used a variational approach in which the trial wave functions were expanded in terms of gaussian basis sets. The hydrogenic binding energies were found to increase with magnetic field.

The characteristics of ***acceptors in quantum wells*** have been studied in detail by Masselink et al. (1983, 1984, 1985, 1986). Acceptor binding energies were calculated in a multiband effective-mass approximation. The valence band structure of GaAs and other III–V semiconductors is more complicated as compared to the isotropic, non-degenerate conduction band structure. It is well known that the valence band structure consists of the degenerate heavy- and light-hole bands and the split-off band. The kinetic energy term of the Hamiltonian is not a scalar as for donors, but a matrix because of the multiple valence bands. To obtain the acceptor energy, a trial function of the appropriate symmetry must be constructed. The trial function typically contains a large number of variational parameters. The ground-state energy is then calculated using the variational method, i.e. minimizing the energy with respect to all variational parameters. The resulting energy is taken as a good approximation to the true ground state energy. Finally, the binding energy is determined by subtracting the acceptor ground-state energy from the lowest valence subband edge. The latter energy can be calculated as described above, but without the Coulomb term in the Hamiltonian. The acceptor binding energies depend on the quantum well width in the same qualitative way as the donor binding energies. The acceptor binding energy increases with decreasing quantum well thickness, reaches a maximum at small L_z, and finally decreases for very small L_z. This dependence is qualitatively the same as displayed by donors (see Fig. 10.21 and 10.22). The acceptor binding energy was also investigated in the presence of an external magnetic field (Masselink et al., 1985). Different central cell potentials were employed for chemically different acceptors. The calculated acceptor energies were found to agree well with experimental acceptor binding energies.

https://doi.org/10.1017/CBO9780511599828.013 Published online by Cambridge University Press

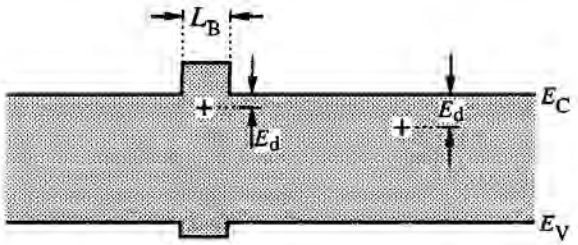


Fig. 10.23. Energy band diagram with donor levels (i) in a quantum barrier and (ii) in the bulk. The donor level in the quantum barrier has a smaller activation energy compared to the donor in the bulk.

Impurities in quantum barriers have different characteristics as compared to impurities in the bulk (Tsang et al., 1992). Consider a semiconductor heterostructure of Type I consisting of a thick well material and a very thin barrier material as shown in Fig. 10.23. Assume further that the heterostructure can be selectively doped either in the thin barriers or in the well. Impurities in the well will have bulk-type properties if the thickness of the well is much larger than the effective Bohr radius of the impurity. However, the characteristics of impurities in the barrier can be significantly changed by the barrier potential. To illustrate the effect of the quantum barrier, we consider hydrogenic donors in a quantum barrier as shown in Fig. 10.23. In addition to the *attractive* Coulomb potential, the *repulsive* barrier potential must be taken into account. For sufficiently thin and sufficiently low barriers, the attractive Coulomb potential dominates. In this case, the barrier thickness is much smaller than the effective Bohr radius of the donor, i.e. $L_B << a_B^*$. Hence, donor impurities in the quantum barrier have a bound state. However, the effective activation energy and the impurity wave function will be different as compared to the bulk value. We define the 'effective activation energy' of the donor to be the difference between the lowest continuum state of the semiconductor and the ground-state energy of the donor, as schematically shown in Fig. 10.23. For thin barriers, the effective donor activation energy is expected to be reduced as compared to the activation energy in the bulk. For sufficiently thick and high barriers, the impurity state is shifted above the continuum edge of the well, which corresponds to a *negative* effective activation energy of the impurity. The impurity will then be ionized at all temperatures. The case of negative effective activation energy is reminiscent of selectively doped heterostructures, in which no freeze-out effects are observed even at the lowest temperatures.

https://doi.org/10.1017/CBO9780511599828.013 Published online by Cambridge University Press

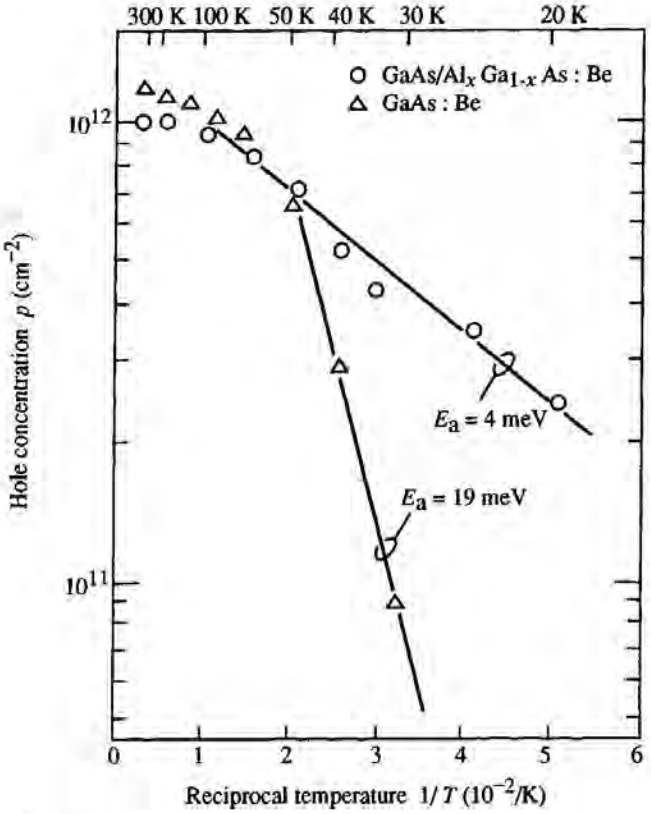


Fig. 10.24. Hole concentration versus reciprocal temperature for a Be-doped $Al_xGa_{1-x}As/GaAs$ quantum barrier structure and homogeneously Be-doped GaAs. The activation energy of Be acceptors in the doped quantum barrier structure is significantly lower as compared to homogeneously doped GaAs (after Tsang et al., 1992).

Experimental results on doping of quantum barriers were reported by Tsang et al. (1992) for Be doping of $Al_xGa_{1-x}As/GaAs$ heterostructures. The authors showed that the activation energy of impurities can be 'engineered' by appropriate parameters of the quantum barrier. The Hall carrier concentration of the Be-doped heterostructure is shown in Fig. 10.24 as a function of reciprocal temperature for doping in the wide GaAs wells (triangles) and for doping of the thin $Al_xGa_{1-x}As$ barriers (circles). The slope of the carrier concentration versus reciprocal temperature was used to deduce the effective activation energy of the Be impurities using the proportionality $p \propto \exp(-E_a/kT)$. Activation energies of 4 and 19 meV were inferred for doping of the barriers and for doping of the

https://doi.org/10.1017/CBO9780511599828.013 Published online by Cambridge University Press

wells, respectively. The activation energy of 19 meV obtained for doping of the well is close to the expected value for Be-doped bulk GaAs. The much lower activation energy of 4 meV obtained for doping of the barrier demonstrates that the activation energy of impurities can be strongly reduced by quantum-barrier doping. The thickness of the $Al_{0.30}Ga_{0.70}As$ barriers and GaAs wells used for the experiments are 15 Å and 210 Å, respectively. The two-dimensional Be density in the barriers is 2×10^{10} cm^{-2}. Thus, the average Be-to-Be impurity spacing is much larger than the critical spacing required for the Mott transition.

https://doi.org/10.1017/CBO9780511599828.013 Published online by Cambridge University Press

11

Delta doping

Epitaxially grown semiconductors can be doped by incorporating impurities during growth. During molecular-beam epitaxy (MBE) and during organometallic vapor-phase epitaxy (OMVPE) the doping process is continuous and the growth processes are not influenced by the doping process. During delta doping the doping process is fundamentally different. In the first step of the doping process, epitaxial growth is suspended. In the second step, doping impurities are deposited on the non-growing semiconductor surface. In the third step, regular crystal growth is resumed.

This doping procedure results in very narrow doping distributions, typically one or a few monolayers wide. Such narrow doping distributions can be considered as δ-function-like. The doping profile can then be written as

$$N(z) = N^{2D}\,\delta(z - z_D) \tag{11.1}$$

where N^{2D} is the two-dimensional doping density per cm^2. Impurities are confined to the plane $z = z_D$ of a cartesian coordinate system. The first report of such a growth-interrupted dopant deposition is due to Bass (1979), who found that a strong surface adsorption of Si to the non-growing GaAs surface results in sharp doping spikes. The widths of the doping spikes were not explicitly mentioned in the publication. However, a doping profile shown in the publication reveals a width of approximately 250 Å. Adsorption of dopants to the non-growing crystal surface may also be the origin of high dopant concentrations of the substrate–epilayer interface found earlier by Di Lorenzo (1971). The versatility of growth-interrupted doping was realized by Wood et al. (1980), who

https://doi.org/10.1017/CBO9780511599828.014 Published online by Cambridge University Press

mentioned that complex doping profiles can be achieved by 'atomic-plane' or δ-doping. The authors further found that Ge doping of GaAs leads to reduced autocompensation. However, the publication does not investigate possible diffusion of dopants from the atomic plane. Clear indications of such diffusion in δ-doped semiconductors were first found by Lee et al. (1985). They concluded that diffusion over 126 Å occurred during crystal growth. It was not until 1988 that Schubert et al. (1988a) showed that highly confined Si doping profiles in GaAs can be achieved at growth temperatures ≤ 550 °C. Si dopants were spatially confined to a layer whose thickness was found to be comparable to the lattice constant. Diffusion over more than two lattice constants was excluded. This chapter summarizes the structural, electronic, and optical properties of δ-doped III–V semiconductors. In addition, device applications of δ-doped semiconductors and the advantages of such applications are discussed.

11.1 Electronic structure

Impurities are confined to one atomic monolayer in δ-doped semiconductors grown under idealized conditions which include the absence of diffusion and other redistribution effects as well as the availability of atomically flat crystal growth. Such an idealized δ-doped III–V semiconductor is shown in Fig. 11.1. Impurities occupy group-III (cation) sites and are located in an atomic plane of the semiconductor. Certainly, such doping distributions are idealized and we refer to Sect. 12.2 for the experimental assessment of spatial impurity distributions in δ-doped semiconductors.

The doping distribution shown in Fig. 11.1 results in a one-dimensional, V-shaped electrostatic potential. To illustrate the V-shaped potential, we consider a sheet of donors with density N_D^{2D} located in the xy-plane at $z = z_D$. The electric field and the potential of a δ-function-like dopant distribution are obtained by integration of Poisson's equation

$$\frac{d^2\phi}{dz^2} = -\frac{d\mathcal{E}}{dz} = -\frac{eN_D(z)}{\varepsilon} \tag{11.2}$$

where e is the elementary charge and $\varepsilon = \varepsilon_r\varepsilon_0$ is the permittivity of the semiconductor. The electric field is obtained by integration as

$$\mathcal{E}(z) = \begin{cases} -\frac{1}{2}\frac{eN_D^{2D}}{\varepsilon} & \text{for } z < z_D \\ +\frac{1}{2}\frac{eN_D^{2D}}{\varepsilon} & \text{for } z > z_D \end{cases} \tag{11.3a}$$

https://doi.org/10.1017/CBO9780511599828.014 Published online by Cambridge University Press

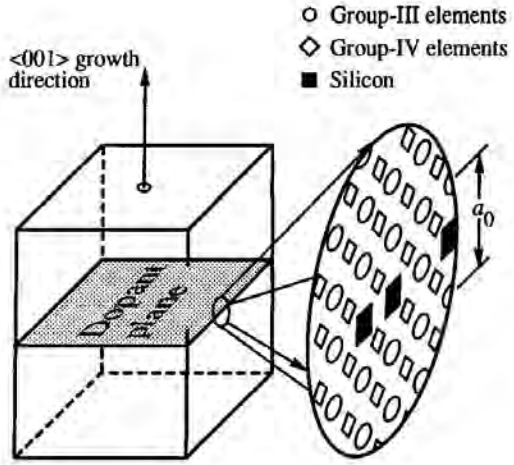


Fig. 11.1. Schematic illustration of a semiconductor grown in the <001> direction containing Si impurities in a group-III plane of a zincblende structure.

or

$$\mathcal{E}(z) = -\frac{1}{2}\frac{eN_D^{2D}}{\varepsilon} + \frac{eN_D^{2D}}{\varepsilon}\,\sigma(z - z_D) \quad \text{for all } z \tag{11.3b}$$

where $\sigma(z - z_D)$ is the step-function. The integration constant required for the solution of Eq. (11.2) is chosen to obtain a symmetric field, i.e. $|\mathcal{E}(z < z_D)| = |\mathcal{E}(z > z_D)|$, as shown in Fig. 11.2. The second integration of Poisson's equation yields the potential

$$\phi(z) = \begin{cases} -\dfrac{eN_D^{2D}}{2\varepsilon}(z - z_D) & \text{for } z < z_D \\ \dfrac{eN_D^{2D}}{2\varepsilon}(z - z_D) & \text{for } z > z_D \end{cases} \tag{11.4a}$$

or

$$\phi(z) = -\frac{eN_D^{2D}}{2\varepsilon}(z - z_D) + \frac{eN_D^{2D}}{\varepsilon}(z - z_D)\,\sigma(z - z_D) \quad \text{for all } z\,. \tag{11.4b}$$

The potential well given by this equation is V-shaped and is illustrated in Fig. 11.2. (Equation (11.4) is actually the negative potential, i.e. the potential for electrons).

It is worthwhile noting that the singularity of the δ-function is physically

https://doi.org/10.1017/CBO9780511599828.014 Published online by Cambridge University Press

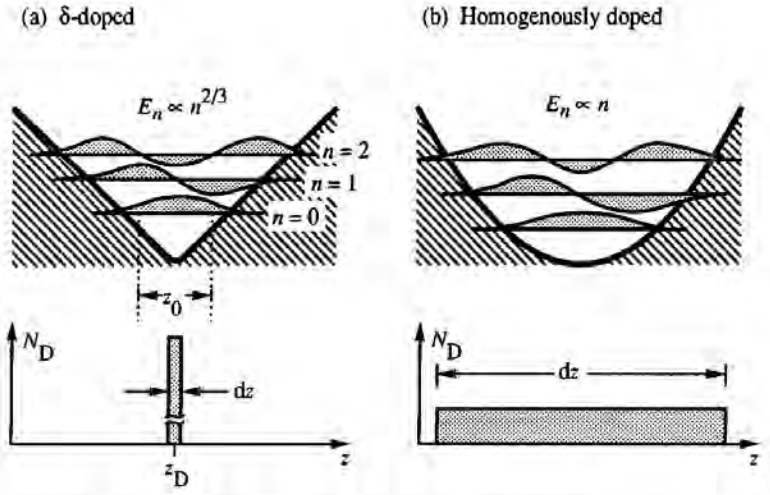


Fig. 11.2. Comparison of a δ-doped and a homogeneously doped potential well. The subband energies are proportional to $n^{2/3}$ and to n for the δ-doped and the homogeneously doped well, respectively.

problematic: According to Eq. (11.1), N_D approaches infinity for $z \to z_D$. Of course, the doping density cannot exceed the host lattice site concentration (e.g. 2.2139×10^{22} cation sites per cm^3 in GaAs) in a real semiconductor. It is useful, however, to recall that mostly the *integral* properties of the doping distribution are relevant. For example, the potential and the electric field are (according to Poisson's equation) *integral* properties of the δ-function. Therefore, the singularity of the δ-function does not represent a problem.

The V-shaped potential of Eq. (11.4) is a result of the impurity charges. In addition to the impurity charges, the charges of free carriers must be taken into account. In the following, we first consider impurity charges only. Free carrier charges can be neglected, if the δ-doped semiconductor is depleted of free carriers, e.g. in the case of doping superlattices (see Sect. 10.3). Subsequently, undepleted δ-doped semiconductors will be considered.

The slopes of the V-shaped potential well, caused by a sheet of charged impurities, depend on the doping concentration. The slopes of the V-shaped potential well (i.e. the electric field) are $> 10^4$ V/cm for typical doping densities. The spatial width of the potential then becomes comparable to the de Broglie wavelengths of carriers. Size quantization (Schrieffer, 1957) occurs and quantum effects must be taken into account via the Schrödinger equation. The V-shaped potential well can then be termed a *quantum* well.

https://doi.org/10.1017/CBO9780511599828.014 Published online by Cambridge University Press

Innoscience1366-00139132

The V-shaped quantum well problem can be solved (i) exactly and analytically using Airy functions, (ii) using the variational method, (iii) the WKB method, and (iv) in a zero-under approximation. These methods were reviewed by Schubert (1990a). All of the methods provide very similar results. The variational method, which will be discussed below, provides excellent trade-off between simplicity and accuracy for the solutions of the V-shaped well problem.

11.1.1 Variational solutions of the V-shaped well

The variational method is a simple approach to obtain the wave functions and eigenstate energies of a one-dimensional quantum well problem. The accuracy of the eigenstate energies and the wave functions certainly depends on the quality of the trial function but is usually very good. The usefulness of the variational approach for quantum wells was first demonstrated for the triangular well of a Si/SiO_2 inversion layer (Fang and Howard, 1966).

The calculation of the eigenstate energies and wave functions of the V-shaped quantum well can be conveniently carried out in the effective-mass approximation. The one-dimensional V-shaped potential well problem then leads to text-book type Hamiltonian operators. Using the product method, the wave function in such a one-dimensional quantum well potential can be written as

$$\boxed{\psi^{c,v}_{n,k_x,k_y}(x,y,z) = e^{ik_x x}\, e^{ik_y y}\, \psi^{c,v}_n(z)\, u^{c,v}(x,y,z)} \tag{11.5}$$

where $u^{c,v}(x,y,z)$ is the periodic Bloch-type eigenfunction close to the zone center of the conduction (c) or valence (v) band (where the effective-mass approximation is valid). The terms $e^{ik_x x}$ and $e^{ik_y y}$ indicate the free movement of carriers in the x- and y-direction. The following calculations are restricted to conduction-band type Bloch-functions, $u^c(x,y,z)$, and to those of the valence band, $u^v(x,y,z)$. The function $\psi^{c,v}_n(z)$ is the eigenfunction of the nth bound state of the Hamiltonian

$$H = -\frac{\hbar^2}{2m^*}\frac{\partial^2}{\partial z^2} + eV(z) \tag{11.6}$$

where $V(z)$ is the potential of either the conduction or the valence band edge. The function $\psi^{c,v}_n(z)$ is varying slowly on the length scale of the lattice constant ($a_0 \cong 5$ Å), while the Bloch function is periodic in the lattice constant. Therefore, $\psi^{c,v}_n(z)$ is called the envelope function. The following calculation will be carried out within the framework of the envelope-function approximation (Bastard, 1981). For simplicity we consider one band only and omit the superscripts, c,v.

https://doi.org/10.1017/CBO9780511599828.014 Published online by Cambridge University Press

The following trial-function for the ground state is of even symmetry (see Fig. 11.2), and is exponentially decaying for large absolute values of z.

$$\psi_0(z) = \begin{cases} A_0(1 + \alpha_0 z)\mathrm{e}^{-\alpha_0 z} & (z \geq 0) \\ A_0(1 - \alpha_0 z)\,\mathrm{e}^{\alpha_0 z} & (z<0)\,. \end{cases} \tag{11.7}$$

The constant A_0 is determined by the normalization condition $\langle\psi|\psi\rangle = 1$ to be $A_0^2 = 2\alpha_0/5$. The trial-parameter α_0 determines the exponential decay of the wave function in the classically forbidden region, i.e. beyond the classical turning points. The expectation value of the ground-state energy is given by

$$\langle E_0\rangle = \langle\psi|H|\psi\rangle = \frac{1}{5}\left[\frac{\hbar^2}{2m^*}\alpha_0^2 + \frac{9}{2}\frac{e\mathcal{E}}{\alpha_0}\right]. \tag{11.8}$$

Minimization of $\langle E_0\rangle$ with respect to the trial-parameter α_0 yields

$$\alpha_0 = \left[\frac{9}{4}\,e\mathcal{E}\,\frac{2m^*}{\hbar^2}\right]^{1/3}. \tag{11.9}$$

Insertion of this result into Eq. (11.7) yields the normalized ground-state wave function. Insertion into Eq. (11.8) yields the ground-state energy according to

$$\boxed{E_0 = \frac{3}{10}\left[\frac{9^2}{2}\right]^{1/3}\left[\frac{e^2\hbar^2\mathcal{E}^2}{2m^*}\right]^{1/3}} \tag{11.10}$$

Comparison of this variational result with the mathematically exact result yields that both methods agree to within 1% (Schubert, 1993).

The calculation for the wave function and energy of the first excited state is performed analogously. The trial-parameter α_1 is used in the wave function

$$\psi_1(z) = \begin{cases} A_1 z\,\mathrm{e}^{-\alpha_1 z} & (z \geq 0) \\ A_1 z\,\mathrm{e}^{\alpha_1 z} & (z < 0)\,. \end{cases} \tag{11.11}$$

The normalization condition yields $A_1^2 = 2\alpha_1^3$. The expectation value for the energy is given by

https://doi.org/10.1017/CBO9780511599828.014 Published online by Cambridge University Press

$$\langle E_1 \rangle = \frac{\hbar^2}{2m^*}\,\alpha_1^2 + \frac{3}{2}\,\frac{e\mathcal{E}}{\alpha_1}\,. \tag{11.12}$$

The minimization of the energy expectation value yields the trial parameter

$$\alpha_1 = \left(\frac{3}{4}\,e\mathcal{E}\,\frac{2m^*}{\hbar^2}\right)^{1/3} \tag{11.13}$$

and finally the eigenstate energy of the first excited state

$$\boxed{E_1 = \frac{3}{2}\left(\frac{9}{2}\right)^{1/3}\left(\frac{e^2\hbar^2\mathcal{E}^2}{2m^*}\right)^{1/3}} \tag{11.14}$$

The requirements for the second excited state wave function are (i) even symmetry, (ii) two nodes, and (iii) exponential decay of the wave-function amplitude beyond the classical turning points. The following trial-function satisfies these requirements

$$\psi_2(z) = \begin{cases} A_2(\alpha_2^2\,z^2 - 1)\,(1 + \alpha_2 z)\,e^{-\alpha_2 z} & (z \geq 0) \\ A_2(\alpha_2^2\,z^2 - 1)\,(1 - \alpha_2 z)\,e^{\alpha_2 z} & (z < 0) \end{cases} \tag{11.15}$$

where the constant $A_2^2 = (4/63)\,\alpha_2$ is obtained from the normalization condition. The calculation of the energy expectation value is quite tedious and yields

$$\langle E_2 \rangle = \frac{1}{7}\left[3\alpha_2^2\,\frac{\hbar^2}{2m^*} + \frac{47}{2}\,\frac{e\mathcal{E}}{\alpha_2}\right]. \tag{11.16}$$

The minimum of $\langle E_2 \rangle$ is obtained for

$$\alpha_2 = \left(\frac{47}{12}\right)^{1/3}\left(e\mathcal{E}\,\frac{2m^*}{\hbar^2}\right)^{1/3} \tag{11.17}$$

which results in the eigenstate energy of the second excited state

$$\boxed{E_2 = \frac{9}{7}\left(\frac{47}{12}\right)^{2/3}\left(\frac{e^2\hbar^2\mathcal{E}^2}{2m^*}\right)^{1/3}} \tag{11.18}$$

The deviation of this variational result from the exact solution is < 2% (Schubert,

https://doi.org/10.1017/CBO9780511599828.014 Published online by Cambridge University Press

1993).

It is worthwhile pointing out that the V-shaped well and the triangular well share some of the eigenstate energies and wave functions. The triangular well has one infinitely steep wall and a second wall of slope $\mathcal{E}$. Potential wells of such triangular shape occur in selectively doped $Al_xGa_{1-x}As/GaAs$ heterostructures and in Si/SiO_2 inversion layers. The first excited state of the V-shaped well coincides with the ground state of the triangular well. Furthermore, the third excited state of the V-shaped well coincides with the first excited state of the triangular well.

11.1.2 Solutions of the parabolic well

A uniform doping distribution results in a potential well of parabolic shape. Consider a semiconductor with a spatially uniform donor impurity concentration N_D. Assume further that the doped layer is depleted of free carriers. Such a situation occurs, for example, in homogeneously doped doping superlattices (see Sect. 10.3). The corresponding parabolic potential well is shown in Fig. 11.2(b). The parabolic potential of the conduction band edge is given by

$$\phi(z) = \frac{e^2}{2\varepsilon} N_D z^2 . \tag{11.19}$$

The exact solutions of the eigenstate (subband) energies are the *harmonic oscillator solutions* given by (Saxon, 1968)

$$E_n = \left[n + \frac{1}{2}\right] \hbar e \left[\frac{N_D}{\varepsilon m^*}\right]^{1/2} \quad \text{for} \quad n = 0,1,2 \cdots . \tag{11.20}$$

The subband separation is constant and independent of the quantum number, i.e. $E_n \propto n$.

11.1.3 Self-consistent solutions of the V-shaped potential

In Sects. 11.1.1 and 11.1.2 the energetic subband structure of a V-shaped and parabolic potential well was calculated without taking into account the charge of free *carriers* in the potential well. The total charge of free carriers equals the total charge of ionized dopants in a δ-doped semiconductor with a single dopant sheet (the n^- or p^--type background concentration, which always occurs in a realistic semiconductor, is neglected). Therefore, the δ-doped carrier system is *neutral*, i.e. the electric field $\mathcal{E} \to 0$ for distances sufficiently far from the doped region.

A *self-consistent* calculation is required if the charge of free carriers is taken into account. Such self-consistent calculations simultaneously satisfy Poisson's and Schrödinger's equation. Poisson's equation allows one to calculate the potential as a function of the spatial coordinates x, y, z from a given charge

https://doi.org/10.1017/CBO9780511599828.014 Published online by Cambridge University Press

337-TA-1366 RX-0255

distribution (both ionized dopant charge and free carrier charge). On the other hand, Schrödinger's equation enables one to calculate the charge distribution in a given potential.

Self-consistent calculations are greatly simplified if the charge distribution is assumed to depend on one spatial coordinate only. Such one-dimensional self-consistent calculations of the energy-space structure of semiconductor quantum systems (see e.g. Ando, 1982a, 1982b; Stern and Das Sarma, 1984; Vinter, 1984) were initially carried out for selectively doped $Al_xGa_{1-x}As/GaAs$ heterostructures. The solution of Poisson's equation is straightforward whereas the accurate solution of Schrödinger's equation is more elaborate. Therefore, several groups used approximate solutions of the Schrödinger equation, including the variational solution (Stern, 1983; Fang and Howard, 1966) and the WKB approximation (Ando, 1985).

The band diagram obtained from a self-consistent calculation is shown in Fig. 11.3 for δ-doped GaAs. The two-dimensional doping density of the structure is 5×10^{12} cm^{-2} located at $z = 599-601$ Å. The doping charge is assumed to be distributed homogeneously over 2 Å. A low temperature of $T = 4$ K was assumed for the calculation. Figure 11.3 reveals that four subbands are populated at the chosen doping density. The electron densities in each subband are as follows: $n_0 = 3.05 \times 10^{12}$ cm^{-2}, $n_1 = 1.18 \times 10^{12}$ cm^{-2}, $n_2 = 0.531 \times 10^{12}$ cm^{-2}, and $n_3 = 0.188 \times 10^{12}$ cm^{-2}.

Comparison of the width of the dopant distribution with the spatial extent of the free carrier distribution allows one to define a δ-doped semiconductor. The spatial extent of the electron distribution of the ground-state subband is approximately 50 Å. Higher excited states have a wider distribution. In δ-doped semiconductors, the dopant distribution is much narrower than the free carrier distribution. In Fig. 11.3, the dopants are assumed to be distributed within 2 Å. It is, however, quite obvious that any impurity distribution with a spatial extent $\ll$ 50 Å will result in a free carrier distribution very similar to the one shown in Fig. 11.3.

As a numerical example, we consider the spatial extent of the ground-state wave function using the variational wave function of Eq. (11.7). We define the spatial extent of the wave function as

$$z_0 = 2(\langle z^2 \rangle - \langle z \rangle^2) \tag{11.21}$$

where $\langle z \rangle$ is the position expectation value of the ground-state wave function. Using Eqs. (11.7)–(11.10), one obtains

https://doi.org/10.1017/CBO9780511599828.014 Published online by Cambridge University Press

RX-0255.464

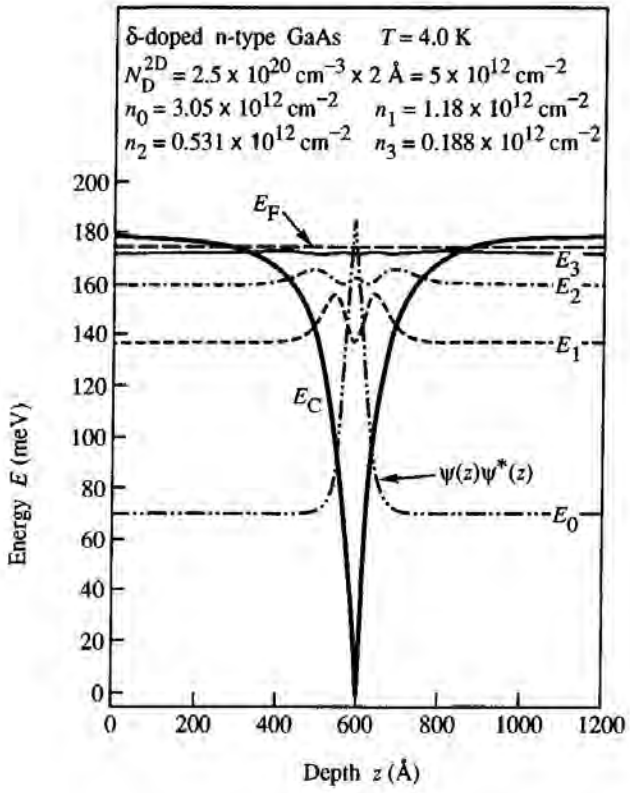


Fig. 11.3. Subband structure and charge distribution in a δ-doped semiconductor obtained from the self- consistent solution of Poisson's and Schrödinger's equation. At a doping density of $5 \times 10^{12}\,cm^{-2}$, four eigenstates are populated.

$$z_0 = 2\sqrt{\frac{7}{5}}\left(\frac{4}{9}\,\frac{\hbar^2}{e\mathcal{E}2m^*}\right)^{1/3} \tag{11.22}$$

For an n-type doping concentration of $N_D^{2D} = 5 \times 10^{12}\ cm^{-2}$ one obtains $\mathcal{E} = 3.45 \times 10^5$ V/cm and $z_0 = 46$ Å.

We thus define δ-function-like doping distributions as follows: ***one-dimensional doping distributions are δ-function-like, if the spatial extent of the doping distribution is much narrower than the ground-state wave function of the V-shaped quantum well***; the width of the ground-state wave function is given by Eq. (11.22). Application of this definition to the band diagram shown in Fig. 11.3 implies that any doping distribution localized within a length << 50 Å can be considered to be δ-function-like. For example, distribution widths of dz = 2 Å or dz = 20 Å can both be regarded as δ-function-like. It is clear from

https://doi.org/10.1017/CBO9780511599828.014 Published online by Cambridge University Press

337-TA-1366 RX-0255

this definition, that impurities need not be confined to a single monolayer, in order to result in a δ-function-like doping profile.

11.1.4 Discreteness of charge

The discreteness of charge has not been taken into account in the self-consistent and variational calculations described above. Instead, the charge was assumed to be distributed homogeneously in the dopant plane (jellium model). The coherence length of the wave function in the lateral direction (i.e. the direction of the dopant plane) allows us to estimate the effect of dopant density fluctuations experienced by the free carriers assuming random distribution of dopants. The phase-coherence length in the lateral direction can be estimated from the inelastic scattering time

$$\tau_{\text{inel}} = \mu m^* / e \tag{11.23}$$

where μ is the carrier mobility. Certainly, any scattering event, both elastic *and* inelastic, changes the phase of the electron, but since the elastic scattering time is difficult to estimate, only the inelastic time is estimated in Eq. (11.23). The Fermi velocity

$$\tfrac{1}{2} m^* v_F^2 = E_F - E_0 \tag{11.24}$$

allows one to estimate the mean free path between two inelastic scattering events according to

$$l_{\text{inel}} = v_F \, \tau_{\text{inel}} \, . \tag{11.25}$$

As a numerical example, we consider electrons in GaAs with a density $N_D^{2D} = 1 \times 10^{13}$ cm^{-2}, a mobility of $\mu = 2000$ cm^2/V s, and a Fermi energy of $E_F - E_0 = 100$ meV. The mean free path is estimated to be $l_{\text{inel}} = 550$ Å. Within an area $l_{\text{inel}} \times l_{\text{inel}}$, there are an average of 300 dopant atoms. This number fluctuates depending on location, since the distribution of dopants can be assumed to be random. The average fluctuation of doping atoms within this area is $\sqrt{300} = 17$ assuming Poisson statistics. The relative variation in doping atoms is $\pm\sqrt{N}/N \cong 0.06$. Because the energy of the lowest state is proportional to $\left[N_D^{2D}\right]^{1/3}$ (see Eqs. (11.3) and (11.10)), the state energies fluctuate by approximately ±4%. At lower doping densities the density fluctuations of the doping atom become larger.

The fluctuations in the subband structure of δ-doped semiconductors are due to the fact that dopant atoms are an 'infrequent' event. Only several tens to several hundreds of dopant atoms are within the area defined by the coherence length of the electron wave function. In compositional quantum wells (e.g.

https://doi.org/10.1017/CBO9780511599828.014 Published online by Cambridge University Press

RX-0255.466

$Al_xGa_{1-x}As$/GaAs) such uncertainties are exceedingly small (<< 1%). Potential fluctuations due to compositional fluctuations are negligibly small because the potential is defined by a very *large* number of Al and Ga atoms. Consequently, the Poisson statistical fluctuations $\sqrt{N}/N$ are negligible in compositional quantum wells.

Exchange effects, correlation effects, and an energy-dependent effective mass due to a non-parabolic dispersion relation were taken into account in self-consistent calculations on heterostructures (see e.g. Ando, 1982a and 1982b; Stern and Das Sarma, 1984). Exchange, correlation, and non-parabolicity effects are adequate also for δ-doped structures. However, their influence is typically smaller than the uncertainties due to random dopant distribution. Thus, it does not appear useful to consider exchange and correlation effects and, at the same time, ignore effects due to random dopant distribution. Random potential fluctuations can be taken into account by truly three-dimensional self-consistent calculations, in which a random placement of dopants is realized. Unfortunately, such three-dimensional calculations are quite elaborate and have not hitherto been carried out.

11.1.5 Superlattices with V-shaped potentials

Alternating n- and p-type δ-doping spikes equally spaced and of the same density result in a periodic potential with sawtooth-shaped band-edge potentials. Such doping superlattices have a number of unusual optical and electronic properties including a recombination lifetime which strongly depends on the superlattice period. Experimental properties of doping superlattices are discussed in detail in Sect. 10.3 and 11.5. Here, only theoretical aspects of the superlattice band structure are discussed. Complete self-consistent calculations of the band structure and the charge distribution of compensated and non-compensated δ-doped GaAs sawtooth superlattices as a function of period and doping concentration have been reported by Proetto and coworkers (Proetto, 1990; Ferreira and Proetto, 1990, 1991; Reboredo and Proetto, 1992).

The Kronig–Penney model can be used to calculate the dispersion relation and the wave functions in δ-doped doping superlattices (Schubert, 1993). The calculation of the superlattice dispersion relation and the eigenstate energies are carried out in the effective-mass approximation. The sawtooth-shaped periodic potential is given by

https://doi.org/10.1017/CBO9780511599828.014 Published online by Cambridge University Press

$$V(z) = \begin{cases} (z - mz_p)\,\mathcal{E} \\ \\ (-z - mz_p)\,\mathcal{E} \end{cases} \quad \text{for } m = 0, \pm 1, \pm 2, \cdots \tag{11.26}$$

where z_p is the superlattice period. The electric field, $\mathcal{E}$, and the amplitude of the superlattice potential, V_{zz}, are related by $V_{zz} = \frac{1}{2}\mathcal{E}\, z_p$. The wave function in this periodic, one-dimensional potential can be obtained by the product method using the wave function

$$\psi^{c,v}_{n,k_x,k_y}(x,y,z) = e^{ik_x x}\, e^{ik_y y}\, \psi^{c,v}_n(z)\, u^{c,v}(x,y,z) \tag{11.27}$$

where $e^{ik_x x}$ and $e^{ik_y y}$ represent plane electron waves in the lateral directions (x- and y-directions), $\psi^{c,v}_n(z)$ is the envelope wave function of the conduction (c) or valence (v) band, and $u^{c,v}(x,y,z)$ is the conduction- or valence-band Bloch function of the host material. Note that the envelope function $\psi_n(z)$ depends on z only and describes the quantized motion in the z-direction. The subscript n refers to the nth quantized state of the superlattice. The solution of the envelope function in a linear periodic potential are Airy functions (Abromowitz and Stegun, 1972) which can be applied to doping superlattices (Schubert, 1993). Using this approach, the miniband structure, including its wave functions, miniband width, etc., can be calculated.

The broadening of subbands into minibands allows one to estimate the efficiency of vertical transport in doping superlattices using the Kronig–Penney model. The effective mass along the z-direction, i.e. perpendicular to the doping planes, can be calculated using this model. Using the definition of the effective mass $m^*_z = \hbar^2 \left[d^2 E_z(k_z)/dk_z^2 \right]^{-1}$ and the linearized dispersion relation from the Kronig–Penney model, one obtains the effective dispersion mass for motion in perpendicular direction

$$m^*_{z,n} = \frac{\hbar^2}{z_p^2 \Delta E_n} \tag{11.28}$$

where $2\Delta E_n$ is the energetic width of the nth miniband. Large superlattice periods result in small miniband widths, i.e. (according to Eq. (11.28)) into large effective masses. Carrier transport along the z-direction is then strongly reduced. On the other hand, short periods result in large miniband widths, i.e. small effective dispersion masses and more efficient transport along the superlattice direction (Schubert, 1993).

https://doi.org/10.1017/CBO9780511599828.014 Published online by Cambridge University Press

11.2 Growth, localization, and redistribution

Delta-doped semiconductors can be fabricated solely by epitaxial growth techniques such as OMVPE and MBE. Other doping techniques such as implantation or diffusion are not capable of producing sharp doping profiles. The assessment of the spatial localization of impurities requires the use of highly sensitive techniques such as secondary ion mass spectrometry (SIMS), capacitance–voltage profiling (CV), or Auger spectroscopy. These techniques have resolution widths of 10–20 Å, which allows the accurate determination of spatial localization and redistribution effects. Redistribution of impurities in δ-doped semiconductors is due to several effects. Diffusion, drift, and segregation have been found at high growth temperatures. Furthermore, redistribution of impurities can occur during epitaxial growth as well as during post-growth annealing. In this section, the topics of crystal growth, spatial localization, and redistribution of impurities are summarized and discussed. Although the three topics are interrelated, they are discussed separately for the convenience of the reader.

11.2.1 Growth by VPE

The first report on growth-interrupted doping of III–V semiconductors is due to Bass (1979) who reported the occurrence of Si and Ge doping spikes in GaAs grown by OMVPE. It was general practice during sulphur doping experiments to initiate the hydrogen sulphide flow before growth was started. This was done to reduce the sulfur memory effect. However, if this procedure was done for Si doping, a pronounced Si doping spike occurred at the substrate–epitaxial layer interface. Bass (1979) concluded that Si adsorbs strongly on the GaAs surface before growth is initiated. The adsorption persisted at substrate temperatures below or at the growth temperature. Measurements of the Si doping profile after completion of the epitaxial growth revealed that the Si distribution was several hundred ångströms wide.

More recently, Hobson et al. (1989) reported Zn δ-doping in GaAs grown by OMVPE. The narrowest impurity profiles were 70 Å wide and were obtained for Zn concentrations not exceeding 3×10^{18} cm^{-3}. The δ-doped layers were formed as follows. First, the TMGa was switched to the vent line, stopping growth for 10 s. This was followed by introduction of DEZn for a duration of 5–60 s and then switched back to vent, allowing another 10 s before resuming regular epitaxial growth.

Yang et al. (1992) reported Si δ-doping in AlGaAs/GaInAs heterostructures grown by atmospheric pressure OMVPE. Despite the relative high growth temperatures of 650–700 °C, very narrow doping profiles of 32 Å full width at

https://doi.org/10.1017/CBO9780511599828.014 Published online by Cambridge University Press

half-maximum (FWHM) were obtained. The authors pointed out that the typical broadening observed in Si δ-doped GaAs grown by MBE at high temperatures was not observed during OMVPE. The δ-doped heterostructures had high sheet concentrations as well as high electron mobilities.

Si δ-doping was also reported by flow-rate modulation epitaxy (FME) which is a growth technique related to OMVPE (Kobayashi et al., 1986; Makimoto, 1986). In FME, organometallics and hydrides are used as group-III and group-V precursors, respectively. The two precursors are provided alternately, resulting in the growth of one GaAs molecular layer per cycle. This unique characteristic allowed the authors to selectively δ-dope a Ga or an As plane with Si. Higher free carrier concentrations (by a factor of 5) were obtained when the Ga plane was doped. The different concentrations were attributed to a higher SiH_4 sticking coefficient on the atomic As layer compared to a Ga layer. Very narrow Si doping profile widths < 30 Å were obtained for Si densities of 1.1×10^{13} cm^{-3}. The excellent spatial localization was attributed to the growth temperature which was approximately 100 °C lower in FME as compared to conventional OMVPE.

11.2.2 Growth by MBE

During the δ-doping deposition process, epitaxial growth of the III–V semiconductor is suspended. The epitaxial growth is interrupted by closing the group–III element shutter of the effusion cell. The group-V element effusion cell is kept open to provide an As-stabilized surface. Since most popular dopant species, such as Si, Be, Zn, etc., occupy cation sites in III–V semiconductors, the anion-stabilized surface makes cation sites readily available. Typically, the growth temperature is kept between 400 °C and 630 °C for the growth of δ-doped GaAs, i.e. below the congruent sublimation temperature. It is well known that the sticking coefficient of excess As on an As-rich GaAs surface is zero at these growth temperatures (see for example Joyce, 1985), i.e. the surface stoichiometry is maintained.

Upon termination of epitaxial growth, the dopant effusion cell is opened and dopants are evaporated on the non-growing semiconductor surface. It was first realized that Ge is strongly adsorbed (chemisorbed) by the GaAs surface and does not reevaporate significantly. Dopants thus accumulate on the crystal surface during the deposition. The evaporation of dopants on an As-stabilized surface was shown to result in reduced autocompensation for Ge-doping (Wood et al., 1980), since virtually all As sites are occupied and Ge is incorporated predominantly on Ga sites. Similar observations were made for Si in GaAs (Schubert et al., 1987a) and for Si in $Al_x Ga_{1-x} As$ (English et al., 1987).

https://doi.org/10.1017/CBO9780511599828.014 Published online by Cambridge University Press

The two-dimensional (2D) density of donors or acceptors, $N_{D,A}^{2D}$, deposited during growth interruption can be calculated from the growth suspension time, τ, and the dopant cell temperature T. The 2D dopant density is given by

$$N^{2D} = N v_g \tau \tag{11.29}$$

where N is the three-dimensional dopant concentration obtained at the doping cell temperature T and a growth rate v_g. For example, a time $\tau = 18$ s is required to deposit 10^{12} dopants per cm^2 at a dopant cell temperature, which results in a 3D concentration of 2×10^{18} cm^{-3} at a growth rate of 1 μm/hr. It is advisable to choose a *high* dopant cell temperature and keep the growth interruption time minimal and hence reduce the incorporation of unwanted impurities. After dopant deposition, the regular crystal growth is resumed. For atomically flat crystal surfaces and in the absence of diffusion or segregation processes, dopants are confined to a single monolayer of the host semiconductor.

The surface reconstruction changes during growth interruption and during dopant deposition. During growth below the congruent sublimation temperature at Ga/As_4 flux ratios close to one, a (1×1) surface reconstruction on GaAs (001) is found by reflection high-energy electron diffraction (RHEED). For Ga/As_4 flux ratios < 1, a (2×4) surface reconstruction is found. When the Ga flux is terminated, the surface remains As-stabilized and in a (2×4) As-rich reconstruction. After prolonged deposition of Si on GaAs, a change from the (2×4) to the (1×3) surface reconstruction occurs (Schubert et al., 1986b).

11.2.3 Assessment of localization by SIMS

Secondary ion mass spectrometry (SIMS) is a powerful structural technique with high depth resolution. SIMS has been employed to study the spatial localization of impurities in δ-doped III–V semiconductors by several research groups (Beall et al., 1988, 1989; Lanzillotto et al., 1989; Schubert et al., 1990d). These reports concluded that δ-function-like doping profiles of Si and Be in GaAs can be achieved at sufficiently low growth temperatures. In this case, impurities are confined to one or a few monolayers of the host semiconductor. Detectable broadening of the impurity distribution was found at elevated growth temperatures and at high impurity densities.

The SIMS profile of a Be δ-doped GaAs film is shown in Fig. 11.4. A narrow peak is observed at a depth of ~200 Å which corresponds to the Be δ-doped layer. The full width at half maximum of the Be peak is 29 Å, which is the narrowest SIMS profile measured for δ-doped GaAs grown at typical growth temperatures. Such narrow SIMS profiles can only be obtained under optimized measurement conditions such as a low primary ion energy (1–2 keV), a shallow

https://doi.org/10.1017/CBO9780511599828.014 Published online by Cambridge University Press

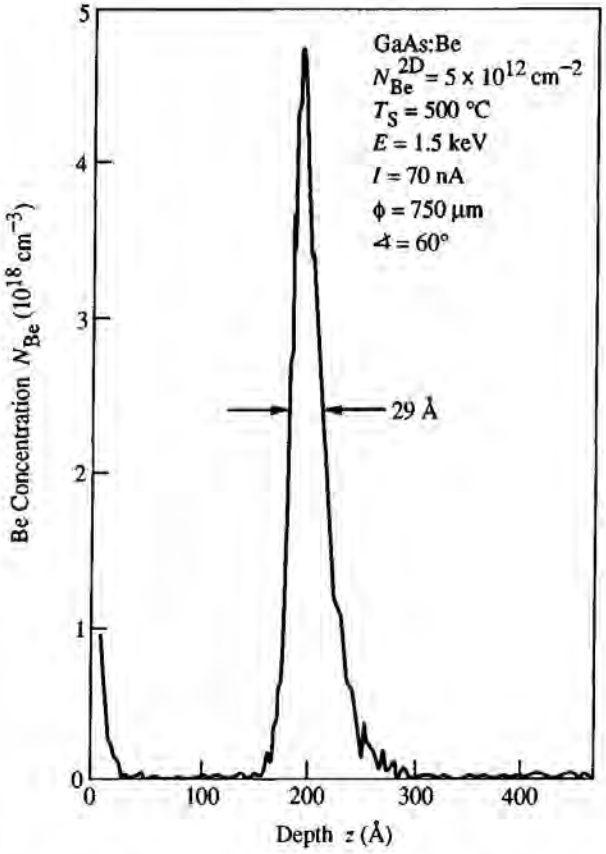


Fig. 11.4. Secondary ion mass spectrometry (SIMS) profile on epitaxial GaAs containing a Be δ-doped layer 200 Å below the surface. The following parameters were used for the MBE growth and the SIMS measurement: growth temperature 500 °C, primary ion energy 1.5 keV, primary ion current 70 nA, raster diameter 750 μm, sputtering angle 60°.

sputtering angle (60°), and a shallow depth of the δ-doped layer (100–300 Å). Several broadening mechanisms determine the width of the SIMS profiles. The two dominant broadening mechanisms are (i) surface roughening and (ii) ion mixing, also called the 'knock-on' effect (Benninghoven et al., 1987). Surface roughening is expected to broaden SIMS profiles symmetrically, while the knock-on effect skews the profile predominantly along the sputter direction. The symmetric shape of the profile shown in Fig. 11.4 indicates that surface roughness is the dominant broadening mechanism rather than the 'knock-on' effect.

The resolution of the SIMS technique is generally obtained by assuming that the shape of the profile is gaussian (Benninghoven et al., 1987). The symmetric gaussian distribution is justified since the profile shown in Fig. 11.4 is indeed

https://doi.org/10.1017/CBO9780511599828.014 Published online by Cambridge University Press

symmetric. Provided that diffusion effects are negligible in the sample shown in Fig. 11.4, the measured profile is given by the resolution function of the SIMS technique. The resolution of the technique, Δz_R, is defined as twice the standard deviation of the gaussian distribution, i.e., $\Delta z_R = 2\sigma_r$. Since the full width at half-maximum is 2.36 times larger than the standard deviation of a gaussian distribution, the resolution of our measurement under optimized conditions is $\Delta z_R = 25$ Å.

If impurities diffuse out of the δ-doped plane, the measured SIMS profiles broaden as well. Assuming that the impurity profiles after diffusion are gaussian, the measured width of the SIMS profile is given by

$$\Delta z_M^2 = \Delta z_D^2 + \Delta z_R^2 \tag{11.30}$$

where $\Delta z_D = 2\sigma_D$ is the width of the impurity profile after diffusion. The resolution $\Delta z_R = 25$ Å and its reproducibility are known. Therefore, we can determine the smallest impurity distribution width, i.e. diffusion length, which can be determined by the technique. As an example, we choose a diffusion length for impurities of $\Delta z_D/2 = \sigma_D = \sqrt{2D\tau} = 10$ Å and obtain from Eq. (11.30) $z_M = 32$ Å which corresponds to a FWHM = 38 Å representing a significant broadening as compared to the profile shown in Fig. 11.4. Thus, diffusion lengths of ≤10 Å can clearly be detected. This demonstrates that SIMS is currently the most sensitive structural method to determine impurity diffusion lengths in semiconductors.

The depth dependence of the SIMS resolution is usually expressed by the linear equation

$$\Delta z_R = \alpha + \beta z \tag{11.31}$$

where α is the resolution for $z = 0$ and β is a parameter which represents the deterioration of the resolution with depth. The deterioration of depth resolution increases with sputter depth because of the roughening of the crater surface due to the statistical nature of the sputter process. The parameter β can be obtained from the broadening of the peak width with depth (Schubert et al., 1990d). Evaluation of β yielded $\beta = 5 \times 10^{-3}$ for low-energy sputtering conditions. Similar values were obtained by Clegg and Beall (1989) and Lanzillotto et al. (1989).

11.2.4 Assessment of localization by the CV-technique

The capacitance–voltage profiling technique has been used extensively to assess the spatial localization of impurities in δ-doped semiconductors (Bass, 1979; Lee et al., 1985; Sasa et al., 1985; Schubert et al., 1988a, 1990a). The capacitance–voltage (CV) profiling is a well-known electrical characterization

https://doi.org/10.1017/CBO9780511599828.014 Published online by Cambridge University Press

technique to spatially resolve impurity distributions in semiconductors. During the measurement, the capacitance of a metal–semiconductor junction, a p^+n-, or an n^+ p-junction is measured as a function of the applied bias. For such junctions, the CV-concentration, N_{CV}, is inferred from the CV-measurement using the equation

$$N_{CV} = \frac{-2}{e\varepsilon}\left(\mathrm{d}\frac{1}{C^2}/\mathrm{d}V\right)^{-1} = \frac{C^3}{e\varepsilon}\frac{\mathrm{d}V}{\mathrm{d}C} \tag{11.32}$$

where e and ε are the elementary charge and the permittivity of the semiconductor, respectively, and C is the capacitance of the junction per unit area. The CV-depth, z_{CV}, is obtained from the reciprocal of the capacitance

$$z_{CV} = \varepsilon/C\,. \tag{11.33}$$

Equations (11.32) and (11.33) allow one to plot N_{CV} versus z_{CV}, which is called the *CV-profile*.

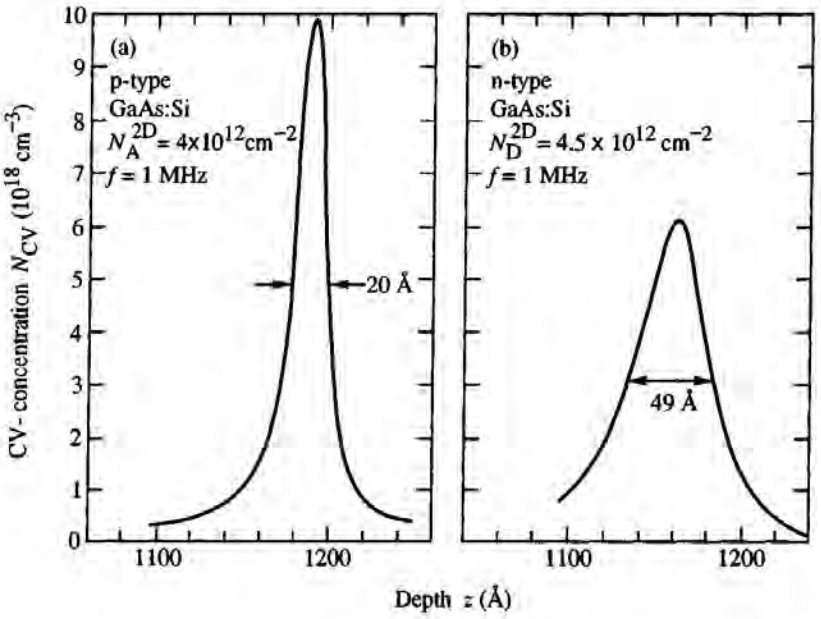


Fig. 11.5. CV-profiles on (a) p-type and (b) n-type δ-doped GaAs. The Be and Si densities are 4.0×10^{12} and $4.5\times10^{12}\,cm^{-2}$, respectively.

The CV-profiles measured at 300 K of Be and Si δ-doped GaAs are shown in Fig. 11.5. The Be and Si densities are 4×10^{12} and $4.5\times10^{12}\,cm^{-2}$, respectively. The CV-profile widths are 20 Å and 49 Å for the Be and Si profile,

https://doi.org/10.1017/CBO9780511599828.014 Published online by Cambridge University Press

respectively. Note that the profile widths are significantly different for the p-type and n-type profile. The difference can thus not be explained by the conventional Debye limitation of the CV-profiling technique.

The spatial resolution of the CV-profiling technique is given by the screening length and the spatial extent of the carrier system for classical and quantum-mechanical carrier distributions, respectively. If the doping concentration varies along the growth direction, the free carrier profile is smeared out as compared to the doping profile. Kennedy et al. (1968) and Kennedy and O'Brien (1969) showed, that the resolution of the CV-technique is limited to the majority carrier screening length. Furthermore, the authors showed that the CV-profile $N_{CV}(z)$, closely follows the free carrier profile, $n(z)$. The majority carrier screening or Debye length in non-degenerately doped semiconductors is given by

$$r_D = \sqrt{\frac{\varepsilon kT}{e^2 n}} \,. \tag{11.34}$$

The Thomas–Fermi screening length for degenerately doped semiconductors is

$$r_{TF} = \pi^{2/3} \sqrt{\frac{\varepsilon \hbar^2}{e^2 m^* (3n)^{1/3}}} \tag{11.35}$$

Note that the two screening lengths have different dependences on n and T.

The spatial resolution of the CV-profiling technique in *semiconductors with quantum confinement* was shown to be limited to the spatial extent of the carrier wave function (Schubert et al., 1990a). This result can be understood as follows. Consider a quantized electron system described by a wave function $\psi(z)$. The position expectation value of the electron system is $\langle z \rangle = \langle \psi | z | \psi \rangle$. The differential capacitance per unit area of such an electron system equals

$$C = \varepsilon / \langle z \rangle \,. \tag{11.36}$$

Upon application of a bias, the position expectation value of the quantized electron system changes due to the potential perturbation caused by the bias. Comparison of Eqs. (11.36) and (11.33) yields that $z_{CV} = \langle z \rangle$, i.e. the CV-depth (at a certain bias) equals the position expectation value of the electron system (at a certain bias). Thus, the *resolution* of the CV-technique, Δz_{CV}, is given by the change of the position expectation value, $\Delta \langle z \rangle$, upon sweeping the bias, i.e.

$$\Delta z_{CV} = \Delta \langle z \rangle \,. \tag{11.37}$$

Schubert et al. (1990a) showed that the change in position expectation value is approximately equal to the spatial width of the wave function, z_0, i.e. approximately equal to the width of the confining potential. For δ-doped

https://doi.org/10.1017/CBO9780511599828.014 Published online by Cambridge University Press

semiconductors, the spatial extent of the ground-state wave function has been calculated using a variational method. The resolution, i.e. CV-profile width, was obtained as

$$\Delta z_{CV} = z_0 = 2\sqrt{\frac{7}{5}}\left(\frac{4}{9}\frac{\varepsilon\hbar^2}{e^2 N^{2D} m^*}\right)^{1/3} \tag{11.38}$$

Using this result, the calculated resolution for the two profiles shown in Fig. 11.5 is given by Δz_{CV} = 26 Å and 48 Å, respectively, which agrees very well with the experimental result. Thus, the CV-profiles shown in Fig. 11.5 are resolution limited, i.e. broadening of the impurity distribution due to redistribution effects is negligible.

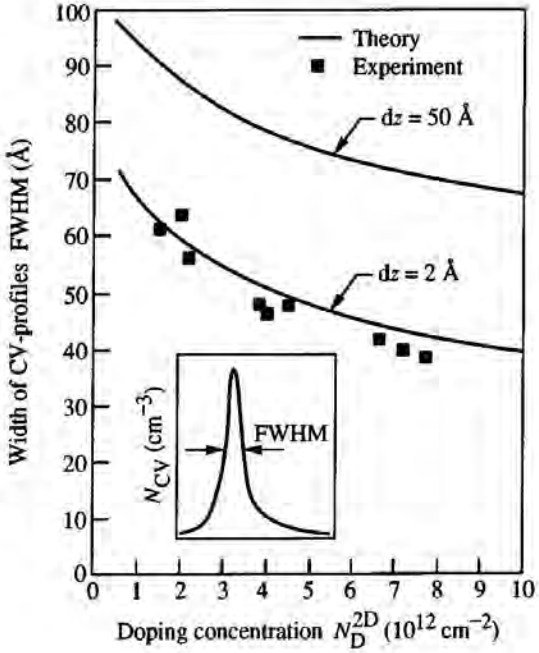


Fig.11.6. Comparison of theoretical (solid lines) and experimental (squares) full-widths at half-maximum (FWHM) of CV-profiles obtained from n-type δ-doped GaAs at different doping densities. The two theoretical curves are obtained from self-consistent calculations assuming doping distribution widths of 2 Å (δ-doped) and 50 Å (pulse-doped). Good agreement is obtained, only if diffusion is assumed to be negligible.

Self-consistently calculated CV-profile widths are shown in Fig. 11.6 as a function of n-type doping density in GaAs (Schubert et al., 1988a). Size quantization of the carrier system was taken into account via the Schrödinger equation. The impurity distribution assumed for the calculation is top-hat-shaped with a width of dz = 2Å (δ-doping) and dz = 50 Å (pulse doping). Comparison of the calculated width with experimentally measured widths (squares) indicates

https://doi.org/10.1017/CBO9780511599828.014 Published online by Cambridge University Press

that the profile widths are again resolution limited. Furthermore, an impurity distribution width of dz = 50 Å is too wide to account for the experimental results.

11.2.5 Assessment of localization by Auger technique

Auger electron spectroscopy is usually not considered to be a useful technique to study impurity distributions in semiconductors. This is due to the low surface sensitivity of Auger spectroscopy of about 0.1%–1%. For Si in GaAs, 10^{19} cm^{-3} is considered a high doping concentration, but in terms of bulk atomic concentration, 10^{19} cm^{-3} equals about 0.02%, i.e. below the typical Auger sensitivity. Nevertheless, Webb (1989) showed that Auger electron spectroscopy can be very useful for studying the segregation of impurities in δ-doped semiconductors. Doping densities of 10^{13} cm^{-2} exceed 1% in atomic surface concentration which can be detected by Auger analysis.

In order to investigate Si segregation, Webb (1989) grew a buffer layer of undoped GaAs by MBE, then deposited 3×10^{13} cm^{-2} Si atoms, and finally grew a 10 Å GaAs cap layer. Without any Si segregation, a decrease in the Si-Auger-electron intensity by a factor of $\exp(10\ \text{Å}/l_{\text{electron}}) \cong 7$ is expected for an electron mean free path of $l_{\text{electron}} = 5$ Å. If segregation does occur, the attenuation factor will be smaller. Thus, Auger electron spectroscopy allows one to study impurity redistribution towards the surface in δ-doped semiconductors with a sufficiently high impurity density.

Webb (1989) investigated segregation of Si in δ-doped GaAs as a function of growth temperature using Auger spectroscopy. The results of the study are summarized as follows. No segregation was detectable at growth temperatures of 520 °C, indicating good spatial confinement of Si δ-doped GaAs even at Si densities as high as 3×10^{13} cm^{-2}. Considering the high spatial resolution of the experiment, it can be concluded that the Si impurities are confined to a layer of thickness <10 Å. At elevated growth temperatures of approximately 540–590 °C, Si segregation did occur. The redistribution of Si increased at higher growth temperatures. An activation energy of 2.4 eV was estimated for the thermally activated redistribution of Si impurities.

11.2.6 Redistribution of impurities

Spatial redistribution of impurities can occur during epitaxial growth at elevated growth temperatures as well as during post-growth annealing. The magnitude of the impurity profile broadening depends on a number of parameters such as the temperature, impurity species, growth conditions, defect concentration in the semiconductor, etc. Despite the large number of parameters, there are two general tendencies for impurity redistribution. First, the magnitude of

https://doi.org/10.1017/CBO9780511599828.014 Published online by Cambridge University Press

redistribution increases at high temperatures. Second, for some impurity species (e.g. Be or Zn), the magnitude of redistribution increases strongly with impurity concentration.

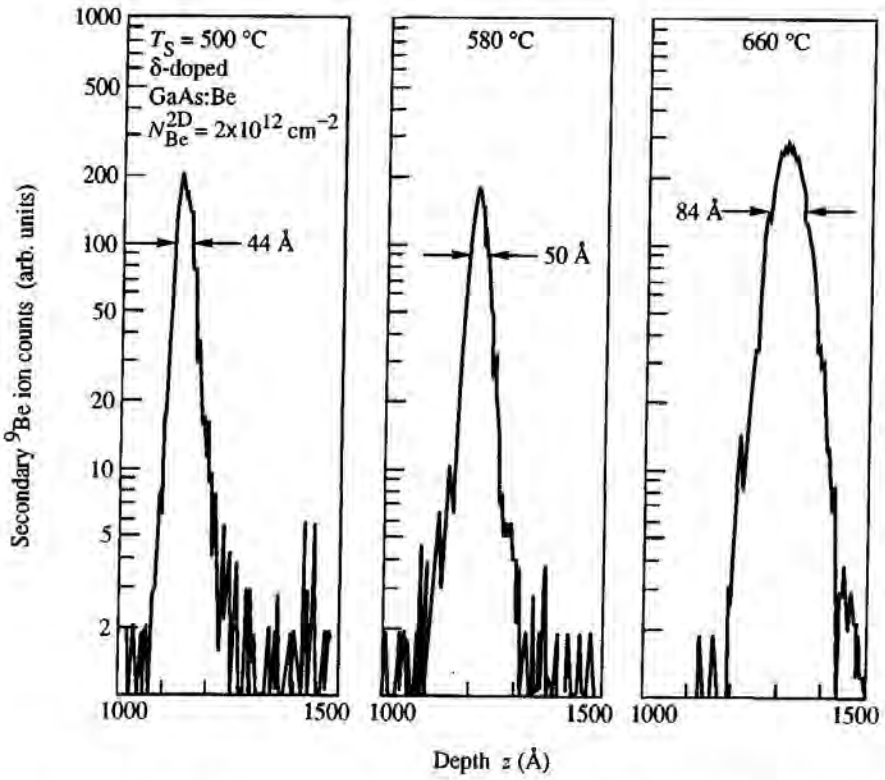


Fig. 11.7. Secondary ion mass spectrometry (SIMS) profiles on three Be δ-doped GaAs samples grown at 500, 580, and 660 °C. The SIMS profiles broaden systematically at high growth temperatures.

An example of impurity redistribution during growth is shown in Fig. 11.7 for Be δ-doped GaAs grown by MBE at temperatures of 500 °C, 580 °C, and 660 °C. The Be impurity profile in Fig. 11.7 was measured by SIMS. The nominal Be density of the three samples is 2×10^{12} cm^{-2}. At low growth temperatures of 500 °C, the width of the Be profile is 44 Å which is a resolution-limited profile for the measurement conditions employed. As the growth temperature is increased to 580 °C, the profile width increases to 50 Å. The profile broadening is more pronounced for a growth temperature of 660 °C where the profile width is 84 Å. The basic trend of impurity profile broadening at elevated growth temperatures has been observed for many different impurities such as Be, Zn, C, and Si, as well as different III–V semiconductors such as

https://doi.org/10.1017/CBO9780511599828.014 Published online by Cambridge University Press

GaAs, $Al_xGa_{1-x}As$, $Ga_{0.47}In_{0.53}As$, $Al_{0.48}In_{0.52}As$ and other materials (Schubert, 1990b; Schubert et al., 1989b, 1990c). The first indication of impurity redistribution in δ-doped semiconductors was reported by Lee et al. (1985).

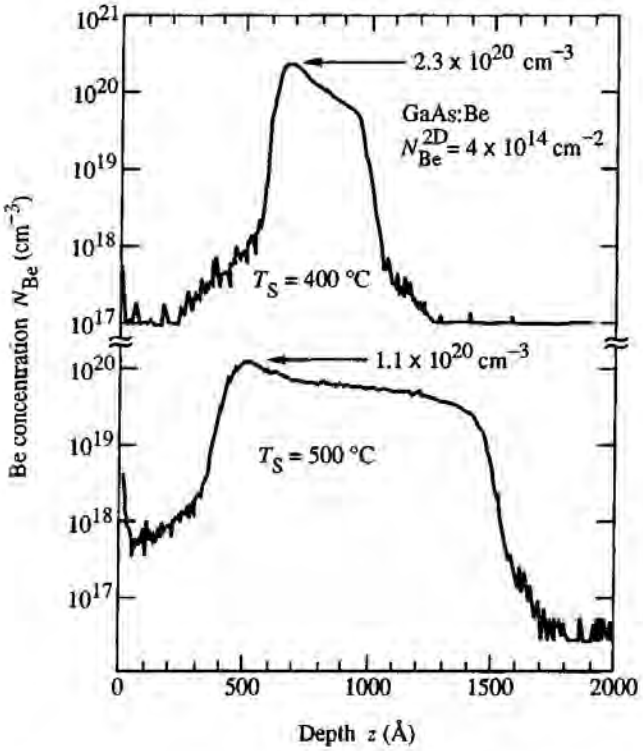


Fig. 11.8. Secondary ion mass spectrometry profile of Be δ-doped GaAs grown at (top) 400 °C and (bottom) 500 °C. The lower growth temperature results in reduced broadening and a higher Be peak concentration.

The occurrence of *impurity redistribution during growth* cannot be explained by a single physical mechanism. Instead, several redistribution mechanisms are required to fully account for the multitude of redistribution effects occurring during growth at elevated growth temperatures. The mechanisms and their physical driving forces were discussed in detail in Chap. 8. Here, we restrict ourselves to summarizing briefly the mechanisms. *Diffusion* of impurities results in a symmetric (i.e. gaussian) impurity distribution which increases in width with temperature. The diffusion coefficient can depend on the impurity concentration. For example, the substitutional–interstitial model (see Chap. 8) predicts an increase of the diffusion coefficient with the concentration according to a power law. Redistribution of impurities toward the semiconductor surface is termed

https://doi.org/10.1017/CBO9780511599828.014 Published online by Cambridge University Press

impurity segregation. The driving force for surface segregation can be (i) an electric field due to a surface dipole (Schubert et al., 1990b) or (ii) a lower energy of the impurity atom on the surface as compared to the bulk (Harris et al., 1984). The lower surface energy can be due to a different bonding configuration and strength of the impurity on the surface as opposed to the bulk. Some impurities exhibit a *rigid upper limit* of their concentration (e.g. $N_{Be,}\max \cong 10^{20}$ cm^{-3} in GaAs). The physical mechanism limiting the maximum concentration can be a chemical solubility limit. In addition, *repulsive interaction* between impurities can also explain the maximum concentration limit observed for some impurities in semiconductors. According to this model (see Chap. 8), the maximum achievable doping concentration increases with decreasing growth temperature. Experimental results confirming this trend are shown in Fig. 11.8. The illustration shows the Be profiles of two GaAs samples grown by MBE at different temperatures. The Be impurities of density 4×10^{14} cm^{-2} were deposited during growth interruption. Subsequently, a 1000 Å thick top layer was grown by MBE. The entire growth and the Be deposition were performed at the two temperatures 500 °C and 400 °C. The profiles of Fig. 11.8 show (i) that significant broadening occurs for both growth temperatures, and (ii) that the profile of the sample grown at 400 °C is narrower and has a higher maximum concentration as compared to the sample grown at 500 °C. The change in width and maximum concentration is approximately a factor of two for the decrease in temperature by 100 °C. Thus, the results illustrated in Fig. 11.8 are consistent with the model of repulsive interaction between impurities.

The redistribution of impurities in III–V semiconductors follows some general tendencies which depend primarily on the impurity element rather than on the host semiconductor. The general characteristics of impurities used in δ-doping are summarized as follows.

Beryllium: Be is a relatively stable p-type impurity in III–V semiconductors. Excellent spatial localization can be achieved for concentrations below 10^{13} cm^{-2} (see also Chap. 8). However, when bulk concentrations are in the high 10^{19} cm^{-3} range, strong redistribution of Be in GaAs occurs (Schubert et al., 1990c).

Zinc: The characteristics of Zn are qualitatively similar to Be. Good spatial localization can be achieved at low growth temperatures and low Zn densities. However, strong spatial redistribution occurs for high Zn concentrations, typically in the $10^{18} - 10^{19}$ cm^{-3} range. Quantitatively, Zn is a faster diffuser than Be in many III–V semiconductors.

https://doi.org/10.1017/CBO9780511599828.014 Published online by Cambridge University Press

337-TA-1366 RX-0255

Carbon: C diffuses very slowly in III–V semiconductors and is characterized by exceptional stability (see also Chap. 8). However, the electrical activity of C was found to decrease for C densities exceeding 10^{12} cm^{-2} in GaAs (Nagle et al., 1991).

Silicon: Excellent spatial localization can be achieved with Si at low growth temperatures (see also Chap. 8). The electrical activity decreases strongly for Si densities exceeding 10^{13} cm^{-2} in GaAs (see also Sect. 11.3).

11.3 Transport properties

The electronic properties of δ-doped semiconductors are fundamentally different from homogeneously doped semiconductors. Impurities are randomly distributed in such homogeneously doped semiconductors. In contrast, impurities are confined to a plane in δ-doped semiconductors. This confinement results in changes of the electronic and transport properties of δ-doped as compared to homogeneously doped semiconductors which will be discussed below.

The free carrier concentrations of Be and Si δ-doped GaAs at T = 77 and 300 K are shown in Fig. 11.9 as a function of the impurity concentration (Schubert et al., 1986c). The 2D impurity density was inferred from the deposition time, growth rate, and the impurity effusion cell flux using Eq. (11.29). The 2D Hall carrier density was then measured for the n-type and p-type samples shown in Fig. 11.9 at T = 77 and 300 K. The solid line represents full activation of the impurities, i.e. $n^{2D} = N_D^{2D}$ and $p^{2D} = N_A^{2D}$. The n- as well as the p-type carrier concentration closely follow the solid line for impurity densities $\leq 10^{13}$ cm^{-2} indicating full electrical activation of the impurities. Full electrical activity of Be δ-doped GaAs is maintained at concentrations exceeding 10^{13} cm^{-2}. However, broadening of the Be distribution may occur at such high densities (Schubert et al., 1990c).

For Si doping densities exceeding 10^{13} cm^{-2}, the free carrier concentration saturates at approximately 10^{13} cm^{-2}. The saturation of the free carrier concentration was investigated by several groups. Beall et al. (1989) concluded that the free carrier saturation is caused by non-substitutional Si impurities in GaAs. The authors demonstrated the presence of electrically inactive Si complexes, Si_{As} acceptors, and $Si_{Ga} - Si_{As}$ pairs in heavily δ-doped GaAs. Similar results were previously reported by Maguire et al. (1987) for homogeneously doped GaAs. Schubert et al. (1990a) confirmed the conclusion of electrically inactive impurities by a comparison of CV and Hall measurements. Koenraad et al. (1990a) concluded from measurements under hydrostatic pressure that the saturation is *not* caused by the population of DX-centers. The exact

https://doi.org/10.1017/CBO9780511599828.014 Published online by Cambridge University Press

RX-0255.481

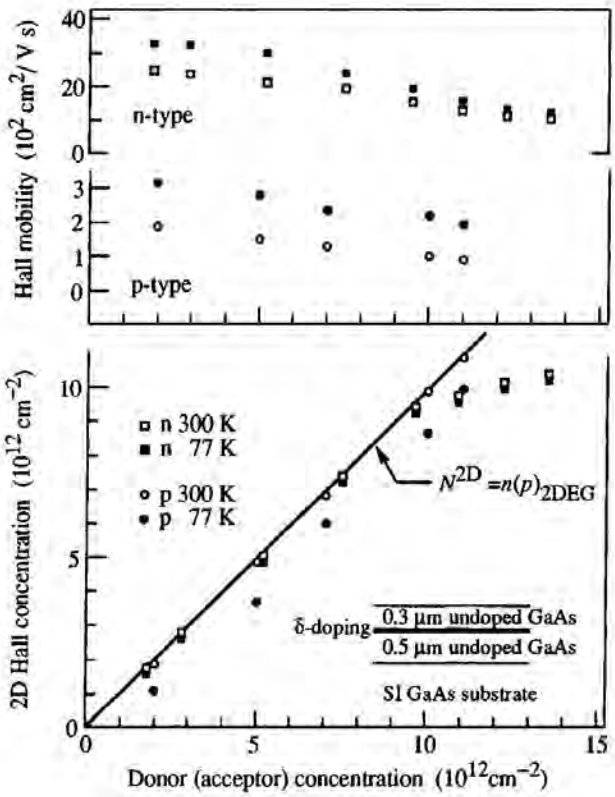


Fig. 11.9. Mobility (top) and free carrier Hall concentration (bottom) of Si and Be δ-doped GaAs versus dopant concentration.

density at which the saturation occurs, depends on the crystal growth conditions. The saturation density varies between 8×10^{12} cm^{-2} and 2.5×10^{13} cm^{-2} (Gillman et al., 1988).

The carrier mobility in δ-doped semiconductors is significantly different from homogeneously doped semiconductors. Schubert et al. (1987a) showed that ionized impurity scattering in δ-doped GaAs is reduced compared to homogeneously doped GaAs. Experimental electron mobilities of δ-doped GaAs at $T = 300$ K are shown in Fig. 11.10 as a function of the equivalent 3D doping concentration. This equivalent concentration is inferred from the 2D density according to $N_D = \left[N_D^{2D}\right]^{3/2}$. The equivalent 2D and 3D doping densities have the same mean distance between impurity atoms.

The experimental points shown in Fig. 11.10 are next compared with theoretical electron mobilities of n-type GaAs obtained from the Hilsum relation (Hilsum, 1974) shown by the solid line. At low doping concentrations, the

https://doi.org/10.1017/CBO9780511599828.014 Published online by Cambridge University Press

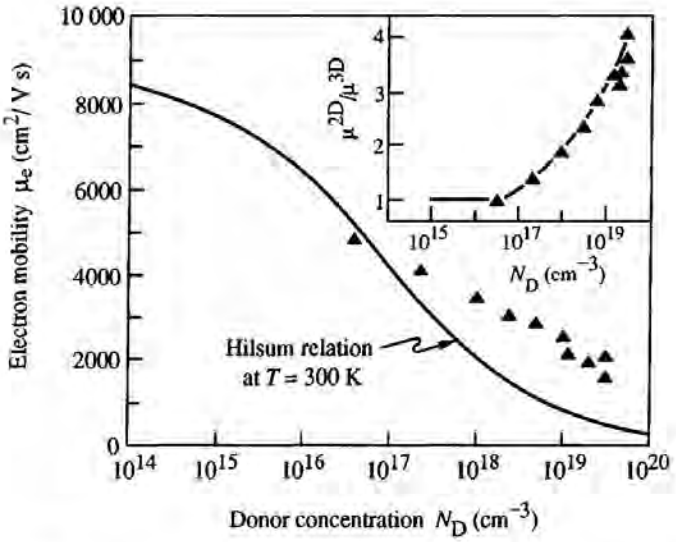


Fig. 11.10. Electron mobility versus doping concentration in homogeneously doped GaAs (solid line, Hilsum relation) and δ-doped GaAs (experimental points). Significantly higher mobilities are found in δ-doped GaAs. The mobility enhancement is shown in the inset.

mobilities of 3D- and 2D-doped GaAs coincide. However, at high doping concentrations, the mobility of 2D-doped GaAs significantly exceeds the mobility of homogeneously doped material (see Fig. 11.10 for illustration). At a concentration of $N_D^{3D} = 3.5 \times 10^{19}$ cm^{-3}, the mobility-enhancement μ^{2D}/μ^{3D} is more than a factor of 4. The enhancement is shown in the inset of Fig. 11.10. The distinguishing feature is the *increasing enhancement* of the electron mobility *at high doping concentrations*.

Temperature-dependent Hall measurements were performed to clarify the origins of the mobility enhancement (Schubert et al., 1987a). The electron mobility depends weakly on temperature in the entire temperature range, indicating a reduced role of impurity scattering. Ionized impurity scattering in conventionally, *non-degenerately*, 3D-doped samples depends on the sample temperature according to (Brooks–Herring)

$$\mu_{II} = \frac{128(2\pi)^{1/2}\,\varepsilon^2 (kT)^{3/2}}{(m^*)^{1/2}\,N_D^{3D}\,e^3}\left[\ln\frac{24m^*\,\varepsilon(kT)^2}{n\,e^2\,\hbar^2}\right]^{-1}. \qquad (11.39)$$

If impurity scattering were important, a dependence of $\mu \propto T^{3/2}$ would be expected at low temperatures. Ionized impurity scattering in *degenerately* doped semiconductors is beset with a number of difficulties (Chattopadhyay and Queisser, 1981), and cannot be expressed in closed form. However, a weaker

https://doi.org/10.1017/CBO9780511599828.014 Published online by Cambridge University Press

337-TA-1366 RX-0255

temperature dependence is expected for degenerate doping, since the *Fermi* velocity rather than the *thermal* velocity determines the average kinetic energy of carriers. The Fermi velocity depends weakly on temperature. A temperature dependence of $\mu \propto T^{0.29}$ is found in low temperatures for a heavily δ-doped sample. The weak $T^{0.29}$ dependence is significantly smaller than the $T^{1.5}$ dependence inferred from Eq. (11.39), indicating the strong degeneracy of the electron gas.

Two theoretical origins will be discussed for the mobility enhancement, i.e. (i) high degeneracy of the Fermi gas, and (ii) spatial electron–donor separation in the $n = 1, 3, \ldots$ subbands. The 2DEG of δ-doped epitaxial layers is highly degenerate (i.e. high kinetic energy parallel to the donor plane). Carriers energetically close to the Fermi surface, which are in turn most relevant to elastic and inelastic scattering, have a kinetic energy of $E_F - E_n$ where E_n is the eigenstate energy. The kinetic energy can exceed the thermal energy kT considerably. Consequently, the temperature-dependent elastic impurity scattering is reduced as long as the kinetic energy term, $E_F - E_n$, dominates, which occurs at high concentrations. The latter condition is fulfilled in the entire temperature range investigated. It is worthwhile noting that the eigenstate energy itself is partly potential and partly kinetic (in the perpendicular direction to the well plane). The kinetic part can be calculated from

$$\langle E_{kin} \rangle = E_n - \langle \psi(x) \, | E_c(x) | \, \psi(x) \rangle \qquad (11.40)$$

and is usually a considerable fraction of the total eigenstate energy. The kinetic part of the eigenstate energy does not, however, enter the calculation of ionized impurity scattering in Eq. (11.39).

Spatial separation of free electrons from their parent ionized donor impurities occur in the odd-labeled ($n = 1, 3, \ldots$) subbands. Carriers in the $n = 1$ state therefore have zero probability of being in the donor plane, resulting in a mobility enhancement of electrons in odd-numbered eigenstates. This electron–donor separation in real space in δ-doped structures is reminiscent of the carrier–impurity separation in selectively doped heterostructures.

A mobility enhancement in δ-doped GaAs was also found by Koenraad et al. (1990b) using cyclotron resonance measurements. They attributed the enhanced mobility to the small overlap between the ionized donors and the electron wave function, especially for states with high subband index. Subsequently, an enhancement of electron mobility was also found for Sb δ-doped Si (Gossmann and Schubert, 1993).

The electronic wave function in δ-doped semiconductors can be influenced further by compositional quantum wells. Masselink (1991a) showed that the

https://doi.org/10.1017/CBO9780511599828.014 Published online by Cambridge University Press

RX-0255.484

overlap of the electronic ground-state wave function of a square-shaped well is maximized if the impurities are confined to the center of the well. In this case, the electron mobility of the ground state is lower as compared to bulk GaAs doped at the same level. High field transport measurements in $Al_xGa_{1-x}As$/GaAs quantum wells revealed an increasing differential mobility with increasing electric field (Masselink, 1991b). The large increase in differential mobility was attributed to heating of electrons out of the symmetric ground state into the antisymmetric first excited state. Because the excited state has a node at the δ-doped plane of impurities, these hot electrons have a much smaller overlap with ionized impurities in the well center and therefore have a higher mobility.

Delta-doping in n-type $Al_xGa_{1-x}As$ was shown to strongly influence the formation of DX-centers (Etienne and Thierry-Mieg, 1988). The number of DX-centers in $Al_{0.32}Ga_{0.68}As$ was found to decrease with increasing doping concentration. At sufficiently high doping densities, the effect of persistent photoconductivity, which is known to be due to DX-centers, vanishes. A physical mechanism causing the reduction of DX-centers was proposed by Koenraad (1990a), who argued that the energy of the DX-level depends on the doping concentration. The DX-level shifts away from the Γ conduction band minimum in heavily δ-doped GaAs and, most likely, $Al_xGa_{1-x}As$. Since the DX-level shifts to higher energies, it becomes unpopulated. As a result, persistent photoconductivity and free carrier freeze out, which are associated with the DX-center, are not observed in heavily δ-doped $Al_xGa_{1-x}As$.

Elastic electron scattering of carriers by ionized impurities in δ-doped semiconductors has been considered by Levi et al. (1989) for *random* and *ordered* distributions of impurities in the δ-doped plane. It is a common assumption that impurities in homogeneously doped semiconductors are distributed randomly, i.e. are distributed according to the Poisson distribution (Shockley, 1961). In δ-doped semiconductors, the distribution of impurities in the δ-doped plane is usually also assumed to be poissonian. However, Levi et al. (1989) proposed that, under suitable growth conditions, high-density δ-doping may result in partial spatial ordering of the impurity atoms. A reduction of the elastic scattering rate by up to a factor of four was predicted. To date, experimental evidence for ordered doping distributions in III–V semiconductors has not been reported. However, Headrick et al. (1990 and 1991) reported on δ-doping with a full one monolayer coverage of boron (B) impurities in Si. The mobilities measured were comparable to highly B-doped bulk Si.

https://doi.org/10.1017/CBO9780511599828.014 Published online by Cambridge University Press

11.4 Electronic devices

The employment of δ-doping opens up new possibilities for device structures. First, the δ-doping technique allows one to improve and optimize known semiconductor device structures. As will be shown below, a δ-function-like doping profile represents the optimum doping distribution for many well-known device structures. For example, δ-doping in high-mobility heterostructures minimizes remote ionized impurity scattering. Thus, modulation-doped heterostructures are *optimized* by the employment of the δ-doping technique. Furthermore, δ-doping profiles in semiconductors are the ultimate spatial distribution of dopants. It is well-known that the performance and speed of semiconductor devices increase as the spatial dimensions of the device structure decrease. Narrower doping distributions are a natural consequence of the spatial scaling process. Delta-doped semiconductors therefore play an increasingly important role in semiconductor devices scaled down to their ultimate spatial limit.

Second, δ-doped semiconductors lead to entirely novel concepts that cannot be realized in conventional, homogeneously doped structures. Delta-doped structures exhibit a quantized free carrier distribution at sufficiently high doping densities. Such a quantized free carrier system can only be achieved in δ-doped structures but not in homogeneously doped structures. Examples of structures that can be realized only by the δ-doping technique will be discussed below.

11.4.1 Non-alloyed ohmic contacts

Ohmic contacts play a central role in semiconductor devices. Ohmic contact metallizations usually consist of a dopant such as Be, Zn, or Ge, and a low-resistance metal such as Au. Upon alloying, dopants diffuse into the semiconductor and form a highly doped semiconductor–metal junction. Ohmic metal–semiconductor contacts are tunnel contacts and their contact resistance is determined by the barrier height and the width of the depletion region. While the barrier height is a constant for a given metal–semiconductor junction, the width of the depletion region depends on the doping concentration. High doping concentrations decrease the width of the depletion region and lower the contact resistance. The high doping concentrations achievable by the δ-doping technique are therefore advantageous for low-resistance ohmic contact formation.

The band diagram of a δ-doped metal–semiconductor contact is shown in Fig. 11.11 (Schubert et al., 1986b). The δ-doped layer with density N^{2D} is located at a distance z_D from the metal–semiconductor junction. The figure also shows that the effective tunnel barrier thickness depends on the voltage applied to the junction. The doping density must be sufficiently high in order to lower the

https://doi.org/10.1017/CBO9780511599828.014 Published online by Cambridge University Press

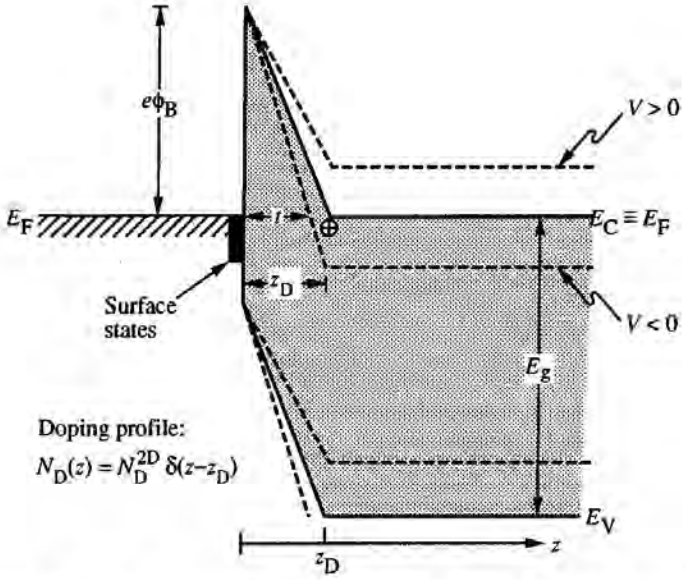


Fig. 11.11. Band diagram of a δ-doped non-alloyed ohmic contact. Since the thickness t is small (~20 Å), tunneling is the dominant transport mechanism across the Schottky barrier.

conduction band at the doped region to or below the Fermi level. The minimum doping density is then given by

$$N^{2D} \geq \frac{\varepsilon \phi_B}{e z_D} \tag{11.41}$$

where ε, e, and ϕ_B are the permittivity, elementary charge and the semiconductor barrier height, respectively.

The specific contact resistance, ρ_c, of a δ-doped ohmic contact can be calculated as a function of the distance z_D, based on an isotropic, parabolic semiconductor band structure and the well-known Fowler–Nordheim tunneling current equation. The result of the calculation is (Schubert et al., 1986b)

$$(\rho_c)^{-1} = \left(\frac{e}{2\pi\hbar z_D}\right)^2 (\hbar + z_D\sqrt{em^*\phi_B})\exp\left(-\frac{2z_D}{\hbar}\sqrt{em^*\phi_B}\right). \tag{11.42}$$

Here the electron effective mass, m^*, is the mass associated with motion perpendicular to the metal–semiconductor interfacial plane. At high doping concentrations, contact resistances $< 10^{-8}\ \Omega\ \text{cm}^2$ can be inferred from Eq. (11.42).

The current–voltage characteristic of a non-alloyed ohmic contact is shown in

https://doi.org/10.1017/CBO9780511599828.014 Published online by Cambridge University Press

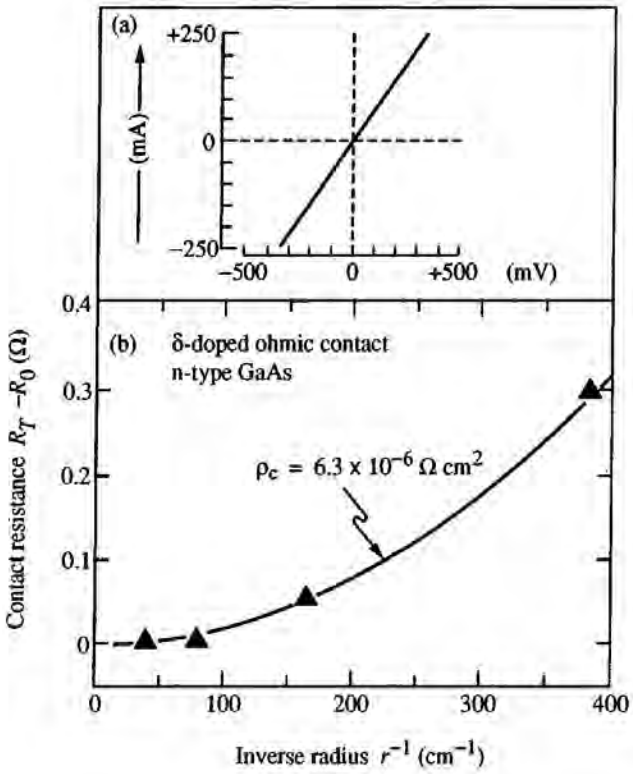


Fig. 11.12. (a) Current–voltage characteristic of the non-alloyed δ-doped ohmic contact to n-type GaAs. Evaluation of the specific contact resistance of typical δ-doped contacts reveals a specific contact resistance of $6.3 \times 10^{-6}\ \Omega\ cm^2$. The lowest contact resistances measured are in the 1×10^{-6} to $2 \times 10^{-6}\ \Omega\ cm^2$ range.

Fig. 11.12(a) for a GaAs:Si sample grown by MBE. The characteristic is strictly linear. The evaluation of the specific contact resistance is shown in Fig. 11.12(b) for circular contacts of various diameters. Evaluation of the contact resistance yields $\rho_c = 6.3 \times 10^{-6}\ \Omega\ cm^2$. Further experimental details were reported by Schubert et al. (1986b).

Non-alloyed ohmic contacts have a smooth surface morphology due to the lack of any thermal processing. The smooth surface morphology is advantageous for photolithographic processing of small patterns. Furthermore, the smooth surface morphology of the metal permits use of the metal as a reflector for optical radiation. Such reflectors are required in many optoelectronic devices.

11.4.2 Elimination of heterojunction band discontinuities

Heterojunction band discontinuities will be an important aspect of future high-speed devices. In these devices, the employment of band discontinuities allows

https://doi.org/10.1017/CBO9780511599828.014 Published online by Cambridge University Press

the realization of novel concepts. On the other hand, heterojunction band discontinuities can have detrimental effects in some devices. Specifically, the current flow across a heterojunction is clearly impeded by heterojunction barriers.

Heterojunction band discontinuities can be completely eliminated in either the conduction band or the valence band by using the δ-doping technique and compositional grading of the heterojunction (Gossmann and Schubert, 1993). The elimination is based on the compensation of the electric field of a doping dipole by the quasi-electric field caused by the compositional grading of the heterojunction. Consider a junction between two semiconductors 'A' and 'B'. In the interfacial region, the alloy $A_{1-x}B_x$ is formed, where x is the alloy composition. The junction is graded *linearly*, if the composition x depends *linearly* on the spatial coordinate. If we further assume that the energy gap of the semiconductor $A_{1-x}B_x$ depends linearly on the composition and that the ratio $\Delta E_C/\Delta E_V$ does not depend on the composition, then a quasi-electric field exists in the graded region of the heterojunction. Assuming that Δz is the length of the graded region, then the magnitude of the quasi-field is given by $\mathcal{E} = (\Delta E_C/e\Delta z)$ and $(\Delta E_V/e\Delta z)$ for the conduction and valence band, respectively.

A δ-doping dipole can compensate the quasi-electric field at heterojunction band discontinuities. Consider a dipole that consists of a donor and an acceptor sheet separated by Δz. The donor and acceptor doping densities $N_D^{2D} = N_A^{2D} = N^{2D}$ are assumed to be equal. Then the structure will be 'compensated', i.e. will not contain free carriers originating from impurities. The electric field of the dipole can be calculated from Poisson's equation; the magnitude of the field is given by

$$\mathcal{E} = (e/\varepsilon)\, N^{2D} . \tag{11.43}$$

Equating the quasi-field caused by compositional grading and the field caused by the doping dipole allows one to determine the required impurity density according to

$$N^{2D} = \frac{\varepsilon \Delta E_C}{e^2 \Delta z} . \tag{11.44}$$

At this doping density, the built-in field due to the graded composition exactly compensates the electric field due to the doping dipole. Thus, the band discontinuity is eliminated.

Heterojunction band discontinuities can also be eliminated by using modulation doping and parabolic grading (Schubert et al., 1992). Another possibility of modifying the properties of heterojunctions constitutes the concept of 'tuning' the magnitude of band discontinuities by doping dipoles (Capasso

https://doi.org/10.1017/CBO9780511599828.014 Published online by Cambridge University Press

et al., 1985a and 1985b). The doping dipoles are closely spaced δ-doped donor and acceptor sheets. For appropriately selected donor and acceptor concentrations, the 'effective' discontinuity can be tuned over a wide range of energies. Thus, the two concepts of *tuning* (doping without grading) and *elimination* (doping and compositional grading) of heterojunction band discontinuities allow significant modifications of such junctions.

11.4.3 Schottky–Gate field effect transistors

The properties of field-effect transistors improve as the spatial dimensions of the transistor are scaled down in size. The specific method of improvement depends on the type of field-effect transistor considered. In this section, δ-doped *homostructure* field-effect transistors (FETs) and selectively δ-doped *heterostructure* FETs are discussed. (Board et al., 1981; Schubert and Ploog 1985; Schubert et al., 1986c).

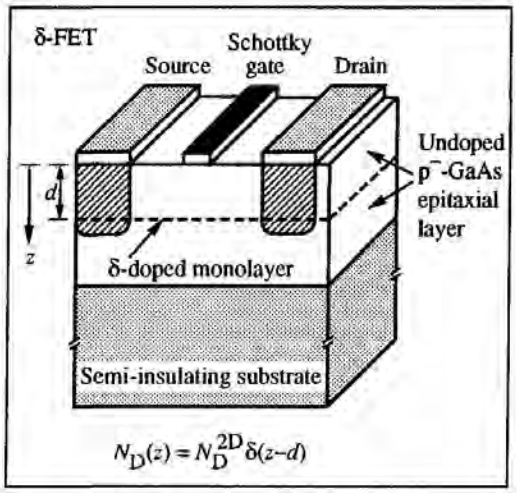


Fig. 11.13. Delta-doped GaAs metal–semiconductor field-effect transistor (δ-FET). The conductive channel is a Si δ-doped layer located at a distance d below the Scottky gate.

A schematic illustration of a δ-doped FET is shown in Fig. 11.13. The simplest structure of such an FET consists of a semi-insulating substrate and an epitaxial layer containing a δ-doped spike. A highly doped region near the semiconductor surface improves ohmic contact resistance as well as the source resistance of the device (Schubert et al., 1986a).

The advantages of the δ-doped Schottky-gate FET are (i) reduced short-channel effects, (ii) higher transconductance, and (iii) higher speed, as compared to a homogeneously doped FET. Reduced short-channel effects are due to the proximity of the channel to the gate metal and the minimized spatial width of the electron channel. The δ-doping technique allows one to place the doped channel

https://doi.org/10.1017/CBO9780511599828.014 Published online by Cambridge University Press

in close proximity to the gate. Furthermore, the spatial width of the electron channel is reduced as compared to a homogeneously doped channel. Short channel effects become important if the gate-to-channel distance and the spatial extent of the channel become comparable to the gate length. Since the spatial dimensions of the doping profile are minimized for δ-doped FETs, short-channel effects are less prominent in δ-doped FETs as compared to regular FETs with the same gate length.

The high transconductance of δ-doped FETs is a result of the proximity of the Schottky gate to the electron channel. It is well known that the transconductance of an FET increases with decreasing gate-to-channel distance. The increased transconductance can be derived from either the Shockley transistor model (graded channel approximation) or the saturated velocity transistor model. From a planar capacitor point of view, the increased transconductance is a result of the increased amount of induced charge per unit gate voltage.

An increase in the transit frequency of δ-doped FETs results, if the decreased gate-to-channel distance is accompanied by a shorter gate length. The transit frequency of an FET is given by

$$f_t = \frac{g_m}{2\pi C_{GS}} \tag{11.45}$$

where g_m is the transconductance and C_{GS} is the gate-source capacitance. This capacitance can be approximated by the gate-to-channel capacitance. The latter increases if the gate-to-channel separation is reduced and decreases with reduced gate length. Thus, higher speed operation is inferred from Eq. (11.45) due to the increased transconductance of the δ-doped FET.

The gate-to-source and the drain-source current–voltage characteristics of a δ-doped FET are shown in Fig. 11.14 (Schubert et al., 1986a). The FET was fabricated in a two-mask self-aligned process using non-alloyed ohmic contacts. The transconductance of the 1 μm gate length device is 240 mS/mm.

Delta doping has also been applied to selectively doped heterostructure transistors (Schubert et al., 1987c). The devices are characterized by a high density of the electron gas at the hetero interface. High free carrier densities result in improved transconductance as well as in lower source-to-channel series resistance. Electron densities exceeding 1.5×10^{12} cm^{-2} at 300 K were demonstrated with δ-doped heterostructures. Low-temperature measurements revealed that two electronic subbands are occupied with a total electron density exceeding 10^{12} cm^{-2}. High transconductances of 350 mS/mm were obtained in such selectively δ-doped heterostructures with a gate length of 1 μm.

https://doi.org/10.1017/CBO9780511599828.014 Published online by Cambridge University Press

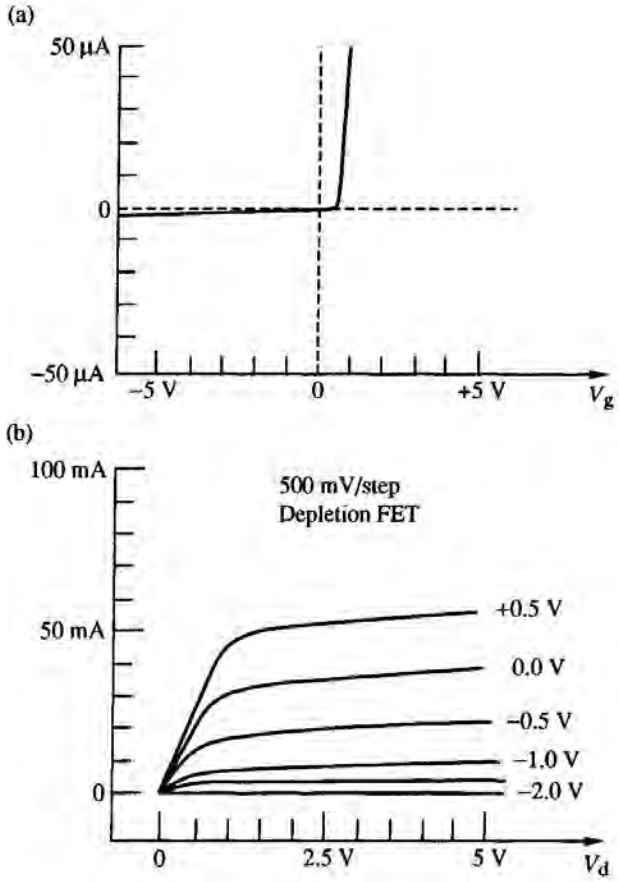


Fig. 11.14. (a) Gate-source and (b) drain-source current–voltage characteristics of a δ-doped depletion-mode metal–semiconductor field-effect transistor (MESFET) with a gate length of 1.3 μm, a width of 150 μm, and a transconductance of 240 mS/mm.

11.4.4 Bipolar transistors

The employment of the δ-doping technique in bipolar transistors is motivated by the decrease in achievable base layer thicknesses. The thickness of the base layer is of special importance. Majority carriers from the emitter traverse the base by either a diffusive motion (thick base layers) or by ballistic flight (thin base layers). For both transport models, i.e. diffusive and ballistic transport, a thin base is advantageous for minimum transit time. A reduction of transit time simultaneously reduces the probability of recombination in the base. In other words, the transport factor of the base, which is a well-known quantity in bipolar transistor analysis, increases with decreasing base thickness.

https://doi.org/10.1017/CBO9780511599828.014 Published online by Cambridge University Press

The concept of δ-doping in homojunction bipolar transistors was motivated by the potentially greater speed achievable (Schubert et al., 1984). Delta-doping in bipolar transistors was first realized in heterostructure devices made of III–V semiconductors grown by MBE (Malik et al., 1988b). The authors pointed out that the base transit time can be reduced by confining the dopants to a thin sheet.

Another application of the δ-doping technique in bipolar transistors is in the collector layer. A doping dipole of closely spaced p- and n-type doping sheets was employed to create a built-in electric field in the collector layer adjacent to the base layer (Tokumitsu et al., 1990). The purpose of the field is to sweep out majority carriers from the base-collector junction region which have traversed the base. The carriers will enter the neutral collector region more rapidly due to the electric field. The overall speed of the transistor can thus be improved by the dipole layer.

11.4.5 Diodes

The field distribution in semiconductor diodes is critical for many diodes, for example planar barrier diodes, IMPATT diodes, etc. The δ-doping technique allows one to tailor the potential and electric field of the diode leading to improved electrical characteristics. The planar barrier diode (Malik et al., 1980a, 1980b, 1982) is a majority carrier diode. It has a low capacitance due to the absence of the diffusion capacitance of conventional bipolar diodes. Therefore, the planar barrier diode is well suited for high-speed operation of mixer diodes and other applications. Furthermore, the planar barrier diode allows one to 'tailor' the current–voltage characteristic to a much higher degree than conventional pn-junction diodes. The planar barrier diode consists of an n-type region, an intrinsic region, a p-type δ-doped region, an intrinsic region, and finally an n-type region. Two optional n-type δ-doped sheets may be included at the boundary between the n-type and the intrinsic region. The p-type δ-doped region in the center of the diode is completely depleted of holes. The diode is thus a unipolar device. Symmetric as well as asymmetric current–voltage characteristics can be achieved by adjusting the thicknesses of the two intrinsic regions.

IMPATT or impact avalanche transit time diodes are active devices used for microwave generation in the frequency range 50–150 GHz. The diodes have an avalanche multiplication region and a transit time region. The multiplication region has a high electric field while the transit time region has a constant lower electric field. It is desirable to control the field distribution accurately in order to obtain devices with well-controlled characteristics. Owing to the stringent requirements of the IMPATT diodes, it was proposed to employ the δ-doping technique for improved characteristics (Schubert et al. 1984). IMPATT diodes

https://doi.org/10.1017/CBO9780511599828.014 Published online by Cambridge University Press

337-TA-1366 RX-0255

incorporating δ-doped layers were grown by Si MBE (Luy, 1990). The author reported efficiencies exceeding 10% at a frequency of 100 GHz. The improvements were attributed to layer design, packaging, and resonator circuit design. Furthermore, a δ-doped spike effectively restricted the ionization region. Delta-doped IMPATT diodes made from III–V semiconductors have not been reported.

11.5 Optical devices

The initial proposal for superlattices comprised not only compositional superlattices, e.g. of the type $Al_xGa_{1-x}As/GaAs$, but also ***doping superlattices*** (Esaki and Tsu, 1970). Such doping superlattices consist of a periodic sequence of alternating n-type and p-type regions in a semiconductor. A periodic potential results along the semiconductor growth direction due to positive and negative impurity charges. The periodic superlattice potential results in novel electronic properties not observed in conventional semiconductors. Shortly after the initial proposal of doping superlattices, published work was exclusively of a theoretical nature (Ovsyannikov, 1971; Romanov, 1972; Döhler, 1972a and 1972b; Romanov and Orlov, 1973). Experimental work started in the 1980s and included the observation of the tunability of the energy gap in doping superlattices (Döhler et al., 1981) and the first observation of quantum-confined interband transitions (Schubert et al., 1988b and 1989a). Extended reviews on doping superlattices have now become available (Schubert, 1990a; Döhler, 1986; Ploog and Döhler, 1983).

The band diagram of a symmetric δ-doped doping superlattice is shown in Fig. 11.15(a). The symmetric superlattice consists of alternating n-type and p-type doping sheets separated by $z_p/2$. Using the same n- and p-type doping densities ($N_D^{2D} = N_A^{2D}$) results in a depleted doping superlattice with a sawtooth-shaped band diagram. This is called a sawtooth superlattice (Schubert et al., 1985c). Using different thicknesses between the doping sheets results in an asymmetric band structure as shown in Fig. 11.15 (Glass et al., 1989). Note that the conduction band and valence band edges vary *parallel* in doping superlattices. This characteristic is different from compositional $Al_xGa_{1-x}A/GaAs$ superlattices, where the band edges vary *antiparallel* as shown in Fig. 11.15(b).

The band diagram of a symmetric sawtooth doping superlattice including its quantized electronic states is shown in greater detail in Fig. 11.16. For symmetric doping superlattices with the same donor and acceptor densities, the total band modulation can be calculated from Poisson's equation and is given by

https://doi.org/10.1017/CBO9780511599828.014 Published online by Cambridge University Press

RX-0255.494

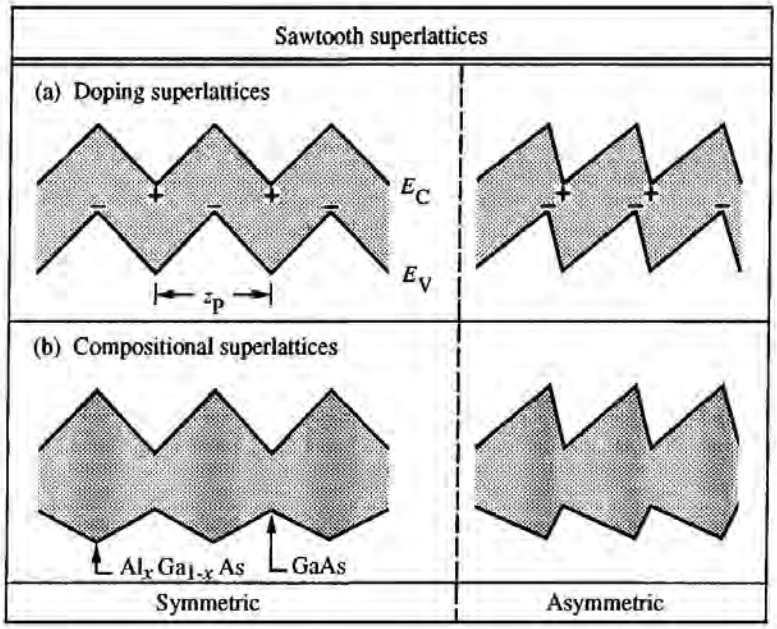


Fig. 11.15. Symmetric and asymmetric sawtooth superlattices. In doping superlattices, the conduction- and valence-band edges are parallel whereas they are antiparallel in compositional superlattices.

$$V_{zz} = eN^{2D}z_p/4\varepsilon\,. \tag{11.46}$$

The effective energy gap of the doping superlattice, E_g^{SL}, is defined as the lowest transition energy between quantum-confined conduction and valence band states, i.e.

$$\boxed{E_g^{SL} = E_g - eV_{zz} + E_0^e + E_0^{hh}} \tag{11.47}$$

where E_g is the original gap energy of the host lattice. It is thus possible to extend the energy gap of any semiconductor to lower energies by using the doping superlattice concept.

A second important property of doping superlattices is the relatively weak oscillator strength of optical transitions. The location of maximum electron concentration is shifted with respect to the location of maximum hole concentration by half a superlattice period, as shown in Fig. 11.16. As a result, the transition matrix element, which is proportional to the overlap of the electron and hole wave functions, is reduced as compared to the bulk case. Due to the

https://doi.org/10.1017/CBO9780511599828.014 Published online by Cambridge University Press

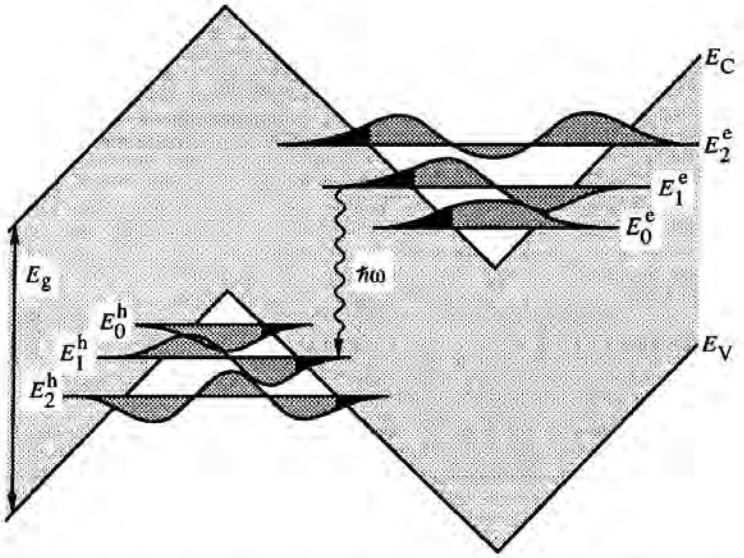


Fig. 11.16. Schematic band diagram of a sawtooth superlattice. The overlap of electron and hole wave functions increases exponentially with subband index.

weaker oscillator strength in doping superlattices, optical measurements are frequently performed at low temperatures (Ploog and Döhler, 1983).

Delta-doped superlattices are the optimum doping superlattice structure. It was shown that the potential modulation of the band edges is maximized by δ-doping. Furthermore, potential fluctuations are minimized in such structures due to the confinement of impurities to a sheet (Schubert, 1990a). As a result, smaller periods can be achieved in the sawtooth superlattice as compared to the conventional doping superlattice structure.

The remainder of this section emphasizes device applications of doping superlattices, including superlattice light-emitting diodes (LEDs) and lasers. The spectroscopic properties of doping superlattices, including quantum-confined interband transitions, were discussed in Chap. 10.

11.5.1 Perpendicular transport

Transport in semiconductor structures in which the dopant plane is perpendicular to the transport direction were reported by Malik et al. (1980a, 1980b). They used n-i-p-i-n doping profiles which result in a triangular barrier structure and obtained a rectifying majority carrier diode. Subsequently, Kazarinov and Luryi (1981) calculated the charge injection over such a triangular barrier. They obtained an exact expression for the current–voltage characteristic of the triangular barrier

https://doi.org/10.1017/CBO9780511599828.014 Published online by Cambridge University Press

diode, which was in agreement with results published by Malik et al. (1980b). Further experimental results and a comparison with theoretical results were reported by Gossard et al. (1982).

The study of electron transport in δ-doped doping superlattices revealed drastic differences between short-period and long-period doping superlattices (Schubert et al., 1987b). A new type of negative differential conductivity (NDC) was found in long-period doping superlattices. In short-period doping superlattices, NDC is not observed. Instead, efficient electron transport is found in the perpendicular direction to the superlattice planes in short-period superlattices. Furthermore, Sun and Liu (1991) showed that a diode-like current–voltage characteristic is obtained at room temperature in a sawtooth doping superlattice. At $T = 77$ K, S-type NDC was observed resulting from avalanche multiplication in the superlattice region.

A three-terminal δ-doped barrier switching device with S-shaped negative differential resistance was proposed and realized by Baillargeon et al. (1989). The authors showed that the S-type NDC can be controlled by the third terminal. The barrier height was increased and decreased according to the voltage applied to that terminal. The results showed that the device could be used for oscillators at frequencies exceeding 20 GHz.

Resonant tunneling in δ-doped structures was studied by Wang et al. (1991) and Houng et al. (1992). The authors used p^+-type δ-doping embedded in an n^+ region and n^+-type δ-doping embedded between two metal–semiconductor contacts. The resonant tunneling process was evidenced by structure in the current–voltage curves. A peak-to-valley ratio of 1.5 was reported. Finally, transmission resonances and transmission coefficients were calculated using Airy functions.

11.5.2 Light-emitting diodes

Light-emitting diodes (LEDs), with an active region consisting of a doping superlattice, emit light of energy *below* the band gap of the host semiconductor. As evidenced by Eq. (11.47), the superlattice energy gap can be smaller than the gap of the host semiconductor. Thus, doping superlattice LEDs offer a unique characteristic not found in other semiconductor structures. A sketch of an edge-emitting sawtooth doping superlattice diode is shown in Fig. 11.17 along with the δ-function-like doping profile and the sawtooth-shaped band diagram (Schubert et al., 1985b). The edge-emitting diode has $Al_xGa_{1-x}As$ confinement layers and a GaAs active region. The p-n junction is located at the superlattice region, which results in carrier recombination in the superlattice region.

Electroluminescent spectra of the LEDs operating at 300 K are shown in

https://doi.org/10.1017/CBO9780511599828.014 Published online by Cambridge University Press

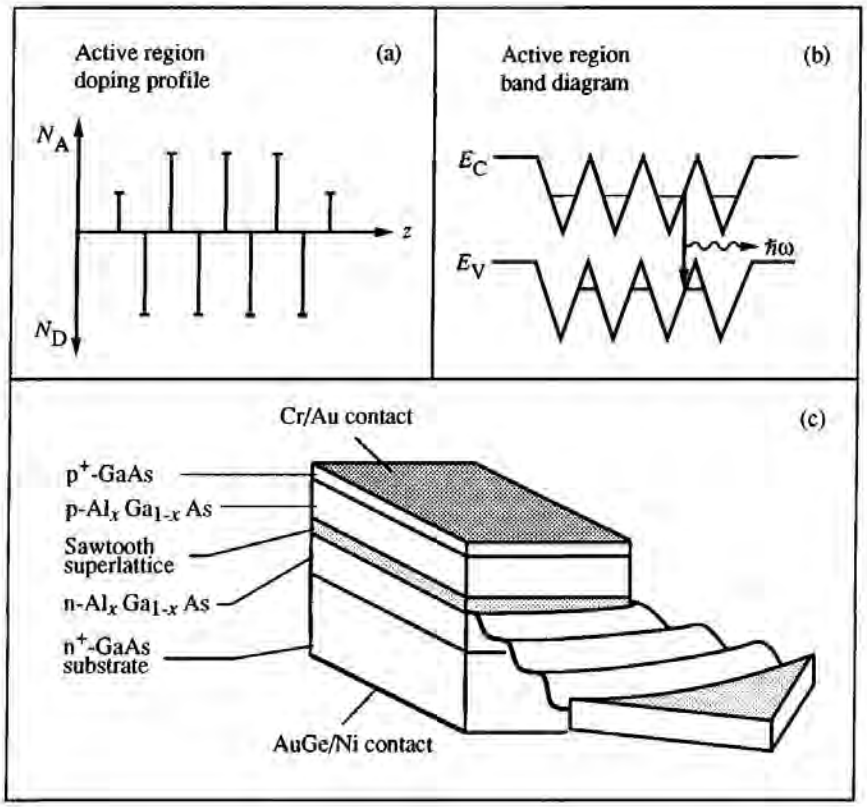


Fig. 11.17. (a) Doping profile, (b) band diagram, and (c) basic structure of the edge-emitting sawtooth superlattice light-emitting diode. The doping superlattice in the active region is sandwiched between $Al_xGa_{1-x}As$ confinement layers.

Fig. 11.18 for three different excitation currents. The period of the doping superlattice active region is $z_p = 200$ Å and the δ-doping densities are $N_D^{2D} = N_A^{2D} = 5 \times 10^{12}$ cm^{-2}. The peak wavelength of the LED is $\lambda \cong 960$ nm, i.e. well below the band gap of GaAs. These wavelengths were inaccessible to conventional GaAs LEDs. At the wavelength corresponding to the bandgap energy of the GaAs host material, no luminescence signal is detected, demonstrating the superlattice character of the active region of the LED.

The three electroluminescence spectra exhibit a small shift of the peak wavelength to shorter wavelengths with increasing excitation intensity, shifting from 966 nm at low excitation intensity to 959 nm at high excitation intensity. The total shift in energy is small if compared to the total linewidth of the luminescence line ($\Delta\lambda > 50$ nm). The energy upshift is probably due to (i) band filling effects and (ii) screening of ionized impurities by free carriers. The latter

https://doi.org/10.1017/CBO9780511599828.014 Published online by Cambridge University Press

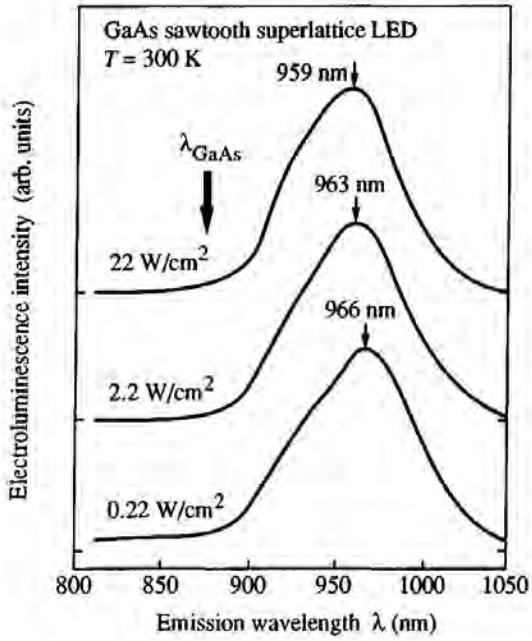


Fig. 11.18. Room-temperature electroluminescence spectra of a GaAs sawtooth superlattice light-emitting diode at three injection current densities. The current densities equal power densities of 0.22, 2.2, and 22 W/cm^2.

effect has been discussed extensively in the literature (Ploog and Döhler, 1983). Larger tuning ranges were observed in doping superlattice light-emitting diodes with longer periods (Hasnain et al., 1986). The authors used selective contacts for the n-type and p-type regions. The period of the superlattice reported by the authors was 600 Å and 900 Å.

11.5.3 Lasers

Lasers are one of the most interesting device applications for doping superlattices. Tunable lasers are desirable for optical wavelength multiplex communication systems. On the other hand, optical transitions in doping superlattices are inherently of weaker oscillator strength as compared to bulk material. Thus, their realization requires high quality epitaxial material. First attempts to realize a doping superlattice laser revealed optical amplification, i.e. gain (Jung et al., 1983). However, laser emission was not achieved.

The first doping superlattice current injection laser (Schubert et al., 1985a) was realized in GaAs using the δ-doping technique with no evidence for tunability. Laser emission in doping superlattices was also reported by Vojak et al. (1986). The photo-pumped lasers emitted below the bandgap of GaAs, also with no evidence for tunability. The first tunable doping superlattice laser was realized by inhomogeneous excitation of the Fabry–Perot cavity (Schubert et al. 1989c). A schematic sketch of the layer sequence, the active region doping

https://doi.org/10.1017/CBO9780511599828.014 Published online by Cambridge University Press

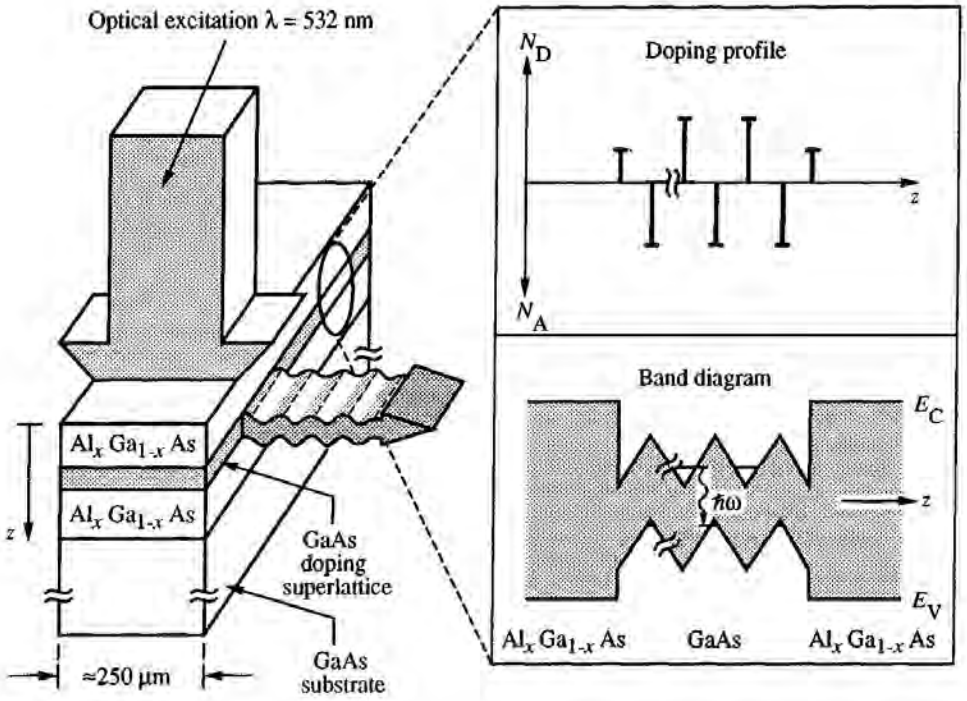


Fig. 11.19. Geometry used for optical excitation of the optically excited tunable sawtooth superlattice laser. The active region doping profile and the band diagram are shown on the right.

profile, and the corresponding band diagram are shown in Fig. 11.19. After epitaxial growth, the layers were cleaved into stripes of nominal 250 μm length and 1 cm width. A frequency-doubled Nd-doped Q-switched YAG laser (λ = 532 nm) was used for optical excitation. Light emission from the sample was detected with a Si detector using gated detection. The laser samples were cooled in a variable-temperature He cryostat.

The spontaneous and stimulated emission spectra at T = 5K are shown in Fig. 11.20 together with the light output versus excitation intensity curve. In the spontaneous emission regime at low excitation intensity, the peak wavelength moves to shorter wavelengths with increasing excitation intensity. At higher excitation intensities, stimulated emission occurs, which is accompanied by the characteristic kink in the light output curve of Fig. 11.20 and a narrowing of the emission spectrum to values much below the thermal energy kT. However, the peak wavelength does not change in the stimulated emission regime. Such a constant emission energy is not unexpected, since upon reaching the laser threshold, the Fermi level remains constant and additional carriers undergo

https://doi.org/10.1017/CBO9780511599828.014 Published online by Cambridge University Press

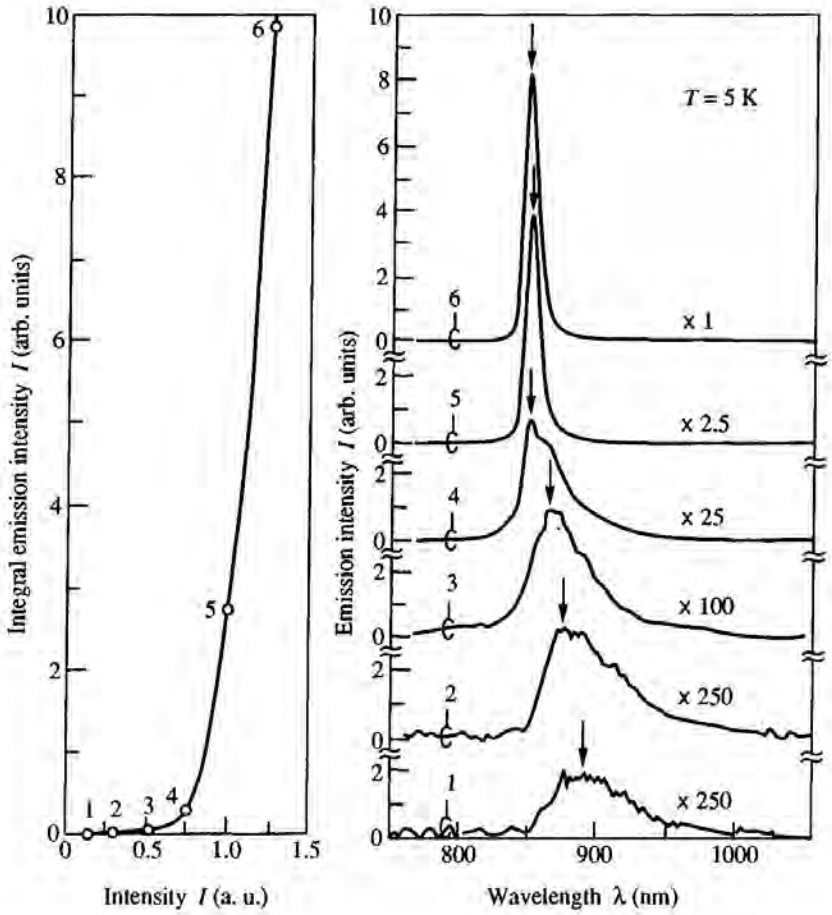


Fig. 11.20. Low-temperature (left) emission intensity versus excitation intensity of the tunable sawtooth doping superlattice laser, and (right) optical spectra below, at, and above threshold intensity. The wavelength remains constant after the laser threshold is reached.

stimulated recombination with a correspondingly very short lifetime. Thus, the emission energy remains constant for different excitation intensities in the stimulated emission regime.

The emission energy can be tuned continuously by inhomogeneous excitation of the Fabry–Perot cavity. Such inhomogeneous excitation is achieved by displacing the exciting beam from its centered position, as shown in the top part of Fig. 11.21. The inhomogeneous excitation results in a higher laser emission energy as compared to the symmetric excitation. Figure 11.21 reveals that the tuning range of the laser is approximately 35 Å. This tuning range does not represent a fundamental limit. The tuning range is limited by the intensity

https://doi.org/10.1017/CBO9780511599828.014 Published online by Cambridge University Press

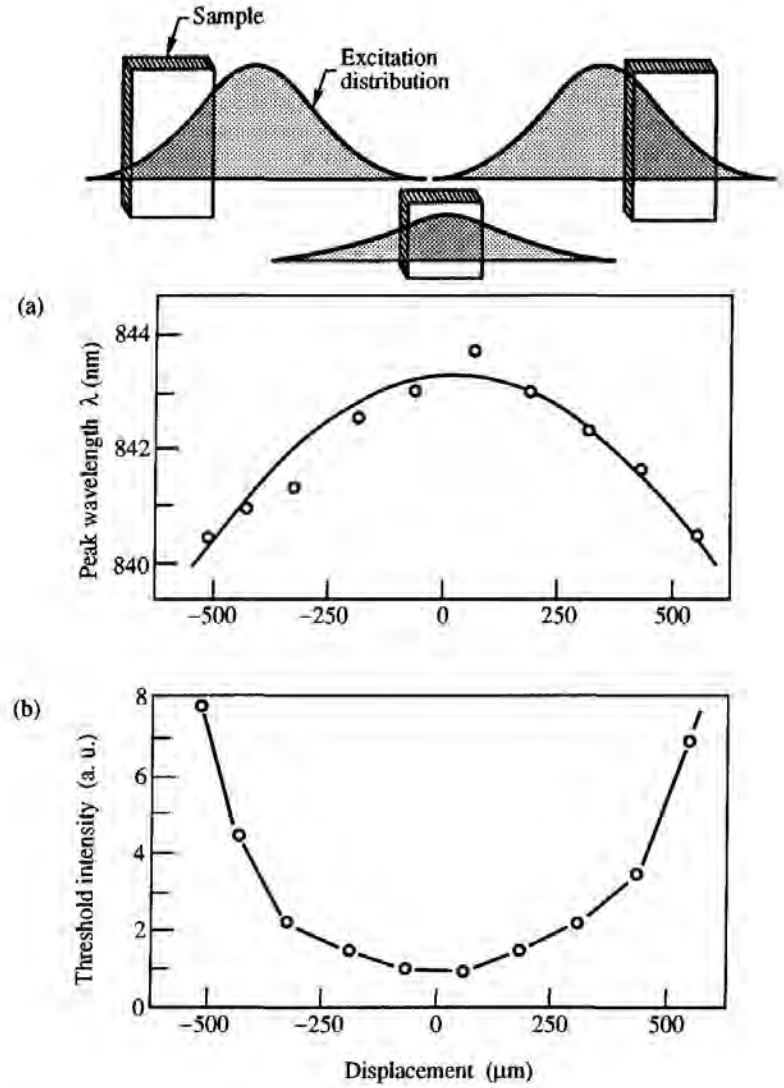


Fig. 11.21. (a) Peak wavelength of the tunable sawtooth doping superlattice laser versus displacement of the optical excitation beam. Tunability of the laser emission is achieved over $\Delta\lambda \equiv 35$ Å. (b) Threshold intensity of the laser versus displacement of the exciting beam. The top part of the figure schematically shows the displacement of the exciting beam with respect to the laser bar.

distribution of the exciting source. A wider tuning range can be expected for a more inhomogeneous excitation, which could be achieved in a two- or three-section current-injection laser.

Simultaneously, as the peak of the stimulated emission shifts to shorter wavelengths, the excitation intensity required to reach threshold increases, as

https://doi.org/10.1017/CBO9780511599828.014 Published online by Cambridge University Press

337-TA-1366 RX-0255

illustrated in Fig. 11.21(b). However, it is important to visualize that upon displacement, the sample is excited only by a small part of the exciting beam as shown in the top part of Fig. 11.21. Thus, the increase of threshold intensity is overestimated and the true increase in threshold intensity is not as pronounced as suggested by Fig. 11.21(b).

Under homogeneous excitation conditions, the stimulated emission energy is below the band gap of GaAs. However, the emission energy is much higher than the spontaneous emission energy at low excitation intensities ($E \cong 1.35$ eV). Thus, the superlattice modulation is reduced by photoexcited electrons and holes, which screen the ionized dopant charges of donors and acceptors, respectively. Even though the modulation is reduced, a residual *band modulation is maintained,* as demonstrated by the low emission energy. Thus, stimulated emission is achieved before the bands are completely flat, that is for incomplete screening of dopant charges.

The physical mechanism leading to the tunability of the semiconductor laser can be understood on the basis of increased loss induced by inhomogeneous excitation. As a result of the inhomogeneous excitation, i.e., reduced excitation in one part of the Fabry–Perot cavity, the optical loss is enhanced in this section. In order to obtain stimulated emission, the other section must be subjected to higher excitation. As a result, the band modulation decreases and the superlattice energy gap increases in this section. Once the intentionally induced loss is overcome, stimulated emission occurs. However, the lasing *energy* increases as compared to the homogeneously excited cavity. Thus, tunability of the stimulated emission wavelength is achieved by a different excitation in the two sections of the laser. The principal limit of the tuning range is reached when the flatband condition is achieved in one part of the laser. The corresponding tuning range is approximately 250 Å at low temperatures for the samples studied.

11.5.4 Modulators

Modulation and switching of near-infra-red radiation by means of electrical control is an important functional device characteristic in photonic switching systems. It is desirable that such photonic switching devices (i) have a broad wavelength range in which the light intensity can be modulated, (ii) have a large contrast ratio in the transparent and opaque states, (iii) can operate at voltages compatible with electronic integrated circuits, and (iv) have high-speed capability.

Modulators with such characteristics can be fabricated from doping superlattices with long periods (Schubert and Cunningham, 1988). Contacting the n-type and p-type regions of the superlattice allows one to change the modulation,

https://doi.org/10.1017/CBO9780511599828.014 Published online by Cambridge University Press

Innoscience1366-00139176

RX-0255.503

i.e. the internal electric field of the superlattice, by means of an external bias. Tunneling-assisted absorption (Franz–Keldysh absorption), which occurs at energies below the band gap of the semiconductor, depends exponentially on the electric field. Thus, doping superlattices can be used to modulate the intensity of transmitted light by tunneling-assisted absorption.

Modulation experiments with the conventional doping superlattice structure yielded a transmission change of 22% using selective side-contacts to the superlattice region (Chang-Hasnain et al., 1987). Absorption modulators were also realized with a δ-doped structure (Schubert and Cunningham, 1988). The maximum contrast ratio between the opaque and the transparent state achieved with the δ-doped modulator was 70% at a wavelength of $\lambda \cong 950$ nm.

https://doi.org/10.1017/CBO9780511599828.014 Published online by Cambridge University Press

12

Characterization techniques

Doping and other materials parameters influence the properties of III–V devices in a profound manner. Examples of device parameters which are strongly influenced by the defect and doping concentration are the radiative efficiency of a laser, the minority carrier lifetime in the base of a bipolar transistor, the carrier mobility in the channel of a field-effect transistor, or the quantum efficiency of a pin photo-diode. In this chapter, characterization techniques are discussed that relate directly to shallow impurities as well as deep centers. The characterization techniques are categorized as (i) electronic (ii) optical, and (iii) chemical and structural techniques. Fundamental aspects of characterization techniques as well as practical 'hints' for the experimentalist are emphasized.

12.1 Electronic characterization techniques

Many properties of semiconductors that relate directly to impurities or defects can be assessed by electrical measurements. Such measurements include current–voltage, capacitance–voltage, resistivity, magnetoresistance, and impedance measurements. Frequently, temporal transients of such measurements are of interest, for example the capacitance transient after a semiconductor has been subjected to an electrical pulse. In this section, the Hall effect, capacitance–voltage (CV) profiling technique, deep level transient spectroscopy (DLTS), thermally stimulated capacitance (TSCAP), thermally stimulated current (TSC), and admittance spectroscopy are discussed.

https://doi.org/10.1017/CBO9780511599828.015 Published online by Cambridge University Press

12.1.1 Hall effect measurements

Hall effect measurements (Hall, 1879) allow one to determine the (majority) ***Hall carrier concentration*** of unipolar semiconductors in which the minority carrier concentration can be neglected. The *Hall carrier concentration* differs from the ***true carrier concentration*** by a numerical factor, r_H, which is called the ***Hall factor*** and which is on the order of unity.

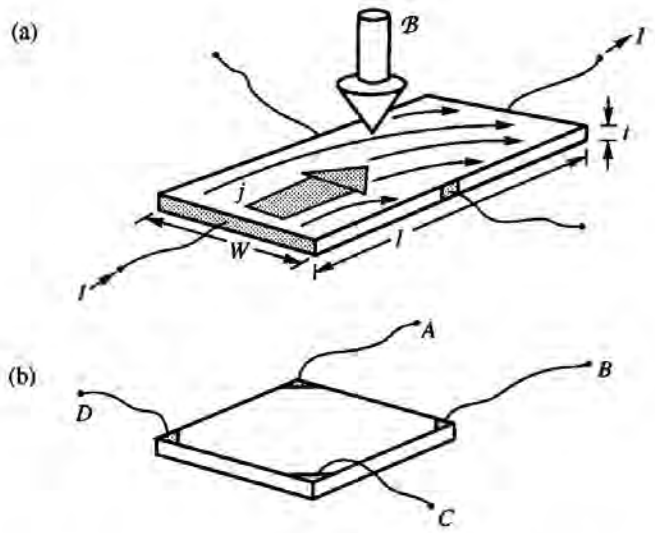


Fig. 12.1. (a) Hall bar geometry and (b) van der Pauw geometry of a semiconductor for Hall effect measurements.

A simple Hall bar geometry is shown in Fig. 12.1(a). The sample is subjected to a current I and to a magnetic field $\mathcal{B}$ perpendicular to the sample surface. Charge carriers flowing through the sample experience the Lorentz force

$$\mathcal{F}_L = -ev \times \mathcal{B} \tag{12.1}$$

where $-e$ is the charge of electrons and v is the carrier velocity. Carriers are deflected by the Lorentz force from their flow pattern without a magnetic field as indicated in Fig. 12.1(a). As a result, an electric field evolves due to the displacement of electron charges. The electric field is called the ***Hall field***. Carriers experience a force in the Hall field of magnitude

$$\mathcal{F}_H = -e\mathcal{E}_H \,. \tag{12.2}$$

The deflection of carriers persists until the Lorentz force is balanced by the Hall force. Equating Eqs. (12.1) and (12.2) yields the Hall carrier concentration

https://doi.org/10.1017/CBO9780511599828.015 Published online by Cambridge University Press

according to

$$\boxed{n_H^{2D} = \frac{I\mathcal{B}}{eV_H}} \tag{12.3}$$

where $V_H = \mathcal{E}_H W$ (see Fig. 12.1a) is the Hall voltage, and n_H^{2D} is the two-dimensional (2D) Hall carrier concentration, i.e. the Hall concentration per unit area. The three-dimensional (3D) carrier concentration is obtained from the 2D concentration by

$$n_H = n_H^{3D} = n_H^{2D}/t \tag{12.4a}$$

where t is the thickness of the sample. If a region of the doped layer of the sample, with thickness W_D, is depleted of free carriers (e.g. surface depletion layer or interface depletion), then Eq. (12.4a) needs to be modified according to

$$n_H = n_H^{2D}/(t - W_D) \tag{12.4b}$$

where t is the total thickness of the doped layer.

The *true* carrier concentration and the Hall carrier concentration are related by the ***Hall factor***, r_H, according to

$$\boxed{n = r_H n_H} \tag{12.5}$$

where r_H is given by

$$r_H = \langle \tau_m^2 \rangle / \langle \tau_m \rangle^2 \tag{12.6}$$

and τ_m is the energy-dependent momentum-relaxation time and $\langle \tau_m \rangle$ is the expectation value of τ_m at a given temperature. The magnitude of the Hall factor is $r_H = 1.18$ for phonon scattering, $r_H = 1.93$ for ionized impurity scattering and $r_H = 1.0$ for degenerately doped semiconductors (Smith, 1978). Thus, the Hall carrier concentration is always equal or smaller than the true carrier concentration, $n_H \leq n$. For simplicity it is frequently assumed that the Hall factor is unity, i.e. $n_H = n$. We finally note that the quantity

$$R_H = \frac{1}{en_H} = \frac{r_H}{en} \tag{12.7}$$

is called the ***Hall coefficient*** and is frequently used in the literature.

The Hall effect measurement and a conductivity measurement allows one to determine the ***mobility*** of carriers. The conductivity of an n-type semiconductor is given by

https://doi.org/10.1017/CBO9780511599828.015 Published online by Cambridge University Press

$$\sigma = en\mu \tag{12.8}$$

where μ is the ***drift mobility***. The drift mobility can be determined, if the conductivity and the carrier concentration are known, that is

$$\mu = \sigma/en\,. \tag{12.9a}$$

If, however, the *true* carrier concentration is unknown but instead the *Hall* carrier concentration is known, then Eq. (12.9a) can be written as

$$\boxed{\mu_H = \sigma/en_H} \tag{12.9b}$$

where μ_H is called the ***Hall mobility***. The Hall mobility deviates from the drift mobility by the Hall factor, and is always larger or equal to the drift mobility, because $\mu_H = \sigma/en_H = \sigma r_H/en = \mu r_H$ and $r_H \geq 1$. In other words, the Hall mobility overestimates the true (drift) mobility.

The ***van der Pauw*** technique (van der Pauw, 1958) is a convenient means of performing Hall and conductivity measurements. A sample with van der Pauw-type geometry is shown in Fig. 12.1(b). The sample is square-shaped and has four ohmic contacts in the corners. The contacts must be much smaller than the sample area. Furthermore, the contacts must be at the very edges of the sample. As an improvement, van der Pauw proposed a 'clover leaf' geometry which reduces the influence of the contacts. In the van der Pauw measurement, a current source is applied to two of the four contacts, e.g. the current enters through contact A and leaves through contact B. The voltage between the contacts C and D is then measured. For convenience, we define the resistance $R_{AB,CD} = V_{CD}/I_{AB}$. Then the Hall coefficient is given by

$$R_H(\mathrm{cm}^2/\mathrm{C}) = \frac{2.5 \times 10^4}{\mathcal{B}}[(R^+_{AC,DB} - R^-_{AC,DB}) + (R^+_{DB,AC} - R^-_{DB,AC})] \tag{12.10a}$$

where R^+ and R^- indicate the forward and reverse polarization of the magnetic induction $\mathcal{B}$, and the magnitude of $\mathcal{B}$ is measured in units of 10^3 gauss. The two-dimensional Hall carrier concentration is then given by

$$n_H^{2D}(\mathrm{cm}^{-2}) = 6.25 \times 10^{18}/R_H \tag{12.10b}$$

where the Hall density is obtained in cm^{-2}. The two-dimensional resistivity of a sample with van der Pauw geometry is given by

https://doi.org/10.1017/CBO9780511599828.015 Published online by Cambridge University Press

$$\rho^{2D}(\Omega) = \frac{\pi}{4 \ln 2} (R_{AD,CB} + R_{DA,CB} + R_{DC,BA} + R_{CD,BA}) . \quad (12.10c)$$

The 2D resistivity is frequently measured in ohms or ohms/square. Finally, the Hall mobility can be obtained from the Hall coefficient and the 2D resistivity

$$\mu_H(\text{cm}^2/\text{V s}) = R_H/\rho^{2D} \quad (12.10d)$$

where R_H and ρ^{2D} are in the units of Eqs. (12.10a) and (12.10c).

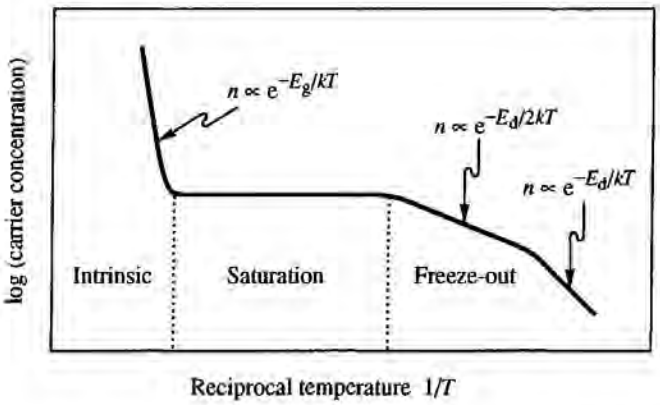


Fig. 12.2. Schematic temperature dependence of the carrier concentration in a doped semiconductor. All impurities are ionized in the saturation regime. Freeze-out of carriers occurs at low temperatures. At high temperatures, the carrier concentration increases due to thermal band-to-band excitation.

Temperature-dependent Hall measurements allow one to evaluate the thermal ionization energy of impurities. The schematic temperature-dependent carrier concentration of an n-type semiconductor is shown in Fig. 12.2. The carrier concentration displays three regions which are the *freeze-out*, the *saturation*, and the *intrinsic* regimes. A detailed discussion of the temperature-dependent carrier concentration was given in Chap. 3. The dependence of the carrier concentration on temperature of an n-type semiconductor with a donor activation energy E_d is

$$n \propto e^{-E_d/2kT} \quad (12.11)$$

which is valid for $N_D >> \frac{1}{2} N_c e^{-E_d/kT} >> N_A$ where N_c is the effective density of states and N_A is the residual acceptor background concentration. At even lower temperatures one may observe a regime

$$n \propto e^{-E_d/kT} \quad (12.12)$$

which is valid for $\frac{1}{2} N_c e^{-E_d/kT} << N_A$, i.e. for very low temperatures or higher

https://doi.org/10.1017/CBO9780511599828.015 Published online by Cambridge University Press

acceptor background concentrations. Thus, Eq. (12.11) rather than Eq. (12.12) applies for most practical purposes, that is high-quality, uncompensated semiconductors. The thermal activation energy of donor impurities can be evaluated from the slope of n versus $(1/T)$ using Eq. (12.11)

$$E_d = -2k \frac{d(\ln n)}{d(1/T)} . \tag{12.13}$$

The numerical factor before the slope has a value of $-2k = -0.172$ meV.

12.1.2 Capacitance–voltage profiling technique

The capacitance–voltage (CV) profiling technique (Thomas et al., 1962; Meyer and Guldbrandsen, 1963; Amron, 1964, 1967) allows one to measure the CV-concentration, N_{CV}, as a function of depth. In the simplest case, that is for a non-compensated, homogeneously doped semiconductor, the CV-concentration equals the electrically active doping concentration. The CV-measurement can be performed on Schottky junctions, p^+ n-junctions, and n^+ p-junctions. The CV-measurement is based on the ***depletion-approximation*** which assumes that the depletion region of a junction contains no free carriers and that the semiconductor is neutral outside the depletion region. The transition between the neutral and the depletion region is assumed to be abrupt. In the following, a metal-to-n-type semiconductor junction will be considered. However, the results are also valid for p^+ n- and n^+p-junctions with $p^+ >> n$ and $n^+ >> p$, respectively.

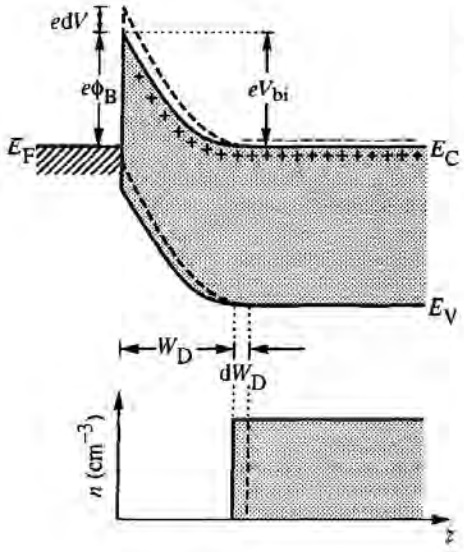


Fig. 12.3. Band diagram and free carrier profile of a semiconductor with the near-surface region depleted of free carriers. Application of a small bias dV changes the depletion width by dW_D.

https://doi.org/10.1017/CBO9780511599828.015 Published online by Cambridge University Press

The band diagram of a semiconductor–metal junction is shown in Fig. 12.3. The barrier height of the junction is ϕ_B. The semiconductor is assumed to be homogeneously n-type doped and uncompensated. The width of the surface depletion region can be obtained from Poisson's equation and is given by

$$W_D = \sqrt{\frac{2\varepsilon}{eN_D}(V_{bi} - V)} \equiv \sqrt{\frac{2\varepsilon}{eN_D}(\phi_B - V)} \qquad (12.14)$$

where V_{bi} is the 'built-in' voltage (see Fig. 12.3), which is $V_{bi} \equiv \phi_B$ for typical doping concentrations; V is the external voltage applied to the Schottky diode. Upon application of a voltage increment, the depletion width increases by

$$dW_D = -\frac{1}{2}\sqrt{\frac{2\varepsilon}{eN_D(\phi_B - V)}}\, dV\,. \qquad (12.15)$$

The change in depletion *charge per unit area*, dQ, for a voltage increment, dV, is given by $dQ = eN_D dW_D$. The differential depletion capacitance per unit area is defined as $C = dQ/dV$ and is given by

$$C = \frac{dQ}{dV} = \frac{1}{2}\sqrt{\frac{2e\varepsilon N_D}{\phi_B - V}} = \frac{\varepsilon}{W_D}\,. \qquad (12.16)$$

The *CV-concentration* is then defined as

$$\boxed{N_{CV} = \frac{-2}{e\varepsilon}\left[\frac{dC^{-2}}{dV}\right]^{-1} = \frac{C^3}{e\varepsilon}\frac{dV}{dC}} \qquad (12.17)$$

Insertion of Eq. (12.16) into Eq. (12.17) shows that the CV-concentration equals the shallow donor concentration, i.e. $N_{CV} = N_D$. This result applies to homogeneously doped, *uncompensated* semiconductors only. For *compensated* semiconductors with $N_D > N_A$, it is easy to show that $N_{CV} = N_D - N_A$. This equation also applies to semiconductors with *amphoteric* impurities, e.g. Si in GaAs, where $N_{CV} = N_D - N_A$. Similarly, *electrically inactive* impurities in semiconductors are not measured by the CV-technique, i.e. $N_{CV} = N_D - N_D^0$, where N_D is the total donor concentration and N_D^0 is the concentration of electrically inactive donors.

The concentration N_{CV} occurs at the depth, z_{CV}, which is defined as

https://doi.org/10.1017/CBO9780511599828.015 Published online by Cambridge University Press

$$\boxed{z_{CV} = \varepsilon/C} \tag{12.18}$$

where C is the differential capacitance per unit area. Using Eqs. (12.14) and (12.16) one can show that $z_{CV} = W_D$ for homogeneously doped semiconductors. Finally, the *CV-profile* is obtained by plotting N_{CV} as a function z_{CV}.

There are several limitations to the CV-technique such as diode breakdown at large reverse voltages, leakage currents of the diode, and deep traps, which contribute to the capacitance signal. Several of these limitations were discussed by Blood and Orton (1978). Large series resistances of junctions used for CV-profiling can have a drastic effect on the measurement (Wiley and Miller, 1975). The current–voltage phase angle is generally a good indicator of the reliability of the CV-measurement. A phase-angle near 90° is desirable for all bias voltages in order to obtain reliable CV-data. Although corrections are possible for phase angles $<90°$, the corrections are not always advisable due to the ambiguity of their origin. A variation of the CV-profiling technique has been demonstrated by Miller (1972). Rather than constant voltage increments, the Miller technique employs constant distance increments which results in a better signal-to-noise ratio.

The ***spatial resolution*** of CV-profiles on semiconductors with a *classical* (non-quantum-mechanical) carrier system is given by the majority carrier screening length (Kennedy et al., 1968, 1969). If the doping impurity concentration varies along a spatial axis, the CV-profile does not coincide with the impurity profile. Furthermore, for abrupt doping profiles, the free carrier concentration does not coincide with the doping concentration. While abrupt changes in the impurity concentration can occur, changes in the free carrier concentration are smeared out with the screening length being the characteristic length. Kennedy et al. (1968, 1969) further showed that the CV-profile, $N_{CV}(z_{CV})$, very closely follows the free carrier profile, $n(z)$. In a non-degenerately doped semiconductor, the majority carrier screening length is the Debye length (see Chap. 1)

$$r_D = \sqrt{\frac{\varepsilon kT}{e^2 n}} \,. \tag{12.19}$$

The Debye length increases with temperature and does not depend on the carrier effective mass. In degenerately doped semiconductors, the majority carrier screening length is the Thomas–Fermi length (see Chap. 1)

https://doi.org/10.1017/CBO9780511599828.015 Published online by Cambridge University Press

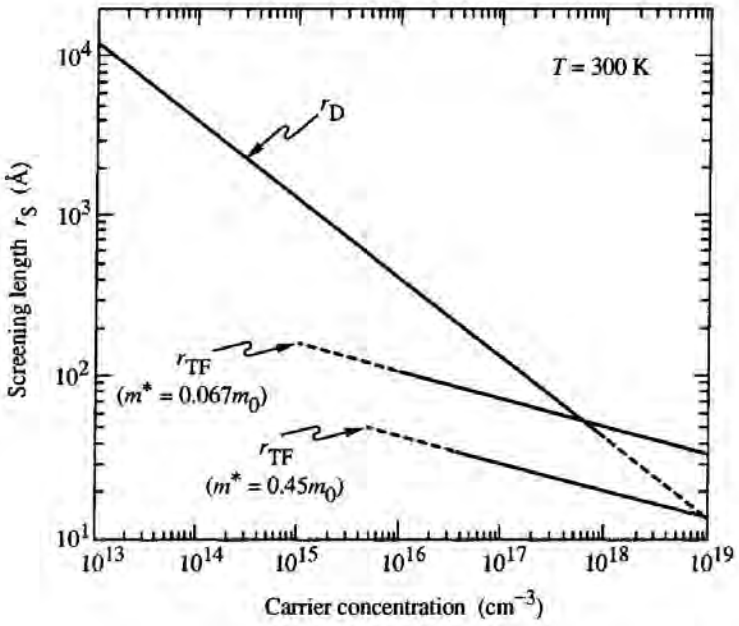


Fig. 12.4. Majority carrier screening length for non-degenerately doped (Debye length, r_D) and degenerately doped (Thomas–Fermi length, r_{TF}) semiconductors. The Thomas–Fermi length is calculated for two different masses.

$$r_{TF} = \pi^{2/3}\sqrt{\frac{\varepsilon\hbar^2}{e^2 m^* (3n)^{1/3}}} \tag{12.20}$$

The Thomas–Fermi screening length is independent of temperature and depends on the carrier effective mass. The calculated Debye length and the Thomas–Fermi screening length are shown in Fig. 12.4 for a temperature of $T = 300$ K. The mass-dependent Thomas–Fermi length is shown for $m^* = 0.067m_0$ and $m^* = 0.45m_0$ which correspond to the electron and heavy-hole effective masses in GaAs.

The ***spatial resolution*** of the CV-profiling technique in semiconductors with ***quantum confinement*** was shown to be limited to the spatial extent of the carrier wave function (Schubert et al., 1990a). This resolution limit is explained as follows. Consider a quantized electron system described by a wave function ψ. The position expectation value of the electron system is $\langle z\rangle = \langle\psi|z|\psi\rangle$. The differential capacitance per unit area of such an electron system equals

$$C = \varepsilon/\langle z\rangle\,. \tag{12.21}$$

Upon application of a bias, the position expectation value of the quantized

https://doi.org/10.1017/CBO9780511599828.015 Published online by Cambridge University Press

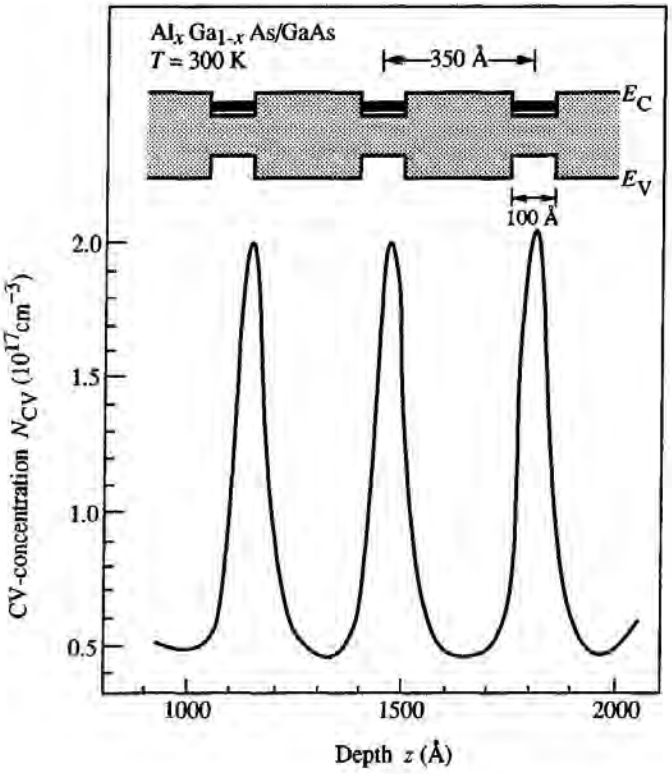


Fig. 12.5. Capacitance–voltage profile of an $Al_xGa_{1-x}As/GaAs$ quantum well structure doped in the GaAs quantum wells.

electron system moves due to the potential perturbation caused by the bias. Recall now, that the depth scale of the CV-measurement is calculated from

$$z_{CV} = \varepsilon/C \,. \tag{12.22}$$

Comparison of Eqs. (12.21) and (12.22) yields $z_{CV} = \langle z \rangle$, i.e. the CV-depth (at a certain bias) equals the position expectation value of the electron system (at a certain bias). Thus, the *resolution* of the CV-technique, Δz_{CV}, is given by the change of the position expectation values, $\Delta\langle z \rangle$, upon sweeping the depleting bias, i.e.

$$\Delta z_{CV} = \Delta\langle z \rangle \,. \tag{12.23}$$

The authors showed that the change in position expectation value is approximately equal to the spatial width of the wave function, i.e. approximately equal to the width of the confining potential. As an example, the CV-profile of an $Al_xGa_{1-x}As/GaAs$ multiquantum well sample is shown in Fig. 12.5. The

https://doi.org/10.1017/CBO9780511599828.015 Published online by Cambridge University Press

quantum wells are Si-doped and have a nominal width of 100 Å. The period of the structure is 350 Å. The half-widths at half-maxima of the peaks are approximately 50 Å. The width agrees with the spatial extent of the quantum well wave function. It is worthwhile noting that neither the (3D) Debye nor the (3D) Thomas–Fermi screening length can be applied to quantized, two-dimensional carrier systems.

In semiconductors with large variations of the doping concentration and especially in semiconductors with quantum confinement, the CV-concentration, N_{CV}, does not have a direct physical meaning. However, the CV-concentration corresponds *approximately* to the free carrier concentration $N_{CV}(z) \equiv n(z)$. This is in contrast to homogeneously doped semiconductors for which the following equation has validity: $N_{CV}(z) = n(z)$. Nevertheless, Kroemer et al. (1980) showed that charge conservation is fulfilled for CV-profiles, that is

$$\int_{-\infty}^{\infty} N_{CV}(z_{CV})\,dz_{CV} = \int_{-\infty}^{\infty} n(z)\,dz\,. \tag{12.24}$$

The equation can be proved by inserting the definitions for N_{CV} (Eq. (12.17)) and z_{CV} (Eq. (12.18)) and by subsequent integration. This property of the CV-technique is very useful. The right-hand side of Eq. (12.24) represents the two-dimensional (2D) carrier density of an electron system. Thus, the 2D carrier density of doped quantum well structures, selectively doped heterostructures, and similar structures can be precisely measured by the CV-profiling technique.

We consider finally the ***influence of deep traps*** on the CV-profiling technique. As an example, we consider a semiconductor with shallow donors and deep donor-like impurities with a constant concentration. The band diagram of a metal–semiconductor junction containing shallow and deep levels is shown in Fig. 12.6. It is useful to differentiate between (i) a neutral region, (ii) a shallow donor depletion region of thickness W_D, (iii) a deep donor depletion region, and (iv) a transition region of thickness λ. The potential drops and widths of the respective regions can be calculated from Poisson's equation for the general case $\lambda \leq W_D$:

$$V_\lambda = \frac{1}{e}(E_F - E_T)\,, \tag{12.25a}$$

$$\lambda = \sqrt{\frac{2\varepsilon}{e^2 N_D}(E_F - E_T)}\,, \tag{12.25b}$$

and

https://doi.org/10.1017/CBO9780511599828.015 Published online by Cambridge University Press

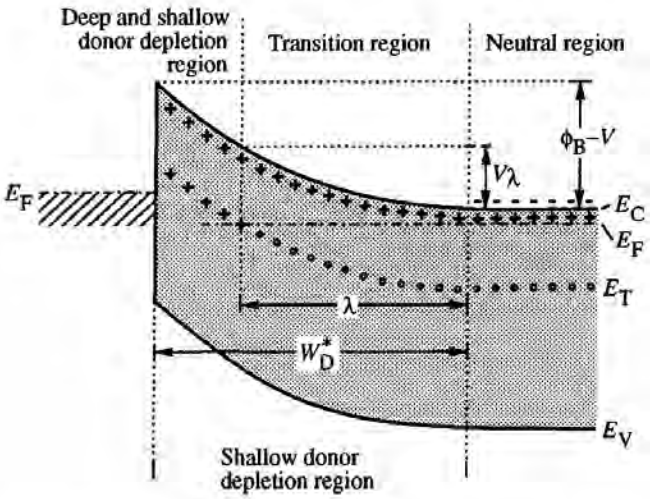


Fig. 12.6. Band diagram of a metal–semiconductor junction with deep and shallow donor impurities. The shallow and deep donor depletion regions are W_D^* and W_D^*–λ, respectively.

$$\phi_B - V = \frac{e}{\varepsilon} W_D^* [N_D \lambda + (N_D + N_T)(\tfrac{1}{2} W_D^* - \lambda)] , \tag{12.26a}$$

$$W_D^* = \frac{N_T \lambda + \sqrt{N_T^2 \lambda^2 + 2(N_D + N_T) \frac{\varepsilon}{e}(\phi_B - V)}}{N_D + N_T} . \tag{12.26b}$$

For $N_T = 0$ or for $\lambda = 0$, Eq. (12.26) reduces to the well-known depletion approximation for shallow impurities. The above equations are valid under equilibrium conditions, i.e. when no transient emission and capture processes of the deep traps occur.

In order to estimate the influence of deep traps, recall that the CV-measurement uses an ac small signal voltage [the frequency of the ac small signal voltage is in the radio-frequency (rf) regime and it is, therefore, frequently called the rf signal] to measure the capacitance at a particular dc voltage. The quasi-dc voltage is swept in a quasi-static (point-by-point) mode in order to obtain the C versus V characteristic. Kimerling (1974) differentiated between three cases to estimate the influence of deep traps. As examples, we consider donor-like traps of concentration N_T in an n-type semiconductor with shallow donor concentration N_D.

https://doi.org/10.1017/CBO9780511599828.015 Published online by Cambridge University Press

Case 1: Very 'slow' traps

At very low temperatures, the emission rates of deep traps is so small, that they 'follow' neither the quasi-dc bias nor the ac signal, i.e. their charge state remains unchanged during the entire measurement. That is, the emission time of the trap is much longer than the period of the ac signal and the time constant of the quasi-dc bias. In this case, the CV-technique gives

$$\boxed{N_{CV} = N_D} \tag{12.27a}$$

$$z_{CV} = W_D = \sqrt{\frac{2\varepsilon}{2N_D}(\phi_B - V)} \tag{12.27b}$$

which is also obtained if no traps were present.

Case 2: 'Slow' traps

At higher temperatures, the trap charge state follows the quasi-dc bias but does *not* follow the ac signal. The entire ac oscillating charge (per unit area) is located at $x = W_D^*$ and has a magnitude of

$$dQ = eN_D\, dW_D^* \tag{12.28a}$$

with a corresponding ac voltage of

$$dV = dQ/C = dQ\, W_D^*/\varepsilon = (e/\varepsilon)\, N_D W_D^* dW_D^* . \tag{12.28}$$

Using the definition of the CV-concentration (Eq. (12.17)) and CV-depth (Eq. (12.18)) along with Eq. (12.26), one obtains

$$\boxed{N_{CV} = N_D + N_T\left[1 - \frac{\lambda}{W_D^*}\right]} \tag{12.29a}$$

$$z_{CV} = W_D^* . \tag{12.29b}$$

The concentration N_{CV} approaches $N_D + N_T$ for deep depletion.

Case 3: 'Fast' traps

At sufficiently high temperatures, the trap charge state follows both the quasi-dc bias and the ac signal. The oscillating charge per unit area consists of the shallow

https://doi.org/10.1017/CBO9780511599828.015 Published online by Cambridge University Press

donor and the trap contribution

$$dQ = eN_D dW_D^* + eN_T dW_D^* . \quad (12.30a)$$

The corresponding ac voltage change is given by

$$dV = dQ/C = \frac{e}{\varepsilon} [N_D W_D^* dW_D^* + N_T (W_D^* - \lambda) dW_D^*] . \quad (12.30b)$$

Using Eqs. (12.17) and (12.18) one obtains

$$\boxed{N_{CV} = N_D + N_T} \quad (12.31a)$$

$$z_{CV} = \frac{N_D W_D^* + N_T (W_D^* - \lambda)}{N_D + N_T} . \quad (12.31b)$$

The CV-result contains the entire charge, since all impurities follow the ac signal. The CV-depth is between the ionization region of shallow donors and traps, i.e. $(W_D^* - \lambda) < z_{CV} < W_D^*$. More specifically, z_{CV} is the gravity point of the charge distribution.

In a similar way, equations for the CV-concentration and the CV-depth can be derived for acceptor-like traps (Kimerling, 1974) or for p-type semiconductors. Results for non-uniform shallow impurity or trap concentration can be much more complicated and are typically not available in analytic form. Major errors in N_{CV} can occur for such a non-uniform impurity and trap concentration. Caution is also required if the trap emission time constant is comparable to either the ac signal or the quasi-dc bias. Major errors can result if the measurement is performed under such conditions.

A modification of the CV-technique is the ***electrochemical CV-profiling technique*** which has been reviewed by Blood (1986). The maximum depth of the regular CV-profiling technique is given by electrical avalanche or tunnel breakdown of the junction. This limitation is avoided in electrochemical CV-profiling which can profile many μm deep into the semiconductor. The electrochemical technique employs an electrolyte as a contact which acts as a rectifying barrier Schottky contact. The electrolyte allows one to measure the capacitance at zero bias. Subsequently, the semiconductor is etched by a photochemical etching process that is carried out in the same apparatus (Faktor et al., 1980). The alternative processes of capacitance measurements and etching allows one to measure the CV-concentration versus depths for very large depths.

https://doi.org/10.1017/CBO9780511599828.015 Published online by Cambridge University Press

12.1.3 Deep level transient spectroscopy (DLTS)

Deep level transient spectroscopy (DLTS) is a widely used, versatile capacitance-technique to characterize deep centers in semiconductors including the trap concentration, activation energy, emission properties, electron- and hole-capture cross sections and other properties (Lang, 1974). DLTS is based on temporal capacitance transients that occur after a rapid bias change of a Schottky diode, a p^+n-, or an n^+ p-junction. After the rapid bias change, a net emission or a net capture of electrons or holes occurs from deep levels until equilibrium is re-established. The charge redistribution in the depletion layer results in a change in capacitance, i.e. a capacitance transient. Using appropriate models, the capacitance transients allow one to determine the characteristics of the deep levels in the depletion region of the junction.

In order to estimate the influence of deep traps on the depletion capacitance of a Schottky diode, let us consider an n-type semiconductor which, in addition to shallow donors, also contains deep donor impurities with a concentration N_T and an ionization energy E_t. The band diagram of such a semiconductor under various bias conditions is shown in Fig. 12.7 where only the deep but not the shallow states are shown for the sake of clarity. The width of the shallow impurity depletion region is denoted as W_D^*. Within the width λ, shallow donors are depleted while deep donors remain neutral (see Eqs. (12.25) and (12.26)).

Upon a rapid bias change, the band diagram of the metal–semiconductor junction changes as illustrated in Fig. 12.7. Immediately after the junction is subjected to a negative bias, deep traps are not in thermal equilibrium, as shown in Fig. 12.7(b). The width of the depletion region increases to a non-equilibrium value of $W_D^* + \Delta W_D$. Subsequently, the traps located above the Fermi level emit carriers until equilibrium conditions are established as shown in Fig. 12.7(c). During the transient emission of carriers, the charge in the depletion region increases, resulting in a decrease of the depletion region from $W_D^* + \Delta W$ to W_D^* and a corresponding *increase* in capacitance.

The charge modulation induced by the ac small signal voltage of the capacitance measurement occurs at the edge of the depletion layer of width W_D^*. It is assumed that the emission rate of deep traps is so low that the charge state of the traps cannot follow the ac signal. The differential capacitance per unit area is then given by

$$C = \varepsilon / W_D^* \,. \tag{12.32}$$

The ***magnitude of the capacitance transient*** is therefore given by the change in depletion layer width during the transient, that is

https://doi.org/10.1017/CBO9780511599828.015 Published online by Cambridge University Press

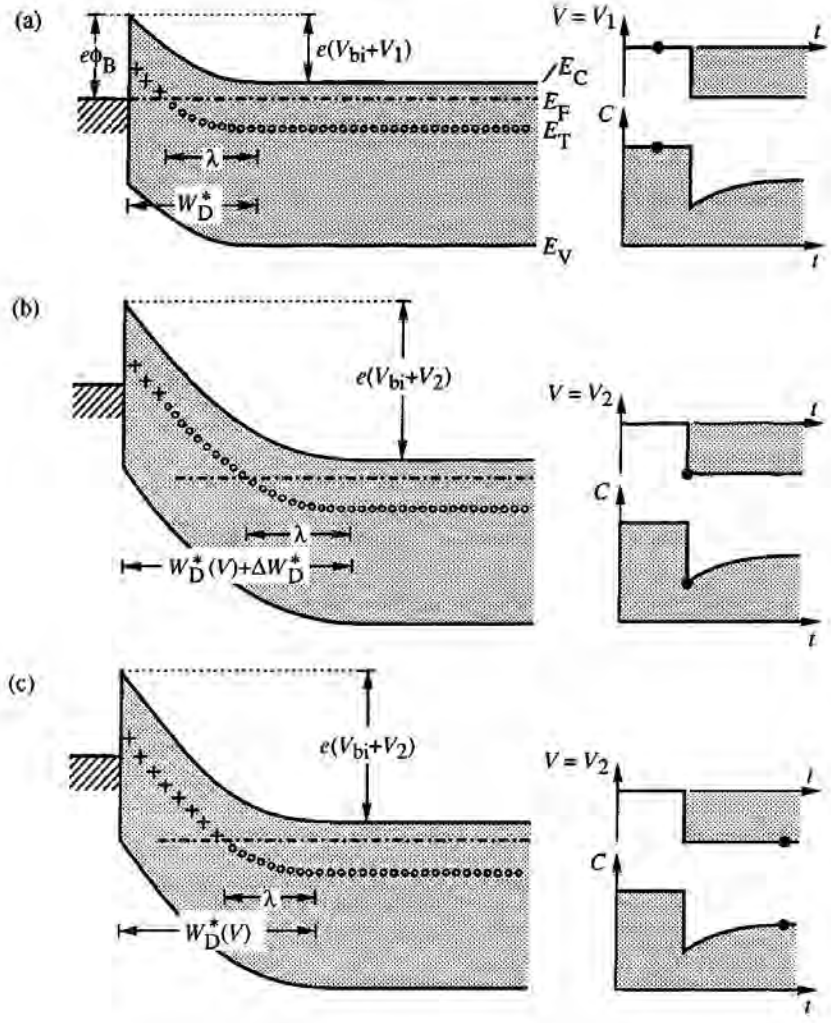


Fig. 12.7. Schematic band diagram of an n-type semiconductor with deep traps (a) under zero bias, (b) immediately following the application of a negative voltage, and (c) in thermal equilibrium. Also shown are the diode voltage pulse and the capacitance transient.

$$\frac{\Delta C}{C} = -\frac{\Delta W_D^*}{W_D^*}. \tag{12.33}$$

In order to calculate the magnitude of the capacitance transient, we consider the voltage drop across the junction and use the approximation $\phi_B \equiv V_{bi}$. The voltage drop across the junction remains *constant* during the capacitance transient (see diagram in Fig. 12.7c). Thus, the *increase* in the deep donor ionization region is compensated by a *decrease* in the shallow donor depletion region. This

https://doi.org/10.1017/CBO9780511599828.015 Published online by Cambridge University Press

337-TA-1366 RX-0255

can be expressed in terms of Poisson's equation by

$$\frac{e}{\varepsilon} W_D^*(V_2) N_D \Delta W_D^* = \frac{e}{\varepsilon} \int_{W_D^*(V_1)-\lambda}^{W_D^*(V_2)-\lambda} z N_T \, dz . \tag{12.34}$$

That is, the potential created by deep donor ionization is compensated by shallow donor neutralization. For a spatially constant trap concentration along the z-axis, the integral can be evaluated to yield

$$\frac{\Delta W_D^*}{W_D^*(V_2)} = \frac{N_T}{2N_D} \left\{ 1 - \frac{2\lambda}{W_D^*(V_2)} \left[1 - \frac{W_D^*(V_1)}{W_D^*(V_2)} \right] - \left[\frac{W_D^*(V_1)}{W_D^*(V_2)} \right]^2 \right\} \tag{12.35}$$

or, using Eq. (12.33),

$$\frac{\Delta C}{C(V_2)} = \frac{N_T}{2N_D} \left\{ 1 - 2\frac{\lambda}{W_D^*(V_2)} \left[1 - \frac{C(V_2)}{C(V_1)} \right] - \left[\frac{C(V_2)}{C(V_1)} \right]^2 \right\} . \tag{12.36}$$

The result can be simplified by assuming $W_D^* \gg \lambda$ and $W_D^*(V_2) \gg W_D^*(V_1)$ which yields

$$\boxed{\frac{\Delta C}{C} = \frac{N_T}{2N_D}} \tag{12.37}$$

This simple and important result (Lang, 1979) illustrates that the concentration of deep traps can be inferred from the magnitude of the capacitance transient.

A quantitative signature of deep level emission and capture transients can be obtained by measuring the capacitance transient as a function of temperature. Capacitance transients of a deep level as measured at different temperatures are shown schematically in Fig. 12.8. In the DLTS measurement the capacitance is measured at two times, t_1 and t_2, and the DLTS signal is defined as

$$S_{DLTS}(T) = \frac{C(t_1) - C(t_2)}{|\Delta C(0)|} \tag{12.38}$$

where $\Delta C(0)$ is the capacitance change due to the voltage pulse at $t = 0$. At very low temperatures, the DLTS signal is small since thermally stimulated emission of carriers from deep levels is negligible. At intermediate temperatures, the DLTS signal reaches a maximum. At high temperatures, the DLTS signal decreases again, because the emission of carriers from deep levels is faster than the measurement time window. Assuming that the capacitance transient is

https://doi.org/10.1017/CBO9780511599828.015 Published online by Cambridge University Press

Innoscience1366-00139194

RX-0255.521

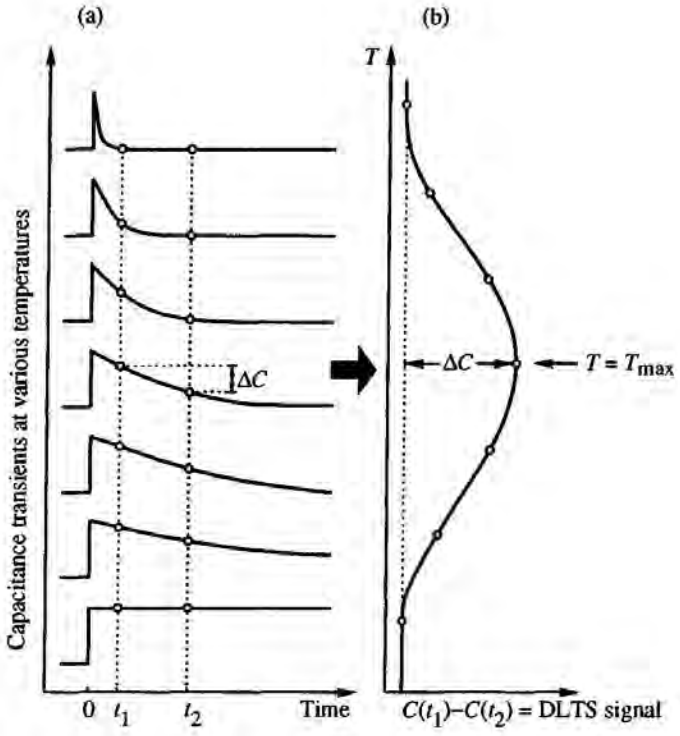


Fig. 12.8. Schematic illustration of (a) capacitance transients at different temperatures and (b) the DLTS signal deduced from the transients (after Lang, 1974).

exponential (Lang, 1974), the DLTS signal can be written as

$$S_{\mathrm{DLTS}}(T) = \mathrm{e}^{-t_1/\tau} - \mathrm{e}^{-t_2/\tau} . \tag{12.39}$$

At a certain temperature, $T_{\max}$, the DLTS signal reaches a maximum. The deep level time constant, τ, at the temperature $T_{\max}$ is denoted as $\tau_{\max}$. The relationship between $\tau_{\max}$ and t_1 and t_2 is determined by differentiating $S_{\mathrm{DLTS}}(T)$ with respect to τ and setting the result equal to zero which yields

$$\tau_{\max} = \frac{t_1 - t_2}{\ln(t_1/t_2)} . \tag{12.40}$$

An alternative method to determine the time constant is to measure the entire transient using many sampling points and fitting an exponential curve to the transient. Lock-in amplifiers and exponential correlates have also been used for this purpose (Miller et al., 1977). The extraction of an exponential capacitance transient can be further facilitated by using a baseline restorer (Miller et al.,

https://doi.org/10.1017/CBO9780511599828.015 Published online by Cambridge University Press

1975).

The capacitance transient at a given temperature can be measured repeatedly. A positive electrical ***filling pulse***, which biases the diode in the forward direction, allows one to measure the capacitance transient of electron traps many times. Signal averaging methods can then be applied. Different magnitudes of the filling pulse further allow one to spatially resolve, i.e. profile trap concentrations. Finally, majority carrier capture rates can be measured by varying the time duration of the filling pulse.

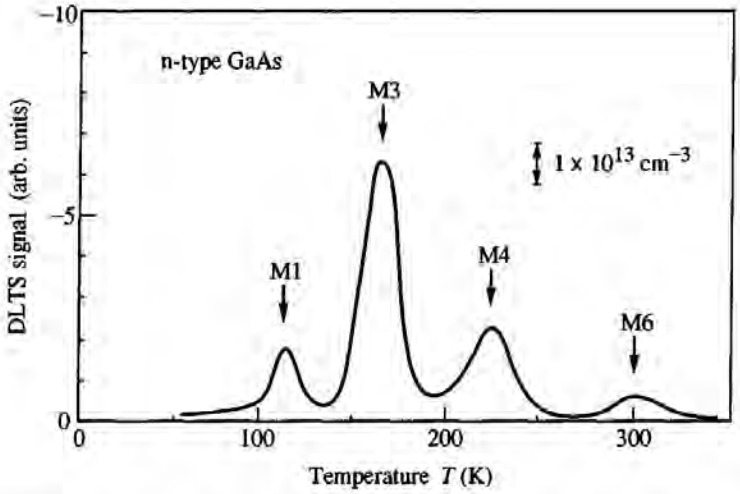


Fig. 12.9. DLTS spectrum of electron traps in n-type GaAs grown by molecular-beam epitaxy.

The experimental DLTS spectrum of n-type GaAs is shown in Fig. 12.9. Four distinct peaks are observed which are labeled M1, M3, M4, and M6 following the assignment of Lang et al. (1976). The four peaks in Fig. 12.9 are attributed to electron traps. Such electron traps emit electrons during the depletion process, i.e. the capacitance *increases* during the transient. Using Eq. (12.38), the DLTS signal is therefore a *negative* quantity for electron traps. Alternatively, hole traps in n-type semiconductors can be measured by a negative filling pulse and a subsequent rapid increase in bias. Hole traps moving below the Fermi level during the rapid bias change emit holes into the valence band. The negatively charged hole traps reduce the shallow donor space charge. As a result, the capacitance decreases during the transient. Thus, hole traps in n-type semiconductors have a *positive* DLTS signal (see Eq. (12.38)).

https://doi.org/10.1017/CBO9780511599828.015 Published online by Cambridge University Press

337-TA-1366 RX-0255

Activation energies of deep traps can be obtained from DLTS measurements by analyzing the emission kinetics of traps. As an example, we consider again electron traps in an n-type semiconductor. Recall (see Chap. 2) that the ***capture probability*** per unit time of an electron trap is given by

$$c_n = n v_{th} \sigma_n \tag{12.41a}$$

where v_{th} is the thermal velocity of free carriers and σ_n is the ***electron capture cross section*** of the trap. For some deep levels, the capture cross section is independent of temperature, e.g. $\sigma_n = 10^{-15}$ cm^2. However, the capture process may be thermally activated for other deep levels. The capture cross section is then expressed in terms of a capture barrier,

$$\sigma_n = \sigma_{n\infty} e^{-E_B/kT} \tag{12.41b}$$

where E_B is the height of the capture barrier and $\sigma_{n\infty}$ is the capture cross section at $T \to \infty$. Non-radiative, thermally activated capture was analyzed by Henry and Lang (1977).

The mean time for an impurity to capture an electron is

$$\tau_c = 1/c_n \,. \tag{12.42}$$

Note that the capture probability per unit time is frequently called the ***capture rate***. The electron ***emission probability*** per unit time is given by (see Chap. 2)

$$e_n = N_c \, v_{th} \sigma_n \frac{1}{g} e^{-(E_C - E_T)/kT} \tag{12.43}$$

where N_c is the effective density of states at the conduction band edge and g is the degeneracy of the trap level. The mean time to emit an electron from a trap is

$$\tau_e = 1/e_n \,. \tag{12.44}$$

Note that the emission probability per unit time is frequently called ***emission rate***. Neglecting interactions of the trap with the valence band, the rate equation for electron emission can be written as

$$\frac{dN_T^0}{dt} = -e_n N_T^0 \tag{12.45}$$

where N_T^0 is the concentration of traps occupied by an electron. The solution of the equation is

$$N_T^0(t) = N_T^0(t = 0) \, e^{-e_n t} \,. \tag{12.46}$$

https://doi.org/10.1017/CBO9780511599828.015 Published online by Cambridge University Press

RX-0255.524

Equations (12.43) and (12.44) allow one to determine the activation energy of a trap by evaluating the emission probability e_n as a function of temperature. In practice, the emission probability is determined by using different time windows (t_1, t_2), which shift the DLTS peak on the temperature scale and allows one to evaluate $\tau_e(T)$ using Eq. (12.40). Finally, the slope of $\tau_e = 1/e_n$ in an Arrhenius plot yields the trap activation energy. Note that the prefactors of Eq. (12.43) have a temperature dependence of T^2, since $N_c \propto T^{3/2}$ and $v_{th} \propto T^{1/2}$. Therefore, Arrhenius plots of T^2/e_n versus $1/T$ can be used to evaluate the activation energy of traps.

The activation energies of electron traps and hole traps in GaAs have been evaluated by Martin et al., (1977) and Mitonneau et al., (1977). The authors used GaAs grown by MBE, VPE, LPE, and by bulk growth techniques and characterized the levels in terms of activation energy and capture cross section (see also Chap. 2). The study revealed that some of the deep levels are characteristic for certain growth technologies and cannot be detected in GaAs grown with different growth methods. Analysis of deep traps in III–V semiconductors by DLTS have also been reported in GaInAs (Mircea et al., 1977), GaPAs (Calleja et al., 1983), and for GaInPAs (Levinson and Temkin, 1983).

Some caution should be exercised when analyzing DLTS results. First, the activation energy is composed of the reaction *enthalpy* and *entropy*. Frequently, the entropy term is neglected and the ionization enthalpy is assumed to be a good approximation for the ionization energy. Second, the measured ionization energy can be lowered by the ***Poole–Frenkel effect*** (see Chap. 2). This effect lowers the effective ionization energy of an impurity in a strong electric field. A clear electric field dependence of the ionization energy has indeed been observed experimentally (Tasch and Sah, 1970; Lang, 1974; Vincent et al., 1979) and has been explained by the lowering of the emission barrier as well as by tunnel-assisted emission through the barrier (see Chap. 2).

Occasionally, ***non-exponential capacitance transients*** are observed in DLTS measurements especially in ternary and quaternary alloy semiconductors. Such non-exponential capacitance transients in alloy semiconductors were explained by broadening of the defect levels caused by microscopic statistical variations of the alloy composition (Omling et al., 1983). Broadening of defect levels or fluctuations of the band edges caused by microscopic variations of the alloy composition result in a distribution of the ionization energies. Consequently, the DLTS signal is a superposition of a distribution of exponential transients. The resulting DLTS signal is non-exponential which was observed experimentally in III–V alloy semiconductors (Omling et al., 1983).

https://doi.org/10.1017/CBO9780511599828.015 Published online by Cambridge University Press

337-TA-1366 RX-0255

12.1.4 Thermally stimulated capacitance (TSCAP) and thermally stimulated current (TSC)

Thermally stimulated capacitance (TSCAP) and thermally stimulated current (TSC) measurements are deep level characterization techniques which can be employed if the sample under investigation has a pn-junction or a metal–semiconductor junction. The methods allow one to identify approximate activation energies and the type of traps, i.e. minority or majority carrier traps. TSCAP and TSC measurements require only simple equipment such as a capacitance bridge, a current meter, and a variable temperature cryostat. In order to fill *majority* carrier traps, the semiconductor junction is cooled to low temperatures with no bias applied to the junction. Subsequently, the junction is reverse biased and heated to room temperature. In order to fill *minority* carrier traps, a pn-junction can be forward biased or optically excited. Again, the junction is subsequently reverse biased and heated to room temperature. At temperatures at which majority carriers are emitted from traps, a step-like increase in the capacitance and a peak in the current occur. Emission of minority carriers from traps results in a step-like decrease of the capacitance and a current peak. The capacitance and current features characteristic for majority carrier traps and minority carrier traps are shown in Fig. 12.10 (Lang, 1979). In the absence of traps, the capacitance does not change with temperature, since it is assumed that the shallow impurities are ionized in the entire temperature range considered, i.e. the depletion width remains constant, as shown in Fig. 12.10(a). The current increases at higher temperatures due to a thermally activated leakage current.

TSC was first proposed by Driver and Wright (1963). TSCAP was proposed and applied to GaAs by Carballes and Lebailly (1968). Sah and coworkers (1967, 1970, 1972, 1976) also contributed significantly to the understanding and analysis of the technique. A quantitative relationship between the trap activation energy, E_t, and the temperature of the maximum-slope capacitance, T_{max}, was given by Buehler and Phillips (1976) for TSCAP measurements

$$E_t = kT_{max} \ln \frac{\alpha k T_{max}^4}{\beta(E_t + 2kT_{max})} \tag{12.47}$$

where α is a constant and β is the heating rate used in the experiment. The authors showed that the equation also applies to TSC measurements, where T_{max} is the temperature of the maximum current (see Fig. 12.10). Exact values for E_t can be obtained from TSC and TSCAP measurements using Eq. (12.47). The constant α in Eq. (12.47) contains the capture cross section of the trap, σ, which cannot be obtained from the TSC and TSCAP measurements. Therefore,

https://doi.org/10.1017/CBO9780511599828.015 Published online by Cambridge University Press

RX-0255.526

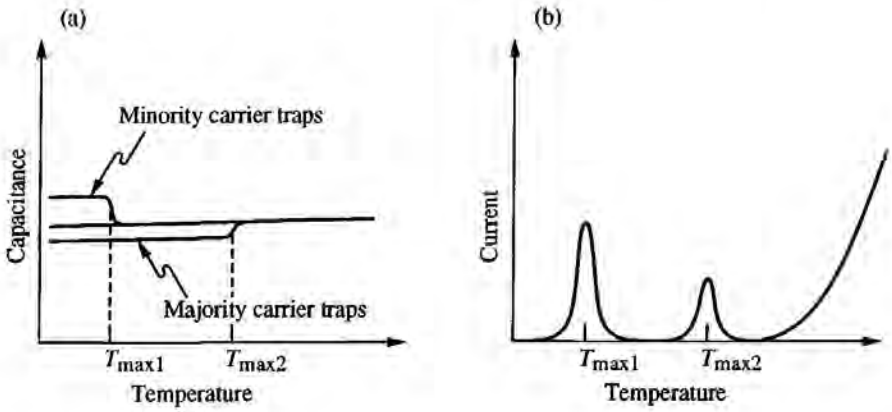


Fig. 12.10. Schematic illustration of (a) a thermally stimulated capacitance (TSCAP) and (b) a thermally stimulated current (TSC) signal of a semiconductor junction. The semiconductor is assumed to have minority and majority carrier traps. The minority carrier traps have a higher concentration and a lower activation energy than the majority carrier traps (after Lang, 1979).

approximate values for the capture cross section must be estimated in order to obtain the desired activation energies.

The total trap concentration can be obtained from the area under a current peak of the TSC curve. The total charge per contact area A is given by

$$Q = \frac{1}{A}\int_t I(t)\,\mathrm{d}t = \frac{1}{A}\int_T I(T)\frac{1}{\beta}\mathrm{d}T \tag{12.48a}$$

which allows one to estimate the trap concentration

$$\boxed{N_T = \frac{1}{e}\,Q/\Delta W_D} \tag{12.48b}$$

where ΔW_D is the change in depletion layer width caused by the reverse bias. Assume that the Schottky diode is cooled under flat band conditions, i.e. under forward bias. The initial depletion layer width is then zero. At the lowest temperature the diode is subjected to a reverse bias V. After heating the diode, the trap depletion layer width is (see Eq. (12.26b))

$$\Delta W_D = W_D^* - \lambda = \frac{N_T\lambda + \sqrt{N_T^2\lambda^2 + 2(N_D + N_T)\frac{\varepsilon}{e}(\phi_B - V)}}{N_D + N_T} - \lambda \tag{12.49}$$

https://doi.org/10.1017/CBO9780511599828.015 Published online by Cambridge University Press

337-TA-1366 RX-0255

which provides, together with Eq. (12.48b), an implicit solution for N_T. The total trap concentration can also be obtained from the step-height of the capacitance in the TSCAP measurement. The change in depletion layer width caused by free carrier emission from traps can be obtained from Eqs. (12.14) and (12.26b) which represent the depletion layer width for ionized shallow and for ionized shallow plus deep impurities, respectively. The change in capacitance (per unit area) is thus given by

$$\Delta C = \varepsilon \left(\frac{1}{W_D^*} - \frac{1}{W_D} \right) \tag{12.50}$$

which allows one to calculate the trap concentration, N_T. Furthermore, the *sign* of the capacitance change allows one to distinguish between minority and majority carrier traps. The TSC and TSCAP techniques work best for trap concentrations $N_T \geq 0.1\ N_D$ and $\Delta E \geq 0.25$ eV.

TSC and TSCAP measurements were reported for several III–V semiconductors including InP (Macrander et al., 1984).

12.1.5 Admittance spectroscopy

Admittance spectroscopy is a deep level characterization technique which can be used to analyze deep levels in the depletion region of a metal–semiconductor junction or a pn-junction. Admittance spectroscopy (Losee, 1972 and 1975) is a powerful equilibrium method which provides activation energies of relatively shallow (< 100 meV) and deep (>> 100 meV) levels as well as their concentrations. Admittance spectroscopy is a further advancement over the TSC method. Rather than measuring the dc signal from a junction, admittance spectroscopy measures the ac admittance. The possibility of measuring the ac admittance at different frequencies allows one to extract more information from the traps as compared to the TSC and TSCAP techniques.

The basic physical concept of admittance spectroscopy is illustrated in Fig. 12.11. The band diagram of a metal–semiconductor junction shown in Fig. 12.11(a) contains deep majority carrier traps in an n-type semiconductor. Upon application of a small-signal voltage of frequency f to the junction, the depletion layer width is modulated. At low temperatures, where the emission rate from the traps is small, the charge state of the deep traps does not 'follow' the ac modulation. At higher temperatures, i.e. for sufficiently large impurity emission rates, the charge modulation due to the ac voltage signal is shown in Fig. 12.11(b). Losee (1975) proposed an electrical circuit shown in Fig. 12.11(c) that can describe the electrical properties of the junction. The circuit describes the traps in terms of a capacitor C_t and a resistor R_t with a time constant

https://doi.org/10.1017/CBO9780511599828.015 Published online by Cambridge University Press

Innoscience1366-00139201

RX-0255.528

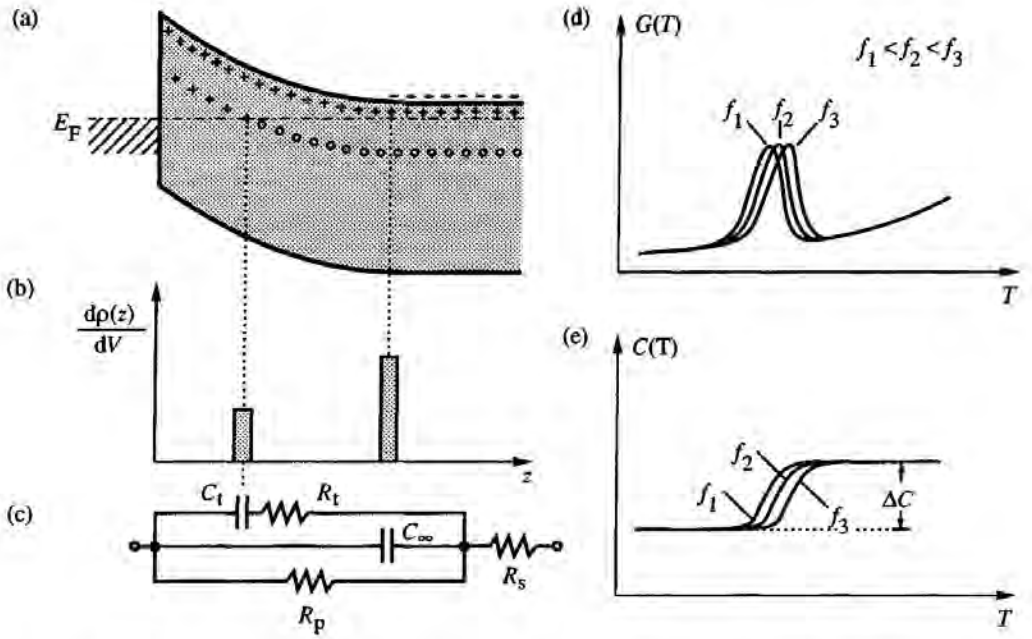


Fig. 12.11. Illustration of the principles of admittance spectroscopy. (a) Band diagram of an n-type semiconductor containing majority carrier traps. (b) Differential small signal charge density as a function of distance. The first and second charge peak are due to deep level emission and free carrier depletion, respectively. (c) Equivalent circuit diagram of the junction (after Losee, 1975). (d) Conductance and (e) capacitance of the junction as a function of temperature for three different measurement frequencies. The peaks of the conductance and the steps in the capacitance move to higher temperature with increasing measurement frequency.

$\tau = R_t C_t = 1/e_n$, where e_n is the emission probability of traps. The capacitor C_∞ describes the junction capacitance for very high frequencies, at which deep traps cannot follow the ac signal. In addition, the two resistors R_p and R_s model the leakage current and series resistance of the diode.

Peaks in the conductance and steps in the capacitance of the diode occur if the measurement frequency is resonant with the reciprocal emission probability of the trap. Schematic conductance and capacitance traces are shown in Fig. 12.11(d) and (e). The emission probability of an electron from a trap is given by (see Chap. 2)

$$e_n = \tau_n^{-1} = N_c \nu_{th} \sigma_n \frac{1}{g} e^{-E_t/kT} \tag{12.51}$$

where g is the degeneracy of the trap level and E_t the activation energy of the trap. In Eq. (12.51), a simple capture probability $c_n = n\nu_{th}\sigma_n$ is assumed. Peaks

https://doi.org/10.1017/CBO9780511599828.015 Published online by Cambridge University Press

337-TA-1366 RX-0255

in the conductance and steps in the capacitance occur at temperatures at which the measurement frequency coincides with the emission probability, that is

$$f \cong e_n \,. \tag{12.52}$$

Since e_n strongly depends on temperature, the peaks in conductance and steps in capacitance depend on the measurement frequency. Inspection of the temperature dependence reveals that the peaks and steps shift to higher temperatures for increasing measurement frequencies. This dependence is schematically shown in Fig. 12.11(d) and (e). A qualitative physical explanation of the conductance peaks and capacitance steps is as follows. At low temperatures or high frequencies, the emission rate is small compared to the measurement time constant, i.e. the traps can *not* follow the ac signal. The capacitance is then given by

$$C_l = \varepsilon / W_D^* \tag{12.53}$$

where W_D^* is given by Eq. (12.26b). At higher temperatures, the traps follow the ac signal. The capacitance is then given by

$$C_h = \varepsilon \left[\frac{W_D^* N_D + (W_D^* - \lambda) N_T}{N_D + N_T} \right]^{-1} \tag{12.54}$$

where the term in the parenthesis is the gravity point of the charge induced by the ac signal. The change in capacitance is then given by

$$\Delta C = C_h - C_l \tag{12.55}$$

which represents an implicit solution for the trap density. At intermediate temperatures or frequencies, the deep level emission follows but lags the ac small signal. A charge oscillation which lags the ac signal implies a current that is in phase with the ac-signal, since $j = \mathrm{d}Q/\mathrm{d}T$. Thus, at intermediate temperatures or frequencies the diode has a finite conductance. Since the conductance above and below the intermediate regime is very small, a peak in the *real part* of the admittance (i.e. conductance) occurs in the intermediate regime. The peak in the conductance occurs approximately when the emission probability of traps at the Fermi level coincides with the oscillation frequency of the ac signal, $f \cong 1/\tau_e \cong e_n$. Losee (1975), in a more rigorous treatment of the problem, calculated the frequency at which the conductance is maximum as

$$\omega = 2\pi f = 1/\tau_n = e_n \,. \tag{12.56}$$

The activation energy of the trap can be obtained from an Arrhenius plot. Rewriting of Eqs. (12.51) and (12.56) yields

https://doi.org/10.1017/CBO9780511599828.015 Published online by Cambridge University Press

RX-0255.530

$$E_t = -k\frac{d}{d(1/T_{max})} \ln \frac{\omega}{N_c \nu_{th} \sigma_n g^{-1}} \quad (12.57)$$

where T_{max} is the temperature of maximum conductance at an angular measurement frequency of ω. Thus, the slope of the Arrhenius plot of $\ln(\omega)$ versus $(1/T_{max})$ is given by $-E_t/k$ and the value of the ordinate intercept at $(1/T_{max}) = 0$ is $(N_c \nu_{th} \sigma_n g^{-1})$. Rather than Arrhenius plots of $\ln(\omega)$ vs $1/T_{max}$, plots of $\ln(\omega T_{max}^{-3/2})$ vs. $1/T_{max}$ and $\ln(\omega T_{max}^{-2})$ vs. $1/T_{max}$ can be found in the literature. The additional temperature dependences $T_{max}^{-3/2}$ and T_{max}^{-2} arise from the temperature dependence of N_c and $N_c \nu_{th}$, respectively.

Admittance spectroscopy has been used in the characterization of a number of III–V semiconductors including GaInPAs (Takanohashi et al., 1984), InP (Takanohashi et al., 1988), AlGaAs (Chakravarty et al., 1989; Duenas et al., 1991), and GaAs (Hickmott, 1991).

12.2 Optical characterization techniques

Optical characterization in III–V semiconductors is a wide field which includes luminescence spectroscopy, absorption spectroscopy, photocurrent spectroscopy, excitation spectroscopy, and Raman spectroscopy. Furthermore, these spectroscopic techniques can be performed under the influence of external perturbations such as electric fields, magnetic fields, or mechanical stress. Optical spectroscopy has been important for both fundamental semiconductor research and technological materials evaluation. Optical spectroscopy always involves majority and minority carriers. The techniques are therefore sensitive to both the majority and minority carrier properties of semiconductors. Since minority carrier properties of semiconductors such as carrier lifetime or radiative efficiency depend sensitively on material quality (i.e. defect concentration), optical spectroscopic techniques are well suited to determine the quality of materials.

The signature of both shallow and deep impurities can be observed in optical techniques. Radiative transitions can involve shallow impurities as the initial or final state of the electronic transitions. The signature of shallow impurities can therefore be seen in luminescence or absorption techniques. Transitions involving deep impurities are mostly non-radiative. Deep impurities are therefore rarely observed in optical spectroscopic techniques. However, deep levels have a profound indirect influence on optical measurements in terms of reducing the radiative efficiency via Shockley–Read recombination processes. This section summarizes and discusses optical spectroscopic techniques with emphasis on extrinsic, i.e. impurity related aspects. The techniques discussed include

https://doi.org/10.1017/CBO9780511599828.015 Published online by Cambridge University Press

337-TA-1366 RX-0255

photoluminescence, electroluminescence, cathodoluminescence, absorption, far-infra-red absorption, photocurrent, excitation, modulation, Raman, and local vibrational mode spectroscopy.

12.2.1 Luminescence spectroscopies

Luminescence spectroscopies probe the radiative intrinsic and extrinsic transitions of semiconductors. High concentrations of non-equilibrium electron–hole pairs are excited by an external source. The detection system typically consists of a monochromator (spectrometer) and a single or multi-channel detector. Photomultiplier tubes, pn-junction diodes, and charge-coupled devices (CCDs) are popular detector types for luminescence spectroscopy. The phase-sensitive 'Lock-In' technique is commonly used to enhance the signal-to-noise ratio of the detection system.

Different excitation sources are used for luminescence experiments. In ***photoluminescence***, an optical source, typically a laser, is used as a means of excitation. The excitation energy is greater than the fundamental gap of the semiconductor in order to generate electron–hole pairs. The lateral excitation spot size depends on the excitation optics and can vary between 1 and 100 μm. The excitation depth is $l \equiv \alpha^{-1}$, where α is the absorption coefficient of the semiconductor at the excitation wavelength. Additional diffusion of free carriers can enlarge the effective excitation volume. In ***electroluminescence***, electrons and holes are injected into a pn-junction by means of electrodes. The requirement of a pn-junction restricts the use of electroluminescence spectroscopy to diode structures. That is, electroluminescence experiments cannot be performed on unipolar materials. In ***cathodoluminescence***, a high-energy electron beam is used for excitation. The energy of a single electron of the cathode beam (>> 1 keV) is much larger than the energy of the fundamental gap. Thus, many electron–hole pairs are excited per incident electron. The probing depth of cathodoluminescence is on the order of a few μm. For example, an electron range of approximately 1 μm has been estimated for a 10 keV electron beam in GaAs (Yacobi and Holt, 1986). The lateral extent of the cathode beam can be several 100 Å for sufficiently high electron energies. However, such values cannot be reached in cathodoluminescence experiments due to free carrier diffusion. Improvement of the lateral resolution can be achieved by means of time-resolved cathodoluminescence in which the incident electron beam and the detected luminescence is gated. Detection of the luminescence for times shortly after the incidence of an electron pulse allows one to improve the lateral resolution of cathodoluminescence.

A schematic band diagram with several extrinsic and intrinsic luminescence

https://doi.org/10.1017/CBO9780511599828.015 Published online by Cambridge University Press

RX-0255.532

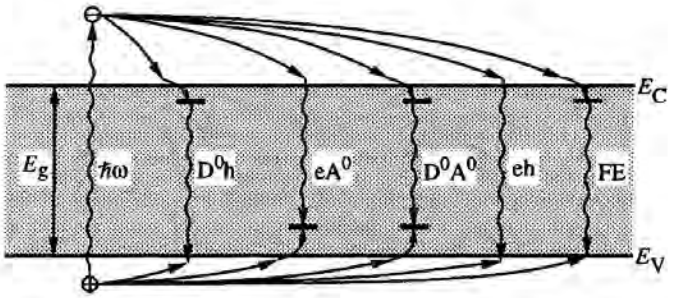


Fig. 12.12. Schematic radiative transitions in direct-gap semiconductors including donor-to-hole (D^0h), electron-to acceptor (eA^0), donor-to-acceptor pair (D^0A^0), band-to-band (eh), and free exciton (FE) transitions.

transitions is shown in Fig. 12.12. Electrons are 'pumped' by the exciting radiation of energy $\hbar\omega$ from the valence to the conduction band. For $\hbar\omega >> E_g$, carriers initially have a high kinetic energy and rapidly thermalize via optical and acoustic phonon scattering. Thermalized carriers can recombine via different recombination channels. In the following, we assume that the semiconductor has a *direct gap*. Optical transitions in a direct-gap semiconductors can occur without the assistance of phonons. We further assume that the wave functions of shallow donors and acceptors are conduction-band-like and valence-band-like, respectively, i.e. optical transitions via shallow impurities are allowed as well. Prominent impurity transitions are ***neutral-donor-to-hole*** ($\mathbf{D^0h}$), and ***electron-to-neutral-acceptor*** ($\mathbf{eA^0}$). The energy of these transitions for $kT \cong 0$ is given by

$$(D^0h): \quad E = E_g - E_d\,, \tag{12.58a}$$

$$(eA^0): \quad E = E_g - E_a \tag{12.58b}$$

where E_d and E_a are the donor and acceptor ionization energies, respectively. At finite temperatures, the peak transition energies increase by a factor of $\frac{1}{2}kT$ (Eagles, 1960)

$$(D^0h): \quad E = E_g - E_d + \tfrac{1}{2}kT \tag{12.59a}$$

$$(eA^0): \quad E = E_g - E_a + \tfrac{1}{2}kT \tag{12.59b}$$

The intensity of the (D^0h) or the (eA^0) transition is given by (Eagles, 1960; Pickering et al., 1983).

https://doi.org/10.1017/CBO9780511599828.015 Published online by Cambridge University Press

$$I_{D^0h,eA^0}(\hbar\omega) \propto (\hbar\omega - E_g + E_{d,a})^{1/2} \exp\left[-\frac{\hbar\omega - E_g + E_{d,a}}{kT}\right] \tag{12.60}$$

where the square-root dependence of the prefactor originates in the density of states and the exponential function originates from a thermal Boltzmann distribution.

The ***donor–acceptor pair*** (D^0A^0) transition is an extrinsic transition occurring in semiconductors with high concentrations of residual donors and acceptors. The energy of donor-to-acceptor transitions is given by

$$(D^0A^0): \quad E = E_g - E_a - E_d + \frac{e^2}{4\pi\varepsilon r} \tag{12.61}$$

where $e^2/4\pi\varepsilon r$ is a Coulomb term and r is the spatial separation between donors and acceptors. The Coulomb term accounts for the electrostatic energy of the (D^+A^-) pair in the ionized final state of the (D^0A^0) transition. A further van der Waals correction to the energy in the (D^0A^0) transition has been discussed by Dean (1973). The distance r between the constituents of the pair can only assume discrete values due to the discreteness of lattice sites. As a consequence, the Coulomb term can assume only discrete values. Therefore, a set of discrete lines is expected for (D^0A^0) transitions. Such discrete lines have indeed been observed in GaP (Thomas et al., 1964). The spacing of the discrete (D^0A^0) lines is not constant in energy. For sufficiently large r, the energy separation between the (D^0A^0) lines decreases, and discrete (D^0A^0) lines cannot be resolved.

Donor–acceptor transitions can only occur, if the separation between the constituents of the pair is larger than a critical radius, r_c (Hopfield, 1964). A (D^+A^-) pair has the electrostatic energy $e^2/4\pi\varepsilon r$. If the pair is neutralized by an electron and a hole, the electrostatic pair interaction energy is zero and an energy $E_d + E_a$ is transferred to the lattice. Thus, the neutralization process can only occur if

$$E_d + E_a \geq \frac{e^2}{4\pi\varepsilon r_c} \tag{12.62}$$

which allows one to evaluate the critical radius r_c. In GaAs and InP, the shallow impurity ionization energies are small which results in a large r_c. Discrete (D^0A^0) transitions are therefore not observed in GaAs, InP, or other semiconductors with small impurity ionization energies. The intensity is proportional to the overlap integral between the electron and hole wave functions,

https://doi.org/10.1017/CBO9780511599828.015 Published online by Cambridge University Press

that is

$$I_{D^0A^0}(\hbar\omega) \propto \exp\left[-\frac{2r}{a_B}\right] \tag{12.63}$$

where a_B is the Bohr radius of the impurity with the smaller binding energy.

Band-to-band **(eh)** recombination involves free electrons in the conduction band that recombine with free holes in the valence band. Band-to-band recombination occurs predominantly at high temperatures, for example room temperature. The energy of (eh) transitions at finite temperatures occurs at

$$\text{(eh)}: \quad E = E_g + \tfrac{1}{2}kT\,. \tag{12.64}$$

The intensity distribution of (eh) recombination is obtained from the density of states and the Fermi–Dirac distribution function and is given by

$$I_{eh}(\hbar\omega) \propto \int_{E_c}^{\hbar\omega - E_g} \rho_{DOS,C}(E) F_e(E) \rho_{DOS,V}[1 - F_e(E - \hbar\omega)]\, dE \tag{12.65}$$

where ρ_{DOS} and F_e are the density of states and the Fermi–Dirac distribution function and the subscripts C and V refer to the conduction and valence band, respectively. Evaluation of the integral yields

$$I_{eh}(\hbar\omega) \propto (\hbar\omega)^2(\hbar\omega - E_g)^{1/2} \exp\left[\frac{-(\hbar\omega - E_g)}{kT}\right]. \tag{12.66}$$

The equation can be further simplified for $E_g >> kT$ which yields

$$\boxed{I_{eh}(\hbar\omega) \propto (\hbar\omega - E_g)^{1/2} \exp\left[\frac{-(\hbar\omega - E_g)}{kT}\right]} \tag{12.67}$$

The (eh) recombination line has a maximum at $\hbar\omega = E_g + \frac{1}{2}kT$, which is consistent with Eq. (12.64). The full width at half-maximum of the emission line is $\Delta E \cong 1.8kT$ which can be calculated from Eq. (12.67).

Excitonic luminescence is observed at low temperatures such as liquid helium temperature. ***Excitons*** are electron–hole pairs that are bound by coulombic interaction. The coulombic interaction is similar to that of a hydrogen atom. Electron–hole pairs bound by coulombic interaction are called ***free excitons*** if they do not interact with any other center. The free exciton binding energy can be obtained from the analogy of the hydrogen atom and is given by

https://doi.org/10.1017/CBO9780511599828.015 Published online by Cambridge University Press

337-TA-1366 RX-0255

$$E_{FE} = E_g - \frac{m_r^* e^4}{32\pi^2 \varepsilon^2 \hbar^2} \tag{12.68}$$

where ε is the permittivity of the semiconductor and m_r^* is the reduced effective mass

$$\frac{1}{m_r^*} = \frac{1}{m_e^*} + \frac{1}{m_h^*} , \tag{12.69}$$

m_e^* and m_h^* being the effective electron and hole mass, respectively. The effective Bohr radius of the exciton is given by

$$a_B^* = \frac{4\pi\varepsilon\hbar^2}{m_r^* e^2} . \tag{12.70}$$

Equations (12.68) and (12.70) can be expressed as

$$E_{FE} = E_g - \left(\frac{\varepsilon_0}{\varepsilon}\right)^2 \frac{m_r^*}{m_0} E_{Ryd} , \tag{12.71}$$

$$a_B^* = \frac{\varepsilon}{\varepsilon_0} \frac{m_0}{m_r^*} a_B \tag{12.72}$$

where $E_{Ryd} = 13.6$ eV and $a_B = 0.53$ Å are the Rydberg energy and Bohr radius, respectively. As an example, we consider GaAs with $m_e^* = 0.067 m_0$, $m_{hh}^* = 0.45 m_0$, and $m_r^* = 0.058 m_0$. With $\varepsilon_r = \varepsilon/\varepsilon_0 = 13.1$, one obtains $E_{FE} = E_g - 4.6$ meV and $a_B^* = 120$ Å.

Finally, ***bound excitons*** (Haynes, 1960, 1966) are excitons that are bound to an attractive center such as a shallow neutral or ionized impurity, a deep impurity, or some other defect of the semiconductor lattice. The transition energy of bound excitons obeys the relation

$$E_{BE} < E_{FE} . \tag{12.73}$$

That is, the energy of the bound exciton is lowered by the binding center. The bound exciton does not possess kinetic energy since it is bound to a center. The linewidth is the natural linewidth given by the uncertainty principle

$$\Delta E = \hbar\tau \tag{12.74}$$

where τ is the spontaneous lifetime of the exciton. The lineshape of the exciton is therefore lorentzian

https://doi.org/10.1017/CBO9780511599828.015 Published online by Cambridge University Press

Innoscience1366-00139209

RX-0255.536

$$E_{BE} \propto \frac{\Delta E/2\pi}{(E - E_{BE})^2 + \frac{1}{4}\Delta E^2} . \qquad (12.75)$$

Bound excitons in high-purity binary III–V semiconductors can have linewidths as narrow as 0.1 meV (Harris, 1992). Excellent reviews on excitons were given by Rashba and Sturge (1982) and by Dean and Herbert (1979).

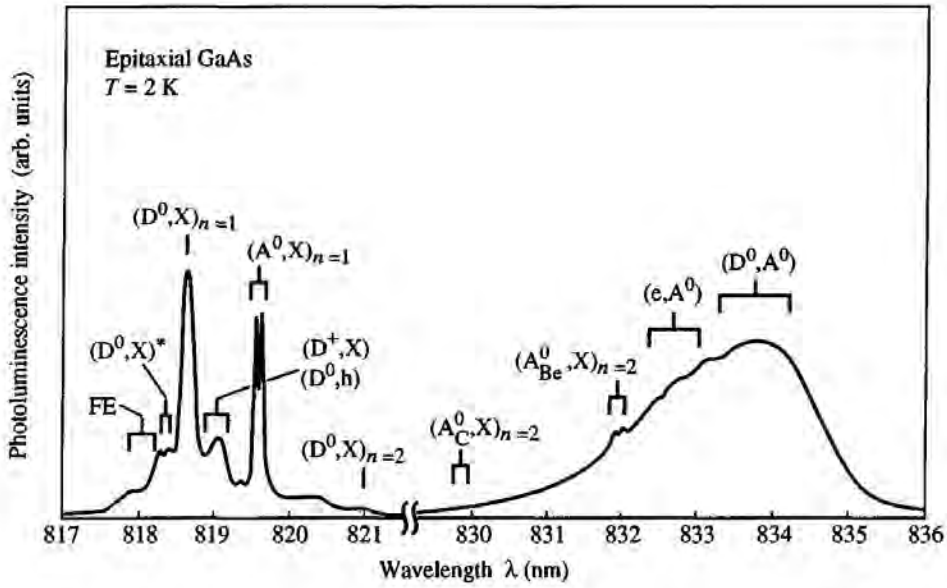


Fig. 12.13. Low-temperature photoluminescence spectrum of epitaxial GaAs. The entire luminescence occurs below the band gap (λ_g = 816 nm) (courtesy of T. D. Harris).

The near-band-edge photoluminescence spectrum of GaAs measured at 2 K is shown in Fig. 12.13. The fundamental gap of GaAs at 2 K is at E_g = 1.519 eV which corresponds to a wavelength of λ_g = 816 nm. No luminescence is observed at that wavelength on the intensity scale of Fig. 12.13 which indicates that (eh) recombination is very weak at low temperatures. The luminescence spectrum displays a wealth of transitions in the near-bandgap regime. Three impurity-assisted transitions can be identified which are the (D^0h), the (eA^0), and the (D^0A^0) transitions. The (eA^0) transition occurs at approximately 832.7 nm which corresponds to an energy of 30.5 meV below the band gap. Beryllium (E_a = 28 meV), Mg (28 meV), or Zn (31 meV) are candidates for the acceptors involved in this transition. The (D^0h) transition at approximately 819 nm corresponds to a donor energy of 5.5 meV. Since many chemically different shallow donors have very similar ionization energies, it is hardly

https://doi.org/10.1017/CBO9780511599828.015 Published online by Cambridge University Press

possible to identify the chemical nature of shallow donors by the energy of the (D^0h) transition in GaAs.

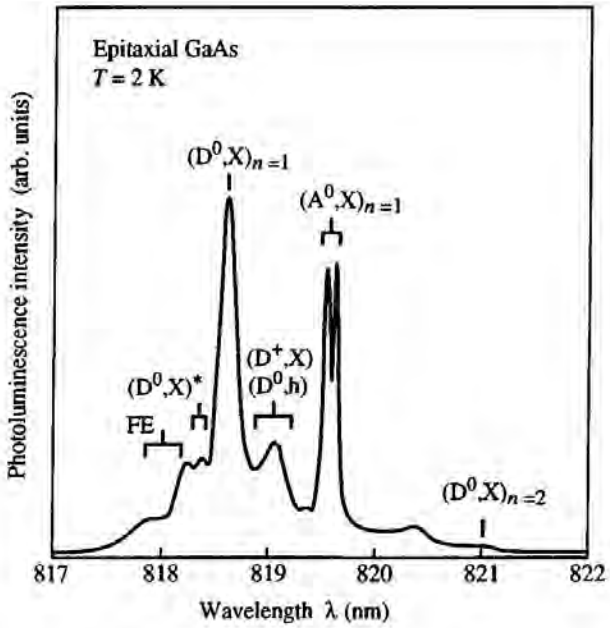


Fig. 12.14. Exitonic regime of a low-temperarure photoluminescence spectrum of epitaxial GaAs (courtesy of T. D. Harris).

The excitonic regime of a low-temperature photoluminescence spectrum of epitaxial GaAs is shown in Fig. 12.14. The major features of the spectrum are the free exciton (FE) and several bound excitons including the neutral-donor-bound exciton $(D^0,X)_{n=1}$, the ionized-donor-bound exciton (D^+,X), and the neutral-acceptor-bound exciton $(A^0,X)_{n=1}$. Note that the (D^+,X) transition and the (D^0h) transition have similar energies and cannot be differentiated spectroscopically. A transition that leaves the neutral donor in an excited state is the $(D^0,X)_{n=2}$ transition occurring at 821 nm. The $(D^0,X)_{n=2}$ transition has a *lower* energy than the $(D^0,X)_{n=1}$ transition since the neutral donor is left in an excited state in the former transition. Analogously, the $(A^0,X)_{n=2}$ transition has a lower energy than the $(A^0,X)_{n=1}$ transition. For a detailed discussion of excitonic and impurity transitions in III–V semiconductors, the reader is referred to Williams and Bebb (1972).

A quantitative relation between the bound exciton (BE) localization energy and the ionization energy of the binding center was found by Haynes (1960).

https://doi.org/10.1017/CBO9780511599828.015 Published online by Cambridge University Press

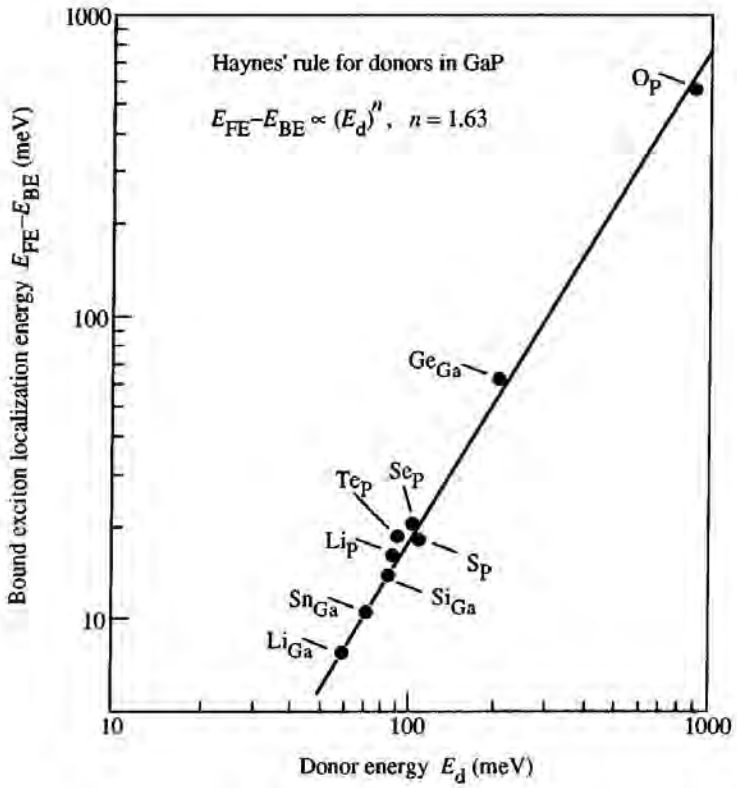


Fig. 12.15. Variation of the bound exciton (BE) localization energy for different donors in GaP (after Dean, 1983).

This relation allows one to identify impurity elements from their BE energy. Let us define the BE localization energy as the energy required to remove the BE from its binding center to obtain a FE and an isolated, non-interacting center. Haynes found experimentally that the BE localization energy increases with the impurity ionization energy. This rule is known as ***Haynes' rule*** and can be written as

$$\boxed{E_{FE} - E_{BE} = \alpha(E_d)^n} \tag{12.76}$$

where E_d is the ionization energy of the binding center, α is a constant with typical values of $0.05 - 0.5$, and n is a constant with typical values of $1.0 - 2.0$. (For acceptors in Si, Haynes found $\alpha = 0.10$ and $n = 1.0$). The variation of the BE localization energy for nine different donors in GaP is shown in Fig. 12.15 (Dean, 1983). The author modeled the binding energy in terms of Eq. (12.76) and found that an exponent of $n = 1.63$ provides a good fit to the experimental data.

https://doi.org/10.1017/CBO9780511599828.015 Published online by Cambridge University Press

In GaAs and InP, the shallow donor and acceptor energies do not vary much for different chemical impurities. It is therefore difficult to evaluate the parameters α and n in Eq. (12.76). Assuming $n=1.0$, the parameter $\alpha \cong 0.2$ and $\alpha \cong 0.1$ for neutral donor and acceptor transitions in GaAs, respectively, as inferred from Fig. 12.14.

The sharpness of the BE lines allows one to resolve many different lines and thereby to identify chemical impurities in III–V semiconductors. A systematic study of acceptor energies in GaAs using the bound exciton, electron-to-acceptor, and donor-to-acceptor lines has been reported by Ashen et al. (1975). Donors in GaAs were identified by Harris et al. (1988), Almassy et al. (1981), and Reynolds et al. (1983). Donor identification in InP using photoluminescence techniques was reported by Dean et al. (1984a, 1984b) and Skolnick et al. (1984).

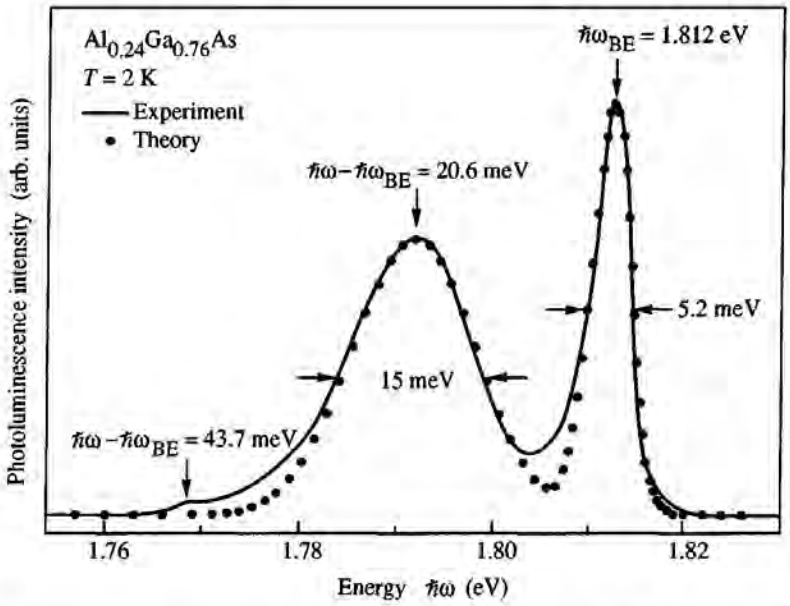


Fig. 12.16. Low-temperature photoluminescence spectrum of $Al_{0.24}Ga_{0.76}As$. Experimental data (solid line) compares well with theoretical data (dots) calculated from alloy broadening.

Spectral features of luminescence spectra are significantly broadened in ternary and quaternary semiconductor alloys by ***alloy broadening*** (Schubert et al., 1984). Consider a ternary semiconductor alloy such as $Al_xGa_{1-x}As$. Assume further that the composition x varies on a microscopic scale and is caused by the random distribution of Al and Ga on the cation sites of the zincblende lattice. Since the bandgap energy depends on the local alloy composition, the gap energy

https://doi.org/10.1017/CBO9780511599828.015 Published online by Cambridge University Press

varies spatially as well. As a result, luminescence of alloys reflects the spatial variation of the bandgap energy. The low-temperature photoluminescence spectrum of $Al_{0.24}Ga_{0.76}As$ shown in Fig. 12.16 illustrates the effect of alloy broadening. The BE line, which is typically 0.1 meV wide in binary III–V semiconductors, has a full width at half-maximum of 5.2 meV. The (eA^0) transition is 15 meV wide. The alloy broadening of the BE and (eA^0) lines can be calculated assuming random distribution of cations or anions. For a ternary alloy semiconductor with composition x (e.g. $Al_xGa_{1-x}As$), the luminescence linewidth is given by (Schubert et al., 1984)

$$\Delta E_{BE} = 2\sqrt{2\ln 2}\,\frac{dE_g}{dx}\left[\frac{x(1-x)}{KV_{exc}}\right]^{1/2} \tag{12.77}$$

where dE_g/dx is the change of the gap energy with composition, and K is the cation density of the semiconductor given by

$$K = 4a_0^{-3} \tag{12.78}$$

which is $K = 2.21 \times 10^{22}\ cm^{-3}$ in GaAs and V_{exc} is the excitonic volume given by

$$V_{exc} = \frac{4}{3}\pi\left[\frac{\varepsilon\, m_0}{\varepsilon_0\, m_r^*}\, a_B\right]^3 . \tag{12.79}$$

The width of the BE line calculated from Eqs. (12.77)–(12.79) agrees with the experimental width as illustrated by the comparison of experimental and theoretical luminescence spectra shown in Fig. 12.16.

The spectral width of the eA^0 line was found to be predominantly determined by the fluctuation of the acceptor energy and is given by (Schubert et al. 1984)

$$\Delta E_{eA^0} = \frac{\Delta E_v}{\Delta E_g}\,\frac{dE_g}{dx}\left[\frac{x(1-x)}{KV_{acc}}\right]^{1/2} \tag{12.80}$$

where $\Delta E_V/\Delta E_g$ is the relative variation of the valence band edge with composition, also called valence band offset; V_{acc} is the volume of the acceptor wave function

$$V_{acc} = \frac{4}{3}\pi\left[\frac{\varepsilon\, m_0}{\varepsilon_0\, m_{hh}^*}\right]a_B \tag{12.81}$$

where m_{hh}^* is the heavy-hole effective mass. The experimental (eA^0) transition-line-width agrees with the calculated linewidth as shown in Fig. 12.16. A

https://doi.org/10.1017/CBO9780511599828.015 Published online by Cambridge University Press

337-TA-1366 RX-0255

$\Delta E_V/\Delta E_g$ ratio of 0.15 was assumed in the calculation. Alloy broadening also prevails in luminescence spectra of other ternary alloy semiconductors such as $Ga_xIn_{1-x}As$, $Al_xIn_{1-x}As$, or $Ga_xIn_{1-x}P$. Luminescence spectra of quaternary III–V semiconductors (see, for example, Göbel, 1982) have even broader luminescence features due to random concentration fluctuations of cations *and* anions.

For completeness, we summarize other broadening mechanisms of luminescence lines in semiconductors. We assume that a radiative electronic transition occurs between an initial and a final state. Each of the two quantum states can be broadened. Two types of broadening mechanisms, namely ***homogeneous*** and ***inhomogeneous broadening*** are differentiated. *Homogeneous* broadening is due to the finite lifetime of an electron occupying a quantum state. This lifetime can be limited by, for example, (i) radiative transitions, (ii) tunneling of the electron to another state (e.g. tunneling of an electron in a multi-quantum well structure from one well to another well), or (iii) scattering of the electron by a phonon to another state. The broadening due to a finite lifetime, τ, can be obtained from the uncertainty relation

$$\Delta E = \hbar/\tau \tag{12.82a}$$

where ΔE is called the ***natural linewidth***. If several physical mechanisms, e.g. recombination, tunneling, and phonon scattering, limit the state lifetime, then the total broadening is given by

$$\Delta E^2 = \Delta E^2_{\text{recombination}} + \Delta E^2_{\text{tunneling}} + \Delta E^2_{\text{phonon}} . \tag{12.82b}$$

The lineshape of a homogeneously broadened luminescence transition is lorentzian (Davydov, 1965)

$$I(E) = \frac{\Delta E/2\pi}{(E - E_{\text{ave}})^2 + \frac{1}{4}\Delta E^2} \tag{12.82c}$$

where E_{ave} is the average luminescence energy.

The *inhomogeneous* broadening mechanisms of a quantum state include any statistical fluctuations which perturb the energy of the state. Examples of such mechanisms are (i) compositional fluctuations in semiconductor alloys, (ii) quantum well width fluctuations in semiconductor heterostructures, or (iii) impurity density fluctuations due to the random distribution of impurities. The lineshape of inhomogeneously broadened transitions depends on the specific broadening mechanism, but, frequently, a gaussian lineshape is assumed.

Finally, the ***thermal broadening*** of radiative transitions is due to the thermal distribution of carriers among a set of quantum states. Thermal broadening of the

https://doi.org/10.1017/CBO9780511599828.015 Published online by Cambridge University Press

RX-0255.542

(eA^0), (D^0h), and (eh) transitions results in a linewidth of

$$\Delta E \cong 1.8\ kT \tag{12.83}$$

as inferred from Eqs. (12.60) and (12.67). Note that thermal broadening is neither a homogeneous nor an inhomogeneous broadening mechanism, since it is *not* due to the broadening of a quantum state. Instead, thermal broadening reflects the distribution of carriers among a set of initial and final states.

12.2.2 Absorption characterization

Light traversing a semiconductor decreases in intensity along the propagation direction due to absorption processes. Consider a light beam propagating along the z-direction which enters an absorbing semiconductor at $z = 0$. The light intensity can then be written as

$$I = I_0\ e^{-\alpha z} \tag{12.84}$$

where α is the ***absorption coefficient*** and I_0 is the light intensity at $z = 0$. Different physical processes give rise to the absorption of photons in semiconductors.

Intrinsic absorption processes are (i) band-to-band (ii) excitonic, (iii) free carrier absorption, (iv) inner-shell electron absorption, and (v) phonon absorption processes. In the near-bandgap wavelength range, band-to-band absorption is the most important process at room temperature. The lowest energy of band-to-band transitions is given by the gap energy of the semiconductor which is also called the ***fundamental absorption edge***.

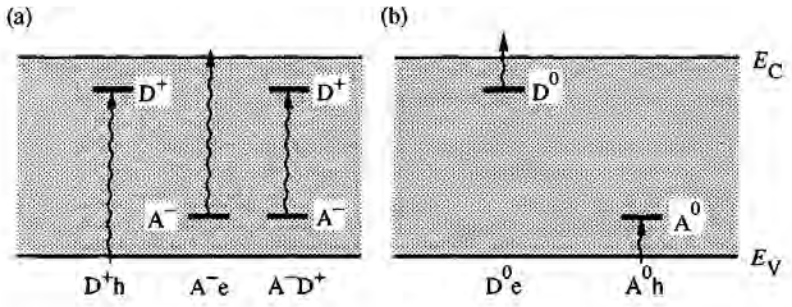


Fig. 12.17. Schematic illustration of (a) the near-band-edge absorption processes D^+h, A^-e, and (b) the far-infra-red absorption processes D^0e and A^0h.

https://doi.org/10.1017/CBO9780511599828.015 Published online by Cambridge University Press

337-TA-1366 RX-0255

Extrinsic absorption processes are illustrated in Fig. 12.17 and are either in the near-bandgap regime or in the far-infra-red regime. Near-gap transitions (Fig. 12.17a) are the valence-band-to-donor (D^+h), the acceptor-to-conduction-band (A^-e), or the acceptor-to-donor (A^-D^+) transition. The far-infra-red (FIR) transitions (Fig. 12.17b) for shallow impurities are the donor-to-conduction-band (D^0e) and the valence-band-to-acceptor (A^0h) transition. The FIR excitation wavelength can be as long as $\lambda = 250\ \mu m$ and requires very different experimental methods as compared to the near-band-edge transitions. A further extrinsic FIR absorption process is due to local vibrational modes of impurities or of impurity pairs. Such local vibrational mode absorption will be discussed later in this section.

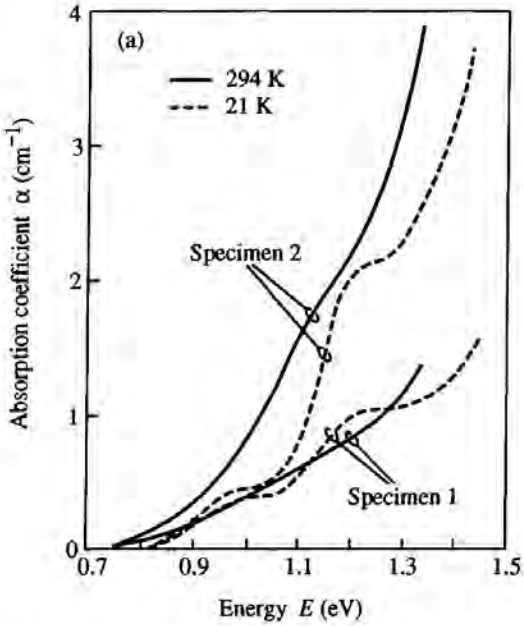
Near-bandgap absorption spectra of GaAs at two different temperatures are shown in Fig. 12.18 (Sturge, 1962). The magnitude of the below-bandgap absorption coefficient (Fig. 12.18a) is several orders of magnitude smaller than that for above-bandgap absorption. The absorption spectra taken at low temperatures ($T = 21$ K) display well-resolved features as compared to the room temperature spectra (T = 294 K). Sturge (1962) proposed that the shoulders observed in Fig. 12.18(a) are associated with impurity levels. The impurity levels are at energies 0.30 eV, 0.47 eV, and 0.70 eV above the valence band or below the conduction band. Comparison of the absorption data with photoconductivity experiments (Bube, 1960) led Sturge (1962) to the conclusion that the 0.47 eV and the 0.70 eV levels are associated with donor levels. Sturge (1962) also showed that the initial rise of the absorption can be described with the empirical formula $\alpha \propto (E - E_i)^2$ where E_i was defined as the *threshold* of an impurity. The threshold, E_i, varied with temperature; however $(E_g - E_i)$ was shown to be constant with temperature. This can be explained if the impurity level is 'attached' to either the valence or the conduction band.

Band-edge and above-band-edge absorption is shown in Fig. 12.18(b) for the two temperatures $T = 21$ K and 294 K. The shift of the onset of absorption reflects the shift of the band edge from $E_g \equiv 1.51$ eV to 1.42 eV for low and high temperatures, respectively. The pronounced enhancement of the band-edge absorption at low temperatures is attributed to free excitonic absorption. Such excitonic enhancement is not observed at room temperature since excitons with a binding energy on the order of 5 meV dissociate rapidly at room temperature.

Several aspects of near-band-edge absorption need to be mentioned. At high doping concentrations, e.g. donor concentrations, the Fermi level moves into the conduction band. Since all states below E_F are occupied, the absorption edge shifts from $E_C - E_V = E_g$ to $E_F - E_V > E_g$. Analogous arguments apply to high acceptor concentrations. The shift of the absorption edge to higher energies

https://doi.org/10.1017/CBO9780511599828.015 Published online by Cambridge University Press

RX-0255.544



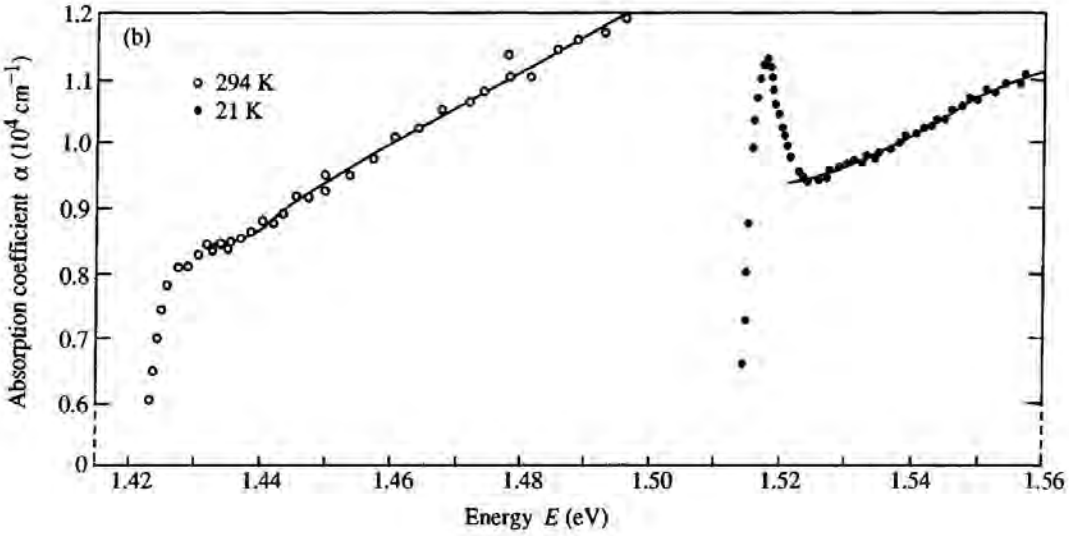


Fig. 12.18. (a) Below-bandgap and (b) above-bandgap absorption spectra in GaAs at T = 21 K and 294 K. Absorption processes below the band gap shown in (a) are due to impurities (Sturge, 1962).

is called the ***Burstein–Moss shift*** (Burstein, 1954; Moss, 1954) and is due to band filling effects. On the other hand, the formation of tail states and bandgap renormalization occur at high doping density which counteracts the band filling. Impurity ***tail states*** are formed when impurity states form an impurity band and finally merge with the valence and conduction band. Impurity tail states were correlated with internal electric fields in the semiconductor caused by random impurity distribution (Redfield, 1963; Pankove, 1965). The authors correlated the

https://doi.org/10.1017/CBO9780511599828.015 Published online by Cambridge University Press

337-TA-1366 RX-0255

magnitude of the band tail with the impurity concentration. In addition to tail states, ***bandgap renormalization*** is a many-body effect at high carrier densities which reduces the band gap. Bandgap renormalization was discussed by Wolf (1962) and others. A detailed discussion of such impurity effects is found in Chap. 1. Even at low impurity concentrations, absorption occurs below the fundamental gap. Urbach (1953) showed that the absorption in the tail follows the relationship $d(\ln\alpha)/d(\hbar\omega) = 1/kT$. Such band tails are referred to as ***Urbach tails***. The temperature dependence of Urbach tails led Knox (1963) to the conclusion that the tails are caused by phonon assisted transitions. For a quantitative discussion of band tails, the reader is referred to Chap. 1.

Photocurrent absorption spectroscopy is a simple alternative to regular absorption spectroscopy. In photocurrent spectroscopy, absorption processes can be detected that create free carriers in the valence or conduction band. These carriers are detected in terms of a current. Two major processes complicate the interpretation of photocurrent measurements. First, *surface recombination* of photogenerated carriers reduces the photocurrent signal. Because of surface recombination, the photocurrent signal is smaller than expected. Surface recombination is especially important for high photon energies, i.e. $\hbar\omega >> E_g$. The absorption coefficient for such photon energies is large, resulting in a small penetration depth $l = \alpha^{-1}$, i.e. free carriers are generated in the near-surface region, in which they are subject to surface recombination. Second, *bulk recombination* of photogenerated carriers reduces the photocurrent signal. This problem can be alleviated, if pin-junctions are used for the photocurrent measurement. Electrons and holes created in the i-region of the diode will be spatially separated by the built-in electric field. The spatially separated electrons and holes do not recombine and thus fully contribute to the photocurrent. Nevertheless, the employment of pin-junctions does not solve the problem of surface recombination. The two problem areas of surface and bulk recombination make photocurrent absorption spectroscopy a qualitative method whose quantitative interpretation is difficult.

For absorption in the far-infra-red (FIR), photocurrent spectroscopy is the preferred method due to its sensitivity and due to the lack of efficient detectors that work in a broad wavelength range, e.g. $\lambda = 100-400\ \mu m$. In addition to photocurrent, photovoltage measurements were used in the FIR region (Stillman et al., 1977), and these are preferred for highly resistive samples.

The FIR conductivity spectrum of high-purity GaAs measured at 4.2 K is shown in Fig. 12.19 (Wolfe and Stillman, 1971). The background impurity concentration of the GaAs sample is in the $10^{13}\ cm^{-3}$ range. The photoconductivity spectrum shows clearly resolved peaks at energies ranging

https://doi.org/10.1017/CBO9780511599828.015 Published online by Cambridge University Press

RX-0255.546

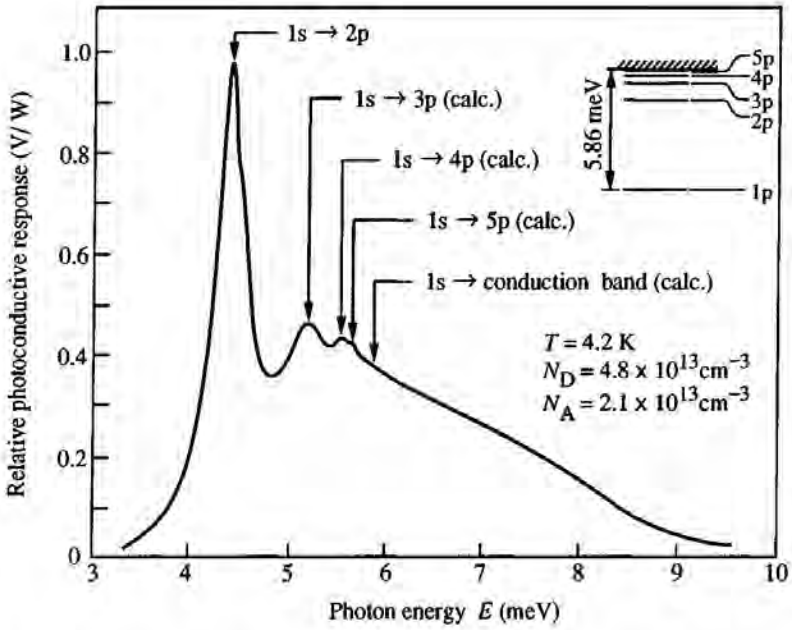


Fig. 12.19. Far-infra-red photoconductivity spectrum of high-purity GaAs. Also shown are theoretical transition energies (arrows) calculated from the hydrogenic model using the experimental (1s → 2p) energy as a fit parameter. The hydrogenic energy level diagram is shown in the inset (after Wolfe and Stillman,1971).

from 4 meV to 6 meV. The major line at 4.40 meV was identified as the 1s→2p transition of a hydrogenic donor impurity, i.e. a transition from the ground state ($n = 1$) to the first excited state ($n = 2$). In zero magnetic field, the 2s and 3s states are degenerate with the 2p and 3p states. However, transitions between the ground state (1s) and the s-type excited states are not allowed. The matrix elements for the transitions, which are proportional to $\langle \psi_{1s} | r | \psi_{2s} \rangle$ and $\langle \psi_{1s} | r | \psi_{3s} \rangle$, are zero, since all of the wave functions ψ_{1s}, ψ_{2s}, and ψ_{3s} are functions of even symmetry with respect to the radius r (Bohm, 1951). Using the energy of the 1s → 2p transition, the authors calculated the 1s → 3p, 1s → 4p, 1s → 5p, and 1s-to-continuum transitions. The energies of the calculated transitions are shown in Fig. 12.19 and agree with the experimental peaks. Using the 1s → 2p transition energy, the shallow donor ionization energy was calculated to be $E_d = 5.86$ meV in GaAs.

If the excited states (2p, 3p, 4p, ···) were really bound states, electrons in these states could not contribute to the conductivity of the sample and the excited-state absorption would not result in peaks in the photoconductivity spectrum. Stillman et al. (1977) proposed several mechanisms by which excited

https://doi.org/10.1017/CBO9780511599828.015 Published online by Cambridge University Press

337-TA-1366 RX-0255

hydrogenic impurity atoms become ionized, that is contribute to the photoconductivity. First, excited-state wave functions are more likely to overlap with neighboring impurities as compared to the spatially localized 1s wave function. Conduction via an excited-state impurity band is then more likely. Second, excited donor atoms can be ionized by field-induced tunneling from the excited state into the conduction band. Third, energetic free electrons can ionize excited-state donors by impact ionization. Fourth, excited donors can be thermally ionized, that is by absorption of one or several phonons. Fifth, an excited donor can be photoionized, that is by absorption of a second photon. Although it is difficult to estimate the relative importance of the processes, it is evident that excited donors can become fully ionized and contribute to the conductivity of the semiconductor.

Finally, FIR radiation can also be absorbed by localized vibrational modes of impurities or impurity pairs. Such absorption will be discussed later in this section.

12.2.3 Raman characterization

Raman characterization is a spectroscopic technique in which elementary excitations are induced by incident light. In the process of an elementary excitation, the incident photon is scattered such that the scattered photon has a different energy than the incident photon. Raman spectroscopy is therefore also called ***inelastic light scattering*** spectroscopy. The energy and momentum balance of a Raman scattering event can be written as

$$E_i \pm E_{exc} = E_s \,, \tag{12.85a}$$

$$k_i \pm q_{exc} = k_s \tag{12.85b}$$

where E_{exc} and q_{exc} are the energy and momentum of the elementary excitation and the subscript i and s refer to the incident and the scattered photon, respectively. The minus sign in Eq. (12.85) is valid if a quantum process is *excited* in the semiconductor. As a result, the energy of the scattered photon is *lower*, i.e. *Stokes shifted*. The plus sign in Eq. (12.85) is valid if an elementary process is *de-excited*. As a result, the energy of the scattered photon is *higher*, i.e. *anti-Stokes*-shifted. The intensity of the Stokes-shifted scattered light is usually much stronger than the intensity of the anti-Stokes-shifted light.

A Raman backscattering measurement configuration is shown in Fig. 12.20(a). The excitation beam has near normal incidence with respect to the sample surface. Also shown is the momentum conservation condition (Fig. 12.20b) for an elementary excitation, i.e. Stokes scattering. The average

https://doi.org/10.1017/CBO9780511599828.015 Published online by Cambridge University Press

RX-0255.548

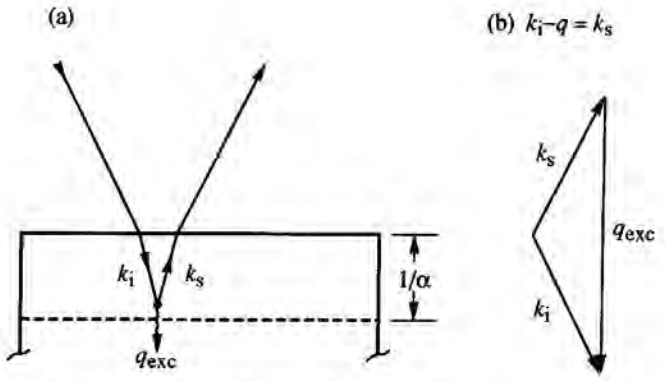


Fig. 12.20. (a) Illustration of the Raman backscattering geometry with wavevector of incident (k_i) and scattered (k_s) light. The penetration depth of the exciting light into the sample is $1/\alpha$. (b) Momentum conservation for Stokes scattering.

probing depth of the incident light beam depends on the absorption coefficient of the semiconductor, $\alpha(\lambda)$, at the wavelength λ of the incident light. The average probing depth of the measurement is $[\alpha(\lambda)]^{-1}$. Thus, the probing depth of Raman scattering can be chosen by proper selection of the excitation wavelength.

The most widespread use of Raman spectroscopy is for lattice vibrations, that is if the elementary excitations are phonons. Due to the small momentum of photons as compared to the range of momenta of phonons, only *optical* (transverse and longitudinal modes) photons can be excited in Raman experiments. Such optical phonons can have zero momentum and a finite energy. Several comprehensive reviews have been published on Raman spectroscopy for optical phonon excitation (see, for example, Cardona and Güntherodt, 1984, 1989).

There are two major areas where Raman spectroscopy is used to characterize impurities. These are ***electronic Raman spectroscopy*** and **local vibrational mode (LVM) Raman spectroscopy**. In electronic Raman spectroscopy, carriers are excited from the ground state of an impurity to an excited impurity state. In LVM Raman spectroscopy, local vibrational modes of impurities or impurity complexes are excited by the incident light.

Electronic Raman spectroscopy was first employed for acceptors in GaAs (Wright and Mooradian, 1968) and GaP (Henry et al., 1966; Chase et al., 1977). The first well-resolved electronic Raman spectra were reported for acceptors in semi-insulating GaAs (Wan and Bray, 1985). These spectra allowed the authors to identify C and Zn in GaAs grown by the liquid encapsulated Czochralski (LEC) technique. Wagner et al. (1986a, 1986b, 1986c, 1988a, 1988b) extensively

https://doi.org/10.1017/CBO9780511599828.015 Published online by Cambridge University Press

337-TA-1366 RX-0255

studied shallow acceptors in semi-insulating GaAs using electronic Raman spectroscopy. The studies revealed that electronic Raman spectroscopy allows one to evaluate quantitatively acceptor concentrations in semi-insulating GaAs (Wagner et al., 1986a). A comparison of electronic Raman and luminescence experiments revealed that quantitative assessment of acceptor concentrations is difficult with either technique. Electronic Raman spectroscopy has also been used for relatively deep acceptors in GaAs (Shanabrook et al., 1986). The concentration of shallow acceptors compensated by the EL2 center in semi-insulating GaAs was studied by Wagner et al. (1988b). Electronic Raman scattering was also reported for donors in $GaAs/Al_xGa_{1-x}As$ quantum wells (Perry et al., 1985a, 1985b). They observed a line which they attributed to $1s \rightarrow 2s$ transitions of the donor and additional peaks attributed to donor-resonance excitations. Gammon et al. (1986) reported electronic Raman transitions for Be acceptor transitions in $GaAs/Al_xGa_{1-x}As$ quantum wells. Experimental line positions were found to agree with theoretical predictions. Although LVM will be discussed in detail in the next section, some specific characteristics of LVM Raman are listed here. As mentioned above, the probing depth of Raman is $(1/\alpha)$ which can be of the order of one or several 1000 Å. It is therefore possible to probe thin layers by LVM Raman, e.g. epitaxially grown layers. Furthermore, LVM Raman allows measurements at relatively high free carrier concentrations. Free carrier absorption, which interferes with the LVM signal (see next section), does not affect the LVM-Raman signal in an excessive way due to the high energy of incident and scattered photons.

12.2.4 Local vibrational mode characterization

Acoustic and optical phonons are thermal vibrations of atoms in a perfect lattice. Such lattice vibrations are propagating plane waves and are thus spatially delocalized. The frequency of optical phonons is approximately given by (Moll, 1964)

$$\omega_{LO} \equiv \omega_{TO} \equiv \sqrt{\frac{k}{M}} \tag{12.86}$$

where k is the force constant of the lattice and M is the mass of a lattice atom. The subscripts LO and TO refer to longitudinal and transverse optical phonon modes, respectively. In compound semiconductors, Eq. (12.86) needs to be modified according to

$$\omega_{LO} \equiv \omega_{TO} \equiv \sqrt{\frac{2k}{M_1 + M_2}} \tag{12.87}$$

https://doi.org/10.1017/CBO9780511599828.015 Published online by Cambridge University Press

RX-0255.550

where M_1 and M_2 are the two atomic masses of the binary compound semiconductor.

The characteristics of lattice vibrations are changed drastically if an impurity atom is added to the lattice. Consider an impurity atom with a mass M_i such that $M_i < M$. The angular frequency of the vibration of an impurity atom is then given in analogy to Eq. (12.86) by

$$\omega_i \equiv \sqrt{\frac{k}{M_i}} \,. \tag{12.88}$$

Since $M_i < M$, the frequency of the impurity vibration is higher as compared to regular lattice vibrations, i.e. the energy of the impurity vibrations, $\hbar\omega_i$, is larger than the (maximum) energy of optical phonons. Hence, the energy of an impurity vibration cannot be transferred to the lattice by the emission of a single phonon. The amplitude of the vibration of the impurity and its neighbors is exponentially attenuated with distance from the impurity (Spitzer, 1971). Such impurity vibrations are called spatially ***localized vibrational modes*** (LVM).

The site of a substitutional impurity atom has tetrahedral symmetry and the potential for small displacements of the impurity is that of a spherical harmonic oscillator (Spitzer, 1971). Thus vibrations in the x-, y-, and z-directions are equivalent and the oscillation mode is triply degenerate. Furthermore, due to the isotropic, spherical potential, only *one* (triply degenerate) fundamental oscillation is expected for a substitutional impurity atom. The calculated and experimental wavenumbers of substitutional impurities in GaAs and InP are shown in Table 12.1.

Several modes of local vibrations with different frequencies may be possible for impurity pairs, impurity clusters, and impurity–native defect complexes. As an example, a $Si_{Ga}-Si_{As}$ pair in GaAs is schematically shown in Fig. 12.21 (Spitzer, 1971). The $Si_{Ga} - Si_{As}$ pair has four vibrational modes which are indicated by arrows. The approximate values for the vibrational angular frequencies are $\omega_1 = 327\ cm^{-1}$, $\omega_2 = 369\ cm^{-1}$, $\omega_3 = 390\ cm^{-1}$, and $\omega_4 = 419\ cm^{-1}$. Not all vibrational modes of impurity complexes may be *infra-red active*, but only those modes in which a dipole moment is changed during the impurity displacement. For the case of the Si–Si pair, all four modes are infra-red active (Spitzer, 1971).

Vibrational modes can have fine structures with several resonances at slightly different frequencies due to isotopes of the semiconductor lattice. For example, Ga has two isotopes with atomic masses 69 and 71 and relative abundances of 60.4% and 39.6%. A substitutional impurity occupying an As site in GaAs has four Ga next neighbors. As a result, five different

https://doi.org/10.1017/CBO9780511599828.015 Published online by Cambridge University Press

Table 12.1. *Fundamental local mode wavenumbers in* cm^{-1} ($8.065\ cm^{-1} \equiv 1$ meV) *for substitutional impurities in GaAs and InP (Newman, 1974).*

	Theory	Experiment
$^{31}P_{As}$	351	355.4
$^{27}Al_{Ga}$	369	362.0
$^{28}Si_{Ga} - {}^{28}Si_{As}$	369	367.2
$^{28}Si_{Ga} - V_{Ga}$		368.5
$^{30}Si_{Ga}$	352	373.4
$^{29}Si_{Ga}$	357.5	378.5
$^{28}Si_{Ga}$	363	383.7
$^{28}Si_{Ga} - {}^{28}Si_{As}$	390	393.0
$^{28}Si_{Ga}$	365	398.2
$^{28}Si_{Ga} - {}^{28}Si_{As}$	419	464.0
$^{11}B_{Ga}$	542	517.0
$^{10}B_{Ga}$	570	540.2
$^{13}C_{As}$	500	561.2
$^{12}C_{As}$	519	582.4
$^{10}B_{In}$	558	543.5
$^{11}B_{In}$	536	522.8

combinations of Ga atoms with different masses are possible which are (1) $4 \times {}^{69}Ga$, (2) $1 \times {}^{71}Ga$ & $3 \times {}^{69}Ga$, (3) $2 \times {}^{71}Ga$ & $2 \times {}^{69}Ga$, (4) $3 \times {}^{71}Ga$ & $1 \times {}^{69}Ga$, and (5) $4 \times {}^{71}Ga$. Due to the strong spatial localization of the vibrational mode at the impurity atom, next neighbor isotopes do not shift the frequency dramatically. A high-resolution detection system is required to resolve the splitting due to isotopes. Furthermore, if the four nearest neighbors consist of two different isotopes, the degeneracy of local mode vibrations along the *x*-, *y*-, and *z*-axis is lifted. Sinai and Wu (1989) calculated the frequencies for such a mixed nearest neighbour environment.

The localized vibrational mode absorption band of ^{12}C in GaAs is shown in Fig. 12.22 (Theis et al., 1982). The measurement is taken at 80 K. The four lines shown in Fig. 12.22 merge to a single line for lower resolutions of the detection system. The single line peaks at $582.4\ cm^{-1}$. A higher resolution of $0.06\ cm^{-1}$ reveals a series of at least four peaks occurring at 582.18, 582.31, 582.41, and

https://doi.org/10.1017/CBO9780511599828.015 Published online by Cambridge University Press

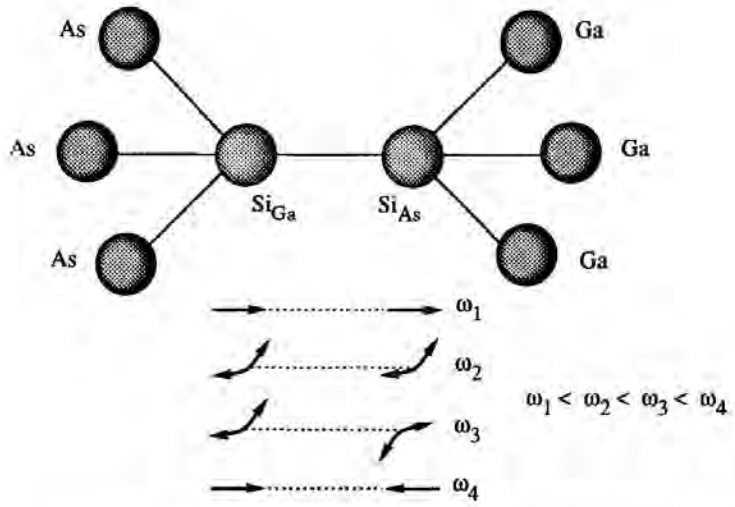


Fig. 12.21. Schematic illustration of the four local vibrational modes of a Si impurity pair in GaAs (after Spitzer, 1971).

582.65 cm^{-1}. The four lines of ^{12}C in GaAs were first observed by Newman et al. (1972) at the same wavenumbers. The overlapping bands were explained by the different isotopic arrangements of the four nearest Ga neighbors of the ^{12}C impurity, and the resulting different mode frequencies. Theis et al. (1982) further concluded that C only rarely occupies Ga sites and estimated the compensation ratio $[C_{Ga}]/[C_{As}] \leq 0.01$. Even at high concentrations, C was shown to mostly occupy As sites for OMMBE grown $Al_xGa_{1-x}As$ (Abernathy et al. 1990).

LVM can be measured by either far-infra-red (FIR) absorption or by Raman spectroscopy. The two techniques are usually referred to as ***LVM-FIR*** and ***LVM-Raman***. A severe limitation of LVM-FIR is free carrier absorption which occurs in the same spectral range as the local vibrational modes. In order to reduce this absorption, the free carrier concentration can be reduced by electron irradiation, by diffusion of a compensating impurities, or by implantation of H, He, or O. However, the species involved in these processes and the impurity under study may interact and change the experimental results as compared to the undamaged semiconductor. The absorption due to free carriers is less significant in LVM-Raman. First, the probing depth of the exciting laser can be chosen to be very small by choosing high-energy excitation ($\hbar\omega >> E_g$). Second, the incident and scattered photons are not subject to free carrier absorption due to the high energy of the photons.

https://doi.org/10.1017/CBO9780511599828.015 Published online by Cambridge University Press

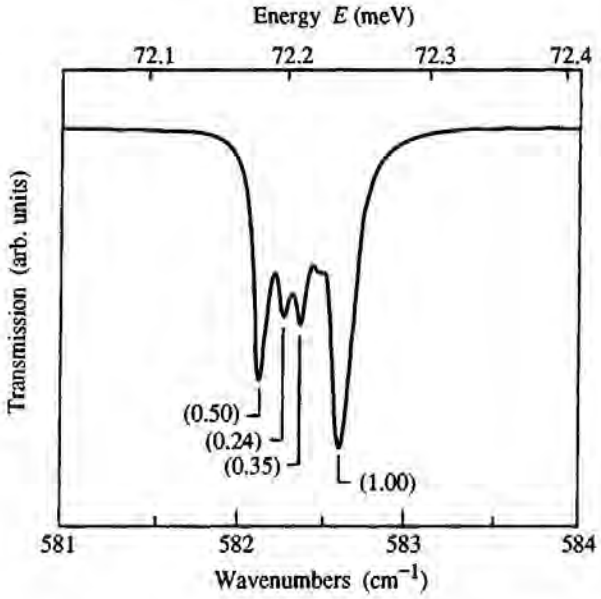


Fig. 12.22. Localized vibrational mode absorption for ^{12}C in GaAs measured at 80 K. The values in parentheses are estimated band stengths (after Theis et al., 1982).

LVM spectroscopy has been widely used for the analysis of Si in GaAs (Ramsteiner et al., 1988; Maguire et al., 1987; Murray et al., 1989; Wagner and Ramsteiner, 1989; Nakamura and Katoda, 1985; Holtz et al., 1986; Leigh and Newman, 1982) which includes Si doping during growth and during post-growth implantation. LVM spectroscopy has also been employed for p-type impurities such as Be (Wagner and Ramsteiner, 1989) and C (Leigh and Newman, 1982; Theis et al., 1982; Kitagawara et al., 1986; Abernathy et al., 1990) in GaAs. The sensitivity of LVM can be very high. Kitagawara et al. (1986) demonstrated a C detection limit of 5×10^{14} cm^{-3} in GaAs. The authors also related the magnitude of the LVM absorption to the C concentration.

12.3 Chemical and structural characterization techniques

Many chemical and structural characterization techniques do not have sufficient sensitivity to be useful for characterization of impurities. Sensitivities of 10^{-9} are required in order to detect impurities at low concentrations in III–V semiconductors. Auger spectroscopy, for example, has a sensitivity of typically $0.1\% = 10^{-3}$. Hence, only very high impurity concentrations can be detected. Although Auger spectroscopy is a widely used semiconductor characterization

https://doi.org/10.1017/CBO9780511599828.015 Published online by Cambridge University Press

technique, it is of limited use for impurity characterization.

In this section, two techniques will be discussed that can be employed for impurity characterization. These techniques are secondary ion mass spectrometry (SIMS), and X-ray diffraction. The most widely used technique is SIMS which has excellent sensitivity and depth resolution. The use of X-ray diffraction is limited to very high impurity concentrations at which the lattice constant of the host semiconductor changes.

12.3.1 Secondary ion mass spectrometry

Secondary ion mass spectrometry (SIMS) is one of the most versatile chemical characterization techniques. During the SIMS measurement, a primary ion beam is used to sputter the specimen. Secondary ions are released from the specimen as a result of the sputter process. Analysis of the secondary ions by means of mass spectrometry allows one to chemically profile and identify the constituents of the specimen.

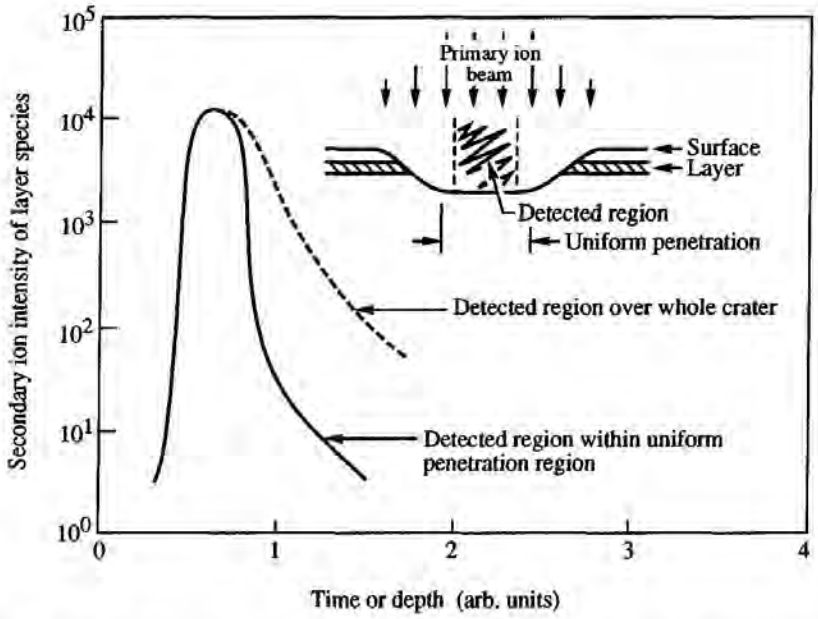


Fig. 12.23. Relationship of depth profile shape to rastered and detected areas during secondary ion mass spectrometry (SIMS) (after Wilson et al., 1989).

The ***primary ion beam*** has typical energies of 1–50 keV and is rastered across a squared area of typically $100 \times 100\ \mu m^2$ to $500 \times 500\ \mu m^2$. The ion beam and the specimen is schematically shown in the inset of Fig. 12.23. The collisions between primary ions and the semiconductor specimen are inelastic. As a result

https://doi.org/10.1017/CBO9780511599828.015 Published online by Cambridge University Press

337-TA-1366 RX-0255

of these collisions, atoms or molecules of the semiconductor are released into the surrounding vacuum. The primary ion beam may have an off-normal incidence with respect to the sample surface. Off-normal incidences $\leq 60°$ are common. At off-normal incidence, the transfer of primary ion momentum occurs primarily in a lateral direction and scattering processes are close to the specimen surface. As a consequence, improved depth resolution is attainable. Typical chemical species of the primary ion beam are O_2^+, Cs^+, Ar^+, Kr^+, and Xe^+. When chemical reactions between the primary ions and the specimen are undesired, noble gas atoms are frequently used as primary ion species. However, the use of O_2^+ and Cs^+ enhance the yields of negative and positive secondary ions, respectively, and thus are most commonly used for the analysis of impurities.

The ***sputter rate*** depends on the primary ion energy, the area profiled, the angle of the incident primary ions, the primary ion species, the primary ion flux, and the semiconductor material. The primary ion flux (ions per unit time), also called the primary beam current, can be easily adjusted. One μA of primary ion current corresponds to 6.25×10^{12} ions/s. Assuming that each primary ion creates one secondary atom and recalling that one monolayer of III–V semiconductors contains about 6×10^{14} atoms/cm^2, a primary ion current of 100 μA is required for a sputter rate of one monolayer per second (for a sputter area of 1 cm^2). In practice, the sputter yield, i.e. the number of specimen atoms sputtered by one primary ion, varies and can assume values of 1–100. Most of the sputtered atoms and molecules are neutral. A small fraction of the particles are ionized, typically $10^{-3} - 10^{-7}$, and this fraction is called the *secondary ion yield*. Secondary ions are extracted by an electric field and analyzed by mass spectrometry. The spectrometric analysis yields the charge-to-mass ratio (e/m) of the secondary ions. Note that isotopes of impurities can be detected by SIMS due to the high mass sensitivity of spectrometers.

The sputtered area and the detected area are schematically shown in Fig. 12.23 (Wilson et al., 1989). During the measurement, the detected element is measured as a function of *time*. The time is later converted to *depth* by measuring the total depth of the sputtered crater. The area of the detected region affects the depth resolution of the SIMS profile. It is desirable to limit the detected region to the area of uniform sputtering. An improved depth resolution is obtained by limiting the area of detection as illustrated in Fig. 12.23. The *concentration* of a measured species is obtained by comparison with a measured standard (e.g. an ion-implanted standard) and by assuming that the secondary ion count varies linearly with the concentration of the detected element.

Historically, the SIMS technique was developed independently by Castaing et al. (1960, 1962) and by Herzog and Liebl (1963). Bennighoven (1970)

https://doi.org/10.1017/CBO9780511599828.015 Published online by Cambridge University Press

Innoscience1366-00139229

RX-0255.556

demonstrated that planar surfaces can be maintained during the sputter process. Several comprehensive reviews on SIMS have been published (Benninghoven et al., 1987; Wilson et al., 1989). A newer development of SIMS is the secondary neutral mass spectrometry (SNMS) which has been reviewed by Oechsner (1984). In SNMS, secondary atoms are ionized after the sputter process (post-ionization), e.g. by means of optical excitation or electron beam bombardment. In conventional SIMS, the secondary ion yield is on the order of $10^{-7} - 10^{-3}$. Due to post-ionization, the secondary ion yield can be increased to assume values close to unity. To date, however, the sensitivity of SNMS was not shown to be superior on a routine basis as compared to conventional SIMS.

Impurities in the mid and high doping regime ($> 10^{17}$ cm^{-3}) can be easily detected by SIMS. For some impurities, the sensitivity is higher allowing detection of impurities in the $10^{13} - 10^{15}$ cm^{-3} concentration range. It is important to note that the concentrations measured by SIMS are the impurity atom concentrations regardless of their *electrical activity*. In some cases, such as highly Si doped GaAs, the *electrically active* Si concentration can be much lower than the Si atom concentration (see, for example, Greiner and Gibbons, 1984).

The depth resolution of the SIMS technique for impurity profiles was investigated by Schubert et al. (1990b) using δ-doped semiconductors. The SIMS profiles of the Be impurity spikes in GaAs had a full width at half-maximum of 29 Å. The resolution of the profiling technique is defined as twice the standard deviation of a gaussian distribution fitted to the experimental profile (Benninghoven et al., 1987). Using this procedure, Schubert et al. (1990b) obtained a resolution of 25 Å. Low-energy sputtering (1.5 keV), a shallow sputtering angle (60° off-normal), and a Be doping spike in the proximity of the surface (200 Å) were required in order to obtain this resolution. Clegg and Beall (1989) used δ-doped semiconductors to analyze the leading and trailing slope of the SIMS profiles over several orders of magnitude of the SIMS signal.

The interpretation of impurity distributions assessed by the SIMS technique is complicated by ***matrix effects***. If an impurity species is detected in a homogeneous semiconductor, the secondary ion yield is constant and does not change with time. This situation can change in semiconductor multilayer structures, since the secondary ion yield of an impurity species depends on the host semiconductor (i.e. matrix). Assume a semiconductor heterostructure comprising two different semiconductors and both containing the same impurity species and the same impurity concentration. Then changes in the semiconductor composition (matrix) result in changes of the secondary ion yield. As a consequence, the SIMS signal of an impurity changes, even if the impurity concentration is the same in the two matrices. This effect is known as the *matrix*

https://doi.org/10.1017/CBO9780511599828.015 Published online by Cambridge University Press

effect. The physical origin of the matrix effect is due to the interdependence of secondary ion yield of an impurity and the host semiconductor composition (Wilson et al., 1989). The presence of electronegative elements such as O, N, or F, can increase the yield of positive secondary ions. As an example, we consider Be impurities in $Al_xGa_{1-x}As$/GaAs heterostructures subjected to O_2^+-sputtering during SIMS (Downey and Hozack, 1989). The Be^+ secondary ion yield increases with the presence of O and O_2 due to its strong electronegativity. The O surface coverage of $Al_xGa_{1-x}As$ is larger compared to GaAs due to the strong Al–O affinity. As a result, the Be^+ secondary ion yield is higher in $Al_xGa_{1-x}As$ and the measured SIMS Be concentrations are higher in $Al_xGa_{1-x}As$. To avoid this artificial reading, a separate calibration standard must be run for each matrix. Even though a separate standard is helpful for bulk material analysis, it is nevertheless problematic for thin multilayer structures and concentration profiles near interfaces (Downey et al., 1990). Matrix effects can be alleviated by using SNMS rather than SIMS. In SNMS, the secondary ion yield approaches unity under idealized conditions and does not depend on the matrix as long as parasitic reactions between the measured species and other constituents of the semiconductor can be neglected. SNMS impurity profiles indeed exhibit a reduced matrix effect as compared to SIMS (Downey et al., 1990).

12.3.2 X-ray diffraction

X-ray diffraction is a versatile characterization technique which is predominantly used to determine lattice constants of ternary and quaternary III–V semiconductors. For example, the lattice constant of epitaxial $Ga_xIn_{1-x}As$ on InP substrates is measured to determine if the epitaxial crystal is lattice-matched to the substrate. X-ray diffraction can also be used to determine the lattice distortion caused by impurities at very high doping concentrations. For example, C impurities cause lattice contraction in GaAs or InP at high C concentrations. The change in lattice constant can be determined by x-ray diffraction. Conversely, impurity concentrations can be determined by x-ray diffraction, assuming that the relation between impurity concentration and lattice constant is known. In this section, the x-ray diffraction technique is discussed with respect to impurity characterization.

Electromagnetic waves are elastically scattered by periodic structures such as semiconductor lattices. The magnitude of the incident and the scattered wavevector are identical due to the elastic nature of the scattering event, i.e.

$$k_{\text{incident}} = k_{\text{scattered}} = \frac{2\pi}{\lambda} \tag{12.89}$$

where k is the magnitude of the wave vector and λ is the wavelength of the

https://doi.org/10.1017/CBO9780511599828.015 Published online by Cambridge University Press

electromagnetic wave. The total reflection of electromagnetic radiation in periodic media is called ***Bragg reflection*** and occurs at specific wavelengths. The nth Bragg reflection condition is given by

$$\boxed{n\lambda = 2d\sin\theta} \tag{12.90}$$

where θ is the angle of incidence with respect to the crystal surface and d is the spacing of the lattice planes of interest, e.g. the (001), (004), (011), or (111) plane. Frequently, the (004) Bragg reflection is used to determine the lattice constant. This reflection originates from xy-planes separated by a quarter of the lattice constant ($a_0/4$). The lattice plane spacing, d, is on the order of the lattice constant, a_0. It is therefore desirable to use electromagnetic wavelengths on the order of the lattice constant, i.e. in the x-ray regime. For practical x-ray generators, the wavelength is a fixed quantity given by atomic core transitions of the x-ray source. In order to observe the Bragg reflections, the angle θ (see Eq. (12.90)) must be varied by 'rocking' the specimen. X-ray rocking curves are thus plots of the diffracted x-ray intensity as a function of the rocking angle θ.

In very highly doped semiconductors, the lattice constant changes and these changes can be detected by x-ray diffraction. Lattice ***contraction*** and lattice ***expansion*** results from impurities which are smaller and larger than the host semiconductor atoms, respectively. For example, C atoms are smaller than either Ga or As resulting in lattice contraction of highly C-doped GaAs. If the highly doped layer is an epitaxial layer grown on a substrate, ***mechanical strain*** occurs between the two layers due to the mismatch in lattice constant. For sufficiently thin mismatched epitaxial layers, the layers are strained *elastically*. Epilayers which exceed a certain *critical layer thickness* relax by means of misfit dislocations. The lattice constant of such relaxed layers is the equilibrium lattice constant which is different from that of the substrate.

An elastically strained epitaxial layer grown on a substrate with a larger lattice constant is shown schematically in Fig. 12.24. The equilibrium lattice constant of the epitaxial layer is assumed to be smaller than that of the substrate. As a result of the lattice mismatch, the epitaxial layer is tetragonally distorted (Hornstra and Bartels, 1978). Tetragonal distortion occurs for symmetry planes such as the (001), (011), or the (111) plane and manifests itself in two different lattice constants in the growth plane, $a_{\|}$, and along the growth direction, $a_{\perp}$. For the *lattice contraction* illustrated in Fig. 12.24, the in-plane lattice constant, $a_{\|}$, is the same as the lattice constant of the substrate, a_0. The normal lattice constant, $a_{\perp}$, is smaller or larger than a_0 for lattice contraction and expansion, respectively.

https://doi.org/10.1017/CBO9780511599828.015 Published online by Cambridge University Press

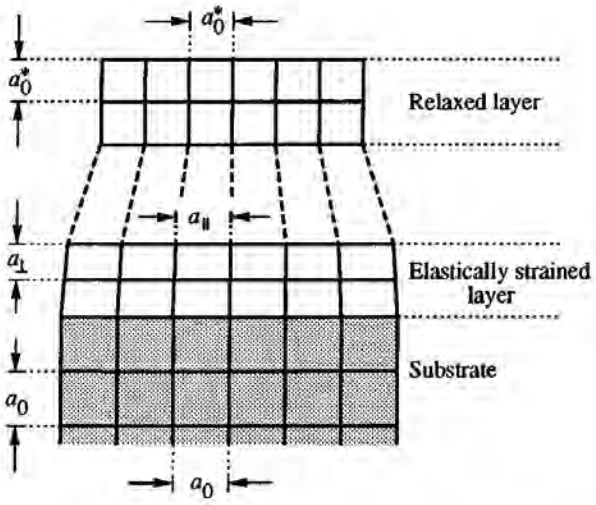


Fig. 12.24. Schematic illustration of a cubic lattice (substrate) with lattice constant a_0, a tetragonally distorted, elastically strained layer with lattice parameters $a_\parallel$ and $a_\perp$, and a relaxed layer with equilibrium lattice constant a_0^*.

Note that the above considerations apply only to elastically strained epitaxial layers. Epitaxial layers exceeding a certain thickness relax and assume an equilibrium lattice constant a_0^* as schematically shown in Fig. 12.24. The transition from a strained layer to a relaxed layer occurs if the elastic strain energy stored in the epitaxial layer exceeds the energy required to create misfit dislocations. Since the elastic strain energy is proportional to the thickness of the epitaxial layer, the two energies coincide at a certain thickness which is called the ***critical thickness***.

Lattice contraction was found in highly C-doped GaAs (Akatsuka et al. 1990, 1991; de Lyon et al., 1990; George et al., 1991; Hoke et al., 1991) and to a smaller extent in Be-doped GaAs (Hoke et al., 1991). The splitting of the x-ray diffraction peaks originating from the GaAs substrate with lattice constant a_0 and the tetragonally distorted GaAs film with the perpendicular lattice constant $a_\perp$ is give by

$$\frac{a_\perp - a_0}{a_0} = -\Delta\theta \cot\theta \tag{12.91}$$

where θ is the diffraction angle (33.024°) for the (004) substrate reflection (Hoke et al., 1991). The lattice constant of GaAs:C can be calculated from the covalent tetrahedral radii of the constituents. The lattice constant, a_0, and the covalent

https://doi.org/10.1017/CBO9780511599828.015 Published online by Cambridge University Press

tetrahedral radius, r, of a compound are related by

$$a_0 = \frac{8}{\sqrt{3}} r . \tag{12.92}$$

Assuming that interstitial C does not perturb the lattice constant, the expected lattice contraction for *relaxed* C-doped GaAs can be calculated

$$a_0^* - a_0 = \frac{4}{\sqrt{3}\ (4/a_0^{*3})} [N_{C_{Ga}}\ (r_C - r_{Ga}) + N_{C_{As}} (r_C - r_{As})] \tag{12.93a}$$

where a_0^* is the relaxed lattice constant of GaAs:C and $(4/a_0^{*3})$ is the concentration of Ga or As sites of the GaAs lattice. For C concentrations $N_C << 10^{22}$ one can approximate $4/a_0^{*3} \equiv 4/a_0^3 \equiv 2.21 \times 10^{22}\ \text{cm}^{-3}$ which yields (de Lyon et al., 1990)

$$a_0^* - a_0 = \frac{4}{\sqrt{3}\ (2.21 \times 10^{22}\ \text{cm}^{-3})} [N_{C_{Ga}} (r_C - r_{Ga}) + N_{C_{As}}\ (r_C - r_{As})] \tag{12.93b}$$

where $N_{C_{Ga}}$ and $N_{C_{As}}$ are the concentrations of C atoms on Ga and As sites, respectively, and r_C, r_{Ga}, and r_{As} are the respective covalent tetrahedral radii. The covalent radii of Ga, As, C and Be are $r_{Ga} = 1.26$ Å, $r_{As} = 1.20$ Å, $r_C = 0.77$ Å, and $r_{Be} = 0.90$ Å, respectively. Due to $r_C < r_{Be}$, a larger lattice contraction is expected for C-doped GaAs as compared to Be-doped GaAs. While de Lyon et al. (1990) used the radii listed above, Hoke et al. (1991) used $r_{Ga} = r_{As} = r_{GaAs} = 1.225$ Å. The quantitative difference between the two approaches is very small. The lattice constant of *elastically strained*, tetragonally distorted C-doped GaAs is given by (de Lyon et al., 1990)

$$(a_\perp - a_0) = \frac{(1 + \nu)}{(1 - \nu)} (a_0^* - a_0) = 1.90\ (a_0^* - a_0) \tag{12.94}$$

where a value of $\nu = 0.31$ has been assumed as the Poisson ratio of the GaAs epilayer. Note that $a_0^* = a_\perp^{\text{relaxed}} = a_\parallel^{\text{relaxed}}$ for the relaxed layer. Comparison of the lattice constant of highly C-doped GaAs measured by x-ray diffraction with the calculated lattice constants (Eqs. (12.93) and (12.94)) yielded agreement between experiment and theory. Quantitatively, the lattice mismatch between highly C-doped GaAs and the substrate can be quite significant. At a C-doping concentration of $10^{21}\ \text{cm}^{-3}$, a lattice mismatch of $0.5 - 0.8\%$ was determined (George et al., 1991). For sufficiently thick films, misfit dislocations are created which deteriorate the minority carrier properties of the material. For example, a decrease in photoluminescence efficiency is expected in films with dislocations.

https://doi.org/10.1017/CBO9780511599828.015 Published online by Cambridge University Press

For completeness, the relations between the substrate lattice constant a_0, the elastically strained constants $a_\perp$ and $a_\parallel$, and the relaxed constant a_0^* are summarized. The in-plane element of the strain tensor, ε, is defined as

$$\varepsilon_\parallel = \frac{a_\parallel - a_0^*}{a_0^*} . \tag{12.95a}$$

For elastically strained epilayers, the lattice constants are

$$a_\parallel = a_0 , \tag{12.95b}$$

$$a_\perp = \left(1 + \frac{2\nu}{1-\nu}\,\varepsilon_\parallel\right) a_0 \tag{12.95c}$$

where ν is again the Poisson number which is 0.31 for GaAs and $\nu \cong 0.3$ for most semiconductors. Thus the knowledge of a_0 and a_0^* allows one to calculate $a_\perp$.

The change in lattice constant predicted by Eqs. (12.93) and (12.94) are *linear* with the C concentration, if the compensation ratio $N_{C_{As}}/N_{C_{Ga}}$ does not depend on the C concentration. Such a linear dependence agrees with ***Vegard's law***. Vegard's law predicts that the lattice constant changes linearly with the composition of a multicomponent system. Consider, for example, a binary system AB consisting of the components A and B. Assuming that A and B have the same crystal structure and that the solid solution A_xB_{1-x} is miscible over the entire composition range, the lattice constant of the binary compound is given by (Vegard's law)

$$\boxed{a_{AB} = a_A x + a_B (1-x)} \tag{12.96}$$

where a_A and a_B are the lattice constants of the material A and B, respectively. Vegard's law in the form of Eq. 12.96 can be applied to compounds such as $Al_xGa_{1-x}As$ (A = AlAs, B = GaAs, $A_xB_{1-x} = Al_xGa_{1-x}As$). However, Eq. 12.96 cannot be applied to systems such as GaAs:C, since a component 'GaC' does not exist.

Note that deviations from Vegards law may occur at very high doping concentrations. Equation (12.93) predicts a *linear* dependence of the lattice constant on the C concentration as long as the C compensation ratio remains constant. However, if the ratio $N_{C_{Ga}}/N_{C_{As}}$ changes at high C doping concentrations, Eq. (12.93) predicts a *non-linear* dependence between the lattice constant and the C concentration. Furthermore, the concentration of interstitial C is expected to increase at high doping concentrations. Such interstitials will

https://doi.org/10.1017/CBO9780511599828.015 Published online by Cambridge University Press

perturb the lattice in a different way than substitutional C atoms, which is also expected to result in a deviation from Vegard's law. To date, however, deviations from Vegard's law in highly C-doped GaAs have not been reported.

https://doi.org/10.1017/CBO9780511599828.015 Published online by Cambridge University Press

Appendix A: Properties of III–V semiconductors

Table A.1 *Characteristics of GaAs, InP, and InAs*

Quantity	Unit	GaAs value	InP value	InAs value
Crystal structure	—	zincblende	zincblende	zincblende
Lattice constant	Å	5.6533	5.8690	6.0583
Band structure	—	direct	direct	direct
Bandgap energy				
(300 K)	eV	1.424	1.350	0.354
(2 K)	eV	1.519	1.425	0.418
Absorption edge (300 K)	μm	0.870	0.918	3.50
Electron affinity	eV	4.07	4.5	4.9
Electron effective mass	m_0	0.067	0.077	0.022
Electron mobility (300 K)	$cm^2/V\ s$	8500	5000	33 000
Heavy hole effective mass	m_0	0.45	0.60	0.40
Light hole effective mass	m_0	0.082	0.12	0.026
Hole mobility (300 K)	$cm^2/V\ s$	400	150	450
Dielectric constant				
ε_r	—	13.1	12.6	15.1
ε_∞	—	10.9	9.61	12.3
Refractive index				
$\lambda = 1.24$ μm	—	3.45	3.22	3.5
Optical phonon energy				
LO	meV	36	43	30
TO	meV	33	37	27
Thermal conductivity (300 K)	W/K cm	0.46	0.68	0.30
Thermal expansion	$10^6\ K^{-1}$	6.4	4.56	4.52
Density	g/cm^3	5.32	4.79	5.67
Melting point	°C	1238	1335	942

(sources are listed in references)

https://doi.org/10.1017/CBO9780511599828.016 Published online by Cambridge University Press

Table A.2 *Characteristics of $Al_xGa_{1-x}As$*

Quantity	Unit	$Al_xGa_{1-x}As$ value
Crystal structure	—	zincblende
Lattice constant	Å	$5.6533+0.0072x$
Band structure	—	$x < 0.45$: direct $x > 0.45$: indirect
Bandgap energy		
(300 K)	eV	$x < 0.45$: $1.424+1.247x$ $x > 0.45$: $1.424+1.247x+1.147(x-0.45)^2$
Electron affinity	eV	$x < 0.45$: $4.07-1.1x$ $x > 0.45$: $3.64-0.14x$
Electron effective mass		
Density of states:		
m^*_Γ	m_0	$0.067+0.083x$
m^*_L	m_0	$0.55+0.12x$
m^*_X	m_0	$0.85-0.07x$
Conductivity:		
m^*_Γ	m_0	$0.067+0.83x$
m^*_L	m_0	$0.11+0.03x$
m^*_X	m_0	$0.32-0.06x$
Electron mobility (300 K)	$cm^2/V\ s$	$x < 0.45$: $8000-22000x+10000x^2$ $x > 0.45$: $255+1160x-720x^2$
Heavy hole effective mass	m_0	$0.45+0.30x$
Light hole effective mass	m_0	$0.08+0.057x$
Hole mobility (300 K)	$cm^2/V\ s$	$370-970x+740x^2$
Dielectric constant		
ε_r	—	$13.1-3.0x$
ε_∞	—	$10.9-2.7x$
Refractive index		
$\lambda=1.239\ \mu m$	—	$3.45-0.54x$
Optical phonon energy		
LO (GaAs like; $x < 1$)	meV	$36.2-6.5x+1.8x^2$
LO (AlAs like; $x > 0$)	meV	$44.6+8.8x-3.3x^2$
TO (GaAs like; $x < 1$)	meV	$33.3-0.6x-1.2x^2$
TO (AlAs like; $x > 0$)	meV	$44.6+0.5x-0.3x^2$
Thermal resistivity (300 K)	K cm/W	$2.27+28.83x-30x^2$
Thermal expansion	$10^6\ K^{-1}$	$6.4-1.2x$
Density	g/cm^3	$5.36-1.6x$
Melting point	°C	$1238-58x+560x^2$

https://doi.org/10.1017/CBO9780511599828.016 Published online by Cambridge University Press

Table A.3 *Characteristics of $Ga_{0.47}In_{0.53}As$ and $Al_{0.48}In_{0.52}As$*

Quantity	Unit	$Ga_{0.47}In_{0.53}As$ value	$Al_{0.48}In_{0.52}As$ value
Crystal structure	—	zincblende	zincblende
Lattice constant	Å	5.8690	5.8690
Band structure	—	direct	direct
Bandgap energy			
(300 K)	eV	0.75	1.450
(2 K)	eV	0.812	1.508
Absorption edge (300 K)	μm	1.65	0.855
Electron effective mass	m_0	0.041	0.083
Electron mobility (300 K)	$cm^2/V\ s$	13 800	4600
Heavy hole effective mass	m_0	0.5	—
Light hole effective mass	m_0	0.051	—
Hole mobility (300 K)	$cm^2/V\ s$	350	—
Dielectric constant			
ε_r	—	14.1	—
ε_∞	—	11.6	—
Refractive index			
$\lambda = 1.65$ μm	—	3.56	—
$\lambda = 1.24$ μm	—	—	3.2
Optical phonon energy			
LO	meV	33	—
TO	meV	28	—
Thermal conductivity (300 K)	W/K cm	0.063	—
Thermal expansion	$10^{-6}K^{-1}$	5.55	—
Density	g/cm^3	5.54	4.85

https://doi.org/10.1017/CBO9780511599828.016 Published online by Cambridge University Press

Table A.4 *Characteristics of GaInPAs (λ = 1.3 and 1.55 μm) lattice matched to InP*

Quantity	Unit	$Ga_{.27}In_{.73}P_{.40}As_{.60}$ value	$Ga_{.40}In_{.60}P_{.15}As_{.85}$ value
Crystal structure	—	zincblende	zincblende
Lattice constant	Å	5.8690	5.8690
Band structure	—	direct	direct
Bandgap energy			
(300 K)	eV	0.953	0.800
(2 K)	eV	1.018	0.881
Absorption edge (300 K)	μm	1.3	1.55
Electron effective mass	m_0	0.053	0.045
Electron mobility			
(300 K, $N_D = 1\times10^{16}$)	$cm^2/V\ s$	6300	7700
Heavy hole effective mass	m_0	0.69	0.64
Light hole effective mass	m_0	0.072	0.062
Hole mobility			
(300 K, $N_A = 1\times10^{17}$)	$cm^2/V\ s$	80	150
Dielectric constant			
ε_r	—	13.3	13.7
ε_∞	—	10.9	11.4
Refractive index			
$\lambda = 1.30$ μm	—	3.52	—
$\lambda = 1.55$ μm	—	3.40	3.55
$\lambda = 1.65$ μm	—	3.38	3.49
Optical phonon energy			
LO_1	meV	41	—
LO_2	meV	32	33
TO_1	meV	40	—
TO_2	meV	28	28
Thermal conductivity (300 K)	W/K cm	0.044	0.043
Thermal expansion	$10^{-6}K^{-1}$	5.32	5.65
Density	g/cm^3	5.26	5.42

https://doi.org/10.1017/CBO9780511599828.016 Published online by Cambridge University Press

Appendix B: Constants and Conversions

Table B.1 *Constants*

α	7.2974×10^{-3}	Sommerfeld's fine structure constant
a_B	0.52918 Å	Bohr radius
ε_0	8.8542×10^{-12} A s/V m	dielectric permittivity in vacuum
e	1.6022×10^{-19} C	elementary charge
c	2.9979×10^{8} m/s	velocity of light in vacuum
E_{Ryd}	13.606 eV	Rydberg energy
h	6.6261×10^{-34} J s	Planck's constant
$\hbar$	1.0546×10^{-34} J s	Planck's constant divided by 2π
k	1.3807×10^{-23} J/K	Boltzmann's constant
μ_0	1.2566×10^{-6} V s/A m	magnetic permeability in vacuum
m_e	9.1094×10^{-31} kg	free electron mass
N_{Avo}	6.0221×10^{23} mol^{-1}	Avogadro's number
R	8.3145 J K^{-1} mol^{-1}	ideal gas constant

Table B.2 *Useful conversions*

1 eV	=	1.6022×10^{-19} J
kT	=	25.86 meV (at 300 K)
E	=	1239.8 / λ (E: photon energy in eV; λ: wavelength in nm)
E	=	$(1/8065.5) \times \lambda^{-1}$ (E: photon energy in eV; λ^{-1}: inverse wavelength in cm^{-1})

https://doi.org/10.1017/CBO9780511599828.017 Published online by Cambridge University Press

References

Preface

Seidman, A. H. and Marshall S. L. (1963) *Semiconductor Fundamentals* **VI** (Wiley, New York) p. 86.

Shockley, W. (1950) *Electrons and Holes in Semiconductors* (Van Nostrand, New York) p. 12.

Wilson, A. H. (1931) *Proc. Roy. Soc. A.* **134**, 279.

Chapter 1

Abarenkov, I. V. and Heine, V. (1965) *Phil. Mag.* **12**, 529.

Abram, R. A., Rees, G. J., and Wilson, B. L. H. (1978) *Adv. Phys.* **27**, 799.

Adler, D. (1982) in *Handbook on Semiconductors* **1**, eds. Moss, T. S. and Paul, W. (North-Holland, Amsterdam).

Adler, P. N. (1969) *J. Appl. Phys.* **40**, 3554.

Altarelli, M. and Bassani, F. (1982) in *Handbook on Semiconductors* **1**, eds. Moss, T. S. and Paul W. (North Holland, Amsterdam).

Ando, T., Fowler, A. B., and Stern, F. (1982) *Rev. Mod. Phys.* **54**, 437.

Austin, I. G. and Mott, N. F. (1969) *Adv. Phys.* **18**, 41.

Baldareschi, A. and Lipari, N. O. (1973) *Phys. Rev. B***8**, 2697.

https://doi.org/10.1017/CBO9780511599828.018 Published online by Cambridge University Press

Baldareschi, A. and Lipari, N. O. (1974) *Phys. Rev. B***9**, 1525.

Bassani, F., Iadonisi, G., and Preziosi, B. (1969) *Phys. Rev.* **186**, 735.

Bennet, H. S. and Lowney, J. R. (1987) *J. Appl. Phys.* **62**, 521.

Bethe, H. (1942) unpublished.

Böer, K. (1990) *Survey of Semiconductor Physics* (van Nostrand Reinhold, New York).

Bohm, D. (1951) *Quantum Theory* (Prentice-Hall, Englewood Cliffs).

Borowitz, S. (1967) *Fundamentals of Quantum Mechanics* (Benjamin, New York).

Brinkman, W. F. and Rice, T. M. (1973) *Phys. Rev. B***7**, 1508.

Burstein, E. (1954) *Phys. Rev.* **93**, 632.

Casey, H. C., Jr., Sell, D. D., and Wecht, K. W. (1975) *J. Appl. Phys.* **46**, 250.

Casey, H. C., Jr and Stern, F. (1976) *J. Appl. Phys.* **47**, 631.

Chelikowsky, J. R. and Cohen, M. L. (1976) *Phys. Rev. B***14**, 556.

Dapkus, P. D., Holonyak, N. Jr., Rossi, J. A., Williams, L. V., and High, D. A. (1969) *J. Appl. Phys.* **40**, 3300.

Davydov, A. S. (1965) *Quantum Mechanics* (Pergamon, Oxford).

Debye, O. P. and Hückel, E. (1923) *Zeit Phys.* **24**, 185, 305.

Debye, P. and Conwell, E. M. (1954) *Phys. Rev.* **93**, 693.

Deppe, D. G., Gerrard, N. D., Pinzone, C. J., Dupuis, R. D., and Schubert, E. F. (1990) *Appl. Phys. Lett.* **56**, 315.

Efros, A. L. and Shklovskii, B. I. (1975) *J. Phys. C***8**, L49.

Finkelnburg, W. (1958) *Introduction to Atomic Physics* (in German) (Springer, Berlin) p. 97.

Flügge, S. (1971) *Practical Quantum Mechanics* **1** (Springer, Berlin).

Halperin, B. I. and Lax, M. (1966) *Phys. Rev.* **148**, 722.

Halperin, B. I. and Lax, M. (1967) *Phys. Rev.* **153**, 802.

Haug, H. and Schmitt-Rink, S. (1984) *Prog. Quantum Electron.* **9**, 3.

https://doi.org/10.1017/CBO9780511599828.018 Published online by Cambridge University Press

Haug, H. and Schmitt-Rink, S. (1985) *J. Opt. Soc. Am. B2*, 1135.

Hubbard, J. (1963) *Proc. Roy. Soc. (London) Ser. A276*, 238.

Jain, S. C., McGregor, J. M., and Roulston, D. J. (1990) *J. Appl. Phys.* **68**, 3747.

Kane, E. O. (1963) *Phys. Rev.* **131**, 79.

Kohn, W. (1957a) in *Solid State Physics* **5**, eds. Seitz, F. and Turnbull, D. (Academic, New York).

Kohn, W. (1957b) *Phys. Rev.* **105**, 509.

Landsberg, P. T., Neutroschel, A., Lindholm, F. A., and Sah, C. T. (1985) *Phys. Stat. Sol. B130*, 255.

Lax, M. and Halperin, B. I. (1966) *J. Phys. Soc. Japan* **21** (Supplement), 218.

Luttinger, J. M. (1956) *Phys. Rev.* **102**, 1030.

Madelung, O. (1978) *Introduction to Solid-State Theory* (Springer, Berlin).

Mahan, G. D. (1980) *J. Appl. Phys.* **51**, 2634.

Mahan, G. D. (1990) *Many-Particle Physics* (Plenum, New York).

Merzbacher, E. (1970) *Quantum Mechanics* (John Wiley, New York).

Morgan, T. N. (1965) *Phys. Rev.* **139**, A343.

Moss, T. S. (1961) *Optical Properties of Semiconductors* (Academic, New York).

Mott, N. F. (1987) *Conduction in Non-Crystalline Materials* (Clarendon, Oxford).

Mott, N. F. (1990) *Metal–Insulator Transitions* (Taylor & Francis, London).

Olego, D. and Cardona, M. (1980) *Phys. Rev. B22*, 886.

Onton, A., Yacoby, Y., Chicotka, R. J. (1972) *Phys. Rev. Lett.* **28**, 966.

Pantelides, S. T. (1975) in *Advances in Solid State Physics Vol. 15*, ed. Queisser, H. J. (Pergamon-Vieweg, Braunschweig) p. 149.

Pantelides, S. T. (1978) *Rev. Mod. Phys.* **50**, 797.

Pearsall, T. P. (ed.) (1982) *GaInAsP Alloy Semiconductors* (Wiley, New York).

Phillips, J. C. (1970a) *Phys. Rev. B1*, 1540.

https://doi.org/10.1017/CBO9780511599828.018 Published online by Cambridge University Press

Phillips, J. C. (1970b) *Phys. Rev.* **B1**, 1545.

Phillips, J. C. (1973) *Bonds and Bands in Semiconductors* (Academic, New York).

Pollak, M. and Knotek, M. L. (1974) *Phys. Rev.* **B9**, 644.

Saxon, D. S. (1968) *Elementary Quantum Mechanics* (Holden-Day, San Francisco,).

Semelius, B. E. (1986) *Phys. Rev.* **B33**, 8582.

Sherwin, C. W. (1959) *Introduction to Quantum Mechanics* (Henry Holt, New York).

Shklovskii, B. I. and Efros, A. L. (1984) *Electronic Properties of Doped Semiconductors* (Springer, Berlin).

Shockley, W. (1961) *Solid-State Electron.* **2**, 35.

Sommerfeld, A. (1920), see Finkelnburg (1958).

Stern, F. (1967) *Phys. Rev. Lett.* **18**, 546.

Stillman, G. E., Cook, L. W., Roth, T. J., Low, T. S., and Skromme, B. J. (1982) in *GaInAsP Alloy Semiconductors*, ed. Pearsall, T. P. (Wiley, New York).

Stoneham, A. M. (1975) *Theory of Defects in Solids* (Clarendon, Oxford).

Stoneham, A. M. (1986) in *Defects in Semiconductors*, ed. Bardeleben, H. J. (Trans. Tech., Switzerland).

Thomas, D. G. and Hopfield, J. J. (1966) *Phys. Rev.* **150**, 680.

Verie, C. (1967) *Proc. Int. Conf. on II–VI Compounds* (Benjamin, New York) p. 1124.

White, H. E. (1934) *Introduction to Atomic Spectra* (McGraw-Hill, New York).

Wolf, P. A. (1962) *Phys. Rev.* **126**, 405.

Yao, H. and Compaan, A. (1990) *Appl. Phys. Lett.* **57**, 147.

Chapter 2

Banks, P. W., Brand, S., and Jaros, M. (1980) *J. Phys. C.: Solid State Phys.* **13**, 6167.

Baraff, G. A. and Schlüter, M. (1985) *Phys. Rev. Lett.* **55**, 1327.

Bardeen, J. (1947) *Phys. Rev.* **71**, 717.

https://doi.org/10.1017/CBO9780511599828.018 Published online by Cambridge University Press

Bethe, H. A. and Salpeter, E. E. (1957) *Quantum Mechanics of One- and Two-Electron Atoms* (Academic, New York).

Bishop, S. G. (1986) in *Deep Centers in Semiconductors*, ed. Pantelides, S. T. (Gordon and Breach, New York).

Blakemore, J. S. (1967) *Phys. Rev.* **163**, 809.

Blakemore, J. S. (1987) *Semiconductor Statistics* (Dover, New York).

Bourgoin, J. and Lannoo, M. (1983) *Point Defects in Semiconductors II: Experimental Aspects* (Springer, Berlin).

Davydov, A. S. (1976) *Quantum Mechanics*, 2nd ed. (Pergamon, Oxford).

Finkelnburg, W. (1958) *Introduction to Atomic Physics* (in German) (Springer, Berlin).

Frenkel, J. (1938a) *Phys. Rev.* **54**, 647.

Frenkel, J. (1938b) *Tech. Phys. USSR* **5**, 685.

Hall, R. N. (1951) *Phys. Rev.* **83**, 228.

Hall, R. N. (1952) *Phys. Rev.* **87**, 387.

Hartke, J. L. (1968) *J. Appl. Phys.* **39**, 4871.

Henry, C. H. and Lang, D. V. (1977) *Phys. Rev. B***15**, 989.

Hjalmarson, H. P., Vogl, P., Wolford, D. J. and Dow, J. D. (1980) *Phys. Rev. Lett.* **44**, 810.

Huang, K. and Rhys, A. (1950) *Proc. Roy. Soc. (London) A***204**, 406.

Jaros, M. (1982) *Deep Levels in Semiconductors* (Adam Hilger, Bristol).

Jaros, M. and Band, S. (1976) *Phys. Rev. B***14**, 4494.

Korol, E. N. (1977) *Sov. Phys.-Solid State* **19**, 1327.

Kovarskii, V. A. (1962) *Sov. Phys.-Solid State* **4**, 1200.

Landsberg, P. T. (1970) *Phys. Stat. Solidi* **41**, 457.

Lang, D. V. (1974a) *J. Appl. Phys.* **45**, 3014.

Lang, D. V. (1974b) *J. Appl. Phys.* **45**, 3023.

https://doi.org/10.1017/CBO9780511599828.018 Published online by Cambridge University Press

Lang, D. V. and Logan, R. A. (1977) *Phys. Rev. Lett.* **39**, 635.

Lang, D. V., Logan, R. A. and Jaros, M. (1979) *Phys. Rev. B***19**, 1015.

Lannoo, M. and Bourgoin, J. (1981) *Point Defects in Semiconductors I: Theoretical Aspects* (Springer, Berlin).

Lax, M. (1959) *J. Phys. Chem. Sol.* **8**, 66.

Lax, M. (1960) *Phys. Rev.* **119**, 1502.

Lax, M. (1992) private communication.

Madelung, O. (1978) *Introduction to Solid State Theory* (Springer, Berlin).

Martin, G. M., Mitonneau, A., and Mircea, A. (1977) *Electron. Lett.* **13**, 191.

Milnes, A. G. (1973) *Deep Impurities in Semiconductors* (Wiley, New York).

Mitonneau, A., Martin, G. M., and Mircea, A. (1977) *Electron. Lett.* **13**, 666.

Nelson, R. J. (1977) *Appl. Phys. Lett.* **31**, 351.

Pantelides, S. T. (1986) *Deep Centers in Semiconductors: A State of the Art Approach* (Gordon and Breach, New York).

Pons, D. and Makram-Ebeid, S. (1979) *J. Physique* **40**, 1161.

Poole, H. H. (1914) Philos. Mag. **27**, 58.

Queisser, H. J. (1971) in *Advances in Solid State Physics Vol. 11*, (Vieweg, Braunschweig).

Riddoch, F. A. and Jaros, M. (1980) *J. Phys. C: Solid State Phys.* **13**, 6181.

Sah, C. T. (1967) *Proc. IEEE* **55**, 654.

Schubert, E. F. and Ploog, K. (1984) *Phys. Rev. B***29**, 4562.

Seeger, K. (1982) *Semiconductor Physics* (Springer, Berlin).

Sheinkman, M. K. (1965) *Sov. Physics-Solid State* **7**, 18.

Shockley, W. and Read, W. T. (1952) *Phys. Rev.* **87**, 835.

Solar, N. and Burstein, E. (1955) *Phys. Rev.* **98**, 1757.

van Roosbroeck, W. and Shockley, W. (1954) *Phys. Rev.* **94**, 1558.

https://doi.org/10.1017/CBO9780511599828.018 Published online by Cambridge University Press

Vincent, G., Chantre, A., and Bois, D. (1979) *J. Appl. Phys.* **50**, 5484.

Vogl, P. (1981) in *Advances in Solid State Physics* **21** (Vieweg, Braunschweig).

Vogl, P. (1985) in *Advances in Solid State Physics* **25** (Vieweg, Braunschweig).

Zunger, A. (1986) in *Solid State Physics* **39**, eds. Ehrenreich, H. and Turnbull, D. (Academic, New York).

Chapter 3

Blakemore, J. S. (1982) *Sol. State Electron.* **25**, 1067.

Chang, T. Y. and Izabelle, A. (1989) *J. Appl. Phys.* **65**, 2162.

de Boer, J. H. and van Geel, W. C. (1935) *Phys.* **2**, 186.

Ehrenberg, W. (1950) *Proc. Phys. Soc. London.* **A63**, 75.

Frank (1931) Rev. Mod. Phys. **3**, 1.

Joyce, W. B. (1978) *Appl. Phys. Lett.* **32**, 680.

Joyce, W. B. and Dixon, R. W. (1977) *Appl. Phys. Lett.* **31**, 354.

Kittel, C. and Kroemer, H. (1980) *Thermal Physics*, 2nd ed. (Freeman, San Francisco).

Lang, D. V., Grimmeiss, H. G., Meijer, E., and Jaros. M. (1980) *Phys. Rev.* **B22**, 3917.

Laufer, P. M., Pollak, F. H., Nahory, R. E., and Pollak, M. A. (1980) *Solid State Commun.* **36**, 978.

Madelung, O. (1970) *Fundamentals of Semiconductor Physics*, (in German) (Springer, Berlin).

Morin, F. F. (1959) in *Semiconductors*, ed. Hannay, N. B. (Reinhold, New York) p. 31.

Mott, N. F. and Gurney, R. W. (1940) *Electronic Processes in Ionic Crystals* (Oxford University Press, Oxford) p. 156.

Nilsson, N. G. (1973) *Phys. Stat. Sol.* **A19**, K75.

Reif, F. (1965) *Fundamental of Statistical and Thermal Physics* (McGraw-Hill, New York).

https://doi.org/10.1017/CBO9780511599828.018 Published online by Cambridge University Press

Schubert, E. F. and Ploog, K. (1984) *Phys. Rev.* **B30**, 7021.

Smith, R. A. (1986) *Semiconductors* (Cambridge University Press, Cambridge).

Sommerfeld, A. (1928) *Zeitschrift Physik* **47**, 1; see also A. Sommerfeld and N. H. Frank (1931) *Rev. Mod. Phys.* **3**, 1.

Thurmond, C. D. (1975) *J. Electrochem. Soc.* **112**, 1133.

Van Vechten, J. A. and Thurmond, C. D. (1976a) *Phys. Rev.* **B14**, 3539.

Van Vechten, J. A. and Thurmond, C. D. (1976b) *Phys. Rev.* **B14**, 3551.

Chapter 4

Arthur, J. R., Jr. (1968) *Proc. Conf. Struct. Chem. Solid Surfaces*, ed. G. A. Somorjai (Wiley, New York), p. 46–1.

Arthur, J. R., Jr. (1968) *J. Appl. Phys.* **39**, 4032.

Calawa, A. R. (1981) *Appl. Phys. Lett.* **38**, 701.

Chiu, T. H. (1991) et al., unpublished.

Chiu, T. H., Tsang, W. T., Schubert, E. F., and Agyekum, E. (1987) *Appl. Phys. Lett.* **51**, 1109.

Cho, A. Y. (1985) in *The Technology and Physics of Molecular Beam Epitaxy*, ed. Parker E.H.C. (Plenum, New York).

Cho, A. Y. (1971) *J. Vac. Sci. Technol.* **8**, S31.

Cho, A. Y. (1977) *Jpn. J. Appl. Phys.* **16**, Suppl. 16-1, 435.

Cho, A. Y. and Arthur, J. R. (1975) *Prog. Solid-State Chem.* **10**, 157.

Cho, A. Y. and Casey, H. C. (1974) *Jr. Appl. Phys. Lett.* **35**, 288.

Chow, R. and Chai, Y. G. (1983) *Appl. Phys. Lett.* **42**, 383.

Davey, J. E. and Pankey, T. (1968) *J. Appl. Phys.* **39**, 1941.

Dupuis, R. D. and Dapkus, P. D. (1978) *Appl. Phys. Lett.* **32**, 406.

Foxon, C. T. and Joyce, B. A. (1975) *Surf. Sci.* **50**, 434.

https://doi.org/10.1017/CBO9780511599828.018 Published online by Cambridge University Press

Foxon, C. T. and Joyce, B. A. (1977) *Surf. Sci.* **64**, 293.

Foxon, C. T., Boudry, M. R., and Joyce, B. A. (1974) *Surf. Sci.* **44**, 69.

Günther, K. G. (1958) *Zeit. Naturforsch.* **13a**, 1081.

Hellman E. S. and Harris, J. S., Jr. (1987) *J of Cryst. Growth* **81**, 38.

Horiguchi, S., Kimura, K., Kamon, K., Mashita, M., Shimatzu, M., Mihara, M., and Ishii, M. (1986) *Jpn. J. Appl. Phys.* **25**, L979.

Johnston, W. D., Jr., DiGuiseppe, M. A., and Wilt, D. P. (1989) *AT&T Technical Journal* **68**, 53.

Knudsen, M. (1909) *Ann. Phys. (Leipzig)* **4**, 999.

Ludowise, M. I. (1985) *J. Appl. Phys.* **58**, R31.

Manasevit, H. M. (1968) *Appl. Phys. Lett.* **12**, 156.

Manasevit, H. M. and Simpson, W. I. (1969) *J. Electrochem. Soc.* **116**, 1725.

Panish, M. B. (1980) *J. Electrochem. Soc.* **127**, 2729.

Panish, M. B. (1987) *J. Cryst. Growth* **81**, 249.

Panish, M. B. and Temkin, H. (1989) *Annu. Rev. Mater. Sci.*, **19**, 209.

Panish, M. B., Temkin, H., and Sumski, S. (1985) *J. Vac. Sci. Technol. B***3**, 657.

Pütz, N., Heinecke, H., Heyen, M., Balk, P., Weyers, M., and Lüth, H. (1986) *J. Cryst. Growth* **74**, 292.

Razeghi, M., (1989) *The MOCVD Challenge* (Adam Hilger, Bristol).

Schubert, E. F., Cunningham, J. E., Tsang, W. T., and Timp, G. L. (1987) *Appl. Phys. Lett.* **51**, 1170.

Schubert, E. F., Tsang, W. T., Feuer, M. D., and Mankiewich, P. M. (1988) *IEEE Electron Device Letters* **9**, 145.

Stringfellow, G. B. (1989) *Organometallic Vapor-Phase Epitaxy: Theory and Practice* (Academic, Boston).

Swaminathan, V. and Macrander, A. T. (1991) *Materials Aspects of GaAs and InP Based Structures* (Prentice Hall, Englewood Cliffs).

https://doi.org/10.1017/CBO9780511599828.018 Published online by Cambridge University Press

337-TA-1366 RX-0255

Tanaka, H., Itoh, H., O'Hori, T., Takikawa, M., Kasai, K., Takechi, M., Suzuki, M., and Komeno., J. (1987) *Jpn. J. Appl. Phys.* **26**, L1456.

Tietjen, J. J. and Amick, J. A. (1966) *J. Electrochem. Soc.* **113**, 724.

Tsang, W. T. (1985a) *Appl. Phys. Lett.* **45**, 1234.

Tsang, W. T. (1985b) in *Molecular Beam Epitaxy and Heterostructures*, eds. Chang, L. L. and Ploog, K. (Martinus Nijhoff, Dordrecht).

Tsang, W. T. (1989) in *VLSI Electronics: Microstructure Science*, **21**, ed. Einspruch, N. G. (Academic, New York) p. 255.

Tsang, W. T. (1990) private communication.

Tsang, W. T. and Schubert, E. F. (1986) *Appl. Phys. Lett.* **49**, 220.

Tsang, W. T., Dayem, A. H., Chiu, T. H., Cunningham, J. E., Schubert, E. F., Ditzenberger, J. A., Shah, J., Zyskind, J. L., and Tabatabaie, N. (1986) *Appl. Phys. Lett.* **49**, 170.

Tsang, W. T., Levi, A. F. J., and Burkhardt, E. G. (1988) *Appl. Phys. Lett.* **53**, 983.

Tsang, W. T., Schubert, E. F., Chiu, T. H., Cunningham, J. E., Burkhardt, E. G., Ditzenberger, J. A., and Agyekum, E. (1987) *Appl. Phys. Lett.* **51**, 761.

Veuhoff, E., Pletschen, W., Balk, P., and Lüth, H. (1981) *J. Cryst. Growth* **55**, 30.

Chapter 5

Ambridge, T. and Faktor, M. M. (1975a) *J. Appl. Electrochem.* **5**, 319.

Ambridge, T. and Faktor, M. M. (1975b) *Gallium Arsenide and Related Compounds* ed. Bok, J., *Inst. Phys. Conf. Ser.* **24**, 320.

Arthur, J. R. (1973) *Surface Science* **38**, 394.

Ashen, D. J., Dean, P. J., Hurle, D. T. J., Mullin, J. B., White, A. M., and Greene, P. D. (1975) *J. Phys. Chem. Sol.* **36**, 1041.

Beall, R. B., Clegg, J. B., and Harris, J. J. (1988) *Semicond. Sci. Technol.* **3**, 612.

Blakemore, J. (1982) *J. Appl. Phys.* **53**, R123.

https://doi.org/10.1017/CBO9780511599828.018 Published online by Cambridge University Press

Blood, P. (1986) *Semicond. Sci. Technol.* **1**, 7.

Braslau, N. (1981) *J. Vac. Sci. Technol.* **19**, 803.

Calderon, L., Lu, Y., Shen, H., Pamulapati, J., Dutta, M., Chang, W. H., Yang, L. W., and Wright, P. D. (1992) *Appl. Phys. Lett.* **60**, 1597.

Chai, Y. G., Chow, R., and Wood, C. E. C. (1981) *Appl. Phys. Lett.* **39**, 800.

Chang, C. A., Ludeke, R., Chang, L. L., and Esaki, L. (1977) *Appl. Phys. Lett.* **31**, 759.

Chiu, T. H., Ditzenberger, J. A., Luftman, H. S., Tsang, W. T., and Ha, N. T. (1990) *Appl. Phys. Lett.* **56**, 1688.

Cho, A. Y. (1975) *J. Appl. Phys.* **46**, 1733.

Cho, A. Y. and Hayashi, I. (1971) *J. Appl. Phys.* **42**, 4422.

Cho, A. Y. and Panish, M. B. (1972) *J. Appl. Phys.* **43**, 5118.

Collins, D. M., Miller, J. N., Chai, Y. G., and Chow, R. (1982) *J. Appl. Phys.* **53**, 3010.

Davies, G. J., Andrews, D. A., and Heckingbottom, R. (1981) *J. Appl. Phys.* **52**, 7214.

Duhamel, N., Henoc, P., Alexandre, F., and Rao, E. V. K. (1981) *Appl. Phys. Lett.* **39**, 49.

Enquist, P., Hutchby, J. A., and de Lyon, T. J. (1988) *J. Appl. Phys.* **63**, 4485.

Greiner, M. E. and Gibbons, J. F. (1984) *Appl. Phys. Lett.* **44**, 750.

Hamm, R. A., Panish, M. B., Nottenburg, R. N., Chen, Y. K., and Humphrey, D. A. (1989) *Appl. Phys. Lett.* **54**, 2586.

Harris, J. J., Ashenford, D. E., Foxon, C. T., Dobson, P. J. and Joyce, B. A. (1984) *Appl. Phys.* **A33**, 87.

Hartley, F. and Patai, S. (1982) *The Chemistry of the Metal-Carbon Bond* (Wiley, New York) p. 53-71.

Heckingbottom, R. (1985) in *Molecular Beam Epitaxy and Heterostructures* ed. Chang, L. L. and Ploog, K. (Martinus Nijhoff, Dordrecht).

Heiblum, M., Wang, W. I., Osterling, L. E., and Deline V. (1983) *Appl. Phys. Lett.* **54**, 6751.

Hess, K., Stath, N., and Benz, K. W. (1974) *J. Electrochem Soc.: Solid State Sci. Technol.* **121**, 1208.

https://doi.org/10.1017/CBO9780511599828.018 Published online by Cambridge University Press

337-TA-1366 RX-0255

Hirama, V. (1964) *J. Chem. Eng. Data* **9**, 65.

Hobson, W. S., Pearton, S. J., Schubert, E. F., and Cabaniss, G. (1989) *Appl. Phys. Lett.* **55**, 1546.

Hoke, W. E., Lemonias, P. J., Weir, D. G., Hendricks, H. T., and Jackson, G. S. (1991a) *J. Appl. Phys.* **69**, 511.

Hoke, W. E., Lemonias, P. J., Lyman, P. S., Hendricks, H. T., Weir, D. G., and Colombo, P. (1991b) *J. Cryst. Growth* **111**, 269.

Ilegems, M. (1977) *J. Appl. Phys.* **48**, 1278.

Ilegems, M. and O'Mara, W. C. (1972) *J. Appl. Phys.* **43**, 1190.

Ito, H. and Ishibashi, T. (1991) *Jpn. J. Appl. Phys.* **30**, L944.

Joyce, B. A. and Foxon (1977) *Jpn. J. Appl. Phys.* **16**, Suppl. 16-1, 17.

Kadhim, M. A. and Tuck, B. (1972) *J. Mater. Sci.* **7**, 68.

Kirchner, P. D., Woodall, J. M., Freeouf, J. L., Wolford, D. J., Pettit, G. D. (1981) *J. Vac. Sci. Technol.* **19**, 604.

Kittel, C. and Kroemer, H. (1980) *Thermal Physics* 2nd ed. (Freeman, New York) p. 393.

Knudsen, M. (1909) *Ann. Phys. (Leipzig)* **4**, 999.

Kobayashi, N., Makimoto, T., and Horikoshi, Y. (1987) *Appl. Phys. Lett.* **50**, 1435.

Kopf, R. F. and Schubert, E. F. (1990) unpublished.

Künzel, H., Knecht, J., Jung, H., Wünstel, K., and Ploog, K. (1982) *Appl. Phys. A***28**, 167.

Lanzillotto, A. M., Santos, M., and Shayegan, M. (1989) *Appl. Phys. Lett.* **55**, 1445.

Maguire, J., Murray, R., Newman, R. C., Beall, R. B., and Harris, J. J. (1987) *Appl. Phys. Lett.* **50**, 516.

Malik, R. J., Nottenburg, R. N., Schubert, E. F., Walker, J. F., and Ryan, R. W. (1988) *Appl. Phys. Lett.* **53**, 2661.

Malik, R. J., Nagle, J., Micovic, M., Harris, T. D., Ryan, R. W., and Hopkins, L. C. (1992) *J. Vac. Sci. Technol. B***10**, 850.

Marton, L. and Marton C. (1979) (ed.), *Methods of Experimental Physics and Technology* **14**, (Academic, New York) p. 350.

https://doi.org/10.1017/CBO9780511599828.018 Published online by Cambridge University Press

RX-0255.580

McLevige, W. V., Vaidyanathan, K. V., Streetman, B. G., Ilegems, M., Comas, J., and Plew, L. (1978) *Appl. Phys. Lett.* **33**, 127.

Nagle, J., Malik, R. J., Gershoni, D. (1991) *J. Cryst. Growth* **111**, 264.

Ogawa, M. and Baba, T. (1985) *Jpn. J. Appl. Phys.* **24**, L572.

Pfeiffer, L. N. and West, K. W. (1987) unpublished.

Ploog, K. and Fischer, A. (1978) *J. Vac. Sci. Technol.* **15**, 255.

Poole, I., Lee, M. E., Singer, K. E., Frost, J. E. F., Kerr, T. M., Wood, C. E. C., Andrews, D. A., Rothwell, W. J. M., and Davies, G. J. (1988) *J. Appl. Phys.* **63**, 395.

Putley, E. H. (1960) *The Hall-Effect and Related Phenomena* (Butterworths, London).

Reynolds, W. N. (1968) *Physical Properties of Graphite* (Elsevier, Amsterdam).

Rupprecht, H., Woodall, J. M., Konnerth, K. and Pettit, D. G. (1966) *Appl. Phys. Lett.* **9**, 221.

Schubert, E. F. (1990) *J. Vac. Sci. Technol.* **A8**, 2980.

Schubert, E. F. and Kopf, R. F. (1990) unpublished.

Schubert, E. F., Gilmer, G. H., Kopf, R. F., and Luftman, H. S. (1992) *Phys. Rev.* **B46**, 15 078.

Schubert, E. F., Kuo, J. M., Kopf, R. F., Luftman, H. S., Hopkins, L. C., and Sauer, N. J. (1990a) *J. Appl. Phy.* **67**, 1969.

Schubert, E. F., Kuo, J. M., Kopf, R. F., Jordan, A. S., Luftman, H. S., and Hopkins L. C. (1990b) *Phys. Rev.* **B42**, 1364.

Schubert, E. F., Stark, J. B., Chiu, T. H., and Tell, B. (1988) *Appl. Phys. Lett.* **53**, 293.

Schubert, E. F., Tu, C. W., Kopf, R. F., Kuo, J. M., Lunardi, L. M. (1989) *Appl. Phys. Lett.* **54**, 2592.

Skromme, B. J., Stillman, G. E., Obsevstan, J. D., and Chan, S. S. (1984) *J. Electron Mater.* **13**, 463.

Spitzer, W. G. and Panish, M. B. (1969) *J. Appl. Phys.* **40**, 4200.

Stillman, G. E., Cook, L. W., Roth, T. J., Low, T. S., and Skromme, B. J. (1982) in *GaInAsP Alloy Semiconductors*, ed. Pearsall, T. P. (Wiley, New York) p. 121.

https://doi.org/10.1017/CBO9780511599828.018 Published online by Cambridge University Press

337-TA-1366 RX-0255

Subbanna, S., Tuttle, G., and Kroemer, H. (1988) *J. Electron. Mater.* **17**, 297.

Theis, T. N., Mooney, P. M., and Wright, S. L. (1988) *Phys. Rev. Lett.* **60**, 361.

Tuck, B. (1988) *Atomic Diffusion in III–V Semiconductors* (Adam Hilger, Bristol).

Tuck, B. and Kadhim, M. A. (1972) *J. Mater. Sci.* **7**, 585.

Vescan, L., Selders, J., Maier, M., Kräutle, H., and Beneking., H. (1984) *J. Cryst. Growth* **67**, 353.

White, A. M., Dean, P. J., Joyce, B. D., Clarke, R. C., and Taylor, L. L. (1972) *Proc. Int. Conf. Phys. Semicond., Warsaw, 1972* (Polish Scientific Publishers, Warsaw) p. 190.

Williams, E. W., Elder, W., Astles, M. G., Webb, M., Mullin, J. B., Straughan, B., and Tufton, P. J. (1973) *J. Electrochem. Soc.: Solid State Sci. Technol.* **120**, 1741.

Wood, C. E. C. (1978) *Appl. Phys. Lett.* **33**, 770.

Wood, C. E. C. (1985a) in *The Physics and Technology of MBE* ed. Parker, E. H. C. (Plenum, New York) p. 61.

Wood, C. E. C. (1985b) in *Molecular Beam Epitaxy and Heterostructures*, ed. Chang, L. L. and Ploog, K. (Martinus Nijhoff, Dordrecht).

Wood, C. E. C. and Joyce, B. A. (1978) *J. Appl. Phys.* **49**, 4854.

Wood, C. E. C., Desimone, D., Singer, K., and Wicks, G. W. (1982) *J. Appl. Phys.* **53**, 4230.

Yano, M., Suzuki, Y., Ishii, T., Matsushima, Y. and Kimata, M. (1978) *Jpn. J. Appl. Phys.* **17**, 2091.

Chapter 6

Aebi, V., Cooper, C. B., Moon, R. L. and Saxena, R. R. (1981) *J. Crystal Growth* **55** 517.

André, J. P., Gallais, A. and Hallais, J. (1977) in: *Gallium Arsenide and Related Compounds 1976, Inst. Phys. Conf. Ser.* **33a** (Inst. Phys. London) p. 1.

Bass, S. J. (1979) *J. Crystal Growth* **47**, 613.

https://doi.org/10.1017/CBO9780511599828.018 Published online by Cambridge University Press

337-TA-1366 RX-0255

Bass, S. J. and Oliver, P. E. (1977) in *Gallium Arsenide and Related Compounds 1976, Inst. Phys. Conf. Ser.* **33b** (Inst. Phys., London) p. 1.

Blaauw, C., Emmerstosfer, B., and Springthrope, A. J. (1987) *J. Crystal Growth* **84**, 431.

Bottka, N., Sillmon, R. S., and Tseng, W. F. (1984) *J. Crystal Growth* **68**, 54.

Chang, C. Y., Lee, M. K., Su, Y. K., and Hsu, W. C. (1983) *J. Appl. Phys.* **54**, 5464.

Field, R. J. and Ghandhi, S. K. (1986a) *J. Crystal Growth* **74**, 543.

Field, R. J. and Ghandhi, S. K. (1986b) *J. Crystal Growth* **74**, 551.

Fraas, L. M., McLeod, P. S., Cape, J. A., and Partain, L. D. (1984) *J. Crystal Growth* **68**, 490.

Gersten, S. W., Vendura, G. J., and Yeh, Y. C. M. (1986) *J. Crystal Growth* **77**, 286.

Giling, L. J. and van de Ven, J. (1987) in *Advanced Crystal Growth*, ed. Dryburth, P. M., Cockayne, B., and Barraclough, K. G. (Prentice Hall, New York) p. 309.

Glade, M., Grünzmacher, D., Meyer. R., Woelk, E. G., and Balk, P. (1989) *Appl. Phys. Lett.* **54**, 2411.

Glew, R. W. (1982) in *Gallium Arsenide and Related Compounds*, ed. Sugano, T. (Inst. Phys., Bristol) p. 581.

Glew, R. W. (1984) *J. Crystal Growth* **68**, 44.

Hallais, J. P. (1978) *Acta Electron.* **21** 129.

Hayafuji, N., Mizuguchik, Ochi, S., and Murotani, T. (1986) *J. Crystal Growth* **77**, 281.

Heyen, M., Bruch, H., Bachen, K.-H., and Balk, P. (1977) *J. Crystal Growth* **42**, 127.

Houng, Y.-M. and Low, T. S. (1986) *J. Crystal Growth* **77**, 272.

Hsu, C. C., Yuan, J. S., Cohen, R. M., and Stringfellow, G. B. (1986) *J. Crystal Growth* **74**, 535.

Keil, G., Le Metayer, M., Cuquel, A. and LePollotec, D. (1982) *Rev. Phys. Appl.* **17** 405.

Konagai, M., Yamada, T., Akatsuka, T., Nozaki, S., Miyake, R., Saito, K., Fukamachi, T., Tokumitsu, E., and Takahashi, K. (1990) *J. Crystal Growth* **105** 359.

Konagai, M., Yamada, T., Akatsuka, T., Saito, K., Tokumitsu, E., and Takahashi, K. (1989) *J. Crystal Growth* **98**, 167.

https://doi.org/10.1017/CBO9780511599828.018 Published online by Cambridge University Press

RX-0255.583

Kozen, A., Najima, S., Tenmyo, J., and Asahi, H. (1986) *J. Appl. Phys.* **59**, 1156.

Kuech, T. F., Tischler, M. A., Wang, P.-J., Scilla, G., Polenski, R., and Cardone. F. (1988) *Appl. Phys. Lett.* **53**, 1317.

Kuech, T. F., Veuhoff E., and Meyerson, B. S. (1984) *J. Crystal Growth* **68**, 48.

Lewis, C. R., Dietze, W. T., and Ludowise, M. J. (1983) *J. Electron. Mater.* **12**, 507.

Lewis, C. R., Ludowise, M. J., and Dietze, W. T. (1984) *J. Electron. Mater.* **13**, 447.

Manasevit, H. M. and Thorsen, A. C. (1972) *J. Electrochem. Soc.* **119**, 99.

Matsumoto, K., Hidaka, J., and Uchida, K. (1989) *J. Appl. Phys.* **65**, 3849.

Matsumoto, K., Hidaka, J., and Uchida, K. (1990) *J. Crystal Growth* **99**, 329.

Nelson, A. W. and Westbrook, L. D. (1984) *J. Crystal Growth* **68**, 102.

Nishizawa, J. and Kurabayashi, T. (1983) *J. Electrochem Soc.* **130** 413.

Ohno, H., Ikeda, E., and Hasegawa, H. (1984) *J. Crystal Growth* **68**, 15.

Parsons, J. D. and Krajehbrink, F. G. (1983) *J. Electrochem. Soc.* **130**, 1782.

Parsons, J. D. and Krajenbrink, F. V. (1984) *J. Crystal Growth* **68**, 60.

Parsons, J. D., Lichtmann, L. S., Krajenbrink, F. G., and Brown, D. W. (1986) *J. Crystal Growth* **77**, 32.

Pütz, N., Heinecke, H., Heyen, M., Balk, P., Weyers, M., and Lüth, H. (1986) *J. Crystal Growth* **74**, 292.

Razeghi, M. (1989) *The MOCVD Challenge* (Adam Hilger, Bristol).

Roberts, J. S., Mason, N. J., and Robinson, M. (1984) *J. Crystal Growth* **68**, 422.

Roth, A. P., Yakimova, R., and Sundaram, V. S. (1984) *J. Crystal Growth* **68**, 65.

Seki, Y., Tanno, K., Iida, K., and Ichiki, E. (1975) *J. Electrochem. Soc.* **122**, 1108.

Shapira, Y. and Lichtman, D. (1979) in *Methods of Experimental Physics* **14**, eds. Marton, L. and Marton, C. (Academic, New York).

Skevington, P. J., Andrews, D. A., and Davies, G. J. (1990) *J. Cryst. Growth* **105**, 371.

Stringfellow, G. B. (1989) in *Organometallic Vapor-Phase Epitaxy* (Academic, San Diego).

https://doi.org/10.1017/CBO9780511599828.018 Published online by Cambridge University Press

Tanaka, H., Itoh, H., O'Hori, T., Takikawa, M., Kosai, K., Takehi, M., Suzuki, M., and Komeno, J. (1987) *Jpn. J. Appl. Phys.* **26**, L1456.

Timmons, M. L., Chiang, P. K., and Hattangady, S. V. (1986) *J. Crystal Growth* **77**, 37.

Tsang, W. T. (1989) in *VLSI Electronics: Microstructure Science* **21**, ed. Einspruch, N. G. (Academic, New York) p. 255.

Tuck, D. G. (1982) in *Comprehensive Organometallic Chemistry*, eds. Wilkinson, G., Stone, G. A., and Abel, F. W. (Pergamon, Oxford) p. 684.

van de Ven, J., Rutten, G. M. J., Raaijmakers, M. J., and Giling, L. J. (1986) *J. Crystal Growth* **76**, 352.

Veuhoff, E., Kuech, T. F., and Meyerson, B. S. (1985) *J. Electrochem. Soc.* **132**, 1958.

Veuhoff, E., Maier, M., Bachen, K.-H., and Balk, P. (1981) *J. Crystal Growth* **53**, 598.

Weyers, M., Musoff, J., Marx, D., Kohl, A., and Balk, P. (1990) *J. Crystal Growth* **105**, 383.

Weyers, M., Pütz, N., Heinecke, H., Heyer, M., Lüth, H., and Balk, P. (1986) *J. Electron. Mater.* **15**, 57.

Wiley, J. D. (1975) in *Semiconductors and Semimetals* **10**, eds. Willardson, R. K. and Beer, A. C. (Academic, New York) p. 154.

Wood, C. E. C., DeSimeone, D., Singer, K., and Wicks, G. W. (1982) *J. Appl. Phys.* **53**, 4230.

Yakimova, R., Roth, A. P., Williams, D. F., and Sundaran, V. S. (1984) *J. Crystal Growth* **68**, 71.

Yoshida, M., Watanabe, H., and Uesugi, F. (1985) *J. Electrochem. Soc.* **132**, 677.

Zilko, J. L. and Schubert, E. F. (1991) unpublished.

Chapter 7

Aliev, M. I., Safaraliev, G. I. and Abdinova, S. G. (1967) *Phys. Stat. Sol.*, **22**, 741.

Andrews, D. A., Heckingbottom, R., and Davies, G. J. (1983) *Appl. Phys.* **54**, 4421.

Anholt, R., Balasingam, P., Chou, S. Y., Sigmon, T. W., and Deal, M. (1988) *J. Appl.*

https://doi.org/10.1017/CBO9780511599828.018 Published online by Cambridge University Press

Arnold, N., Dämbkes, H., and Heime, K. (1980) *Jpn. J. Appl. Phys.* **19**, Suppl. 19-1, 361.

Arnold, N., Schmitt, R., and Heime, K. (1984) *J. Phys. D.: Appl. Phys.* **17**, 443.

Arthur, J. R. (1967) *J. Phys. Chem. Solids* **28**, 2257.

Astles, M. G., Smith, F. G. H., and Williams, E. W. (1973) *J. Electrochem. Soc.* **120**, 1750.

Bahir, G. and Merz, J. L. (1988) *Inst. Phys. Conf. Ser.* **91**, 467.

Bahir, G., Merz, J. L., Abelson, J. R., and Sigmon, T. W. (1989) *J. Appl. Phys.* **65**, 1009.

Baillargeon, J. N., Cheng, K. Y., Hsieh, K. C., and Wei, C. L. (1990) *J. Cryst. Growth* **105**, 106.

Ballingall, J. M. and Wood, C. E. C. (1982) *Appl. Phys. Lett.* **41**, 947.

Baraff, G. A. and Schlüter, M. (1985) *Phys. Rev. Lett.* **55**, 1327.

Bass, S. J. and Oliver, P. E. (1977) in *Gallium Arsenide and Related Compounds*, ed. Eastman, L. F. (Inst. Phys., Bristol) p. 1.

Beadle, W. E., Tsai, J. C. C., and Plummen, R. D. (1985) *Quick Reference Manual (QRM)*, (Wiley, New York) pp. 2–71.

Beall, R. B., Clegg, J. B., Castagné, J., Harris, J. J., Murray, R., and Newman, R. C. (1989) *Semicond. Sci. Technol.* **4**, 1171.

Benchimol, J. L., Alaoui, F., Le Roux, G., Gao, Y. and Alexandre, F. (1989) *2nd Int. Conf. on Chemical Beam Epitaxy, Houston.*

Biersack, J. P. and Haggmark, L. G. (1980) *Nucl. Instrum. Methods* **174**, 257.

Biersack, J. P. and Ziegler, J. F. (1982) *Ion Implantation Techniques* (Springer, New York) p. 122.

Bose, S. S., Lee, B., Kim, M. H., Stillman, G. E., and Wang, W. I. (1988) *J. Appl. Phys.* **63**, 743.

Braslau, N. (1981) *J. Vac. Sci. Technol.* **19**, 803.

Camlibel, I., Chin, A. K., Guggenheim, H., Singh, S., van Uitert, L. G., and Zydzik, G. J. (1984) *J. Electrochem. Soc.* **131**, 1687.

Chadi, D. J. and Chang, K. J. (1988) *Phys. Rev. Lett.* **61**, 873.

https://doi.org/10.1017/CBO9780511599828.018 Published online by Cambridge University Press

Chai, Y. G., Chow, R., and Wood, C. E. C. (1981) *Appl. Phys. Lett.* **39**, 800.

Cheng, K. Y., Cho, A. Y. and Wagner, W. R. (1981) *J. Appl. Phys.*, **52**, 6328.

Chiang, T.-C., Ludeke, R., Aono, M., Landgren, G., Himpsel, F. J., and Eastman, E. E. (1983) *Phys. Rev. B***27**, 4770.

Chin, A. K. and Bonner, W. A. (1982) *Appl. Phys. Lett.*, **40**, 248.

Cho, A. Y. and Arthur, J. R. (1975) *Prog. Solid State Chem.* **10**, 157.

Cristel, L. A., Gibbons, J. F., and Mylroic, S. (1980) *J. Appl. Phys.* **51**, 6176.

De Souza, J. P., Sadana, D. K., Baratte, H., and Cardone, F. (1990) *Appl. Phys. Lett.* **57**, 1129.

Donnelly, J. P. and Hurwitz, C. E. (1980) *Solid State Electron.* **23**, 943.

Drummond, T. J., Lyons, W. G., Fisher, R., Thorne, R. E., Morkoc, H., Hopkins, C. G. and Evans, C. A., J. (1982) *J. Vac. Sci. Technol.* **21**, 957.

Etienne, B. and Thierry-Mieg, V. (1988) *Appl. Phys. Lett.* **52**, 1237.

Feldman, L. C. and Mayer, J. W. (1986) *Fundamentals of Surface and Thin Film Analysis* (North-Holland, New York).

Ferris, S. D., Leamy, H. J., and Poate, J. M. eds. (1979) *Laser-Solid Interactions and Laser Processing* (American Institute of Physics, New York).

Fujita, S., Bedair, S. M., Littlejohn, M. A. and Hauser, J. R. (1980) *J. Appl. Phys.* **51**, 5438.

Gibbons, J. F., Johnson, W. S., and Mylroic, S. W. (1975) *Projected Range Statistics* (Dowolan, Hutchinson, and Ross, Stroudsburg, PA).

Gill, S. S. and Sealy, B. J. (1984) *J. Appl. Phys.* **56**, 1189.

Gill, S. S. and Sealy, B. J. (1986) *J. Electrochem. Soc.: Solid-State Sci. Technol.* **133**, 2590.

Gilmer, G. H. and Gossmann, H. J. (1993) to be published.

Gilmer, G. H. (1992) personal communication.

Glew, R. W. (1984) *J. Crystal Growth* **68**, 44.

Goldstein, B. (1984) *Phys. Rev.* **121**, 1305.

https://doi.org/10.1017/CBO9780511599828.018 Published online by Cambridge University Press

Greiner, M. E. and Gibbons, J. F. (1984) *Appl. Phys. Lett.* **44**, 750.

Hamm, R. A., Panish, M. B., Nottenburg, R. N., Chen, Y. K., and Humphrey, D. A. (1989) *Appl. Phys. Lett.* **54**, 2586.

Harris, T. D. and Schubert, E. F. (1990) unpublished results.

Harrison, R. J. and Houston, P. A. (1986) *J. Crystal Growth* **78**, 257.

Hartley, F. and Patai, S. (1982) *The Chemistry of the Metal-Carbon Bond* (Wiley, New York) pp. 53–71.

Heckingbottom (1985) in *Molecular Beam Epitaxy and Heterostructures*, eds. L. Chang, L. and Ploog, K. (Martinus Nijhoff, Dordrecht) p. 71.

Heime, K. (1967) *Solid-State Electron.* **10**, 732.

Heime, K. (1989) *InGaAs Field-Effect Transistors* (Research Studies Press LTD., Taunton, England) p. 136.

Hoke, W. E., Lemonias, P. J., Weir, D. G., Hendriks, H. T., and Jackson, G. S. (1991a) *J. Appl. Phys.* **69**, 511.

Hoke, W. E., Lemonias, P. J., Lyman, P. S., Hendriks, H. T., Weir, D., and Colombo, P. (1991b) *J. Cryst. Growth* **111**, 269.

Inada, T., Taka, S., Yamamato, Y. (1981) *J. Appl. Phys.* **52**, 6623.

Iwamoto, T., Mori, K., Mizuta, M. and Kukimoto, H. (1984) *J. Crystal Growth*, **68**, 27.

Kadoya, Y., Sato, A., Kano, H., and Sakaki, H. (1991) *J. Cryst. Growth*, **111**, 280.

Kamiya, T. and Wagner, E. (1977) *J. Appl. Phys.* **48**, 1928.

Kanber, H., Cipolli, R. J., Henderson, W. B., and Whelan, J. M. (1985) *J. Appl. Phys.* **57**, 4732.

Kawaguchi, Y. and Nakashima, K. (1989) *J. Cryst. Growth* **95**, 181.

Kim, S. J. et al. (1987) *IEEE Electron Dev. Lett.* **8**, 518.

Kisker, D. W. and Zawadzki, A. G. (1988) *J. Crystal Growth* **89**, 378.

Kittel, C. and Kroemer, H. (1980) *Thermal Physics*, 2nd ed. (Freeman, New York).

Kohzu, H., Kuzuhara, M., and Takayama, Y. (1983) *J. Appl. Phys.* **54**, 4998.

https://doi.org/10.1017/CBO9780511599828.018 Published online by Cambridge University Press

Krautle, H. (1988) *J. Appl. Phys.* **63**, 4418.

Kreuzer, H. J. (1991) in *Low Temperature Epitaxial Growth of Semiconductors*, ed. Harris, T. (World Scientific, Singapore) p. 1.

Kreyszig, E. (1972) *Advanced Engineering Mathematics*, 3rd ed. (Wiley, New York) p. 726.

Kroger, F. A. (1973) *Chemistry of Imperfect Crystals* 2nd ed. (Elsevier, Amsterdam).

Künzel, H., Knecht, J., Jung, H., Wünstel, K., and Ploog, K. (1982) *Appl. Phys.* **A28**, 167.

Kuphal, E. (1981) *Solid State Electron.* **24**, 69.

Lannoo, M. and Bourgoin, J. (1981) *Point Defects in Semiconductors I*, (Springer, Berlin) p. 203.

Larsen, K. K. and Larsen, A. N. (1990) *Materials Science Forum*, **65-66**, 293.

Lee, B., Bose, S. S., Kim, M. H., Reed, A. D., Stillman, G. E., Wang, W. I., Vina, L., and Colter, P. C. (1989a) *J. Cryst. Growth* **96**, 27.

Lee, B., Bose, S. S., Kim, M. H., Stillman, G. E., and Wang, W. I. (1990) *J. Appl. Phys.* **67**, 255 (1990).

Lee, B., Szafranek, I., Stillman, G. E., Arai, K., Nashimoto, Y., Shimizu, K., Iwata, N., and Sakuma, I. (1989b) *Surf. Interf. Analysis* **14**, 619.

Lievin, J. L., Alexandre, F. and Dubon-Chevaillier, C. (1988) in *Properties of Impurity States in Superlattice Semiconductors* eds., Fong, C. Y., Batra, I. P. and Ciraci, S., (Plenum, New York), p. 19.

Lu, Z. H., Hanna, M. C., Szmyd, D. M., Oh, E. G., and Majerfeld, A. (1990) *Appl. Phys. Lett.* **56**, 177.

Maguire, J., Murray, R., Newman, R. C., Beall, R. B., and Harris, J. J. (1987) *Appl. Phys. Lett.* **50**, 516.

Maier, M. and Selders, J. (1986) *J. Appl. Phys.* **60**, 2783.

Malik, R. J., Nagle, J., Micovic, M., Harris, T. D., Ryan, R. W., and Hopkins, L. C. (1992) *J. Vac. Sci. Technol.* **B10**, 850.

Mathiot, D. and Pfister, J. C. (1982) *J. Physique Letters* **43**, L453.

Mathiot, D. and Pfister, J. C. (1984) *J. Appl. Phys.* **55**, 351.

https://doi.org/10.1017/CBO9780511599828.018 Published online by Cambridge University Press

337-TA-1366 RX-0255

Mathiot, D. and Pfister, J. C. (1989) *J. Appl. Phys.* **66** 1970.

Miller, D. L. and Asbeck, P. M. (1987) *J. Crystal Growth* **81**, 368.

Morgan, T. N. (1972) in *Proc. 11th Int. Conf. on the Physics of Semiconductors*, **2**, ed. Miasek, M. (Elsevier, Amsterdam) p. 989.

Mottram, A., Peaker, A. R. and Sudlow, P. D. (1971) *J. Electrochem. Soc.*, **118**, 318.

Munoz-Yague, A. and Baceinedo, S. (1982) *J. Electrochem. Soc.: Solid-State Sci. and Technol.* **129**, 2108.

Nakajima, M., Takomori, A., Yokosuka, T., Uchiyama, K., and Abe, T. (1989) *2nd Int. Conf. on Chemical Beam Epitaxy, Houston.*

Nanichi, Y. and Pearson, G. L. (1969) *Solid State Electron.* **12**, 341.

Neave, J. H. and Joyce B. A. (1983) *Appl. Phys. A***31**, 190.

Ogawa, M. and Baba, T. (1985) *Jpn. J. Appl. Phys.* **24**, L572.

Panish, M. B., Hamm, R. A., Hopkins, L. C., and Chu, S. N. G. (1990a) *Appl. Phys. Lett.* **56**, 1137.

Panish, M. B., Hamm, R. A., and Hopkins, L. C. (1990b) *Appl. Phys. Lett.* **56**, 2301.

Panish, M. B. (1990) personal communication.

Pearton, S. J. (1988) *Solid State Phenomena* **1&2**, 247.

Pickar, K. A. (1975), in *Applied Solid State Science Vol. 5*, ed. Wolfe, R. (Academic, New York).

Poole, I., Lee, M. E., Singer, K. E., Frost, J. E. F., Kerr, T. M., Wood, C. E. C., Andrews, D. A., Rothwell, W. J. M., and Davies, G. J. (1988) *J. Appl. Phys.* **63**, 395.

Razeghi, M. (1989) *The MOCVD Challenge* (Adam Hilger, Bristol) p. 10.

Ryssel, H. and Biersack, J. P. (1986) in *Process and Device Modeling*, ed. Enggl, W. L. (North-Holland, Amsterdam).

Ryssel, H. and Ruge, I. (1986) *Ion Implantation*, (Wiley, New York).

Schmitt, F., Su, L. M., Franke, D., and Kaumanns, R. (1984) *IEEE Trans. Electron Dev.* **31**, 1083.

Schubert, E. F., Gilmer, G. H., Monroe, D. P., Kopf, R. F., and Luftman, H. S. (1992) *Phys. Rev. B***46**, 15 078.

https://doi.org/10.1017/CBO9780511599828.018 Published online by Cambridge University Press

Schubert, E. F., Kopf, R. F., Kuo, J. M., Luftman, H. S., and Garbinski, P. A. (1990a) *Appl. Phys. Lett.* **57**, 497.

Schubert, E. F., Kuo, J. M., Kopf, R. F., Jordan, A. S., Luftman, H. S., and Hopkins, L. C. (1990b) *Phys. Rev. B***42**, 1364.

Schubert, E. F., Kuo, J. M., Kopf, R. F., Luftman, H. S., Hopkins, L. C., and Sauer, N. J. (1990c) *J. Appl. Phys.* **67**, 1969.

Selberherr, S. (1984) *Analysis and Simulation of Semiconductor Devices* (Springer, Wien) Chap. 3.

Sharma, B. L. (1989) *Solid State Technology*, November issue, 113.

Shockley, W. (1961) *Solid State Electron.* **2**, 35.

Singh, S., Zydzik, G. J., and van Uitert, L. G. (1984) unpublished.

Singh, S., Baiocchi, F., Butherus, A. D., Grodkiewicz, W. H., Schwartz, B., Van Uitert, L. G., Yesis, L., and Zydzik, G. J. (1988) *J. Appl. Phys.* **64**, 4194.

Stringfellow, G. B. (1985) in *Semiconductors and Semimetals* **22**, ed. Tsang, W. T., (Academic, New York) p. 209.

Stringfellow, G. B. (1986) *J. Crystal Growth* **75**, 91.

Stringfellow, G. B. (1989) *Organometallic Vapor-Phase Epitaxy* (Academic, New York).

Tan, T. Y. and Gösele, U. (1988) *Appl. Phys. Lett.* **52**, 1240.

Tell, B. (1991) personal communication.

Teramoto, I. (1972) *J. Phys. Chem. Solids* **33**, 2089.

Theis, T. N., Mooney, P. M., and Wright, S. L. (1988) *Phys. Rev. Lett.* **60**, 361.

Tokumitsu, E. (1990) *Jpn. J. Appl. Phys.* **29**, L698.

Tsang, W. T. (1989) in *VLSI Electronics: Microstructure Science* **21**, ed. Einspruch, N. G. (Academic, New York) p. 255.

Tsang, W. T., Choa, F. S., and Ha, N. T. (1991) *J. Electron. Mater.* **20**, 541.

Valco, G. J., Kapoor, V. J., Biedenbender, M. D., and Williams, W. D. (1989) *J. Electrochem. Soc.* **136**, 175.

Vescan, L., Selders, J., Kräutle, H., Kütt, W., and Beneking, H. (1982) *Electron. Lett.* **18**, 534.

https://doi.org/10.1017/CBO9780511599828.018 Published online by Cambridge University Press

Walukiewicz, W. (1989) *Appl. Phys. Lett.* **54**, 2094.

Wang, K. W. (1987) *Appl. Phys. Lett.* **51**, 2127.

Wang, K. W. (1989) US Patent 4,818,721 April 4.

Weimer, P. K. (1962) *Proc. IRE* **50**, 1462.

Weisberg, L. R. and Blanc, J. (1963) *Phys. Rev.* **131**, 1548.

Wilson, R. G., Novak, S. W. and Zavada, J. M. (1988) *Inst. Phys. Conf. Ser.* **91**, 479.

Wood, C. E. C., Desimone, D., Singer, K. E., and Wicks (1982) *J. Appl. Phys.* **53**, 4230.

Woodhouse, J. D., Donnelly, J. P., Nitishiu, P. M., Owens, E. B., and Ryan, J. L. (1984) *Solid State Electron.* **27**, 677.

Wu, M. C., Su, Y. K., Cheng, K. Y. and Chang, C. Y. (1988) *Solid State Electron.* **31**, 251.

Yamada, T., Tokumitsu, E., Saito, K., Akatsuka, T., Miyauchi, M., Konagai, M. and Takahashi, K. (1989) *J. Crystal Growth* **95**, 145.

Ziegler, J. F., Biersack, J. P. and Cuomo, G., TRIM computer code, Copyright 1991, IBM Corporation.

Ziegler, J. F., Biersack, J. P., and Littmark, U. (1985) *The Stopping Range of Ions in Solids* **1**, (Pergamon, New York).

Chapter 8

Arnold, N., Schmitt, R., and Heime, K. (1984) *J. Phys. D: Appl. Phys.* **17**, 443.

Baraff, G. A. and Schlüter, M. (1985) *Phys. Rev. Lett.* **55**, 1327.

Bardeen, J. (1947) *J. Phys. Rev.* **71**, 717.

Beall, R. B., Clegg, J. B., Castagné, J., Harris, J. J., Murray, R. and Newman, R. C. (1989) *Semicond. Sci., Technol.* **4**, 1171.

Boltaks, B. I., Ksendzov, S., and Rembeza, S. I. (1969) *Sov. Phys. Solid State* **10**, 2186.

Brozel, M. R., Foulkes, E. J., and Tuck, B. (1982) *Phys. Stat. Sol. (a)* **72**, K159.

Brozel, M. R., Tuck, B., and Foulkes, E. J. (1981) *Electron. Lett.* **17**, 532.

https://doi.org/10.1017/CBO9780511599828.018 Published online by Cambridge University Press

Casey, H. C., Jr., Panish, M. B., and Wolfstirn, K. B., (1971) *J. Phys. Chem. Solids* **32**, 571.

Chang, L. L. and Casey, H. C. (1964) *Solid State Electron.* **7**, 481.

Chang, L. L. and Pearson, G. L. (1964a) *J. Appl. Phys.* **35**, 374.

Chang, L. L. and Pearson, G. L. (1964b) *J. Appl. Phys.* **35**, 1960.

Chevrier, J., Armand, M., Huber, A. M., and Linh, N. T. (1980) *J. Electron. Mater.* **9**, 745.

Chiang, T.-C., Ludeke, R., Aono, M., Landgren, G., Himpsel, F. J., and Eastman, D. E. (1983) *Phys. Rev. B***27**, 4770.

Chin, A. K., Camlibel, I., Dutt, B. V., Swaminathan, V., Bonner, W. A., and Ballman, A. A. (1983a) *Appl. Phys. Lett.* **42**, 901.

Chin, A. K., Camlibel, I., Sheng, T. T., and Bonner, W. A. (1983b) *Appl. Phys. Lett.* **43**, 495.

Cunnell, F. A. and Gooch, C. H. (1960) *J. Phys. Chem. Sol.* **15**, 127.

Deal, M. D. and Stevenson, D. A. (1986) *J. Appl. Phys.* **59**, 2398.

Deppe, D. G. and Holonyak, Jr., N. (1988) *J Appl. Phys.* **64**, R93.

Deppe, D. G., Holonyak, Jr. N., Kish, F. A., and Baker, J. E. (1987) *Appl. Phys. Lett.* **50**, 998.

Devine, R. L. S., Foxon, C. T., Joyce, B. A., Clegg, J. B., and Govers, J. P. (1987) *Appl. Phys. A***44**, 195.

Dutt, B. V., Chin, A. K., Camlibel, I., and Bonner, W. A. (1984) *J. Appl. Phys.* **56**, 1630.

Einstein, A. (1905) *Ann. Phys.* **17**, 549.

Einstein, A. (1906) *Ann. Phys.* **19**, 371.

Fane, R. W. and Goss, A. J. (1963) *Solid State Electron.* **6**, 383.

Frank, F. C. and Turnbull, D. (1956) *Phys. Rev.* **104**, 617.

Frieser, R. G. (1965) *J. Electrochem. Soc.* **112**, 697.

Gibbon, C. F. and Ketchow, D. R. (1971) *J. Electrochem. Soc.* **118**, 975.

https://doi.org/10.1017/CBO9780511599828.018 Published online by Cambridge University Press

337-TA-1366 RX-0255

Goldstein, B. (1961) *Phys. Rev.* **121**, 1305.

Goldstein, B. and Keller, H. (1961) *J. Appl. Phys.* **32**, 1180.

Greiner, M. E. and Gibbons, J. F. (1984) *Appl. Phys. Lett.* **44**, 750.

Hamm, R. A., Panish, M. B., Nottenburg, R. N., Chen, Y. K., and Humphrey, D. A. (1989) *Appl. Phys. Lett.* **54**, 2586.

Harris, J. J., Ashenford, D. E., Foxon, C. T., Dobson, P. J., and Joyce, B. A. (1984) *Appl. Phys.* **A33**, 87.

Harris, J. J., Joyce, B. A., Gowers, J. P., and Neave, J. H. (1982) *Appl. Phys.* **A28**, 63.

Heine, V. (1965) *Phys. Rev.* **138**, A1689.

Hofmann, S. and Erlewein, J. (1979) *Surf. Sci.* **77**, 591.

Holmes, D. E., Wilson, R. G., and Yu, P. W. (1981) *J. Appl. Phys.* **52**, 3396.

Huber, A. M., Morillot, G., Bonnet, M., Merenda, P., and Bessoneau, G. (1982) *Appl. Phys. Lett.* **41**, 638.

Huijser, A., van Laar, J., and van Rooy, T. L. (1977) *Surf. Sci.* **62**, 472.

Ihm, J., Chadi, D. J., and Joannopoulos, J. D. (1983) *Phys. Rev.* **B27**, 5119.

Ilegems, M. (1977) *J. Appl. Phys.* **48**, 1278.

Ilegems, M. and O'Mara, W. C. (1972) *J. Appl. Phys.* **43**, 1190.

Kadhim, M. A. and Tuck, B. (1972) *J. Mater. Sci.* **7**, 68.

Kahng, D. (1964) *Bell. Syst. Techn. J.* **42**, 215.

Kaliski, R. W., Nam, D. W., Deppe, D. G., Holonyak, Jr. N., Hsieh, K. C., and Burnham, R. D. (1987) *J. Appl. Phys.* **62**, 998.

Karelina, T. A., Lavrishchev, T. T., Prikhod'ko, G. L., and Khludov, S. S. (1974) *Inorganic Mater.* **10**, 194.

Kato, H., Yokozawa, M., Kohara, R., Okabayashi, Y., and Takayanagi, S. (1969) *Solid State Electron.* **12**, 137.

Kendall, D. L. (1968) in *Semiconductors and Semimetals*, eds. Willardson, R. K. and Beer, A. C. (Academic, New York) p. 163.

https://doi.org/10.1017/CBO9780511599828.018 Published online by Cambridge University Press

Innoscience1366-00139267

RX-0255.594

Kendall, D. L. and Huggins, R. A. (1969) *J. Appl. Phys.* **40**, 2750.

Khludkov, S. S. and Lavrishchev (1976) *Inorganic Mater.* **12**, 972.

Kobayashi, N., Makimoto, T., and Horikoshi, Y. (1987) *Appl. Phys. Lett.* **50**, 1435.

Kundukhov, R. M., Metreveli, S. G., and Siukaev, N. v. (1967) *Sov. Phys.-Semicond.* **1**, 765.

Laidig, W. D., Holonyak, Jr., N., Camvas, M. D., Hess, K., Coleman, J. J., Dapkus, P. D., and Bardeen, J. (1981) *Appl. Phys. Lett.* **38**, 776.

Laidig, W. D., Holonyak, Jr., N., Coleman, J. J. and Dapkus, P. D. (1982) *J. Electron. Mater.* **11**, 1.

Linh, N. T., Huber, A. M., Etienne, P., Morillot, G., Duchemin, P., and Bonnet, M. (1980) in *Semi-Insulating III–V Materials*, ed. Rees, G. J. (Shiva, Nantwich) p. 206.

Longini, R. L. and Greene (1956) *Phys. Rev.* **102**, 992.

Luther, L. C. and Wolfstirn, K. B. (1973) *J. Electron. Mater.* **2**, 375.

Manning, J. R. (1968) *Diffusion Kinetics for Atoms in Crystals* (van Nostrand, Princeton) pp. 95, 166.

Matino, H. (1974) *Solid State Electron.* **17**, 35.

McLevige, W. V., Vaidyanathan, K. V., Streetman, B. G., Ilegems, M., Comas, J., and Plew, L. (1978) *Appl. Phys. Lett.* **33**, 127.

Meehan, K., Holonyak, Jr., N., Brown, J. M., Nixon, M. A., Gavrilovic, P., and Burnham, R. D. (1984) *Appl. Phys. Lett.* **45**, 549.

Mei, P., Yoon, H. W., Venkatesan, T., Schwarz, S. A., and Harbison, J. P. (1987) *Appl. Phys. Lett.* **50**, 1823.

Mott, N. F. (1938) *Proc. Cambridge, Philos. Soc.* **34**, 568.

Nanichi, Y. and Pearson, G. L. (1969) *Solid State Electron.* **12**, 341.

Oberstar, J. D., Streetman, B. G., Baker, J. E., and Williams, P. (1981) *J. Electrochem. Soc.* **128**, 1814.

Palfrey, H. D., Brown, M., and Willoughby, A. F. W. (1981) *J. Electrochem. Soc.* **128**, 2224.

https://doi.org/10.1017/CBO9780511599828.018 Published online by Cambridge University Press

337-TA-1366 RX-0255

Palfrey, H. D., Brown, M., and Willoughby, A. F. W. (1983) *J. Electron. Mater.* **12**, 863.

Panish, M. B. (1973) *J. Phys.* **44**, 2659.

Panish, M. B., Hamm, R. A., and Hopkins, L. C. (1990) *Appl. Phys. Lett.* **56**, 2301.

Panish, M. B., Hamm, R. A., Ritter, D., Luftman, H. S., and Cotell, C. M. (1991) *J. Crystal Growth* **112**, 343.

Pankove, J. I. and Johnson, N. M. (1991) ed., *Hydrogen in Semiconductors* (Academic, New York).

Phillips, J. C. (1973) *Bonds and Bands in Semiconductors* (Academic, New York) p. 222.

Prince, F. C., Oren, M., and Lam, M. (1986) *Appl. Phys. Lett.* **48**, 546.

Rekalova, G. I., Kebe, U., Persiyanov, T. V., Krymov, V. M., and Krymova, E. D. (1971) *Sov. Phys.-Semicond.* **5**, 134.

Rekalova, G. I., Shakov, A. A., and Gavrushko, A. A. (1969) *Sov. Phys.-Semicond.* **2**, 1452.

Risken, H. (1984) *The Fokker–Planck Equation* (Springer, Berlin).

Schillmann, E. (1962) in *Compound Semiconductors*, eds. Willardson, R. K. and Goering, H. L. (Reinhold, New York) p. 358.

Schneider, M. and Nebauer, E. (1975) *Phys. Stat. Sol. (a)* **32**, 333.

Schottky, W. (1940) *Naturwissenschaften* **26**, 843.

Schottky, W. (1940) *Z. Phys.* **41**, 570.

Schubert, E. F., Kuo, J. M., Kopf, R. F., Jordan, A. S., Luftman, H. S., and Hopkins, L. C. (1990a) *Phys. Rev. B* **42**, 1364.

Schubert, E. F., Kuo, J. M., Kopf, R. F., Luftman, H. S., Hopkins, L. C., and Sauer, N. J. (1990b) *J. Appl. Phys.* **67**, 1969.

Schubert, E. F., Stark, J. B., Chiu, T. H., and Tell, B. (1988) *Appl. Phys. Lett.* **53**, 293.

Schubert, E. F., Tu, C. W., Kopf, R. F., Kuo, J. M., and Lunardi, L. M. (1989) *Appl. Phys. Lett.* **54**, 2592.

Shaw, D. (1975) *Phys. Stat. Sol. (B)* **72**, 11.

Shishiyanu, F. S. and Boltaks, B. I. (1966) *Sov. Phys.-Solid State* **8**, 1053.

https://doi.org/10.1017/CBO9780511599828.018 Published online by Cambridge University Press

Shishiyanu, F. S., Gheorghiu, V. G., and Palazov, S. K. (1977) *Phys. Stat. Sol. A***40**, 29.

Shockley, W. and Last, J. T. (1957) *Phys. Rev.* **107**, 392.

Showan, S. R. and Shaw, D. (1969) *Phys. Stat. Sol.* **32**, 97.

Small, M. B., Potemski, R. M., Reuter, W., and Ghez, R. (1982) *Appl. Phys. Lett.* **41**, 1068.

Spicer, W. E., Gregory, P. E., Chye, P. W., Babalola, I. A., and Sukegawa, T. (1975) *Appl. Phys. Lett.* **27**, 617.

Spicer, W. E., Lindau, I., Skeath, P., Su, C. Y., and Chye, P. W. (1980) *Phys. Rev. Lett.* **44**, 420.

Sze, S. M. and Wei, L. Y. (1961) *Phys. Rev.* **124**, 84.

Tan, T. Y. and Gösele, U. (1987) *J. Appl. Phys.* **61**, 1841.

Tan, T. Y. and Gösele, U. (1988) *Appl. Phys. Lett.* **52**, 1240.

Tuck, B. (1988) *Atomic Diffusion in III–V Semiconductors* (Adam Hilger, Bristol).

Tuck, B. and Adegboyega, G. A. (1979) *J. Phys. D: Appl. Phys.* **12**, 1895.

Tuck, B. and Badawi, M. H. (1978) *J. Phys. D: Appl. Phys.* **11**, 2541.

Tuck, B. and Hooper, A. (1975) *J. Phys. D.: Appl. Phys.* **8**, 1806.

Tuck, B. and Jay, P. R. (1977a) *J. Phys. D: Appl. Phys.* **10**, 1315.

Tuck, B. and Jay, P. R. (1977b) *J. Phys. D.: Appl. Phys.* **10**, 2089.

Tuck, B. and Zahari, M. D. (1977a) in *Gallium Arsenide and Related Compounds 1976, Inst. Phys. Conf. Ser.* **33a**, p. 177.

Tuck, B. and Zahari, M. D. (1977b) *J. Phys. D.: Appl. Phys.* **10**, 2473.

Uskov, V. A. (1974) *Sov. Phys.-Semicond.* **8**, 1573.

Vasudev, P. K., Wilson, R. G., and Evans, C. A. (1980) *Appl. Phys. Lett.* **37**, 837.

Vieland, L. J. (1961) *J. Phys. Chem. Solids* **21**, 318.

Watanabe, K., Matsuoka, Y., Imamura, Y., and Ito, K. (1982) in *Gallium Arsenide and Related Compounds 1981, Inst. Phys. Conf. Ser. 63* p. 1.

Weisberg, L. R. and Blanc, J. (1963) *Phys. Rev.* **131**, 1548.

https://doi.org/10.1017/CBO9780511599828.018 Published online by Cambridge University Press

337-TA-1366 RX-0255

Willoughby, A. F. W. (1983) in *Defects in Semiconductors II*, eds. Mahajan, S. and Corbett, J. W. (Elsevier, New York) p. 237.

Wilson, R. B. (1982) in *Gallium Arsenide and Related Compounds 1981, Inst. Phys. Conf. Ser. 63*, p. 1.

Wolfe, C. M. and Nichols, K. H. (1977) *Appl. Phys. Lett.* **31**, 356.

Wolfe, C. M. and Stillman, G. E. (1973) *Solid State Commun.* **12**, 283.

Wood, C. E. C. and Joyce, B. A. (1978) *J. Appl. Phys.* **49**, 4854.

Yamada, M., Tien, P. K., Martin, R. J., Nahony, R. E., and Ballman, A. A. (1983) *Appl. Phys. Lett.* **43**, 594.

Yamazaki, H., Kawasaki, Y., Fujimoto, M., and Kudo, K. (1975) *Jpn. J. Appl. Phys.* **14**, 717.

Young, A. B. and Pearson, G. L. (1970) *J. Phys. Chem. Sol.* **31**, 517.

Zschauer, K.-H. and Vogel, A. (1970) in *Proc. 3rd Int. Symp. GaAs*, (Institute of Physics, London), p. 100.

Chapter 9

Ainslie, N. G., Blum, S. E., and Woods, J. F. (1962) *J. Appl. Phys.* **33**, 2391.

Allen, J. W. (1960) *Nature* **187**, 403.

Baba, T., Mizuta, M., Fujisawa, T., Yoshino, J., and Kukimoto, H. (1989) *Jpn. J. Appl. Phys.* **28**, L891.

Baba, T., Mizutani, T., and Ogawa, M. (1983) *Jpn. J. Appl. Phys.* **22**, L627.

Bachelet, G. B., Schlüter, M., and Baraff, G. A. (1983) *Phys. Rev. B***27**, 2545.

Bachrach, R. Z. and Bringans, R. D. (1983) *J. Vac. Sci. Technol. B***1**, 142.

Baraff, G. A. (1992) in *Deep Centers in Semiconductors*, 2nd ed., ed. Pantelides, S. T. (Gordon and Breach, Philadelphia) p. 547.

Baraff, G. A., Lannoo, M., and Schlüter, M. (1988) *Phys. Rev. B***38**, 6003.

Bergman, K., Omling, P., Samuelson, L., and Grimmeiss, H. G. (1988) in *Semi-Insulating III-V Materials*, eds. Grossmann, G. and Ledebo, L. (Adam Hilger,

https://doi.org/10.1017/CBO9780511599828.018 Published online by Cambridge University Press

RX-0255.598

Bristol).

Boenig, H. V. (1982) *Plasma Science and Technology* (Cornell University Press, Ithaca).

Briddon, P. and Jones, R. (1989) *Inst. Phys. Conf. Ser.* **95**, 459.

Calawa, A. R. (1978) *Appl. Phys. Lett.* **33**, 1020.

Chadi, D. J. (1992) *Phys. Rev. B***46**, 6777.

Chadi, D. J. and Chang, K. J. (1988a) *Phys. Rev. Lett.* **60**, 2187.

Chadi, D. J. and Chang, K. J. (1988b) *Phys. Rev. Lett.* **61**, 873.

Chadi, D. J. and Chang, K. J. (1989) *Phys. Rev. B***39**, 10063.

Chadi, D. J. and Zhang, S. B. (1991) *J. Electron Mater.* **20**, 55.

Chand, N., Henderson, T., Clem, J., Masselink, W. T., Fischer, R., Chang, Y. C., and Morkoc, H. (1984) *Phys. Rev. B***30**, 4481.

Chen, Y. K., Temkin, H., Tanbun-Ek, T., Logan, R. A., and Nottenburg, R. A. (1989) *IEEE Electron Dev. Lett.* **10**, 162.

Chevallier, J., Clerjaud, B., and Pajot, B. (1991) in *Hydrogen in Semiconductors*, eds. Pankove, J. I. and Johnson, N. M. (Academic, New York).

Chevallier, J., Jalil, A., Azoulay, R., and Mircea, A. (1986) *Materials Science Forum* **10-12**, 591.

Chevallier, J., Pajot, B., Jalil, A., Mostefaoui, R., Rahbi, R., and Boissy, M. C. (1988) *Mat. Res. Soc. Symp. Proc.* **104**, 337.

Corbett, J. W. (1971) in *Ion Implantation*, eds. Eisen, F. H. and Chadderton, L. T. (Gordon and Breach, London).

Cotton, F. A. (1971) *Chemical Applications of Group Theory* 2nd ed. (Wiley, New York).

Dabrowski, J. and Scheffler, M. (1988) *Phys. Rev. Lett.* **60**, 2183.

Dabrowski, J. and Scheffler, M. (1989) *Phys. Rev. B***40**, 10391.

Dean, P. (1986) in *Deep Centers in Semiconductors*, ed Pantelides, S. T. (Gordon and Breach, New York) p. 185.

Devenaud, B. and Favennec (1979) *Inst. Phys. Conf. Ser.* **45**, 292.

https://doi.org/10.1017/CBO9780511599828.018 Published online by Cambridge University Press

337-TA-1366 RX-0255

Dischler, B., Fuchs, F., and Kaufmann, U. (1986) *Appl. Phys. Lett.* **48**, 1282.

Dutta, N. K. (1989) *AT&T Techn. J.* **68**, 5.

Ennen, H. and Schneider, J. (1985) in *Defects in Semiconductors*, eds. Kimerling, L. C. and Parsey, J. M., Jr. (TMS-AIME) p. 115.

Ennen, H., Kaufmann, U., Pomrenke, G., Schneider, J., Windscheif, J. and Axmann, A. (1983a) *J. Cryst. Growth* **64**, 165.

Ennen, H., Schneider, J., Pomrenke, G., and Axmann, A. (1983b) *Appl. Phys. Lett.* **43**, 943.

Favennec, P. N. (1976) *J. Appl. Phys.* **47**, 2532.

Fertin, J. L., Lebailly, J., and Deyris, E. (1967) *Gallium Arsenide and Related Compounds 1966, Inst. Phys. Conf. Ser.* **3**, 46.

Foyt, A. G., Lindley, W. T., Wolfe, C. M., and Donnelly, J. P. (1969) *Solid State Electron.* **12**, 209.

Fujisawa, T., Yoshino, J., and Kukimoto, H. (1990) *Jpn. J. Appl. Phys.* **29**, L388.

Garmire, E., Stoll, H., Yariv, A., and Hunsperger, R. G. (1972) *Appl. Phys. Lett.* **21**, 87.

Gershenzon, M. and Mikulyak, R. M. (1962) *Solid State Electron.* **5**, 313.

Gooch, C. H., Hilsum, C., and Holeman, B. R. (1961) *J. Appl. Phys.* **32**, 2069.

Guenter, K. G. (1958) *Z. Naturforschung* **13a**, 1081.

Haisty, R. W., Mehal, E. W., and Stratton, R. (1962) *J. Phys. Chem. Solids* **23**, 829.

Hofmann, D., Müller, G., and Streckfuss, N. (1989) *Appl. Phys.* **A48**, 315.

Holmes, D. E., Chen, R. T., Elliot, K. R. and Kirkpatrick, C. G. (1982) *Appl. Phys. Lett.* **40**, 46.

Huber, A. M., Linh, N. T., Valladon, M., Debrun, J. L., Martin, G. M., Mitonneau, A., and Mircea, A. (1979) *J. Appl. Phys.* **50**, 4022.

Iseler, G. W. (1979) *Inst. Phys. Conf. Ser.* **45**, 144.

Ishibashi, T., Tarucha, S., and Okamoto, H. (1982) *Jpn. J. Appl. Phys.* **21**, L476.

Jackson, G. S., Hall, H. O., Guido, L. J., Plano, W. E., Pan, N., Holonyak, Jr. N., and Stillman, G. E. (1988) *Appl. Phys. Lett.* **52**, 691.

https://doi.org/10.1017/CBO9780511599828.018 Published online by Cambridge University Press

RX-0255.600

337-TA-1366 RX-0255

Jaros, M. (1982) *Deep Levels in Semiconductors* (Adam Hilger, Bristol).

Kainosho, K., Shimakura, H., Kanazawa, T., Inoue, T., and Oda, O. (1990) *Inst. Phys. Conf. Ser.* **106**, 25.

Kaminska, M. (1984) *Proc. 17th Int. Conf. Phys. Semicond.* (Springer, New York) p. 741.

Kaminska, M., Skowronski, M., Lagowski, J., Parsey, J. M., and Gatos, H. C. (1983) *Appl. Phys. Lett.* **43**, 302.

Kaminska, M., Skowronski, M., and Kuszko, W. (1985) *Phys. Rev. Lett.* **55**, 2204.

Kaniewska, M. and Kaniewski, J. (1985) *Solid State Commun.* **53**, 485.

Kasatkin, V. A., Kesamanly, F. P., Makarenko, V. K., Masterov, V. F., and Samorukov, B. E. (1981a) *Sov. Phys. Semicond.* **14**, 1092.

Kasatkin, V. A., Kesamanly, F. P., and Samorukov, B. E. (1981b) *Sov. Phys. Semicond.* **15**, 352.

Kaufman, U. (1989) in *Advances in Solid State Physics*, **29**, (Vieweg, Braunschweig).

Kazmierski, C., Theys, B., Rose, B., Mircea, A., Jalil, A., and Chevallier (1989) *J. Electron. Lett.* **25**, 1933.

Khachaturyan, K. A., Awshalom, D. D., Rozen, J. R., and Weber, E. R. (1989) *Phys. Rev. Lett.* **63**, 1311.

Kim, H. K., Hwang, J. S., Noh, S. K., and Chung, C. H. (1986) *Jpn. J. Appl. Phys.* **25**, L888.

Kinchin, G. H. and Pease, R. S. (1955) *Rept. Progr. Phys.* **18**, 1.

Klein, P. B., Herry, R. L., Kennedy, T. A., and Wilsey, N. D. (1986) in *Defects in Semicond.*, ed. von Bardeleben, H. J., *Materials Science Forum* **10-12**, 1259.

Klein, P. B., Moore, F. G., and Dietrich, H. B. (1991) *Appl. Phys. Lett.* **58**, 502.

Kopev, P. S., Ivanov, S. V., Yegorov, A. Yu., and Uglov, D. Yu (1989) *J. Cryst. Growth* **96**, 533.

Künzel, H., Fischer, A., Knecht, J., and Ploog, K. (1983) *Appl. Phys.* **A32**, 69.

Künzel, H., Ploog, K., Wünstel, K., and Zhou, B. L. (1984) *J. Electron. Mater.* **13**, 281.

https://doi.org/10.1017/CBO9780511599828.018 Published online by Cambridge University Press

Innoscience1366-00139274

RX-0255.601

337-TA-1366 RX-0255

Lang, D. V. (1986) in *Deep Centers in Semiconductors*, ed. Pantelides, S. T. (Gordon and Breach, New York).

Lang, D. V. and Logan, R. A. (1975) *J. Electron. Mat.* **4**, 1053.

Lang, D. V. and Logan, R. A. (1977) *Phys. Rev. Lett.* **39**, 635.

Lang, D. V., Logan, R. A., and Jaros, M. (1979) *Phys. Rev. B* **19**, 1015.

Lindquist, P. F. (1977) *J. Appl. Phys.* **48**, 1262.

Long, J. A., Riggs, V. G., and Johnston, Jr. W. D. (1984) *J. Cryst. Growth* **69**, 10.

Makram-Ebeid, S., Gautard, D., Devillard, P., and Martin, G. M. (1982) *Appl. Phys. Lett.* **40**, 161.

Martin, G. M. and Makram-Ebeid, S. (1986) in *Deep Centers in Semiconductors*, ed. Pantelides, S. T. (Gordon and Breach, New York).

Martin, G. M., Mitonneau, A., and Mircea, A. (1977) *Electron. Letters* **13**, 191.

Matsumura, T., Emori, H., Terashima, K., and Fukuda, T. (1983) *Jpn. J. Appl. Phys.* **22**, L154.

McCluskey, F. P., Pfeiffer, L., West, K. W., Lopata, J., Lamont–Schnoes, M., Harris, T. D., Pearton, S. J., and Dautremont–Smith, W. C. (1989) *Appl. Phys. Lett.* **54**, 1769.

Miller, M. D., Olsen, G. H., and Ettenberg (1977) *Appl. Phys. Lett.* **31**, 538.

Miniscalco, W. J. (1991) *J. Lightwave Technol.* **9**, 234.

Miyazawa, S. and Nanishi, Y. (1983) *Jpn. J. Appl. Phys.* **22**, Supplement 22-1, 419.

Mizuta, M., and Kitano, T. (1987) *Appl. Phys. Lett.* **52**, 126.

Mizuta, M. and Mori, K. (1988) *Phys. Rev. B* **37**, 1043.

Mizuta, M., Tachikawa, M., Kukimoto, H., and Minomura, S. (1985) *Jpn. J. Appl. Phys.* **24**, L143.

Monberg, E. M., Brown, H., Chu, S. N. G., and Parsey, J. M. (1988) *Proc. 5th Conf. on Semi-insulating III–V Materials* (Malmö, Sweden).

Monberg, E. M., Gault, W. A., Dominguez, F., and Simchock, F. (1987) *J. Cryst. Growth* **83**, 174.

Mooney, P. M. (1990) *J. Appl. Phys.* **67**, R1.

https://doi.org/10.1017/CBO9780511599828.018 Published online by Cambridge University Press

RX-0255.602

Mooney, P. M., Theis, T. N., and Calleja, E. (1991) *J. Electron. Mater.* **20**, 23.

Müller, G. (1987) in *Advanced Crystal Growth*, eds. Dryburgh, P. M., Cockayne, B., and Barraclough, K. G. (Prentice Hall, Englewood Cliffs) p. 144.

Mullin, J. B., Royle, A., and Straughan, B. W. (1971) *Inst. Phys. Conf. Ser.* **9**, 41.

Muszalski, J., Babinski, A., Korona, K. P., Kaminska, E., Piotrowska, A., Kaminska, M., Weber, E. R. (1991) *Acta Physica Polonica A***80**, 413.

Nandhra, P. S., Newman, R. C., Murray, R., Pajot, B., Chevallier, J., Beall, R. B., and Harris, J. J. (1988) *Semicond. Sci. Technol.* **3**, 356.

Nelson, R. J. (1977) *Appl. Phys. Lett.* **31**, 351.

Nissen, M. K., Steiner, T., Beckett, D. J. S., and Thewalt, M. L. W. (1990) *Phys. Rev. Lett.* **65**, 2282.

Nissen, M. K., Villemaire, A., and Thewalt, M. L. W. (1991) *Phys. Rev. Lett.* **67**, 112.

Oberstar, J. D., Streetman, B. G., Baker J. E. and Williams, P. (1981) *J. Electrochem. Soc.* **128**, 1814.

Oda, O., Kainosho, K., Kohiro, K., Hirano, R., Shimakura, H., Inoue, T., Yamamoto, H., and Fukui, T. (1991) *Proc. 3rd Int. Conf. InP and Related Materials* (Cardiff, United Kingdom).

Oda, O., Katagiri, K., Shinohara, K., Katsura, S., Takahashi, Y., Kainosho, K., Kohiro, K., and Hiranoi, R. (1990) in *Semiconductors and Semimetals*, eds. Willardson, R. K., and Beer, A. C. (Academic Press, Boston).

Orito, F., Tsujikawa, Y., and Tajima, M. (1984) *J. Appl. Phys.* **55**, 1119.

Otsubo, M., Segawa, K., and Miki, H. (1973) *Jpn. J. Appl. Phys.* **12**, 797.

Ozeki, M., Komeno, J., and Ohkawa, S. (1979) *Fujitsu Sci. Tech. J.* **15**, 83.

Pajot, B., Chevallier, J., Chaumont, J., and Azoulay, R. (1988a) *Mat. Res. Soc. Symp. Proc.* **104**, 345.

Pajot, B., Newman, R. C., Murray, R., Jalil, A., Chevallier, J., and Azoulay, R. (1988b) *Phys. Rev. B***37**, 4188.

Pankove, J. I., Zanzucchi, P. J., Magee, C. W., and Lucovsky, G. (1985) *Appl. Phys. Lett.* **46**, 421.

https://doi.org/10.1017/CBO9780511599828.018 Published online by Cambridge University Press

337-TA-1366 RX-0255

Pao, Y.-C., Liu, D., Lee, W. S., and Harris, J. S. (1986) *Appl. Phys. Lett.* **48**, 1291.

Peale, R. E., Mochizuki, Y., Sun, H., and Watkins, G. D. (1992a) *Phys. Rev. B***45**, 5933.

Peale, R. E., Sun, H., and Watkins, G. D. (1992b) *Phys. Rev. B***45**, 3353.

Pearton, S. J. (1990) *Materials Science Reports* **4**, 313.

Pearton, S. J., Corbett, J. W., and Shi, T. S. (1987a) *Appl. Phys. A***43**, 153.

Pearton, S. J., Dautremont-Smith, W. C., Chevallier, J., Tu, C. W., and Cummings, K. D. (1986) *J. Appl. Phys.* **59**, 2821.

Pearton, S. J., Dautremont-Smith, W. C., Lapato, J., Tu, C. W., and Abernathy, C. R. (1987b) *Phys. Rev. B***36**, 4260.

Samuelson, L., Omling, P., Titze, H., and Grimmeiss, H. G. (1981) *J. Cryst. Growth* **55**, 164.

Schubert, E. F. and Ploog, K. (1984) *Phys. Rev. B***30**, 7021.

Schubert, E. F., Fischer, A., and Ploog, K. (1985) *Phys. Rev. B***31**, 7937.

Seager, C. H. (1991) in *Hydrogen in Semiconductors*, eds. Pankove, J. I. and Johnson, N. M. (Academic, New York) p. 17.

Seager, C. H. and Ginley, D. S., *Sandia Report, SAND82-1701*, p. 19.

Shimakura, H., Kainosho, K., Inoue, T., Yamamoto, H., and Oda, O. (1989) *Proc. Int. Conf. Sci. Technol. Defect Control in Semiconductors* (Yokohoma, Japan).

Spaeth, J.-M., Krambrock, K. and Hofmann, D. M. (1990) in *20th Int. Conf. Phys. Semicon. Vol. 1*, ed. Anastassakis, E. M. and Joannopoulus, J. D. (World Scientific, Singapore) p. 441.

Speier, P., Schemmel, G., and Kuebart, W. (1986) *Electron. Lett.* **22**, 1217.

Stavola, M., Pearton, S. J., Lopata, J., Abernathy, C. R., and Bergman, K., (1989) *Phys. Rev. B***39**, 8051.

Stavola, M., Kozuch, D. M., Abernathy, C. R., and Hobson, W. S. (1991) *Proc. E. MRS Fall Meeting* (MRS, Pittsburgh).

Steeples, K., Dearnaley, G., and Stoneham A. M. (1980) *Appl. Phys. Lett.* **36**, 981.

Street, R. A. and Mott, N. F. (1975) *Phys. Rev. Lett.* **35**, 1293.

https://doi.org/10.1017/CBO9780511599828.018 Published online by Cambridge University Press

RX-0255.604

Sugiura, H., Kawashima, M., and Horikoshi, Y. (1986) *Jpn. J. Appl. Phys.* **25**, 950.

Tachikawa, M., Mizuta, M., and Kukimoto, H. (1984) *Jpn J. Appl. Phys.* **23**, 1594.

Taguchi, A., Taniguchi, M., and Takahei, K. (1992) *Appl. Phys. Lett.* **60**, 965.

Tajima, M. (1987) *Jpn. J. Appl. Phys.* **26**, L885.

Tajima, M., Iino, T., and Ishida, K. (1987) *Jpn. J. Appl. Phys.* **26**, L1060.

Takikawa, M. and Ozeki, O. (1985) *Jpn. J. Appl. Phys.* **24**, 303.

Tell, B., Brown Goebler K. F., Cunningham, J. E., Chiu, T. H., and Jan, W. Y. (1990) *Appl. Phys. Lett.* **56**, 2657.

Temkin, H., Chen, Y. K., Garbinski, P., Tanbun-Ek, T., and Logan, R. A. (1988) *Appl. Phys. Lett.* **53**, 2534.

Theis, T. N (1990) *Proceedings of the MRS* (Boston).

Tu, L. W., Wang, Y. H., Schubert, E. F., Weir, B. E., Zydzik, G. J., and Cho, A. Y. (1992) unpublished.

Van der Ziel, J. P., Tsang, W. T., Logan, R. A., and Augustyniak, W. M. (1981) *Appl. Phys. Lett.* **39**, 376.

Vincent, G. and Bois, D. (1978) *Solid State Commun.* **27**, 431.

Von Neida, A. E., Pearton, S. J., Hobson, W. S., and Abernathy, C. R. (1989) *Appl. Phys. Lett.* **54**, 1540.

Wagner, E. E., Mars, D. E., Hom, G., and Stringfellow, G. B. (1980) *J. Appl. Phys.* **51**, 5434.

Watanabe, M. O. and Maeda, H. (1984) *Jpn. J. Appl. Phys.* **23**, L734.

Watanabe, M. O., Morizuka, K., Mashita, M., Ashizawa, Y., and Zohta, Y. (1984) *Jpn. J. Appl. Phys.* **23**, L103.

Weber, E. R. (1985) in *Microscopic Identification of Electronic Defects in Semiconductors, Proc. Mat. Res. Soc.*, (MRS, Pittsburgh).

Weber, E. R. (1991) personal communication.

Wesch, W., Wendler, E., Götz, G., and Kekelidse, N. P. (1989) *J. Appl. Phys.* **65**, 519.

Wolford, D. J. Editor (1991) *J. Electron. Mater.* **20** pp. 1-70.

https://doi.org/10.1017/CBO9780511599828.018 Published online by Cambridge University Press

337-TA-1366 RX-0255

Zakharenkov, L. F., Kasatkin, V. A., Kesamanly, F. P., Samorukov, B. E., and Sokolova, M. A. (1981) *Sov. Phys. Semicond.* **15**, 946.

Zavada, J. M., Jenkinson, H. A., Sarkis, R. G., and Wilson, R. G. (1985) *J. Appl. Phys.* **58**, 3731.

Zavada, J. M., Wilson, R. G., Novak, S. W., Von Neida, A. R., and Pearton, S. J. (1988) *Mat. Res. Soc. Symp. Proc.* **104**, 331.

Zhang, S. B. and Chadi, D. J. (1990) *Phys. Rev. B***42**, 7174.

Ziegler, J. F., Biersack, J. P., and Cuomo, G. (1991) TRIM computer code, copyright, IBM Corporation.

Chapter 10

Alexandre, F., J., Goldstein, L., Leroux, G., Joncour, M. C., Thibierge, H., and Rao, E. V. K. (1985) *Vac. Sci. Technol. B***3**, 950.

Ando, T. (1982a) *J. Phys. Soc. Jpn.* **51**, 3893.

Ando, T. (1982b) *J. Phys. Soc. Jpn.* **51**, 3900.

Ando, T. (1985) *J. Phys. Soc. Jpn.* **54**, 2676.

Ando, T. and Mori, S. (1979) *J. Phys. Soc. Japan* **47**, 1518.

Bastard, G. (1981) *Phys. Rev. B***24**, 4714.

Bastard, G., Mendez, E. E., Chang, L. L., and Esaki, L. (1982) *Phys. Rev. B***26**, 1974.

Brooks, H. in *Advance in Electronics and Electron Physics*, ed. Marton, L. (Academic, New York, 1955) p. 85, p. 156.

Casey, H. C. and Panish, M. B. (1978) in *Heterostructure Lasers* (Academic, New York) Part B, p. 16.

Chattopadhyay, D. and Queisser, H. J. (1981) *Rev. Mod. Phys.* **53**, 745.

Chaudhuri, S. and Bajaj, K. K. (1984) *Phys. Rev. B***29**, 1803.

Cho, N. M., Kim, D. J., Madhukar, A., Newman, P. G., Smith, D. D., Aucoin, T., and Iafrate, G. J. (1988) *Appl. Phys. Lett.* **52**, 2037.

https://doi.org/10.1017/CBO9780511599828.018 Published online by Cambridge University Press

Conwell, E. and Weisskopf, V. F. (1950) *Phys. Rev.* **77**, 388.

Dingle, R., Stormer, H. L., Gossard, A. C., and Wiegmann, W. (1978) *Appl. Phys. Lett.* **33**, 665.

Döhler, G. H. (1972a) *Phys. Stat. Sol.* **52**, 79.

Döhler, G. H. (1972b) *Phys. Stat. Sol.* **52**, 533.

Döhler, G. H. (1986) *IEEE J. Quant. Electron.* **22**, 1682.

Döhler, G. H., Künzel, H., Olego, D., Ploog, K., Ruden, P., Stolz, H. J., and Abstreiter, G. (1981) *Phys. Rev. Lett.* **47**, 864.

Drummond, T. J., Kopp, W., Fischer, R. J., and Morkoc, H. (1982) *J. Appl. Phys.* **53**, 1028.

Drummond, T. J., Kopp, W., Morkoc, H., Hess, K., Cho, A. Y., and Streetman, B. G. (1981a) *J. Appl. Phys.* **52**, 5689.

Drummond, T. J., Morkoc, H., Sn, S. L., Fischer, R. J., and Cho, A. Y. (1981b) *Electron. Lett.* **17**, 870.

Esaki, L. and Tsu, R. (1970) *IBM J. Res. Develop.* **14**, 61.

Fang, F. F. and Howard, W. E. (1966) *Phys. Rev. Lett.* **16**, 797.

Greene, R. L. and Bajaj, K. K. (1983) *Solid State Commun.* **45**, 825.

Greene, R. L. and Bajaj, K. K. (1985a) *Phys. Rev. B***31**, 913.

Greene, R. L. and Bajaj, K. K. (1985b) *Solid State Commun.* **53**, 1103.

Greene, R. L. and Bajaj, K. K. (1988) *Phys. Rev. B***37**, 4604.

Harris, J. J., Foxon, C. T., Lacklison, D. E., and Barnham, K. W. J. (1986) *Superlattices and Microstructures* **2**, 563.

Hess, K. (1979) *Appl. Phys. Lett.* **35**, 484.

Hess, K., Morkoc, H., Shichijo, H., and Streetman, B. G. (1979) *Appl. Phys. Lett.* **35**, 469.

Kohn, W. (1957) *Solid State Phys.* **5**, 257.

Kopf, R. F., Schubert, E. F., and Harris, T. D. (1991) *Appl. Phys. Lett.* **58**, 631 and references therein.

https://doi.org/10.1017/CBO9780511599828.018 Published online by Cambridge University Press

Mailhiot, C., Chang, Y.-C., and McGill, T. C. (1982a) *J. Vac. Sci. Technol.* **21**, 519.

Mailhiot, C., Chang, Y.-C., and McGill, T. C. (1982b) *Phys. Rev. B***26**, 4449.

Masselink, W. T., Chang, Y. C., and Morkoc, H. (1984) *J. Vac. Sci. Technol. B***2**, 376.

Masselink, W. T., Chang, Y.-C., Morkoc, H., Litton, C. W., Bajaj, K. K., and Yu, P. W. (1986) *Solid State Electron.* **29**, 205.

Masselink, W. T., Chang, Y.-C., and Morkoc, H. (1983) *Phys. Rev. B***28**, 7373.

Masselink, W. T., Chang, Y.-C., and Morkoc, H. (1985) *Phys. Rev. B***32**, 5190.

Mimura, T. (1983) *Jpn. Annu. Rev. Electron., Comput., & Telecommun: Semicond. Technology* **8**, 277.

Mori, S. and Ando, T. (1980) *J. Phys. Soc. Japan* **48**, 865.

Noda, T., Tanaka, M. and Sakaki, H. (1991) *J. Cryst. Growth* **111**, 348.

Pfeiffer, L. (1990) personal communication.

Pfeiffer, L., Schubert, E. F., West, K. W., and Magee, C. W. (1991) *Appl. Phys. Lett.* **58**, 2258.

Pfeiffer, L., West, K. W., Stormer, H. L., and Baldwin, K. W. (1989a) *Appl. Phys. Lett.* **55**, 1888.

Pfeiffer, L., West, K. W., Stormer, H. L., and Baldwin, K. W. (1989b) *Mat. Res. Symp. Proc.* **145**, 3.

Ploog, K. and Döhler, G. H. (1983) *Adv. Phys.* **32**, 285.

Price, P. J. (1981) *Ann. Phys.* **133**, 217.

Price, P. J. (1984a) *Solid State Commun.* **51**, 607.

Price, P. J. (1984b) *Surf. Sci.* **143**, 145.

Proetto, C. R. (1990) *Phys. Rev. B***41**, 6036.

Romanov, Y. A. (1972) *Sov. Phys. Semicond.* **5**, 1256.

Romanov, Y. A. and Orlov, L. K. (1973) *Sov. Phys. Semicond.* **7**, 182.

Schubert, E. F. (1990) *Optical and Quantum Electronics* **22**, S141.

Schubert, E. F., Cunningham, J. E. and Tsang, W. T. (1987a) *Phys. Rev. B***36**, 1348.

https://doi.org/10.1017/CBO9780511599828.018 Published online by Cambridge University Press

Schubert, E. F., Cunningham, J. E., Tsang, W. T., and Timp, G. L. (1987b) *Appl. Phys. Lett.* **51**, 1170.

Schubert, E. F., Harris, T. D. and Cunningham, J. E. (1988a) *Appl. Phys. Lett.* **53**, 2208.

Schubert, E. F., Harris, T. D., Cunningham, J. E. and Jan W. (1989a) *Phys. Rev. B***39**, 11011.

Schubert, E. F., Horikoshi, Y. and Ploog, K. (1985) *Phys. Rev. B***32**, 1085.

Schubert, E. F., Pfeiffer, L., West, K. W., and Izabelle, A. (1989b) *Appl. Phys. Lett.* **54**, 1350.

Schubert, E. F., Ullrich, B., Harris, T. D. and Cunningham, J. E. (1988b) *Phys. Rev. B***38**, 8305.

Seeger, K. (1982) *Semiconductor Physics* (Springer, Berlin).

Stern, F. (1983) *Appl. Phys. Lett.* **43**, 974.

Stern, F. and Das Sarma, S. (1984) *Phys. Rev. B***30**, 840.

Stormer, H. L. (1983) *Surface Science* **132**, 519.

Stormer, H. L., Dingle, R., Gossard, A. C., and Wiegmann, W. (1978) *Inst. Phys. Conf. Ser.* **43**, ed. Wilson, B. L. (Inst. Physics, London) p. 557.

Stormer, H. L., Dingle, R., Gossard, A. C., Wiegmann, W., and Sturge, M. D. (1979) *Solid State Commun.* **29**, 705.

Stormer, H. L., Gossard, A. C., Wiegmann, W., and Baldwin, K. (1981a) *Appl. Phys. Lett.* **39**, 912.

Stormer, H. L., Gossard, A. C., and Wiegmann, W. (1981b) *Appl. Phys. Lett.* **39**, 712.

Stormer, H. L., Pinczuk, A., Gossard, A. C., and Wiegmann, W. (1981c) *Appl. Phys. Lett.* **38**, 691.

Tsang, W. T., Schubert, E. E., and Cunningham, J. E. (1992) *Appl. Phys. Lett.* **60**, 115.

Urbach, F. (1953) *Phys. Rev.* **92**, 1324.

Vinter, B. (1983) *Solid State Commun.* **48**, 151.

Vinter, B. (1984) *Appl. Phys. Lett.* **44**, 307.

Walukiewicz, W., Ruda, H. E., Lagowski, J., and Gatos, H. C. (1984) *Phys. Rev. B***30**, 4571.

https://doi.org/10.1017/CBO9780511599828.018 Published online by Cambridge University Press

337-TA-1366 RX-0255

Wolfe, C. M., Stillman, G. E., and Lindely, W. T. (1970) *J. Appl. Phys.* **41**, 3088.

Chapter 11

Abramowitz, M. and Stegun, L. A. (eds.) (1972) *Handbook of Mathematical Functions*, (National Bureau of Standards, Washington D.C.).

Ando, T. (1982a) *J. Phys. Soc. Jpn.*, **51**, 3893.

Ando, T. (1982b) *J. Phys. Soc. Jpn.*, **51**, 3900.

Ando, T. (1985) *J. Phys. Soc. Jpn.*, **54**, 2676.

Baillargeon, J. N., Cheng, K. Y., Laskar, J., and Kolodzey, J. (1989) *Appl. Phys. Lett.* **55**, 663.

Bass, S. J. (1979) *J. Cryst. Growth* **47**, 613.

Bastard, G. (1981) *Phys. Rev. B***24**, 5693.

Beall, R. B., Clegg, J. B., and Harris, J. J. (1988) *Semicond. Sci. Technol.* **3**, 612.

Beall, R. B., Harris, J. J., Clegg, R. J., Gowers, J. P., Joyce, B. A., Castagnè, J., and Welch, V. (1989) in *Gallium Arsenide and Related Compounds 1988* ed. Harris, J. S. (IOP Publishing Ltd, Bristol).

Benninghoven, A., Rüdenauer, F. G., and Werner, H. W. (1987) *Secondary Ion Mass Spectrometry* (Wiley, New York).

Board, K., Chandra, A., Wood, C. E. C., Judaprawira, S., and Eastman, L. F. (1981) *IEEE Trans. Electron Dev.* **28**, 505.

Capasso, F., Cho, A. Y., Mohammed, K., and Foy, P. W. (1985a) *Appl. Phys. Lett.* **46**, 664.

Capasso, F., Mohammed, K., and Cho, A. Y. (1985b) *Vac. Sci. Technol. B***3**, 1245.

Chang-Hasnain, C. J., Hasnain, G., Johnson, N. M., Döhler, G. H., Miller, J. N., Whinnery, J. R., and Dienes, A. (1987) *Appl. Phys. Lett.* **50**, 915.

Chattopadhyay, D. and Queisser, H. J. (1981) *Rev. Mod. Phys.* **53**, 745.

Clegg, J. B. and Beall, R. B. (1989) *Surf. Interface Anal.* **14**, 307.

https://doi.org/10.1017/CBO9780511599828.018 Published online by Cambridge University Press

RX-0255.610

337-TA-1366 RX-0255

Di Lorenzo, J. V. (1971) *J. Electrochem. Soc.* **118**, 1645.

Döhler, G. H. (1972a) *Phys. Stat. Sol.* **52**, 79.

Döhler, G. H. (1972b) *Phys. Stat. Sol.* **52**, 533.

Döhler, G. H. (1986) *IEEE J. Quant. Electron.* **22**, 1682.

Döhler, G. H., Künzel, H., Olego, D., Ploog, K., Ruden, P., Stolz, H. J., and Abstreiter, G. (1981) *Phys. Rev. Lett.* **47**, 864.

English, J. H., Gossard, A. C., Störmer, H. L., and Baldwin, K. W. (1987) *Appl. Phys. Lett.* **50**, 1826.

Esaki, L. and Tsu, R. (1970) *IBM J. Res. Develop.* **14**, 61.

Etienne, B. and Thierry-Mieg, V. (1988) *Appl. Phys. Lett.* **52**, 1237.

Fang, F. F. and Howard, W. E. (1966) *Phys. Rev. Lett.* **16**, 797.

Ferreira, J. M. and Proetto, C. R. (1990) *Phys. Rev. B***42**, 5657.

Ferreira, J. M. and Proetto, C. R. (1991) *Phys. Rev. B***44**, 11231.

Gillman, G., Vinter, B., Barbier, E., and Tardella, A. (1988) *Appl. Phys. Lett.* **52**, 972.

Glass, A. M., Schubert, E. F., Wilson, B. A., Bonner, C. E., Cunningham, J. E., Olson, D. H., and Jan, W. (1989) *Appl. Phys. Lett.* **54**, 2247.

Gossard, A. C., Kazarinov, R. F., Luryi, S., and Wiegmann, W. (1982) *Appl. Phys. Lett.* **40**, 832.

Gossmann, H. J. and Schubert, E. F. (1993) *CRC Crit. Rev. Solid State Mater. Sci.* **18**, 1.

Harris, J. J., Ashenford, D. E., Foxon, C. T., Dobson, P. J., and Joyce, B. A. (1984) *Appl. Phys. A***33**, 87.

Hasnain, G., Döhler, G. H., Whinnery, J. R., Miller, J. N., and Dienes, A. (1986) *Appl. Phys. Lett.* **49**, 1357.

Headrick, R. L., Weir, B. E., Levi, A. F. J., Eaglesham, D. J., and Feldman, L. C. (1990) *Appl. Phys. Lett.* **57**, 2779.

Headrick, R. L., Weir, B. E., Levi, A. F. J., Freer, B., Bevk, J., and Feldman, L. C. (1991) *J. Vac. Sci. Technol. A***9**, 2269.

Hilsum, C. (1974) *Electron Lett.* **10**, 259.

https://doi.org/10.1017/CBO9780511599828.018 Published online by Cambridge University Press

RX-0255.611

Hobson, W. S., Pearton, S. J., Schubert, E. F., and Cabaniss, G. (1989) *Appl. Phys. Lett.* **55**, 1546.

Houng, M. P., Wang, Y. H., Chen, H. H., and Pan, C. C. (1992) *Solid State Electron.* **35**, 67.

Joyce, B. A. (1985) in *Molecular Beam Epitaxy and Heterostructures*, eds. Chang, L. L. and Ploog, K. (Martinus Nijhoff, Boston) p. 37.

Jung, H., Döhler, G. H., Göbel, E. O., and Ploog, K. (1983) *Appl. Phys. Lett.* **43**, 40.

Kazarinov, R. F. and Luryi, S. (1981) *Appl. Phys. Lett.* **38**, 810.

Kennedy, D. P. and O'Brien (1969) *IBM J. Res. Dev.* **13**, 212.

Kennedy, D. P., Murley, P. C., and Kleinfelder, W. (1968) *IBM J. Res. Dev.* **12**, 399.

Kobayashi, N., Makimoto, T., and Horikoshi, Y. (1986) *Jpn. J. Appl. Phys.* **25**, L746.

Koenraad, P. M., de Lange, W., Blom, F. A. P., Leys, M. R., Perenboom, J. A., Singleton, J., van der Vleuten, W. C., and Wolter, J. (1990a) *Materials Science Forum* **65 & 66**, 461.

Koenraad, P. M., Voncken, A. P. J., Singleton, J., Blom, F. A. P., Langerak, C. J. G., Leys, M. R., Perenboom, J. A., Spermon, S. J. R. M., van der Vlenten, W. C., and Wolter, J. H. (1990b) *Surface Science* **228**, 538.

Lanzillotto, A.-M., Santos, M., and Shayegan, M. (1989) *Appl. Phys. Lett.* **55**, 1445.

Lee, H., Schaff, W. J., Wicks, G. W., Eastman, L. F., and Calawa, A. R. (1985) *Inst. Phys. Conf. Ser.* **74**, 321.

Levi, A. F. J., McCall, S. L., and Platzman, P. M. (1989) *Appl. Phys. Lett.*, **54**, 940.

Luy, J.-F. (1990) *Thin Solid Films* **184**, 185.

Maguire, J., Murray, R., Newman, R. C., Beall, R. B., and Harris, J. J. (1987) *Appl. Phys. Lett.* **50**, 516.

Makimoto, T., Kobayashi, N., and Horikoshi, Y. (1986) *Jpn. J. Appl. Phys.* **25**, L513.

Malik, R. J. and Dixon, S. (1982) *IEEE Elec. Dev. Lett.* **3**, 205.

Malik, R. J., AuCoin, T. R., Ross, R. L., Board, K., Wood, C. E. C., and Eastman, L. F. (1980b) *Electron. Lett.* **16**, 836.

https://doi.org/10.1017/CBO9780511599828.018 Published online by Cambridge University Press

Malik, R. J., Board, K., Eastman, L. F., Wood, C. E. C., AuCoin, T. R., and Ross, R. L. (1980a) *Gallium Arsenide and Related Compounds, Inst. Phys. Conf. Ser.* **56**, 697.

Malik, R. J., Lunardi, L. M., Walker, J. F., and Ryan, R. W. (1988a) *IEEE Electron Dev. Lett.* **9**, 7.

Malik, R. J., Nottenburg, R. N., Schubert, E. F., Walker, J. R., and Ryan, R. W. (1988b) *Appl. Phys. Lett.* **53**, 2661.

Masselink, W. T. (1991a) *Phys. Rev. Lett.* **66**, 1513.

Masselink, W. T. (1991b) *Appl. Phys. Lett.* **59**, 694.

Nagle, J., Malik, R. J., and Gershoni, D. (1991) *J. Cryst. Growth* **111**, 264.

Ovsyannikov, M. I., Romanov, Y. A., Shabanov, V. N., and Loginova, R. G. (1971) *Sov. Phys. Semicond.* **4**, 1919.

Ploog, K. and Döhler, G. H. (1983) *Adv. Phys.* **32**, 285.

Proetto, C. R. (1990) *Phys. Rev. B* **41**, 6036.

Reboredo, F. A. and Proetto, C. R. (1992) *Solid State Commun.* **81**, 163.

Romanov, Y. A. (1972) *Sov. Phys. Semicond.* **5**, 1256.

Romanov, Y. A. and Orlov, L. K. (1973) *Sov. Phys. Semicond.* **7**, 182.

Sasa, S., Muto, S., Kondo, K., Ishikawa, H., and Hiyamizu, S. (1985) *Jpn. J. Appl. Phys. Lett.* **24**, L602.

Saxon, D. S. (1968) *Elementary Quantum Mechanics* (Holden-Day, San Francisco).

Schrieffer, J. R. (1957) in *Semiconductor Surface Physics*, ed. by R. H. Kingston (Univ. of Pennsylvania Press, Philadelphia) pp. 55–69.

Schubert, E. F. (1990a) *Optical and Quantum Electronics* **22**, S141.

Schubert, E. F. (1990b) *J. Vac. Sci. Technol. A* **8**, 2980.

Schubert, E. F. (1993) in *Semiconductor and Semimetals*, ed. Gossard, A. C. (Academic, New York).

Schubert, E. F. and Cunningham, J. E. (1988) *Electron. Lett.* **24**, 980.

Schubert, E. F. and Ploog, K. (1985) *Jpn. J. Appl. Phys. Lett.* **24**, L608.

https://doi.org/10.1017/CBO9780511599828.018 Published online by Cambridge University Press

Schubert, E. F., Cunningham, J. E., and Tsang, W. T. (1986a) *Appl. Phys. Lett.* **49**, 1729.

Schubert, E. F., Cunningham, J. E., and Tsang, W. T. (1987a) *Solid State Commun.* **63**, 591.

Schubert, E. F., Cunningham, J. E., and Tsang, W. T. (1987b) *Appl. Phys. Lett.* **51**, 817.

Schubert, E. F., Cunningham, J. E., Tsang, W. T., and Chiu, T. H. (1986b) *Appl. Phys. Lett.* **49**, 292.

Schubert, E. F., Cunningham, J. E. and Tsang, W. T. and Timp, G. L. (1987c) *Appl. Phys. Lett.* **51**, 1170.

Schubert, E. F., Fischer, A., Horikoshi, Y. and Ploog, K. (1985a) *Appl. Phys. Lett.* **47**, 219.

Schubert, E. F., Fischer, A. and Ploog, K. (1985b) *Electron Lett.* **21**, 411.

Schubert, E. F., Fischer, A., and Ploog, K. (1986c) *IEEE Transactions on Electron Devices*, **33**, 625.

Schubert, E. F., Harris, T. D., Cunningham, J. E., and Jan, W. (1989a) *Phys. Rev. B***39**, 11011.

Schubert, E. F., Horikoshi, Y. and Ploog, K. (1985c) *Phys. Rev. B***32**, 1085.

Schubert, E. F., Kopf, R. F., Kuo, J. M., Luftman, H. S., and Garbinski, P. A. (1990a) *Appl. Phys. Lett.* **57**, 497.

Schubert, E. F., Kuo, J. M., Kopf, R. F., Jordan, A. S., Luftman, H. S., and Hopkins, L. C. (1990b) *Phys. Rev. B***42**, 1364.

Schubert, E. F., Kuo, J. M., Kopf, R. F., Luftman, H. S., Hopkins, L. C., and Sauer, N. J. (1990c) *J. Appl. Phys.* **67**, 1969.

Schubert, E. F., Luftman, H. S., Kopf, R. F., Headrick, R. L., and Kuo, J. M. (1990d) *Appl. Phys. Lett.* **57**, 1799.

Schubert, E. F., Ploog, K., Fischer, A., and Horikoshi, Y. (1984) Europ. Patent No. 0183146 A2.

Schubert, E. F., Stark, J. B., Ullrich, B., and Cunningham, J. E. (1988a) *Appl. Phys. Lett.* **52**, 1508.

Schubert, E. F., Tu, C. W., Kopf, R. F., Kuo, J. M., and Lunardi, L. M. (1989b) *Appl. Phys. Lett.* **54**, 2592.

https://doi.org/10.1017/CBO9780511599828.018 Published online by Cambridge University Press

Schubert, E. F., Tu, L. W., Zydzik, G. J., Kopf, R. F., Benvenuti, A., and Pinto, M. R. (1992) *Appl. Phys. Lett.* **60**, 466.

Schubert, E. F., Ullrich, B., Harris, T. D., and Cunningham, J. E. (1988b) *Phys. Rev. B***38**, 8305.

Schubert, E. F., van der Ziel, J. P., Cunningham, J. E., and Harris, T. D. (1989c) *Appl. Phys. Lett.* **55**, 757.

Shockley, W. (1961) *Solid-State Electron.* **2**, 35.

Stern, F. (1983) *Appl. Phys. Lett.* **43**, 974.

Stern, F. and Das Sarma, S. (1984) *Phys. Rev. B***30**, 840.

Sun, C.-Y. and Liu, W.-C. (1991) *Appl. Phys. Lett.* **59**, 2823.

Tokumitsu, E., Dentai, A. G., Joyner, C. H., and Chandrasekhar, S. (1990) *Appl. Phys. Lett.* **57**, 2841.

Vinter, B. (1984) *Appl. Phys. Lett.* **44**, 307.

Vojak, B. A., Zajac, G. W., Chambers, F. A., Meese, J. M., Chumbley, P. E., Kaliski, R. W., Holonyak, N., Jr., and Nam, D. W. (1986) *Appl. Phys. Lett.* **48**, 251.

Wang, Y. H., Houng, M. P., Chen, H. H., and Wei, H. C. (1991) *Electron. Lett.* **27**, 1667.

Webb, C. (1989) *Appl. Phys. Lett.* **54**, 2091.

Wood, C. E. C., Metze, G. M., Berry, J. D., and Eastman, L. F. (1980) *J. Appl. Phys.* **51**, 383.

Yang, G. M., Park, S. G., Seo, K. S., and Choe, B. D. (1992) *Appl. Phys. Lett* **60**, 2380.

Chapter 12

Abernathy, C. R., Pearton, S. J., Manasreh, M. O., Fischer, D. W., and Talwar, D. N. (1990) *Appl. Phys. Lett.* **57**, 294.

Akatsuka, T., Miyake, R., Nozaki, S., Yamada, T., Konagai, M., and Takahashi, K. (1990) *Jpn. J. Appl. Phys.* **29**, L537.

Almassy, R. J., Reynolds, D. C., Litton, C. W., Bajaj, K. K., and McCoy, G. L. (1981) *Solid State Commun.* **38**, 1053.

https://doi.org/10.1017/CBO9780511599828.018 Published online by Cambridge University Press

337-TA-1366 RX-0255

Amron, I. (1964) *Electrochem. Tech.* **2**, 337.

Amron, I. (1967) *Electrochem. Tech.* **5**, 94.

Ashen, D. J., Dean, P. J., Hurle, D. T., Mullin, J. B., White, A. M., and Greene, P. D. (1975) *J. Phys. Chem. Solids* **36**, 1041.

Benninghoven, A. (1970) *Z. Phys.* **230**, 403.

Benninghoven, A., Rüdenauer, F. G., and Werner, H. W. (1987) *Secondary Ion Mass Spectrometry: Basic Concepts, Instrumental Aspects, Applications and Trends* (Wiley, New York).

Blood, P. (1986) *Semicond. Sci. Technol.* **1**, 7.

Blood, P. and Orton, J. W. (1978) *Rep. Prog. Phys.* **41**, 157.

Bohm, D. (1951) *Quantum Theory* (Prentice-Hall, Englewood Cliffs).

Bube, R. H. (1960) *J. Appl. Phys.* **31**, 315.

Buehler, M. G. and Phillips, W. E. (1976) *Solid State Electron.* **19**, 777.

Burstein, E. (1954) *Phys. Rev.* **93**, 632.

Calleja, E., Munoz, E., and Garcia, F. (1983) *Appl. Phys. Lett.* **42**, 528.

Carballes, J. C. and Lebailly, J. (1968) *Solid State Commun.* **6**, 167.

Cardona, M. and Güntherodt, G. (1984) *Light Scattering in Solids Vol. IV* (Springer, Berlin).

Cardona, M. and Güntherodt, G. (1989) *Light Scattering in Solids Vol. V* (Springer, Berlin).

Castaing, R. and Slodzian, G. (1962) *Compt. Rend.* **255**, 1893.

Castaing, R., Jouffrey, B., and Slodzian, G. (1960) *Compt. Rend.* **251**, 1010.

Chakravarty, S., Subramanian, S., Sharma, D. K., and Arora, B. M. (1989) *J. Appl. Phys.* **66**, 3955.

Chase, L. L., Haynes, W., and Ryan, J. F. (1977) *J. Phys. C* **10**, 2957.

Clegg, J. B. and Beall, R. B. (1989) *Surf. Interface Anal.* **14**, 307.

Davydov, A. S. (1965) *Quantum Mechanics*, 2nd ed. (Pergamon, Oxford).

https://doi.org/10.1017/CBO9780511599828.018 Published online by Cambridge University Press

Dean, P. J. (1973) in *Progress in Solid State Chemistry* **8**, eds. McCaldin, J. O. and Somorjai, G. (Pergamon, New York).

Dean, P. J. (1983) *Proc. Int. Conf. Phys. Semicond., Physica B***117**, 140.

Dean, P. J. and Herbert, D. C. (1979) *Excitons*, ed. Cho, K. (Springer, Berlin) p. 55.

Dean, P. J., Skolnick, M. S., Cockayne, B., MacEwan, W. R., and Iseler, G. W. (1984a) *J. Cryst. Growth* **67**, 486.

Dean, P. J., Skolnick, M. S., and Taylor, L. L. (1984b) *J. Appl. Phys.* **55**, 957.

de Lyon, T. J., Woodall, J. M., Goorsky, M. S., and Kirchner, P. D. (1990) *Appl. Phys. Lett.* **56**, 1040.

Downey, S. W. and Hozack, R. S. (1989) in *Secondary Ion Mass Spectrometry (SIMS VII)*, eds. Benninghoven, A., Evans, C. A., McKeegan, K. D., Storm, H. A., and Werner, H. W. (Wiley, New York), p. 283.

Downey, S. W., Emerson, A. B., Kopf, R. F., and Kuo, J. M. (1990) *Surf. and Interf. Anal.* **15**, 781.

Driver, M. C. and Wright, G. T. (1963) *Proc. Phys. Soc. (London)* **81**, 141.

Duenas, S., Izpura, I., Arias, J., Enriquez, L., and Barbolla, J. (1991) *J. Appl. Phys.* **69**, 4300.

Eagles, D. M. (1960) *J. Phys. Chem. Solids* **16**, 76.

Faktor, M. M., Ambridge, T., Elliott, C. R., and Regnault, J. C. (1980) in *Current Topics in Materials Science* **6**, ed. Kaldis E. (North Holland, New York).

Gammon, D., Merlin, R., Masselink, W. T., and Morkoc, H. (1986) *Phys. Rev. B***33**, 2919.

George, T., Weber, E. R., Nozaki, S., Yamada, T., Konagai, M., and Takahashi, K. (1991) *Appl. Phys. Lett.* **59**, 60.

Göbel, E. O. (1982) in GaInAsP *Alloy Semiconductors*, ed. Pearsall, T. P. (Wiley, New York) p. 313.

Greiner, M. E. and Gibbons, J. F. (1984) *Appl. Phys. Lett.* **44**, 750.

Hall, E. H. (1879) *Am. J. Math.* **2**, 287.

Harris, T. D. (1992) personal communication.

https://doi.org/10.1017/CBO9780511599828.018 Published online by Cambridge University Press

337-TA-1366 RX-0255

Harris, T. D., Skolnick, M. S., Parsey, Jr., J. M. and Bhat, R. (1988) *Appl. Phys. Lett.* **52**, 389.

Haynes, J. R. (1960) *Phys. Rev. Lett.* **4**, 361.

Haynes, J. R. (1966) *Phys. Rev. Lett.* **17**, 860.

Henry, C. H. and Lang, D. V. (1977) *Phys. Rev. B* **15**, 989.

Henry, C. H., Hopfield, J. J., and Luther, L. C. (1966) *Phys. Rev. Lett.* **17**, 1178.

Herzog, R. K. and Liebl, H. (1963) *J. Appl. Phys.* **34**, 2893.

Hickmott, T. W. (1991) *Phys. Rev. B* **44**, 13487.

Hoke, W. E., Lemonias, P. J., Weir, D. G., Hendricks, H. T., and Jackson, G. S. (1991) *J. Appl. Phys.* **69**, 511.

Holtz, M., Zallen, R., Geissberger, A. E., and Sadler, R. A. (1986) *J. Appl. Phys.* **59**, 1946.

Hopfield, J. J. (1964) in *Proc. 7th Int. Conf. on the Phys. of Semicond.* (Academic, New York) p. 725.

Hornstra, J. and Bartels, W. J. (1978) *J. Cryst. Growth* **44**, 513.

Kennedy, D. P. and O'Brien (1969) *IBM J. Res. Develop.* **13**, 212.

Kennedy, D. P., Murley, P. C., and Kleinfelder, W. (1968) *IBM J. Res. Develop.* **12**, 399.

Kimerling, L. C. (1974) *J. Appl. Phys.* **45**, 1839.

Kitagawara, Y., Itoh, I., Noto, N., and Takenaka, T. (1986) *Appl. Phys. Lett.*, **48**, 788.

Knox, R. S. (1963) *Theory of Excitons* (Academic, New York).

Kroemer, H., Chien, W.-Y., Harris, Jrs. J. S., and Edwall, D. D. (1980) *Appl. Phys. Lett.* **36**, 295.

Lang, D. V. (1974) *J. Appl. Phys.* **45**, 3023.

Lang, D. V. (1979) in *Thermally Stimulated Relaxation in Solids*, ed. Bräunlich, P. (Springer, New York).

Lang, D. V., Cho, A. Y., Gossard, A. C., Ilegems, M., and Wiegmann, W. (1976) *J. Appl. Phys.* **47**, 2558.

https://doi.org/10.1017/CBO9780511599828.018 Published online by Cambridge University Press

Innoscience1366-00139291

RX-0255.618

Leigh, R. S. and Newman, R. C. (1982) *J. Phys. C: Solid State Phys.* **15**, L1045.

Levinson, M. and Temkin, H. (1983) *Appl. Phys. Lett.* **42**, 605.

Losee, D. L. (1972) *Appl. Phys. Lett.* **21**, 54.

Losee, D. L. (1975) *J. Appl. Phys.* **46**, 2204.

Macrander, A. T., Schwartz, B., and Focht, M. W. (1984) *J. Appl. Phys.* **55**, 3595.

Maguire, J., Murray R., Newman, R. C., Beall, R. B., and Harris, J. J. (1987) *Appl. Phys. Lett.* **50**, 516.

Martin, G. M., Mitonneau, A., and Mircea, A. (1977) *Electron. Lett.* **13**, 191.

Meyer, N. I. and Guldbrandson, T. (1963) *Proc. IEEE* **51**, 1631.

Miller, G. L. (1972) *IEEE Trans. Electron Devices* **19**, 1103.

Miller, G. L., Lang, D. V., and Kimerling, L. C. (1977) *Ann. Rev. Mater. Sci.* **7**, 377.

Miller, G. L., Ramirez, J. V., and Robinson, D. A. H. (1975) *J. Appl. Phys.* **46**, 2638.

Mircea, A., Mitonneau, A., and Hallais, J. (1977) *Phys. Rev. B* **16**, 3665.

Mitonneau, A., Martin, G. M., and Mircea, A. (1977) *Electron. Lett.* **13**, 666.

Moll, J. L. (1964) *Physics of Semiconductors*, (McGraw-Hill, New York).

Moss, T. S. (1954) *Proc. Phys. Soc. (London) B* **76**, 775.

Murray, R., Newman, R. C., Sangster, M. J. L., Beall, R. B., Harris, J. J., Wright, P. J., Wagner, J., and Ramsteiner, M. (1989) *J. Appl. Phys.* **66**, 2589.

Nakamura, T. and Katoda, T. (1985) *J. Appl. Phys.* **57**, 1084.

Newman, R. C. (1974) *Infrared Studies of Crystal Defects* (Taylor and Francis, London).

Newman, R. C., Thompson, F., Hyliands, M., and Peast, R. F. (1972) *Solid State Commun.* **10**, 505.

Oechsner, H., ed. (1984) *Thin Film and Depth Profile Analysis* (Springer, New York).

Omling, P., Samuelson, L., and Grimmeiss, H. G. (1983) *J. Appl. Phys.* **54**, 5117.

Pankove, J. I. (1965) *Phys. Rev.* **140**, A2059.

Perry, T. A., Merlin, R., Shanabrook, B. V., and Comas, J. (1985a) *J. Vac. Sci. Technol. B3*, 636.

https://doi.org/10.1017/CBO9780511599828.018 Published online by Cambridge University Press

Perry, T. A., Merlin, R., Shanabrook, B. V., and Comas, J. (1985b) *Phys. Rev. Lett.* **54**, 2623.

Pickering, C., Tapsten, P. R., Dean, P. J., and Ashen, D. J. (1983) *Inst. Phys. Conf. Ser.* **65**, 469.

Ramsteiner, M., Wagner, J., Emnen, H., and Maier, M. (1988) *Phys. Rev. B***38**, 10 669.

Rashba, E. I. and Sturge, M. D. (1982) *Excitons* (North-Holland, Amsterdam).

Redfield, D. (1963) *Phys. Rev.* **130**, 916.

Reynolds, D. C., Litton, C. W., Smith, E. B., Bajaj, K. K., Collins, T. C., and Pilkuhn, M. H. (1983) *Phys. Rev. B***28**, 1117.

Sah, C. T. (1967) *Proc. IEEE* **55**, 654, 672.

Sah, C. T. (1976) *Solid-State Electron.* **19**, 975.

Sah, C. T., Chan, W. W., Fu, H. S., and Walker, J. W. (1972) *Appl. Phys. Lett.* **20**, 193.

Sah, C. T., Forbes, L., Rosier, L. L., and Tasch Jr., A. F. (1970) *Solid State Electron.* **13**, 759.

Schubert, E. F., Göbel, E. O., Horikoshi, Y., Ploog, K., and Queisser, H. J. (1984) *Phys. Rev. B***30**, 813.

Schubert, E. F., Kopf, R. F., Kuo, J. M., Luftman, H. S., and Garbinski, P. A. (1990a) *Appl. Phys. Lett.* **57**, 497.

Schubert, E. F., Luftman, H. S., Kopf, R. F., Headrick, R. L., and Kuo, J. M. (1990b) *Appl. Phys. Lett.* **57**, 1799.

Shanabrook, B. V., Moore, W. J., and Bishop, S. G. (1986) *Phys. Rev. B***33**, 5943.

Sinai, J. J. and Wu, S. Y. (1989) *Phys. Rev. B***39**, 1856.

Skolnick, M. S., Dean, P. J., Groves, S. H., and Kuphal, E. (1984) *Appl. Phys. Lett.* **45**, 962.

Smith, R. A. (1978) *Semiconductors* (Cambridge University Press, Cambridge) p. 123.

Spitzer, W. (1971) in *Advances in Solid State Physics Vol. XI*, ed. Madelung, O. (Pergamon-Vieweg, Braunschweig).

Stillman, G. E., Wolfe, C. M., and Dimmock, J. O. (1977) in *Semiconductor and Semimetals Vol. 12*, eds. Willardson, R. K. and Beer, A. C. (Academic, New York).

https://doi.org/10.1017/CBO9780511599828.018 Published online by Cambridge University Press

Sturge, M. D. (1962) *Phys. Rev.* **127**, 768.

Takanohashi, T., Komiya, S., Yamazaki, S., Kishi, Y., and Umebu, I. (1984) *Jpn. J. Appl. Phys. (Lett.)* **23**, L849.

Takanohashi, T., Tanahashi, T., Sugawara, M., Kamite, K., and Nakajima, K. (1988) *J. Appl. Phys.* **63**, 1961.

Tasch, A. F. and Sah, C. T. (1970) *Phys. Rev. B***1**, 800.

Theis, W. M., Bajaj, K. K., Litton, C. W., and Spitzer, W. G. (1982) *Appl. Phys. Lett.* **41**, 70.

Thomas, C. O., Kahng, D., and Manz, R. C. (1962) *J. Electrochem. Soc.* **109**, 1055.

Thomas, D. G., Gershenzon, M., and Trumbore, F. A. (1964) *Phys. Rev.* **133**, A269.

Urbach, F. (1953) *Phys. Rev.* **92**, 1324.

Van der Pauw, L. J. (1958) *Philips Res. Rep.* **13**, 1.

Vincent, G., Chantre, A., and Bois, D. (1979) *J. Appl. Phys.* **50**, 5484.

Wagner, J. and Ramsteiner, M. (1986) *Appl. Phys. Lett.* **49**, 1369.

Wagner, J. and Ramsteiner, M. (1989) *IEEE J. Quant. Electron.* **25**, 993.

Wagner, J. and Seelewind, H. (1988) *J. Appl. Phys.* **64**, 2761.

Wagner, J., Ramsteiner, M., Seelewind, H., and Clark (1988) *J. Appl. Phys.* **64**, 802.

Wagner, J., Seelewind, H., and Kaufmann, U. (1986a) *Appl. Phys. Lett.* **48**, 1054.

Wagner, J., Seelewind, H., and Koidl, P. (1986b) *Appl. Phys. Lett.* **49**, 1080.

Wan, K. and Bray, R. (1985) *Phys. Rev. B32*, 5265.

Wiley, J. D. and Miller, G. L. (1975) *IEEE Trans. Electron Devices* **22**, 265.

Williams, E. W. and Bebb, H. B. (1972) in *Semiconductors and Semimetals* **8**, eds. Willardson, R. K. and Beer, A. C. (Academic, New York) p. 181

Wilson, R. G., Stevie, F. A., and Magee, C. W. (1989) *Secondary Ion Mass Spectrometry* (Wiley, New York).

Wolf, P. (1962) *Phys. Rev.* **126**, 405.

Wolfe, C. M. and Stillman, G. E. (1971) in *Gallium Arsenide and Related Compounds 1970*, (Inst. Phys. and Phys. Soc., London) p. 3.

https://doi.org/10.1017/CBO9780511599828.018 Published online by Cambridge University Press

337-TA-1366 RX-0255

Wright, G. B. and Mooradian, C. (1968) *Proc. 9th Inst. Conf. Phys. Semicon., Moscow, 1968* (Nauka, Leningrad) p. 1067.

Yacobi, B. G. and Holt, D. B. (1986) *J. Appl. Phys.* **59**, R1.

Appendixes

Adachi, S. (1985) *J. Appl. Phys.* **58**, R1.

Adachi, S. (1992) *Physical Properties of III-V Semiconductor Compounds* (Wiley, New York).

Blakemore, J. S. (1982) J. Appl. Phys. **53**, R123.

Casey, H. C. Jr., and Panish, M. B. (1978) *Heterostructure Lasers, Part A and B* (Academic, San Diego).

Landolt-Bornstein (1982) *Numerical Data and Functional Relationships in Science and Technology*, New Series, Hellwege, K.-H. (ed), *Group III: Crystal and Solid State Physics, Vol. 17, Semiconductors* (Springer, Berlin).

Landolt-Bornstein (1987) *Numerical Data and Functional Relationships in Science and Technology*, New Series, Madelung, O, (ed), *Group III: Crystal and Solid State Physics, Vol. 22, Semiconductors* (Springer, Berlin).

Neuberger, M. (1971) III-V semiconductor-data tables in *Handbook of Electronic Materials* **2**, (Plenum, New York).

Neuberger, M. (1972) III-V semiconductor-data tables in *Handbook of Electronic Materials* **7**, (Plenum, New York).

Pearsall, T. P. (ed) (1982) *GaInAsP Alloy Semiconductors* (Wiley, New York).

Properties of Gallium Arsenide, 2nd edition (INSPEC, IEE, London, 1990).

Properties of Indium Phosphide (INSPEC, IEE, London, 1991).

Shur, M. (1990) *Physics of Semiconductor Devices* (Prentice Hall, Englewood Cliffs).

https://doi.org/10.1017/CBO9780511599828.018 Published online by Cambridge University Press

Index

absorption, 39–40, 52–53, 195, 288, 371, 520–5
absorption characterization, 520–5
absorption coefficient, 520
absorption in doping superlattices, 418
acceptor, 2; *see also* hydrogenic acceptors, shallow acceptor
acceptor degeneracy, 25
acceptor energy, *see* ionization energy
acceptor–hydrogen complex, 378–9
acceptor in quantum barrier, *see* impurity in quantum barrier
acceptor in quantum well, *see* impurity in quantum well
acceptor wave functions, 22
actinides, 390–1
activation energy, 132
activation energy of impurities, *see* ionization energy
admittance spectroscopy, 505–8
AlGaAs, 292, 542
AlInAs, 543
AlInP, 292
alloy broadening, 517–19
AlSb, 25
amphotericity, 189, 198, 277–90, 301–3
annealing temperature, 270
antisite defect, 367–8, 373
antisite–interstitial pair, 367, 368
approximations for Fermi–Dirac integral of order $j=+\frac{1}{2}$, 107–14
approximations for Fermi–Dirac integral of order $j=0$, 115–16
approximations for Fermi–Dirac integral of order $j=-\frac{1}{2}$, 117
As_2 dimers, 199–200
As_4 tetramers, 199–200
Auger recombination, 70
Auger spectroscopy, 454
autocompensation, 189, 191, 198, 199–200, 255, 277–90, 301–3

baffle zone, 163
band filling, *see* Burstein–Moss shift
band structure, 22–3
band tails, 44–8
band-to-band transitions, 512
bandgap narrowing, 48–53
bandgap renormalization, *see* bandgap narrowing
bandgap shrinkage, *see* bandgap narrowing
Bardeen states, *see* surface states
Be, 182–5, 271, 276, 292, 328, 457
Be precursors, 219–22
Bloch function, 20
Bohr magneton, 11
Bohr model, *see* hydrogen atom model
Bohr radius, 9
Boltzmann distribution, 103
Boltzmann–Matano method, 316
bound exciton, 512–19
Bragg reflection, 536
Bridgman technique, 386–7
Brooks–Herring approximation, 399
brownian motion, 307–8
bulk equilibrium, 251–2, 279
Burstein–Moss shift, 37–41, 53
Burstein–Moss shift in two-dimensional systems, 39

C, 190–2, 292, 332, 458
C precursors, 230–3
Ca, 186
calibration, *see* doping calibration
capacitance change, 505
capacitance transient, 496–8, 502
capacitance–voltage profile, *see* CV profile
capping layer, 275

Published online by Cambridge University Press

337-TA-1366 RX-0255

capture, 60
capture cross section, 61, 74
capture energy, 74
capture energy of DX-centers, 361
capture probability, 61
capture rate, 61
capture transient, 63
carrier concentration, 118–36
cascade recombination, 69
cathodoluminescence, 509
Cd, 188–189
Cd precursors, 227–30
central cell, 26
central cell corrections, 25–7
central cell potential, 25
characterization techniques, 482–540
chemical-beam epitaxy, 149
chemical shift, 25
chloride vapor-phase epitaxy, 161
circular orbit, 11
co-implantation, 285
collision cascades, 268
compensated semiconductors, 128, 135
compensating native defects, *see* native defects
compensation, *see* autocompensation, compensated semiconductors
compositional distribution coefficient, 259–62
concentration-dependent amphotericity, 279, 286–90
concentration-dependent diffusion, 187–8, 274–5, 321–4, 291, 320
configuration coordinate diagram, 72–3
configuration coordinate diagram of DX-center, 362
configuration coordinate diagram of EL2 center, 370
congruent evaporation temperature, 253
continuity equation, 311–12
Conwell–Weisskopf approximation, 399
correlation energy, 364
coulombic repulsion, 293
Coulomb potential, 7
Cr, 336, 385–7
cracker cell, 147–8
critical thickness, 537
crucible, 140–1
CV concentration, 488
CV depth, 489
CV profile resolution, 450–4, 489–92
CV profiling, 487–95
Czochralski technique, 365–6, 385–7

D, *see* deuterium
dead volume, 156
Debye screening radius, 31, 489–90
deep donor, 125–8
deep level, 54–77, 354–91, 492–5
deep level transient spectroscopy, 496–503
deep impurity, *see* deep level
deep trap, *see* deep level
defect, 379; *see also* deep level, antisite defect, Frenkel defect, Schottky defect
defect formation energy, 299
degenerate states, 13
degeneracy, 22
delta doping, 407–11, 433–81
delta doping in bipolar transistors, 469–70
delta doping in diodes, 470
delta doping in doping superlattices, 412–22, 471–81
delta doping in field-effect transistors, 467–9
delta doping in heterojunctions, 465–7
delta doping in lasers, 476–80
delta doping in LEDs, 474–6
delta doping in modulators, 480–1
delta doping in ohmic contacts, 463–5
delta doping in superlattices, 414–22
density of states, 80–93
density of states in 3D systems 83, 93
density of states in 2D systems 87, 93
density of states in 1D systems 88, 93
density of states in 0D systems 89, 93
density-of-states effective mass, 84–5
density of states in presence of tail states, 46
depletion approximation, 487–8
depletion layer, 170, 394
deuterium, 375–6
devices, 463–81
diffusion, 307–38; *see also* concentration-dependent diffusion, hydrogen diffusion, impurity–defect complex diffusion, interchange diffusion, interstitial diffusion, self diffusion, substitutional diffusion, substitutional–interstitial diffusion
diffusion along imperfections, 325
diffusion barrier, 308
diffusion coefficient, *see* diffusion constant
diffusion constant, 188
diffusion constants of impurities, 328–37, 376, 382
diffusion constants for self diffusion, 251, 349–50
diffusion constant gradient, 310
diffusion hop, 307
diffusion in closed system, 275–6
diffusion in open system, 275–6
diffusion length, 60, 274, 313
diffusion measurement, 326–8
diffusion mechanisms, 316–25
discreteness of charge, 443–4
distribution coefficient, 245; *see also* compositional distribution coefficient,

Published online by Cambridge University Press

RX-0255.624

thermodynamic distribution coefficient
DLTS, *see* deep level transient spectroscopy
DLTS spectrum, 500
donor, 2; *see also* hydrogenic donors, shallow donor
donor–acceptor pair transition, 511
donor-complex center, *see* DX-center
donor degeneracy, 21
donor energy, *see* ionization energy
donor–hydrogen complex, 377
donor in quantum barrier, *see* impurity in quantum barrier
donor in quantum well, *see* impurity in quantum well
donor wave functions, 20
doping calibration, 170–7
doping distribution in delta-doped semiconductors, 446–58
doping during epitaxial growth, 249–62
doping efficiency, 222, 267, 357
doping filament, *see* filament doping
doping homogeneity, 177–81, 213–19
doping in heterostructures, 392–412
doping incorporation by diffusion, 272–7
doping incorporation by implantation, 262–72
doping incorporation during MBE, 251–8
doping incorporation during OMVPE, 251–8
doping impurity flux, 165
doping precursors, 208–47
doping profile, 176–9, 326–7, 346–7, 449–56, 487–95
doping saturation, *see* saturation
doping superlattice, 412–22, 471–81
doping uniformity, 177–81, 213–19
drift mobility, 485
drift velocity, 309–10
DX-center, 303–4, 355–65, 462

effective Bohr radius, 19, 23
effective density of states, 89–93
effective density of states in 3D systems, 91, 93
effective density of states in 2D systems, 92–3
effective density of states in 1D systems, 92–3
effective mass, 18
effective-mass-like acceptors, *see* hydrogenic acceptors
effective-mass-like donors, *see* hydrogenic donors
effective Rydberg energy, 19, 23
effective Rydberg energy of impurity in quantum barrier, 429–31
effective Rydberg energy of impurity in quantum well, 426–8
effusion cell, 141–2, 167–9
Einstein relation, 310
EL2 defect, 58, 365–73
electrochemical profiling, 174, 495
electroluminescence, 509
electronegativity, 26
electron gas, 94
electronic structure of delta-doped semiconductors, 434–45
electronic structure of delta-doped superlattices, 444–45
elemental dopants, 181–207
elemental doping in CBE and OMMBE, 211–13
elemental sources, 165–207
elliptical orbits, 11
emission, 60
emission energy, 74
emission energy of DX-centers, 361
emission probability, 62
emission rate, 62
emission transient, 63
endothermic reaction, 131
energy distribution function, 94
enthalpy, 249
entropy, 249–50
envelope function, 20
epitaxy 137–64
equilibrium, *see* bulk equilibrium, local equilibrium, surface equilibrium
equipartition law, 99, 166
Er, 390–1
exciton, 512–19
exothermic reaction, 131

Fang–Howard wave function, 395–6
far-infra-red absorption, 523
Fe, 337, 387
Fe precursors, 388
Fermi–Dirac distribution, 103–7
Fermi–Dirac integral of order $j=+\frac{1}{2}$, 107–14
Fermi–Dirac integral of order $j=0$, 114–16
Fermi–Dirac integral of order $j=-\frac{1}{2}$, 116–17
Fermi gas, 104
Fermi level pinning, 293
Fermi-level-pinning induced surface drift, 343–9
fermion, 104
fickian diffusion, 311–16
filament doping, 170–3
finite reservoir, 312
first-order surface segregation, 339–43
flow controller, 146, 151
flow transient, 159
fluid dynamics, 260
flux distribution, 169
formation energy, 249, 299
Franck–Condon energy, *see* Franck–Condon shift
Franck–Condon principle, 72
Franck–Condon shift, 73, 360

Published online by Cambridge University Press

337-TA-1366 RX-0255

free exciton, 512–19
Frenkel defect, 318–19
freeze-out regime, 486
fundamental absorption edge, 520

GaAs, 25, 292, 541
GaAs, *see* semi-insulating GaAs
GaInAs, 292, 543
GaInP, 292
GaInPAs, 544
gaseous doping sources, 208–47
gas manifold, 158
gas-source molecular-beam epitaxy, 146
GaP, 25
GaSb, 25, 292
gaussian distribution, 312–13
Ge, 198–200, 276, 333
Gibbs free energy, 79, 249
group-II dopants, 182–9
group-II doping precursors, 219–30
group-IV dopants, 189–202
group-IV doping precursors, 230–41
group-VI dopants, 202–7
group-VI doping precursors, 241–7
growth, 137–64
growth of delta-doped semiconductors, 446–8
growth rate, 226–7
growth temperature, *see* substrate temperature
growth zone, 163

Hall carrier concentration, 484
Hall coefficient, 484
Hall effect, 483–7
Hall factor, 484
Hall mobility, 484–5
Haynes' rule, 516
hetero-bipolar transistor, 4
heterojunction band discontinuity, 465–7
heterostructure, 392–412
Hg, 189
high doping effects, 34–53
homogeneity, *see* doping homogeneity
homogeneous line broadening, 519
Hooke's law, 360
hopping conduction, 41
Huang–Rhys parameter, 75
hydride, 210
hydride source, 146
hydride vapor-phase epitaxy, 161
hydrogen, 374–84
hydrogen atom model, 7–14
hydrogen atom wave functions, *see* wave functions of hydrogen atom
hydrogen diffusion, 374–9, 382
hydrogen during epitaxial growth, 383–4
hydrogen implantation, 379–83
hydrogenic acceptors, 21–5
hydrogenic donors, 18–21
hydrogenic impurity, 6
hydrogenic wave functions, *see* wave functions of hydrogenic impurities

ideal gas, 94
ideal gas law, 97, 166
ideal gas theory, 97
implantation, 262–72, 379–83
implantation damage, 381–2
implantation profile, 265–70, 381
impurity, 1
impurity-assisted luminescence transitions, 510–20
impurity band, 41–4
impurity band conduction, 41
impurity band width, 43–4
impurity characteristics, 248–305
impurity–defect complex diffusion, 318
impurity drift, 309–10
impurity in quantum barrier, 422–32
impurity in quantum well, 422–32
impurity incorporation, *see* doping incorporation
impurity-induced layer disordering, 349–53
impurity luminescence, 390–1
impurity neutralization, 377
impurity passivation, 377
impurity scattering, 398–404
InAs, 25, 292, 541
infinite reservoir, 272–3, 313
inhomogeneous line broadening, 519
intra-center absorption, 371–2
intrinsic carrier concentration, 119–20, 133
intrinsic semiconductors, 118–20, 132–3
InP, 25, 292, 541
InP, *see* semi-insulating InP
InSb, 25
insulator-to-metal transition, *see* Mott transition
interchange diffusion, 324
interstitial diffusion, 321
intra-center absorption, 371
intrinsic carrier concentration, 119–20, 133
intrinsic regime, 123–4
inverted heterostructure, *see* heterostructure
ion implantation, *see* implantation
ionization energy, 20, 36–7, 121, 394
ionization energy of DX-center, 355–7
ionization energy of impurity in quantum barrier, 429–31
ionization energy of impurity in quantum well, 426–8
ionization regime, 123–4
ionized impurity scattering, *see* impurity scattering
isoelectronic impurity, 26

Published online by Cambridge University Press

RX-0255.626

Kane function, 46
Knudsen cell, *see* effusion cell

lanthanides, 390–1
large lattice relaxation, 71–5
laser, 476–80
lattice contraction, 536–40
lattice expansion, 536–40
lattice relaxation, *see* large lattice relaxation, small lattice relaxation
lattice relaxation through breathing mode, 365
lattice relaxation through broken bond, 362–4, 373
law of mass action, 130–2, 249–51
LEC, *see* Czochralski technique
lifetime killer, 55
light-emitting diode, 474–6
line broadening, 519
linear screening, 30
local equilibrium, 251
localized vibrational modes, 528–30
local vibrational mode spectroscopy, 194–5, 287–8, 526–31
longitudinal straggle, *see* straggle
low-pressure organometallic vapor-phase epitaxy, 156
low-temperature GaAs, 367–8
luminescence, *see* impurity luminescence
luminescence in doping superlattices, 420–2
luminescence killer, *see* lifetime killer
luminescence spectroscopy, 509–20
Luttinger parameters, 23, 25

majority carrier, 122
many-body interactions, 48–9
mass-transport limitation, 262
materials, 139
matrix effect, 534
Matthiessen's rule, 400
maximum doping concentration, 290–305
Maxwell–Boltzmann distribution, 102
Maxwell velocity distribution, 99–102
memory effect, 155, 210
metalorganic molecular-beam epitaxy, *see* organometallic molecular-beam epitaxy
metalorganic vapor-phase epitaxy, *see* organometallic vapor-phase epitaxy
metal-to-insulator transition, *see* Mott transition
metastable state, 361, 369
Mg, 185–6, 272, 330
Mg precursors, 222–3
migration, *see* surface migration
minority carrier, 122
minority carrier lifetime, 66–7
mobility, *see* drift mobility, Hall mobility
mobility of free carriers, 192, 231, 240, 247, 398–404, 407–10, 460–2
mobility of impurity ions, 309–10
modulation doped heterostructure, *see* heterostructure
modulator, 480–1
molecular beam, 154
molecular-beam epitaxy, 137–46
Mott criterion, 35–6
Mott density, 36
Mott transition, 34–7
multiphonon recombination, 68–71
multiple valleys, *see* subsidiary minima
multiwafer system, 153

native defects, 297–301
Nd, 390–1
negative-U center, 364
net capture rate, 65
non-linear screening, 30, 33

O, 203, 389–90
O-level, 365
ohmic contacts, 276, 463–5
ordered impurity distributions, 43, 462
organometallic compounds, 150–61, 219–47
organometallic molecular-beam epitaxy, *see* chemical-beam epitaxy
organometallic vapor-phase epitaxy, 153
orientation, 283–5
oxygen implantation, 389

parabolic quantum well, 440
Pauli principle, 16, 49, 80
Pb, 202
persistent photoconductivity, 74–5, 358–9
persistent photocurrent, *see* persistent photoconductivity
phase space filling, *see* Burstein–Moss shift
photocapacitance, 369–70
photocurrent spectroscopy, 523
photoluminescence, 509
Po, 207
Poisson distribution, 296
Poole–Frenkel effect, 75–7, 502
Poole–Frenkel energy, 76
p-orbital, 2, 372
Pr, 390–1
pressure, *see* vapor pressure
pressure controller, 146, 151
principle of detailed balance, 61
projected range, *see* range
projected straggle, *see* straggle
pump, 145, 152

quantization of angular momentum, 8, 11
quantization of energy, 10–18, 395–7, 421–2, 423–32, 434–45

Published online by Cambridge University Press

quantization of energy in doping superlattice, 415–22
quantum barrier, 422–32
quantum number, 13, 16
quantum well, 422–32

radiative recombination, 71, 510–20
Raman characterization, 525–7
random impurity distribution, 43, 296, 462
range, 264–7
rare-earth impurities, 390–1
rate equations, 257
reaction zone, 163
reactor design, 156
recombination, 60; *see also* Auger recombination, cascade recombination, multiphonon recombination, radiative recombination, Shockley–Read recombination
redistribution effects, 306–53
redistribution effects in delta-doped semiconductors, 454–8
Rydberg energy, 10

S, 203–5, 335
S precursors, 241–3
saturation, 189, 302, 459
saturation regime, 123–4
sawtooth superlattices, 412–2, 471–81
scattering mechanisms, 401–4
Schottky defect, 318–19
Schrödinger equation, 15, 423
screened Coulomb potential, 28, 31
screening, 27–34
screening radius, *see* Debye screening radius, Thomas–Fermi screening radius
Se, 205, 271, 292, 335
Se precursors, 243–4
secondary ion mass spectrometry, 532–5
segregation, *see* surface segregation, first-order surface segregation, zero-order surface segregation
selectively doped heterostructures, *see* heterostructures
self-consistent calculation, 440–2
self diffusion, 251, 349–53
semiconductor statistics, 78–136
semi-insulating InP, 379, 385, 387–8
semi-insulating GaAs, 366–7, 374, 379, 385–7
shallow acceptor, 6, 21–5
shallow donor, 6, 18–21
shallow impurity, 6–53
Shockley–Read recombination, 64
Shockley–Read recombination rate, 66, 508
short range potential, 26, 55
Shubnikov–de Haas oscillation, 406
shutter, 142–3
Si, 192–8, 271, 292, 332, 458
Si precursors, 233–8
SIMS, *see* secondary ion mass spectrometry
SIMS resolution, 448–50
small lattice relaxation, 72–3
Sn, 200–2, 276, 292, 334
Sn precursors, 238–241
Sommerfeld fine structure constant, 10
solubility, 304–5
source zone, 161
s-orbital, 2–3, 372
spacer layer, 395, 398, 404–5
spin, 13–14, 49, 104
sp^3-bonded impurity, 59
stagnant layer, 159–60
Stark effect, 13
Stefan–Boltzmann law, 174
strain, 304–5, 536
straggle, 264–7
subband energies of delta-doped semiconductors, 438–9
subband energies of parabolic wells, 440
subband energies of triangular wells, 397, 437–9
subsidiary minima, 27, 85
substitutional diffusion, 317–18
substitutional–interstitial diffusion, 321–4
substitutional impurity, 1
substrate holder, 143–4
substrate orientation, *see* orientation
substrate rotation, 217
substrate temperature, 143–5, 155, 189, 196–7, 252, 256–7, 281, 456
superlattice, *see* doping superlattice
superlattice interdiffusion, *see* impurity-induced layer disordering
surface equilibrium, 251–2, 279
surface migration, 337–49, 410–12
surface segregation, 202, 337–49
surface states, 54, 293, 343
surface structure, 284
surface vacancy concentration, 252–3

tail states, *see* band tails
Te, 206, 292, 336
Te precursors, 244–7
tetrahedral bonds, 58, 363
thermal decomposition, 210
thermal line broadening, 519
thermally stimulated capacitance, 503–8
thermally stimulated current, 503–8
thermocouple, 141
thermodynamics, 249
thermodynamic distribution coefficient, 259
thickness uniformity, 218
Thomas–Fermi screening radius, 31, 490

Published online by Cambridge University Press

337-TA-1366 RX-0255

three temperature method, 137, 368
transport, 458–62, 473–4
trap, *see* deep level
TSCAP, *see* thermally stimulated capacitance
TSC, *see* thermally stimulated current
two-dimensional electron gas, 392–8
two-dimensional screening, 33
two-donor model, 124, 355–9

uncertainty relation, 56–7, 80
uniformity, *see* doping uniformity, thickness uniformity
Urbach tail, 418, 523

V/III flux ratio, 189, 196, 199, 281
van der Pauw technique, 485
vapor-phase epitaxy, 161
vapor pressure, 140, 154, 157
variational calculation, 395–7, 437–40
Vegard's law, 539–40
viscous flow, 154
V-shaped quantum well, 437–43

wave function, *see* Fang–Howard wave function
wave functions of hydrogen atom, 14–17
wave functions of hydrogenic impurities, 3, 14–17
wave functions of impurities in quantum wells, 425

X-ray characterization, 535–40

Yb, 390–1
Yukawa potentials, 32

Zeeman effect, 13
zero-order surface segregation, 338–9
Zn, 186–8, 276, 292, 330, 457
Zn precursors, 223–7

Published online by Cambridge University Press

Innoscience1366-00139302

RX-0255.629